Characterization Strategies for Bone Ultrastructure and Bone-Cell Interfacing Materials

Characterization Strategies for Bone Ultrastructure and Bone-Cell Interfacing Materials

Bryan E. J. Lee, B.Eng.Biosci

A Thesis Submitted to the School of Graduate Studies in Partial Fulfillment of the Requirements
for the Degree Doctor of Philosophy

McMaster University

Doctor of Philosophy (2019)   **McMaster University**
(Biomedical Engineering)   **Hamilton, Ontario, Canada**

Title: Characterization Strategies for Bone Ultrastructure and Bone-Cell Interfacing Materials

Author: Bryan E. J. Lee, B.Eng.Biosci (McMaster University)

Supervisor: Prof. Dr. Kathryn Grandfield

Number of Pages: xvi, 110

Lay Abstract

Bone implant devices are required to treat, augment, or replace bone tissue in dental and orthopaedic applications. These, often metallic, implanted devices have success when a structural and functional connection with natural bone tissue is created, a phenomenon known as osseointegration. Good osseointegration is required to ensure stability of the implant without compromising the quality of life of the patient. In order to improve osseointegration of biomaterials, both sides of the interface, i.e. the bone and implant surface, must be better understood. This thesis focuses on exploring methods to improve the evaluation and understanding of both bone structure at the nanoscale and structured metallic implant surfaces for the design of bone-interfacing biomaterials.

Abstract

The repair of damaged or diseased bone tissue often requires the use of metallic implants which form an interface with the surrounding bone tissue. Understanding this interface is important for improving the outcomes of implant placement and overall health of patients. Bone is a composite material of organic collagen fibrils and inorganic mineral phases that have structural variations across multiple length scales. This heterogeneous and hierarchical nature poses characterization challenges for (i) understanding bone, (ii) creating biomaterial structures that mimic it, and (iii) approaches for evaluating biomaterials. These challenges formed the basis for the three papers presented in this thesis. In Chapter 3, leporine bone was examined using atom probe tomography (APT) to visualize *in vivo* mineralized collagen fibrils, their chemical composition, and spatial arrangement in 3D with sub-nanometer accuracy. This provided new insight into the location of biomineral with respect to collagen and demonstrated the power of APT for understanding collagen-mineral arrangement. In Chapter 4, commercially pure titanium was laser ablated to generate periodic surface structures inspired by the periodicity of collagen. Three different periodicities were generated with submicron-scale roughness and a high degree of reproducibility. All the surfaces were non-cytotoxic and encouraged cells to adhere perpendicular to the orientation of the surface structures. In Chapter 5, a simple five-minute room temperature ionic liquid treatment was developed to investigate the same laser-ablated titanium periodic structures with osteoblast-like cells adhered. The development of this technique fulfills an important niche in biological imaging by allowing for simultaneous and repeated visualization of submicron surface features and wet cells. Therefore, the combined impact of this thesis is novel imaging and biomaterials evaluation strategies to (i) improve understanding of bone structure; (ii) leading to bioinspired biomaterials design; and (iii) new methods for simultaneous biological and biomaterials evaluation.

Acknowledgements

Table of Contents

List of Figures

Figure 3-2. The winding collagen fibrils present with the mineralized matrix of leporine bone represented in three different reconstructed datasets. The carbon isosurfaces (A,B,C) (11 at%) show a fibril-like structure that is not directly parallel to the lift-out but instead appears to have some helical curvature. An individual fibril section from the reconstruction in C is isolated in D and shown along with calcium isosurface (29 at%) in E suggesting that the calcium envelopes the carbon fibril.

Figure 3-3. Isolated collagen fibrils (B) from three different reconstructed datasets (A) with corresponding calcium atomic density maps for the same region (C). A represents the original reconstruction previously shown in Figure 2, B represents the extracted collagen fibril from indicated regions in A, and C shows calcium atomic density maps. The extracted collagen fibril isosurfaces (11 at%) from all three tips show a winding structure (B). Calcium is most dense in the regions outside of the fibril (C), and example shown by the asterisk (*) on the red/top specimen. However, calcium is also present in varying high density regions within the fibrils, most visible in the yellow/middle tip, marked by arrows (^). The dimensions for B and C are identical.

Figure 3-4. Ionic density maps visualized from the y,z and x,y planes of a collagen fibril showing distinct phases of mineral and collagen. Carbon (A) and nitrogen (C) are co-localized to form the collagen fibril while calcium (B) and phosphorus (D) are co-localized to form the mineral. The mineral is predominantly external to the collagen fibril, marked by asterisks (*) in (A) and (B). However, periodic increases in mineral density are visible within the collagen fibril, marked by arrows (^) in (A) and (B). A periodic spacing that approximates to 30 nm, indicated by dashed lines (- - -), can be observed in calcium and phosphorus maps.

Figure 3-5. Demonstration of the spatial relationship between mineral and the collagen fibril. (A) Calcium isosurface (grey, 30.3 at%) alone showing a distinct gap in the centre of the sample. (B) Calcium isosurface rendered with carbon isosurface (blue, 11 at%) showing that the collagen fibril is enveloped completely by the mineral. (C) Carbon isosurface alone with red and purple arrows indicating the directions for the proxigram (D). Movement along the red arrow indicates measurements taken from the edge of the carbon isosurface towards the centre of the collagen fibril, while movement along the purple arrows indicates measurements taken from the edge of the carbon isosurface outwards into the extrafibrillar region. (D) Proxigram shows that while the collagen fibril is carbon and nitrogen dominant (under the red arrow), there are still significant amounts of calcium and phosphorus present suggesting intrafibrillar mineralization.

Figure 3-6. APT of a collagen fibril with representative mass spectra inside and outside of the fibril. An extracted collagen fibril (A; isosurface, 11 at%) along with carbon ionic density map (B) is shown. In the region specific mass spectra (C,D), there are greater quantities of mineral associated ions in the mineral region located exterior to the collagen fibril (D) (e.g. Ca, PO_2) compared to that inside the fibril (C). The select ionic species indicated on the full tip mass spectra are some of those important to bone structure.

Figure 3-7. Cluster analysis of mineral proximity to collagen. Fitted helical model for a collagen fibril alongside extracted *x,y,z* coordinates of collagen fibril (A). Clusters of Ca/P with ratios of 1.4-1.6 (representing ACP) and 1.6-1.8 (representing HA) visualized using *x,y,z* coordinates (B). Histograms illustrating that up to 5 nm away from the fibril there is no difference in the amount of ACP vs. HA (C).

Figure 3-S1: Preparation of sectioned bone into APT tip. An appropriate region of interest was identified in SEM (A/B). The area around the ROI was milled away using Ga ions (C) before being extracted using a micromanipulator (D). The removed section was split into several pieces (E) each of which were sharpened (F/G/H) into the needle shape required to perform APT.

Figure 3-S2: Rotated Isosurfaces Renderings of 3 APT tips: C (11 at%, blue, yellow and red) and Ca (29 at%, grey)

Figure 3-S3: Single isolated fibril section showing C (11 at%, red) and Ca (29 at%, grey). The encapsulation of collagen, represented by carbon, is clear.

Figure 3-S4. Isolated collagen fibrils from three different reconstructed datasets with corresponding calcium and carbon atomic density maps for the same region. Figure 3-3 with carbon ionic maps added. Dimensions for B,C, and D are the identical. D shows that the carbon density matches the spatial coordinates of the isolated collagen fibrils shown via isosurface rendering in B.

Figure 3-S5. Extracted collagen fibril superimposed on atomic density maps of calcium and phosphorous. An extracted fibril, 285 nm in length, is shown to both incorporate and be encapsulated by calcium and phosphorus demonstrating that while extrafibrillar mineralization dominates, intrafibrillar mineralization is also occurring in bone.

Figure 3-S6: Correlative electron tomography from STEM- HAADF images. APT detector and evaporation efficiency reconstruction parameters were altered using structural information from STEM imaging to improve APT reconstruction accuracy. Representative APT tip shown overlapping the STEM image in cyan.

Figure 5-1. Schematic demonstrating the method used in this paper. A) Preparation of samples for imaging. B) Evaluation of cell metabolism following imaging in SEM.

Figure 5-2. Cell metabolism data for cells, plated on 12 well plates that were either exposed to RTIL for 5 minutes or unaltered. There was no statistically significant ($p < 0.05$) difference in cell metabolism of treated and non-treated cells (A). Cells were stained with Nile Red after 3 days and show comparable morphology in RTIL compared to control treatments.

Figure 5-3. Cells adhered to titanium substrates after 5 minutes of ionic liquid treatment. Cells can be observed across the entire substrate (A/B) and in detail with respect to sub-micron features (C/D).

Figure 5-4. Demonstration of cells visualized on laser ablated (A/B) and unmodified (C/D) titanium observed using SEM with ionic liquid treatment alongside correlated fluorescent cell metabolism readings. The difference in position of the cells in (A/C) compared to (B/D) show how the cells are unchanged in shape or location following multiple SEM irradiations sessions and RTIL treatments. (1) – scratch to close cell, (2) – scratch to far cell, (3) – cell to cell.

Figure 5-5. Demonstration of the viability of cells following RTIL treatment and imaging, in low-vacuum mode, in the SEM. Cells appear elongated which is indicative of cellular viability following treatments. Cells were detached from titanium substrates with trypsin and re-plated into empty 12 well plates. Cells were imaged 1 (A) and 3 (B/C) days after replating. (C) shows cells that were stained by Nile Red, a lipid stain.

Figure 5-S1: Example of cells adhered perpendicular to the LIPSS pattern. Cells adhered to LIPSS titanium, and visualized via traditional SEM sample preparation, tended to be adhered perpendicular to the LIPSS pattern.

List of Tables

List of Abbreviations

2D	two-dimensional
2L	2 wt% alginate printed on low calcium papers
3D	three-dimensional
3H	3 wt% alginate printed on high calcium papers
4D	four-dimensional
ABA	alamarBlue™ assay
ACP	amorphous calcium phosphate
ACTB,	beta actin
AFM	atomic force microscopy
AES	auger electron spectroscopy
ALP/ALPL	alkaline phosphatase
APT	atom probe tomography
BF-TEM	bright-field TEM
BSA	bicinchoninic acid
BSE	backscattered electron
CCD	charge-coupled device
cDNA	complementary DNA
DAPI	4′,6-diamidino-2-phenylindole
DNA	deoxyribonucleic acid
ECM	extracellular matrix
EDM	electric discharge machining
EDS/EDX	energy dispersive spectroscopy
EDTA	ethylenediaminetetraacetic acid
EELS	electron energy loss spectroscopy
ELNES	energy-loss near-edge structures
ESEM	environmental scanning electron microscopy
ExCeL	combining Extrusion Printing on Cellulose Scaffolds with Lamination
FBS	fetal bovine serum
FIB	focused ion beam
FITC	fluorescein isothiocyanate
FWHM	full width half maximum
GADH	Glyceraldehyde 3-phosphate dehydrogenase
GIF	gatan imaging filter
HA	hydroxyapatite
HAADF	high angle annular dark-field
IVAS™	Integrated Visualization and Analysis Software
LIPSS	laser induced periodic surface structures
LSFL	low-spatial frequency LIPSS
MMP	matrix metallopeptidase
MMP9	matrix metallopeptidase 9
mRNA	messenger RNA
MTT	3-(4,5-dimethylthiazol-2-yl)-2,5-diphenyltetrazolium bromide

NCPs	non-collagenous proteins
PBS	phosphate buffered saline
PCA	principle component analysis
PCR	polymerase chain reaction
qRT-PCR	quantitative reverse transcription polymerase chain reaction
R_A	average roughness
R_{Max}	maximum roughness depth
RGD	arginylglycylaspartic acid
RNA	ribonucleic acid
ROI	region of interest
RTIL	room temperature ionic liquid
SAED	selected area electron diffraction
SE	secondary electron
SEM	scanning electron microscope
SIMS	secondary ion mass spectrometry
SP	surface plasmon
STEM	scanning transmission electron microscope
TEM	transmission electron microscope
Ti6Al4V	Ti-6Al-4V alloy
TIMP1	tissue inhibitor of metalloproteinases 1
TIMP2	tissue inhibitor of metalloproteinases 2
TXRED	sulforhodamine 101 acid chloride
XRD	x-ray diffraction
XTT	(2,3-Bis-(2-Methoxy-4-Nitro-5-Sulfophenyl)-2H-Tetrazolium-5-Carboxanilide)

Declaration of Academic Achievement

The major results of my PhD research were published or drafted as manuscripts for submission to peer-reviewed journals. They consist of the three following pieces of work:

Lee, B. E. J., Langelier, B., & Grandfield, K. Visualization of *In vivo* Mineralization using Atom Probe Tomography. *(submitted)*

Contributions: In Chapter 3, experimental assistance by technician was required and received from Brian Langelier for APT data acquisition and specimen preparation. I designed the protocol for APT sample preparation with suggestions from Kathryn Grandfield, prepared the tissue, and performed all SEM experiments. STEM tomography assistance was provided by Andreas Korinek and Kathryn Grandfield. I performed the APT data reconstructions, analyzed all data, and prepared all figures and videos. The manuscript was initially drafted by myself and edited by both Brian Langelier and Kathryn Grandfield. The version of the manuscript shown below has been submitted for publication in 2019.

Lee, B. E. J., Exir, H., Weck, A., & Grandfield, K. (2018). Characterization and evaluation of femtosecond laser-induced sub-micron periodic structures generated on titanium to improve osseointegration of implants. *Applied Surface Science*, *441*, 1034–1042.

Contributions: In Chapter 4, collaborator Hourieh Exir carried out the laser modification under the supervision of Arnaud Weck, based on my geometrical recommendations and study design. Travis Casagrande helped prepare samples for TEM analysis and assisted with AES experiments based on my study design. Carmen Andrei assisted with TEM imaging and EELS data collection. All other materials characterization including SEM, AFM, contact angle and *in vitro* evaluation was conducted by myself. Data processing and analysis was all conducted by myself. The manuscript was initially drafted by myself and edited by Hourieh Exir, Arnaud Weck and finally Kathryn Grandfield. This chapter has been published in Applied Surface Science.

Lee, B. E. J., Exir, H., Weck, A., & Grandfield, K. Capturing Mammalian Cell Adhesion to Sub-Micron Surface Features with Ionic Liquids in Low-Vacuum SEM. *(submitted)*

Contributions: In Chapter 5, laser-modified samples were previously synthesized by Hourieh Exir under the supervision of Arnaud Weck as shown in Chapter 4. I designed the experimental protocols and conducted all RTIL treatments, assays, SEM, and resulting data analysis. The manuscript was initially drafted by myself and edited by Hourieh Exir, Arnaud Weck and finally Kathryn Grandfield. The version of the manuscript shown below has been submitted for publication in 2019 with revisions requested and resubmitted.

In addition to the work presented in the main body of this thesis, I am also co-author of three other published articles relevant to my PhD project. The articles are attached in the appendix.

Lee, B. E.J., Luo, L., Grandfield, K., Andrei, C. M., & Schwarcz, H. P. (2019). Identification of collagen fibrils in cross sections of bone by electron energy loss spectroscopy (EELS). *Micron*, 102706.

This work is a complementary to my study of bone structure in this thesis. I conducted all the EELS data analysis and because of my findings wrote the second draft of the manuscript. Lucy Luo prepared samples and conducted experiments with Carmen Andrei. The manuscript was edited by Henry Schwarcz and Kathryn Grandfield. This paper has been published in Micron.

Lee, B. E. J., Ho, S., Mestres, G., Karlsson Ott, M., Koshy, P., & Grandfield, K. (2016). Dual-topography electrical discharge machining of titanium to improve biocompatibility. *Surface and Coatings Technology*, *296*, 149–156.

This work is a complementary to my study of titanium surface modification in this thesis. I wrote the initial manuscript draft, conducted x-ray diffraction experiments, and performed x-ray diffraction and auger electron spectroscopy analysis. *In vitro* tests were performed by Gemma Mestres under the supervision of Marjam Karlsson Ott. Surface modification was performed by Samantha Ho under the supervision of Phil Koshy, and materials characterization by Samantha Ho. This paper has been published in Surface & Coatings Technology.

Lee, B. E.J.*, Shahin-Shamsabadi, A.*, Wong, M, K., Raha, S., Selvaganapathy, R., Grandfield, K. (2019) A Bioprinted *in vitro* Model for Osteoblast to Osteocyte Transformation by Changing Mechanical Properties of the ECM. *Advanced Biosystems. *These authors contributed equally to this work.*

This work is a complementary to my study of improving *in vitro* testing methods in this thesis. A bioprinted model of bone, such as that created herein capable of differentiating osteoblasts to osteocytes, has the potential to be used as an *in vitro* testing platform for other questions in mineralization. This study was conceptualized, designed, and all experiments and data analysis were conducted jointly by Alireza Shahin-Shamsabadi and myself. The manuscript was initially drafted jointly by Alireza Shahin-Shamsabadi and myself. Michael Wong performed polymerase chain reaction (PCR) experiments under the supervision of Sandy Raha. The manuscript was subsequently edited by Ravi Selvaganapathy and Kathryn Grandfield. This paper has been published in Advanced Biosystems and is featured as the back cover.

Chapter 1: Introduction

1.1 Research Motivation

Bone is an essential tissue for the structure and function of the human body [1]. A consequence of use, aging, and growth is that bone is constantly being remodeled, repaired, or replaced [1]. In some instances of trauma or disease, bone is sufficiently damaged or defected to a state that cannot be naturally repaired by the body. In these scenarios, implanted biomaterials, especially dental or orthopaedic implants, have become a commonplace solution. In Canada, $894 M was spent on hip and knee implants in 2017-2018 with an additional $123 M devoted to revision surgeries [2]. The success of these biomaterials is predicated by a strong functional and structural connection formed between the existing bone and the implanted device, defined as osseointegration [3]. Additionally, as our society ages, biomaterials are required to have a greater longevity and early osseointegration becomes even more paramount to successful implant outcomes [4]. Therefore, strategies that improve osseointegration are important to investigate. Understanding both sides of the interface, i.e. bone and biomaterial, is crucial for the design of suitable osseointegrated implants. This creates a sequence of necessary research undertaken in this thesis. Firstly, bone structure must be well-characterized to understand the natural template for bone growth. It follows that biomaterials surfaces could be designed while conscientious of the structure of bone, so-called bioinspired design. Subsequently, methods to accurately evaluate the response of bone cells to these biomaterials are essential to further improve biomaterials design.

Characterizing Bone Structure
Bone is a complex and hierarchical composite material. Its smallest building-block, the mineralized collagen fibril, creates all higher-order structures, and is the first bone structure deposited at the implant interface after initial interactions of proteins and cells [5], [6]. Bone has been well-characterized at the macro-, micro-, and even nanoscale using a variety of microscopy techniques ranging from light microscopy, to scanning electron microscopy (SEM), to transmission electron microscopy (TEM), which are all two-dimensional in nature [7]–[9]. X-ray micro-computed tomography [10], [11], focused ion beam serial sectioning [12], [13], and electron tomography [14], [15] are complementary approaches employed for visualizing bone as a three-dimensional (3D) object. Newer approaches to electron tomography applied to bone-implant interfaces have added a fourth dimension (4D) – chemistry, by incorporating corresponding chemical information to each 3D voxel in a reconstructed volume [16]. The current understanding of the collagen-mineral arrangement within a collagen fibril is based on electron tomography methods only, with no corresponding chemistry. As such, three spatially distinct models for bone exist, with no consensus [7], [17], [18]. A suitable approach to combine 3D and chemical information to probe the collagen-mineral arrangement is needed, and herein was achieved on the atomic scale using atom probe tomography (APT) of oriented specimens of bone. APT is a field

evaporation technique that has started to gain traction with biological samples due to instrumental innovations, such as laser pulsing [19], [20]. APT allows for atomic-scale resolution in 3D with each atom being identifiable from a chemical perspective, and thus provides 4D characterization. In Chapter 3 of this thesis, APT was utilized to probe bone at the atomic level to better understand the variations in the two major phases of bone and their spatial arrangement: the organic collagen fibril and the inorganic bone mineral. This improved understanding can be used to inspire the design of implanted devices.

Bioinspriation in the design of new materials
Designing improved biomaterials for bone repair applications requires knowledge of both bone and the selected material. Several types of materials ranging from polymeric to ceramic to metallic have been used in bone implants [21]. Metallic substrates have become commonplace for bone-implant applications with titanium being the most prominent due to its suitable properties, such as good biocompatibility, wear and corrosion resistance, and higher toughness [22], [23]. Implant materials can be specifically tuned for osseointegration by altering the topography, roughness, wettability, and chemical composition of their surface [24]–[26]. Roughened surfaces with micro-to-nanoscale topography have been shown to improve cellular adhesion and facilitate bone growth [27], [28]. Biomimetic or bioinspired surfaces use knowledge of the natural biological tissue to design implant surfaces tailored for specific applications, which has been applied broadly in the field of bone implants [29]. However, many of the methods of modifying implant surfaces, such as sandblasting or chemical treatment or ion implantation, lack precision in the features they generate [30], deposit undesired products [31], or damage the material [32]. Therefore, better methods for surface modification are needed. Laser ablation is a clean, efficient method of modifying the surface of metallic substrates with a high degree of precision to generate micro-to-nanoscale features [33]. While earlier attempts at laser modification resulted in damage to the ablated surface, pulsed irradiation, as applied herein, can generate unique periodic submicron features with minimal damage [34], [35]. In Chapter 4 of this thesis, laser-induced periodic surface structures (LIPSS) were generated inspired by the periodicity of native collagen fibrils. The optimum periodicity was evaluated with *in vitro* testing methods and the feasibility of the machining approach was assessed.

Evaluating Biomaterials Performance
In vitro testing of biomaterials with mesenchymal or bone-like cells has become a strong analog for their eventual performance *in vivo*. Essential to the performance of a biomaterial is the specific interactions between cells and the biomaterial surface [36]. Conventional methods of evaluating these interactions range from biochemical analyses, such as assays or polymerase chain reaction (PCR), to microscopic analyses, which often utilize fluorescent techniques. Biochemical analyses, such as those performed in Chapter 4, can be quantitative but they provide no qualitative or visual information regarding the specific interactions of the cells with the surface, particularly in the case of structured surfaces [37]–[39]. Conventional fluorescent techniques, on the other hand, provide visual and information but lack the quantitative information and are limited by the diffraction limit

2

of light [40]. The shape and morphology of cells is often quite indicative of their health and how they will respond in the future. This information is most readily obtained through measurements of cell circularity or nucleus size obtained from fluorescent micrographs [41], [42]. However, when considering biomaterials which incorporate micro- to nanoscale surface topography, these features are not visible by light microscopic techniques due to the diffraction limit [43], [44]. Scanning electron microscopy (SEM) typically fills that niche in biomaterials analysis due to its higher-resolution via electron optics [44]. The electron microscope, however, is incredibly dangerous to biological samples due to the requirements of a high-vacuum chamber and electron beam, which can generate heat in non-conductive specimens [45], [46]. Typical preparation of biological samples for SEM is unwieldly due to its time requirements, chemical modifications to the cells, and removal of all liquid [47], [48]. Room temperature ionic liquids (RTILs) are substances that have high conductivity and minimal vapour pressure. RTIL have shown promise for facilitating imaging of bacterial cells, mammalian cells, and some insects without being toxic [49]–[51]. In Chapter 5, RTIL treatments have been adapted and extended to biomaterials research to enable simultaneous imaging of submicron surface features and wet or even living biological cells imaging in the SEM. This will be crucial for improving our understanding of bone cell-material interactions to improve biomaterials for bone-implants.

1.2 Research Objectives

This thesis aimed to explore strategies to advance our understanding of biomineralization, the design of suitable bioinspired biomaterials surfaces, and the subsequent development of novel and more realistic methods for biomaterials characterization. The specific objectives and approaches taken within this thesis are divided by sub-theme as follows:

(i) To elucidate the understanding of bone structure at the atomic scale. This was achieved in Chapter 3 by:

    (a) Developing alternative sample preparation methods for bone, and performing atom probe tomography to visualize bone at the atomic scale with corresponding chemical compositional information;

    (b) Implementing new data processing methods to identify the position of mineral with respect to collagen using both qualitative and quantitative statistical analyses.

Lee, B. E. J., Langelier, B., & Grandfield, K. Visualization of *In vivo* Mineralized Collagen Fibrils using Atom Probe Tomography. *(submitted)*

(ii) To understand the response of bone-like cells to a bioinspired surface created on titanium using laser ablation techniques. This was achieved in Chapter 4 by:

    (a) Using a pulsed femtosecond laser to generate reproducible and consistent linearly induced periodic surface structures inspired by the periodicity of native collagen in bone;

    (b) Characterizing and evaluating these features using materials and *in vitro* testing methods.

Lee, B. E. J., Exir, H., Weck, A., & Grandfield, K. (2018). Characterization and evaluation of femtosecond laser-induced sub-micron periodic structures generated on titanium to improve osseointegration of implants. *Applied Surface Science*, *441*, 1034–1042.

(iii) To develop a new method of evaluating biomaterials that enables simultaneous visualization of cells and surface features. This was achieved in Chapter 5 by:

    (a) Developing a RTIL protocol that allows for the visualization of wet or living mammalian cells in the SEM;

    (b) Using this treatment to facilitate simultaneous observation of cells and biomaterial submicron surface features.

Lee, B. E. J., Exir, H., Weck, A., & Grandfield, K. Capturing Mammalian Cell Adhesion to Sub-Micron Surface Features with Ionic Liquids in Low-Vacuum SEM. *(submitted)*

In addition to the work presented in this thesis, I am also co-author of three other published articles relevant to my PhD project. The articles are attached in the appendix. Combined, these projects represent an additional iteration of the three objectives outlined above and they have been marked as such.

(i) To elucidate the understanding of bone structure:

Lee, B. E.J., Luo, L., Grandfield, K., Andrei, C. M., & Schwarcz, H. P. (2019). Identification of collagen fibrils in cross sections of bone by electron energy loss spectroscopy (EELS). *Micron*, 102706.

(ii) To understand the response of bone-like cells to a bioinspired surface created on titanium:

Lee, B. E. J., Ho, S., Mestres, G., Karlsson Ott, M., Koshy, P., & Grandfield, K. (2016). Dual-topography electrical discharge machining of titanium to improve biocompatibility. *Surface and Coatings Technology*, *296*, 149–156.

(iii) To develop a new method of evaluating biomaterials using bioprinting:

Lee, B. E.J.*, Shahin-Shamsabadi, A.*, Wong, M, K., Raha, S., Selvaganapathy, R., Grandfield, K. (2019) A Bioprinted *in vitro* Model for Osteoblast to Osteocyte Transformation by Changing Mechanical Properties of the ECM. *Advanced Biosystems. *These authors contributed equally to this work.*

1.3 Thesis Chapter Summary

The research objectives presented in the Chapter 1 Introduction above are presented in the following five chapters, divided as follows:

Chapter 2: Background and Literature Review. This chapter provides a summary of topics relevant to this thesis. The overarching topics are: bone structure, high-resolution microscopy techniques (APT and SEM), metallic biomaterial surface modification strategies, and *in vitro* methods for evaluating biomaterials.

Chapter 3: "Visualization of Collagen–Mineral Arrangement as Mineralized *In vivo* using Atom Probe Tomography." This chapter presents the visualization of mineralized collagen fibrils from leporine bone at the atomic scale. Using APT, this work shows intra- and extrafibrillar mineralization of winding collagen fibrils from an *in vivo* source. It also showcases potential applications for APT in the biomineral community through quantitative statistical analyses. This work is currently submitted for publication.

Chapter 4: "Characterization and evaluation of femtosecond laser-induced sub-micron periodic structures generated on titanium to improve osseointegration of implants." This chapter presents a reproducible and controllable method of generating periodic surface structures on titanium. The generated surfaces were reproducible, with submicron features, and promoted the activity of osteoblast-like cells. This work was published in *Applied Surface Science*.

Chapter 5: "Capturing Mammalian Cell Adhesion to Sub-Micron Surface Features with Ionic Liquids in Low-Vacuum SEM." This chapter presents the first use of RTIL to facilitate simultaneous visualization of cells and submicron biomaterial surface features. A facile method to treat cells adhered to biomaterials was developed and was shown to be successful in the SEM. A revised version of this manuscript is currently under review.

Chapter 6: Conclusions. This chapter summarizes the key findings of the research along with contributions and potential future work.

Chapter 2: Background and Literature Review

2.1 Bone

2.1.1 Overview

Bone is a tissue with both mechanical and chemical functions. Mechanically, bone acts as support and protection for vital organs within the body and provides us with mobility, while chemically, it acts a reservoir for important elements, such as calcium (Ca) and phosphorus (P) [52]. The structure of bone, which allows it to perform both functions, is hierarchical and quite complex [12]. Due to its multifaceted role, understanding bone from a structural, physiological and overall health standpoint is important [1]. When considering the increased quantity of bone-interfacing implants being placed, it is important to further develop the knowledge of bone [4]. This thesis focuses on examining bone structure on the atomic scale and using knowledge of that to better design implanted biomaterials.

2.1.2 Bone Composition

The composition of bone can be broadly divided into three major phases: mineral (60 wt%), organic (30 wt%) and water (10 wt%) [53]. The biomineral phase is typically considered to be mostly carbonated hydroxyapatite (HA) [54]. However, recent work has demonstrated that this hydroxyapatite *in vivo* can be substituted for a variety of ions, such as magnesium and strontium leading to diverse compositions [55], [56]. HA in bone exists as elongated crystal plates, with dimensions known to be 2-6 nm thick, 25-50 nm wide and 50-100 nm long [14], [57], [58].The organic phase of bone is primarily composed of Type 1 collagen and assorted non-collagenous proteins (NCPs), which combine together to form extracellular matrix [52]. The structure of collagen itself is hierarchical as it progresses from amino acids (~1 nm) to triple helix tropocollagen molecules (~ 300 nm) to collagen fibrils (~ 1 µm) to collagen fibres (~ 10 µm) [59]. These triple helices have a diameter of 1.5 nm and when arranged in arrays become collagen fibrils with a characteristic, periodic banding pattern in which there are 40 nm gap zones followed by 27 nm overlap zones between the helices [59]. This model of collagen is known as the Hodge and Petruska model [60]. This overall 67 nm banding pattern can be observed in the transmission electron microscope (TEM) [61]. The arrangement of mineral and organic phases of interest due to the unique way in which they interweave within each other to create a mineralized collagen fibril [62]. The mineralized collagen fibril makes the basis for all higher-order hierarchical structure, some outlined in Figure 2-1.
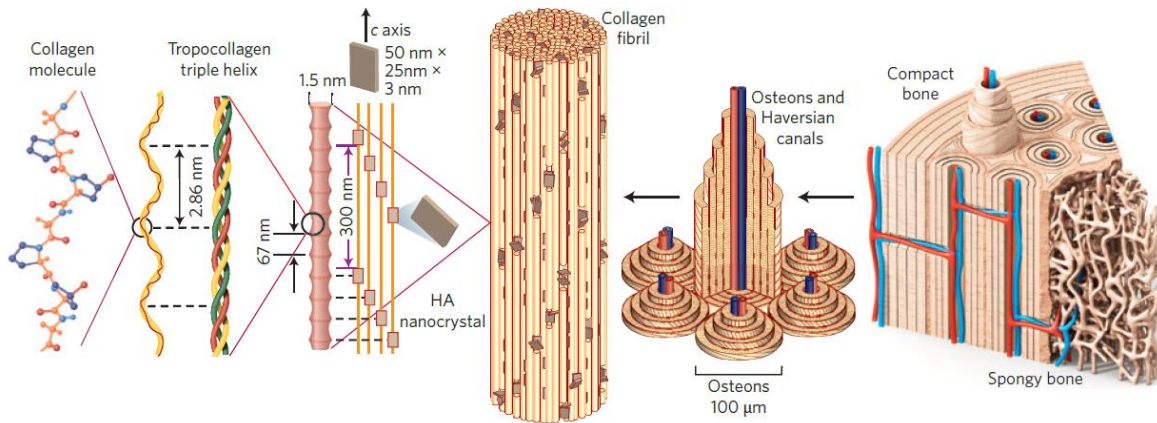
Figure 2-1. Hierarchical structure of bone from the molecular scale to the macroscale.
Reproduced from reference [63] with permissions.

2.1.3 Bone Hierarchical Structure

Bone has a hierarchical structure from the nanoscale to macroscale with 11 general levels of classification being considered [18]. At the nanoscale, or ultrastructural level, the building blocks for the mineral and organic phases are apatite crystals and tropocollagen molecules respectively. The tropocollagen molecules aggregate into arrays to form collagen fibrils which are subsequently mineralized by the apatite crystals [64]. This process is ongoing as the bone ages [64]. In a sense, these mineralized fibrils act as a secondary scale building block for higher-level bone structures as they arrange into collagen fibres. The fibres then arrange themselves into lamellar bone and concentric rings of lamellar bone identify the microscale motif recognized as osteons [64]. It is at this length scale that cortical and trabecular bone separate themselves as the cortical bone contains osteons while trabecular bone contains trabeculae, or struts of lamellar bone generally aligned along the direction of the struts [64], [65].

The ultrastructure of bone and how the collagen fibrils are mineralized, or collagen-mineral arrangement, has been the subject of large debate, with three models presently existing and shown in Figure 2-2. The first, Figure 2-2A, is from electron tomography studies by Landis et al who examined mineralized turkey tendon and observed that mineral crystals in the shape of needles were present in collagen gap zones and then nucleated outwards [66]. This is known as intrafibrillar mineralization. This stems from older work by Katz et al. who proposed that mineral crystals formed within the gap zones in the periodic collagen banding [62]. However, mass to volume comparisons suggested that the total weight of mineral in bone could not fit solely in the gap zones of collagen fibrils, and about 20-30% must be outside the fibrils, known extrafibrillar mineralization [62]. Similar work carried out by Weiner and Traub, demonstrated that the mineral is in the form of plates, closely related with the gap zone region [67]. A different model for bone ultrastructure, proposed by Schwarcz et al. and shown in Figure 2-2B, postulates that extrafibrillar mineral is comprised of curved mineral plates in stacks referred to as "mineral lamellae" that are

separated by less than 1 nm [68], [69]. This model proposes entirely extrafibrillar mineralization, not inside the gap zone of collagen. The third model (Figure 2-2C), by Reznikov et al. summarizes some of these various theories and attributes this misunderstanding to samples extracted from the ordered (aligned collagen fibril arrays) to disordered (unorganized fibril arrays) zones of bone leading to conflicting theories on bone ultrastructure [18]. In her model, bone crystals appear again as needles, this time acicular in shape [18]. Therefore, an understanding of the mineralized fibril and bone ultrastructure is still yet to be completely addressed. Interestingly, all these studies used electron tomography as the dominant materials characterization method despite it lacking direct chemical information.
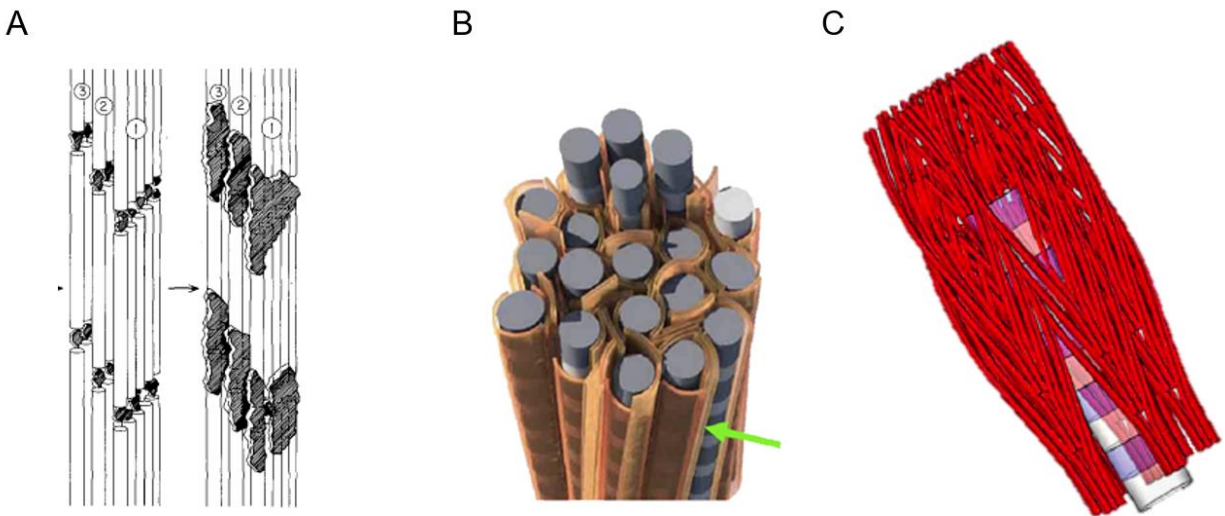
Figure 2-2. Three models of the mineralized collagen fibril. (A) shows a model wherein mineral forms in collagen gap zones and eventually nucleates into plates or intrafibrillar mineralization. (B) proposes that the mineral is located external to the gap zones in curved mineral lamellae or extrafibrillar mineralization. (C) proposes that the mineralized collagen fibril has a number of differing motives: lacy, rosette and filamentous, the latter of which is shown here. (A), (B), and (C) were reproduced with permission from references [17], [7] and [18] respectively.

2.1.4 Bone Remodeling

In addition to being a hierarchical tissue, bone is a dynamic tissue that actively remodels throughout the lifespan of an individual in order to maintain its function both mechanically and chemically. This remodeling can occur due to external damage, homeostasis requirements, or for growth [1]. This process is governed by a series of cellular events which remove old bone and place down new bone [52] (Figure 2-3). The three central cells involved in the process of remodeling are osteoblasts, osteocytes and osteoclasts.

Once an external stimulus initiates the remodeling process, typically through mechanotransduction of osteocytes, osteoclasts are recruited to the remodeling site where they digest mineral and extracellular matrix [64]. Osteoclasts share a similar ancestry to macrophages which allows them

to resorb existing bone through acidification and proteolysis [64]. Osteoblasts are differentiated mesenchymal stem cells and are instead involved in the synthesis of new bone. As the osteoclasts digest old bone, osteoblasts are recruited to the same remodeling site and they begin to secrete new bone matrix known as osteoid [70]. Osteoid is the unmineralized extracellular matrix that forms the collagen fibrils [64]. This process continues until the matrix begins to be mineralized at which time point many of the osteoblasts become encapsulated by the matrix [64]. This encapsulation leads to osteoblasts irreversibly differentiating into osteocytes [64]. These osteocytes then act as mechanosensors that transmit mechanical signals to initiate bone cellular activity, including bone remodeling, and the cycle so continues [64].
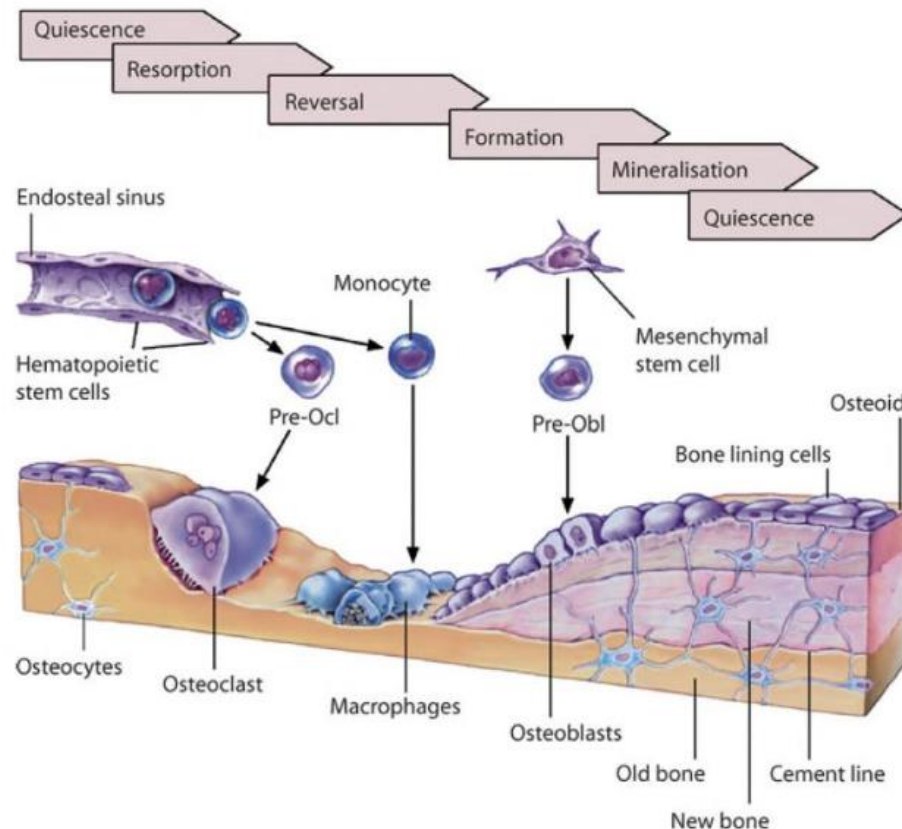
Figure 2-3. Schematic illustrating the cycle between osteocytes, osteoclasts and osteoblasts during the bone remodeling process. Osteocytes, via mechanotransduction, signal that bone needs to be remodeled which recruits osteoclasts to resorb bone and osteoblasts to synthesize new bone as the site of remodeling. Figure reproduced from reference [71] with permission.

The newly deposited bone is referred to as woven bone due to its lack of organization, but over time it is remodeled into a more organized structure known as lamellar bone [52]. Bone resorption and subsequent formation can take up to 6 months to complete [52]. This lengthy remodeling cycle highlights the importance of understanding bone formation and its importance only increases when considering bone remodeling in the context of an implanted device.

2.2 The Bone-Implant Interface

2.2.1 Osseointegration of Implant Materials

Individuals require their natural bone to be supported, replaced or supplemented with implanted devices due to reasons such as injury, disease or age. In Canada, there is a growing number of required bone implants such as joint replacements placed annually, with approximately 59 000 hip and 70 000 knee replacement surgeries performed in 2017-2018, which represents a 17% increase compared to the previous five years [2]. Use of implants carries the risk of significant lifestyle changes for the recipient, rejection via inflammatory responses, or even replacement of the implant [72], [73]. As none of these situations are desirable, work has been conducted to investigate methods to improve implant outcomes. An ideal implant would function seamlessly with natural bone and a structural and function connection between bone and implant material, otherwise known as osseointegration, needs to be present [1].

It is well-known that increasing the roughness or surface area of an implant surface can improve cellular responses and implant integration. However, cellular behavior on the surface is not so easily controlled in order to encourage cell migration or specific differentiation [74]. Cell migration can be guided by chemical or mechanical stimuli, chemotaxis and durotaxis, respectively [75]–[77]. The cells become polarized as a result of these stimuli and move along a gradient [78]. It is known that cells tend to orient their migration towards increasing availability of adhesion sites [79], [80]. The ability of cells to migrate along a surface is very important as the migration and adhesion of cells to biomaterials is part of the initial foreign body response which occurs before osseointegration [81], [82]. Similarly, the foreign body response can occur in response to the chemical composition or functional groups of a biomaterial leading to undesirable fibrous encapsulation or infections [72], [73]. An ideal material is one that is inert and thus avoids excessive chemical reactions, while being capable of being modified into a surface with high surface area to encourage cell adhesion. One such material fitting these parameters, and widely used in bone-implants, is titanium and its alloys.

2.3 Titanium as an Implant Material

2.3.1 Properties of Titanium

Titanium is a material commonly used in implants that possesses many of the properties to allow for good osseointegration [83]. Titanium has the unique combination of high strength, low density, relatively low elastic modulus, high corrosion resistance, along with being biologically inert [84]. One of the major issues with metallic-based implants is that they can corrode and deteriorate when placed in the human body. Titanium avoids this due to the presence of an exterior, natural oxide

layer that forms as a result of reactions with ambient elements [3]. This oxide layer does not form direct chemical bonds with bone tissue, which allows titanium to act similar to an inert, ceramic biomaterial [85]. The combination of high strength and low density also gives titanium a high specific strength [84]. Additionally, since natural bone has a modulus between 4-30 GPa [86], an ideal material for implants should have a modulus close to that of the natural bone to avoid bone resorption as a result of stress shielding [83]. While titanium alloys have elastic modulii as low as 55 GPa which is greater than that of bone, compared to alternatives such as 316L stainless steel (210 GPa) or cobalt-chromium alloys (240 GPa) this is a marked improvement [83]. Compared to nickel implants (skin disease risk), cobalt implants (potentially carcinogenic), or 316L stainless steel (high modulus), the major downside to using titanium is that it is more expensive [83]. Some other issues that have been reported are that Al and V ions that are used in titanium alloys can be released into the body and have potentially negative health effects [87]. It has also been found that debris from titanium alloys have caused inflammatory responses [88]. Despite these issues, titanium is considered one of the premium materials for implants and several surface modifications have been investigated to improve its use for bone.

2.3.2 Surface Modification Strategies on Titanium

Due to its use in the medical industry, various modifications techniques have been applied to titanium with the goal of improving osseointegration. Initially, the metallurgy of titanium should be considered. As an implant needs to be strong, typically α+β or metastable beta class alloys are used [83]. As mentioned previously, the elastic modulus of the material needs to be kept low enough to avoid stress shielding. Other metals such as Nb, Zr, Mo and Ta are considered suitable alloying elements, some of which are beta stabilizers, which decrease the modulus of the material without significantly reducing the strength [89]. The choice of alloyed material also can affect the oxide layer. It has been found that alloying with Nb appeared to stabilize the oxide layer [90]. The two most commonly used forms of titanium for implants are commercially pure titanium and Ti6Al4V with Ti6Al4V being the most common dental implant material [91]. However, commercially pure titanium has a lower modulus than Ti6Al4V and the two materials have similar material properties and osseointegration when utilized *in vivo* [92].

Both the surface chemistry and topography of implants are believed to play a role in the response of bone tissue to implanted devices [93]. In particular, rough and porous surfaces are known to stimulate cellular attachment and differentiation [94] as a result of increasing the bone-implant interface surface area, as shown in the schematic Figure 2-4. For titanium, common surface modifications to increase roughness such as acid etching, electro-erosion processing, sandblasting and machine-tooling as shown in Figure 2-5. The presence of roughness and pores increases the contact area which has been associated with an increase in osteoblast activity [95]. This increased surface area also results in the quantity of oxide present which is beneficial from an osseointegration standpoint. Sandblasted titanium has been found to improve implant retention due to the increased surface area [95],[96],[97]. Usage of acid treatment following sandblasting

has also been considered as it reacts with the 'grit' and the titanium to create additional roughness [97]. Nitrogen ion coating has been observed to improve corrosion resistance [98] and has been used in combination with other treatments such as plasma sprayed coatings [99]. Plasma spraying of titanium with HA has been used in implant studies to generate relatively porous surfaces, compared to densely packed sandblasted titanium surfaces, that were considered more viable for cell growth [99].
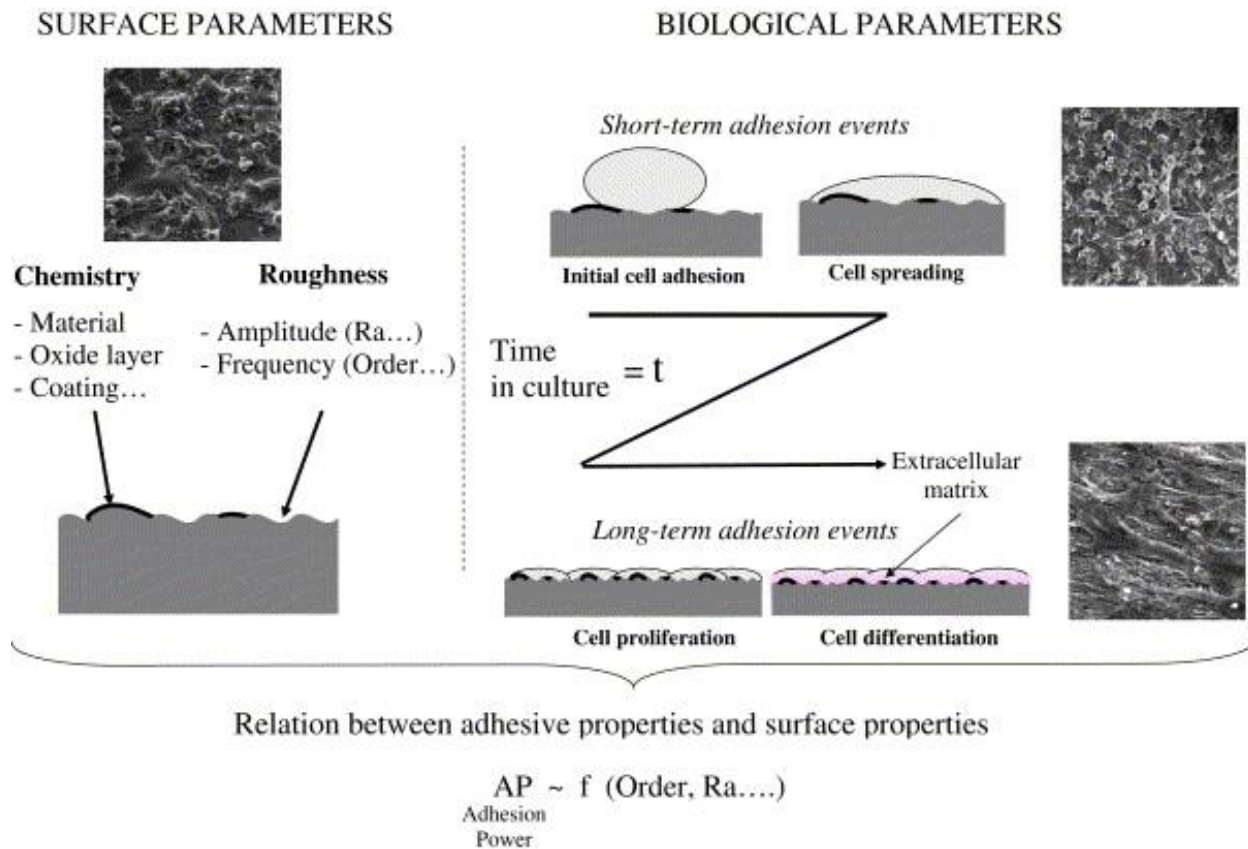
Figure 2-4. Schematic illustrating the various parameters, biological and surface, that are govern interactions between cells and materials. Figure reproduced from reference [100] with permission.

A common approach to improve the osseointegration of titanium involves modification of the oxide layer. Machined and electropolished titanium have shown modest-to-unremarkable changes in the oxide layer [28]. Ideal oxide thickness has been estimated to be greater than 600 nm [101]. Sul et al. used microarc oxidation to create porous structures, increase roughness and generate oxide layers thicker than 1000 nm [93]. Anodization has shown to produce thicker oxide layers that show a larger degree of bone-implant contact as evidenced by screw removal torque studies [28],[102]. Use of piranha and alkaline treatments has generated surfaces with varying morphologies but with alterations to the surface chemistry [31]. Anodic oxidation using phosphorus and calcium has been found to improve cellular adhesion, create micropores up to 2

μm, and increase roughness of the surface [102]. Calcium and phosphorus are known, in particular, to increase bone formation around implants [93],[103]. It has been speculated that rich calcium and phosphorus environments are beneficial for stimulating osteoblast adhesion and growth [104]. The anodic oxidation process can also be altered to optimize the surface as alterations in electrolyte concentration, current density and voltage have been correlated with changes in surface roughness and oxide crystallinity [105]. Another physical approach to modifying the oxide layer and surface roughness, and the one used in this thesis, is laser-modification.
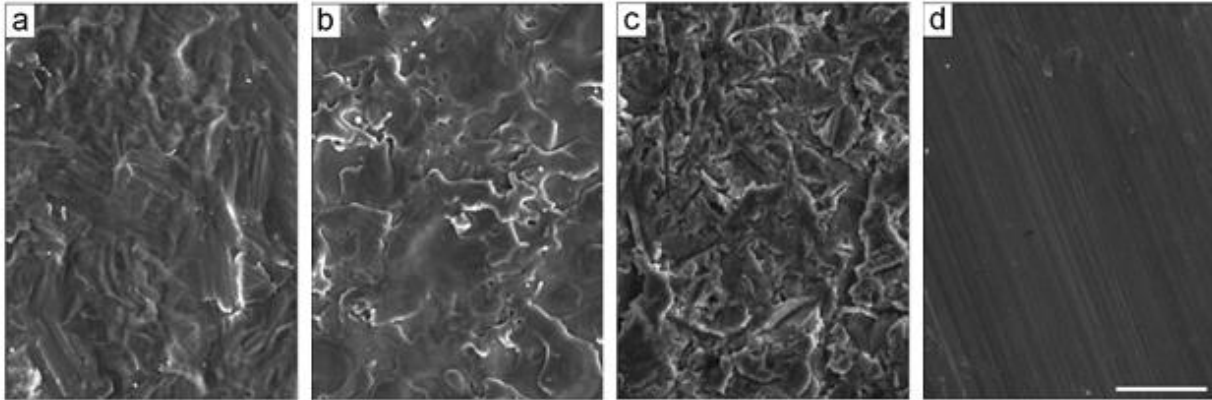
Figure 2-5. Titanium surface modified using (a) acid etching, (b) electro-erosion processing, (c) sandblasting and (d) machine-tooled to generate roughened surfaces. Scale bar is 50 µm. Figure reproduced from reference [106] with permission.

2.3.3 Laser-Modification of Titanium

A less conventional, but promising, method for modifying titanium for implants is the use of industrial lasers. Lasers primarily work by either remelting, alloying, or cladding substrate surfaces to improve material properties such as corrosion or heat resistance [107]. There are a wide variety of types of lasers, many of which have been examined for use in biomedical applications [108]–[110]. Lasers are primarily classified according to the gain medium which corresponds to the possible wavelengths at which lasers can be operated as shown in Table 2-1 [110]. These different types of lasers allow for different modes of operation and thus generation of different surface features [111]. In operation, certain laser parameters such as wavelength, pulse duration, and fluence are important for surface modification along with considerations taken for the material being modified [110]. Altering these parameters can result in microstructure alteration, grain refinement or phase transformations of a given material [110], [111]. Particular for pulse duration, the distinction between long and short pulses dictates whether non-thermal routes are possible [112], [113]. Operating at a pulse duration greater than the femtosecond, or ultrashort pulse, range results in thermal processes dictating surface modification [112]. Conversely, operating at or below this range results in surface modification being dictated by the length of the pulse [112].

Table 2-1. Example laser devices used in microfabrication applications. Variations in the state and the wavelength allow for fabrication of different sized features. Adapted from reference [110] with permission.

Physical State	Medium or Species (Centre Wavelength)	Excitation Methods
Gas (Excimer)	ArF (193 nm)	Electric Discharge
	KrF (248 nm)	
	XeCl (308 nm)	
Solid State	Ti: sapphire (800 nm)	Optical Pumping
	Nd: YAG (1064 nm)	
	Nd: YVO$_4$ (1064 nm)	
	Yb: YAG (1030 nm)	
	Yb: KGW (1030 nm)	
Gas (Molecular)	CO$_2$ (10.6 µm)	Electric Discharge

The major benefits of using laser techniques, compared to other surface modifications techniques, are that they allow for a degree of precision and control over features and are non-contact, rapid, and clean [111]. Variation of pulse duration is known to allow for formation of different morphological features on the surface depending on both pulse duration and the heat affected zone [114]. Nitrogen in particular has been found to be effective when alloying due to the formation of TiN [115]. Laser-modified titanium implants have been reported to have larger removal torques compared to control implants as a result of animal studies [116],[117]. Use of solid and gas state lasers to generate micropores on titanium implants has been examined [118].

Studies involving the Nd:YAG laser increased the surface roughness of titanium at wavelengths of 1064, 532 and 266 nm with 40 ps pulses [118],[119]. Trtica et al. noted the presence of plasma which they believed to provide a potential sterilizing effect against surface contaminants [118]. Excimer lasers, KrF and ArF, have also been used and were able to create holes on the micron scale [120]. These excimer studies noted that while pulse durations in the nanosecond range resulted in the formation of crown-like projections, pulse durations in the picosecond range were able to smooth out these ablations [120]. KrCl and XeCl excimer lasers have also been used with single and multi-pulse irradiations to alter surface roughness, with higher pulse counts leading to greater roughness [121]. Despite producing pronounced periodic wavelike structures, Milovanović et al. found that cracks formed on the surface of Ti alloys when using higher pulse count irradiations [121]. This was believed to be due to the movement of the liquid phase towards the periphery before it resolidified [121]. Use of a Ti:sapphire laser system by Vorobyev et al., with pulses on the femtosecond scale, was able to create nanoscale ripples on titanium plates [35]. However, their treatment also resulted in the formation of craters [35]. Examples of titanium ablated by Nd: YAG and ti:sapphire lasers can be observed in Figure 2-6. Despite all progress, laser modifications often result in the formation of cracks, holes, or craters due to the high cooling rate following removal of the laser which is detrimental to the potential use in clinical settings [107].

Many of the features introduced by laser ablation have no defined structure and are irregular. A consequence of laser ablation has been the formation of laser-induced periodic surface structures (LIPSS) on the surface of metals, semiconductors and insulators [122]. A longstanding theory by Sipe and van Driel proposed that these rippled patterns were long considered to be interference between the incident beam and a surface scattered wave which results in inhomogeneous energy absorption below the surface leading to surface roughness [123], [124]. More recently, Huang et al have added to this model by stating that interference between the surface plasmons and the incident laser are the major contributors to LIPSS formation [125]. These structures have a defined periodicity and their size and orientation can be adjusted by altering laser parameters. Linearly polarized light can result in the structures being elongated perpendicular to the axis of polarization [126]. LIPSS have been generated on titanium [127] and Ti6Al4V [34] with periods in the submicron range and have shown that cells appear to orient themselves parallel to the direction of the ripples. Other work with LIPSS has been performed at the microscale and observed enhanced cellular responses [128]. Reports of cellular experiments with LIPSS shows that cells undergo stresses relative to the LIPSS [129]. The control of cell migration or differentiation onto LIPSS titanium has not been completely deciphered, and additionally, smaller periodicities approaching the nanoscale have not been reached either, until the work presented herein Chapter 4.
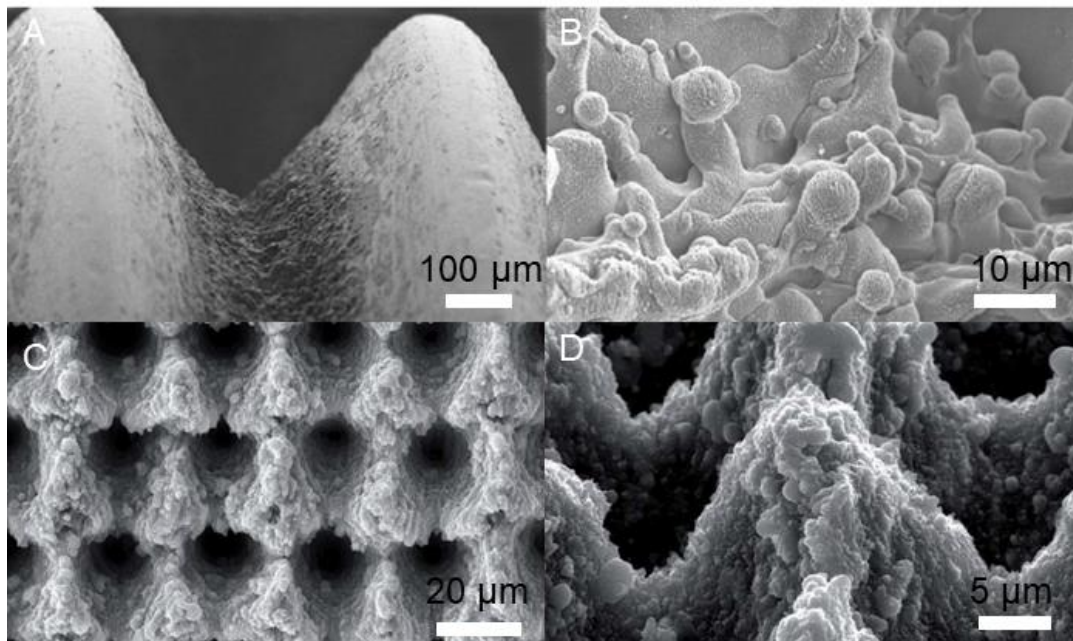
Figure 2-6. Laser-modification of titanium using Nd:YAG (A/B) and Ti:sapphire (C/D) lasers generated reproducible and consistent structures that were either random or periodic in nature. Both (A/B) and (C/D) were reproduced from references [130] and [131] with permission.

2.3.4 Bioinspiration

Designing or fabricating synthetic structures to replace natural occurring ones can be challenging. Application of bioinspired or biomimetic designs to engineering materials has seen limited success thus far primarily due to the requirement of biologists identifying phenomenon that could be utilized in designs [132]. Another challenge with bioinspired design is the inability to replicate the structures exactly as observed in nature. This can be due to biological material that is constantly renewed [132], difficulty in replicating their complexity [63], or due to the requirement of the presence of biological cells. For bone implants, it has been reported by numerous studies that the incorporation of hydroxyapatite to materials can result in improved cellular responses and osseointegration [133]–[135]. Due to the natural presence of HA in bone, the rationale is that incorporating HA will improve the biological response. Other biomaterials design has focused on directing biological response by using queues familiar to cells and proteins. One example is the usage of peptides with the adhesion domains of extracellular matrix (ECM) proteins, such as RGD [136]. The adsorption or immobilization of these peptides to titanium has been observed to improve osteoblast adhesion and proliferation [137], as well as contribute to improved bone density in *in vivo* studies [138]. Dental implants designs have been manufactured on the macroscale to be similar to root formation [139]. While modification of implant surfaces on the meso- [140], micro- [141], and nanoscale [142] have investigated various topographies and finishes, the majority of which do not replicate the structure of bone at those length scales. These existing designs improved cellular responses and osseointegration but the mechanism as to how these designs are directed these improved responses has not been answered [136], [143]. Similar to the methodology for incorporating HA into biomaterials, it follows that the collagen in bone could be used as inspiration for biomaterials design. From bone remodeling it is known that osteoid is first deposited and is subsequently mineralized over time [70]. This deposited osteoid is primarily organic matrix comprised of collagen [70]. As such, it is possible that the distinct periodic spacing, from the previous identified Hodge and Petruska model, that exists in collagen, could be used to guide cellular responses. In Chapter 4, laser ablation techniques were used to generate LIPSS on titanium that were inspired from the sub-micron scale collagen features of native bone.

2.4 *In Vitro* Testing of Biomaterials

2.4.1 Bone Cells

The *in vitro* methods used to test the biocompatibility of the aforementioned surface modifications in the context of osseointegration typically involve the use of osteoblasts or osteoblast-like cells. Protein adsorption is the first event following contact between *in vivo* fluids and the implant material which is immediately followed by cellular attachment [144],[145]. Ideally, implants would be tested *in vivo* but *in vitro* testing is often preferred because efficient, cost-effective

methods are needed to allow for materials development without the unnecessary use of animals. The type of osteoblasts used is important as phenotypes vary between cell lines [144] and because osteoblasts have been found to react to features as small as 10 nm [146]. Clonally derived or immortalized cells, such as neonatal mouse MC3T3E1 or fetal rat RCJ cell lines, have been used due to their alkaline phosphatase (ALP) and collagen Type 1 production [144]. However, each cell line has a unique phenotype which confounds the ability to directly compare morphology between lines [144]. Non-transformed or primary cultured osteoblasts have also been used due to their ability to adapt to alterations in their surrounding environment [144]. The most commonly used cell lines in osseointegration studies are osteosarcoma cell lines [144]. While they do not represent the long-term phenotype of osteoblasts, osteosarcoma cell lines are easy to propagate and maintain in culture and are good measures of the initial phenotype of osteoblasts [144].

There are several common osteosarcoma cells that have been used in studies: MG-63, Saos-2 and U-2 OS [147]. Pautke et al. determined that each cell line produced a differently composed extracellular matrix and that the osteosarcoma cells had smaller cell diameter and cell volume in solution compared to human-derived osteoblasts [147]. It was unsurprisingly found that cell proliferation was much greater with the osteosarcoma lines and that their phenotype did not well represent that of human-derived osteoblasts [144],[147]. Saos-2 cells were found to embody the most mature phenotype due to their production of ALP, bone sialoprotein (BSP) and collagen Type 1 and 3, while U-2 OS only resulted in the production of collagen Type 4, which is typically only found early in differentiation [147]. Production of key compounds for the MG-63 cell line was greater relative to the U-2 OS line but still less than the Saos-2 line [147]. Therefore, in the work represented in Chapters 4 and 5, Saos-2 cell lines have been used.

2.4.2 *In vitro* Cellular Assays for Osseointegration

Evaluation of cell responses to biomaterials can be done using various biochemical assays. These assays are typically used to measure cell viability or cell metabolism. Examples of metabolic assays include tetrazolium salts, such as MTT or XTT [37] and resazurin (commercially known as alamarBlue™) [148] that create terminal and intermediate steps in the electron transport chain step of cell metabolism and doing so approximate the amount of living cells from the frequency of the reaction. The redox reactions of relevant electron carriers during the electron transport chain such as NAD^+ and Cytochromes are outlined alongside the reactions for MTT and resazurin in Table 2-2. It should be noted that MTT is an endpoint assay for examined cells as its potential is intermediate to the electron carriers. This halts the electron transport chain leading to inhibition of cell respiration and eventually cell death. Resazurin, however, does not have this concern and has the benefit of enabling multiplex analysis as the assay does not inhibit cell respiration [38]. The dyes or reagents will emit at a given wavelength which enables fluorescence or absorbance measurements using a plate reader at specific values.

Table 2-2. Example of half-reactions for relevant electron carriers in the electron transport chain. Use of MTT creates a terminal step as it prevents the transfer of electrons from donors to carriers as MTT has a midpoint potential in between the two. Alternatively, resazurin can detect oxidation of any step in the electron transport chain without interfering with the transport of electrons [148].

Half Reaction	Redox Potential (mV)
$NAD^+ + 2H^+ + 2e^- \Leftrightarrow NADH + H^+$	-320
$MTT_{OX} + 2H^+ + 2e^- \Leftrightarrow MTT_{RED}$	-110
$Cytochromes_{OX} + 1e^- \Leftrightarrow cytochromes_{RED}$	+80 to +290
$resazurin + + 2H^+ + 2e^- \Leftrightarrow resorufin$	380

In addition to cell metabolism, the morphology and dimensions of a cell can also be very indicative of how they will respond in the future [143]. As such, visualization of these cells under the microscope using viability stains is also effective. Cells stained with a viability reagent can be evaluated through plate reading or light microscopy depending on the application. Examples of viability stains include live/dead (Calcein AM & ethidium homodimer-1) [149] and neutral red [150]. These images allow for morphological examination of cells as the size and shape of the cells can be indicative of their health. Two examples of measurement parameters are circularity and nuclear area factor, a quantitative measure of apoptosis, which can be used to assess cell morphology [42]. The equations for their calculation can be seen below in Equations 1 and 2. Depending on the cell type, the numerical value from each of these equations has differing value. Specific to bone cells, higher values for circularity and nuclear area factor are associated with healthier cells [41].

$$(1)\ Circularity = \frac{4\pi \times Area}{Perimeter^2} \qquad (2)\ Nuclear\ Area\ Factor = Area \times \left(\frac{4 \times Area}{\pi \times Major\ Axis^2}\right)$$

Another common measure when assessing biomaterials for osseointegration potential is ALP activity. ALP is consistently produced by osteoblasts and is considered a biomarker for bone remodeling [143]. Evaluating the amount of ALP activity can be done using an activity assay. P-nitrophenyl phosphate when dephosphorylated by native ALP produced by cells will turn yellow and the amount of activity can be determined via absorbance readings.

The choice of evaluation method is independent of the biomaterial being examined aside from situations where the biomaterial naturally fluoresces [151] or if its surface is active and can react with the reagents [152], [153]. The concern for some of these techniques, such as MTT or viability stains, is that they act as endpoint analysis [154]. However, some methods such as resazurin or neutral red can allow for multiplexing which is beneficial from an experimental design standpoint.

2.5 Scanning Electron Microscopy Principles for Biological Materials

2.5.1 Biological Imaging and Sample Preparation

Scanning electron microscopy (SEM) is a fundamental materials characterization technique that has applications in numerous fields. For biomaterials, SEM is important when characterizing materials with micro to nanoscale features that cannot be visualized with a light microscope. Secondary (SE) and backscattered electron (BSE) imaging modes are typically used to allow for topographical and compositional contrast information, respectively. The topography of a biomaterial is consistently cited as important for cellular and protein interactions and SEM is ideal for visualizing these surfaces [155]. Related characterization methods such as energy dispersive spectroscopy (EDS) can be used to provide more quantitative compositional information compared to BSE imaging alone. As biomaterials are comprised of a variety of material types, not all these materials are ideal for being placed in the electron microscope. For nonconductive materials, accumulation of electrons can often be problematic and can lead to imaging artifacts, known as charging. As a consequence samples are regularly coated with conductive metals such as carbon, gold or platinum to reduce charging [156], [157]. These issues, however, cannot be resolved when working with liquid-based biomaterials, such as hydrogels, which cannot be coated or maintain their integrity in a typical SEM because of the high-vacuum requirements of the instrumentation [158].

Imaging of cells and their processes is a primary method by which scientists can understand biological processes. Historically, imaging of these samples has been typically conducted with optical or fluorescent microscopy techniques due to their ability to visualize samples in live or real-time conditions. While electron microscopy has extensive use in materials characterization, it has been used in biological experiments to obtain the extra resolution not possible with optical techniques [44]. Doing so often requires that samples undergo significant sample preparation to fix cell membranes, stain low contrast components and dehydrate the specimen for the high vacuum of SEM. However, the advent of super-resolution techniques has enabled optical techniques to achieve nanoscale resolution via creative use of fluorescent tools which has impeded upon the territory once owned by electron microscopy [44]. It is important to note that super-resolution techniques only apply to samples that can be fluorescently tagged and thus the resolution for anything else in the system is limited by the diffraction of light. As such, cells adhered to surfaces with submicron scale features could be visualized but not the substrate they are adhered to.

The majority of electron microscopy conducted with mammalian cells has them prepared with a fixative prior to imaging. These fixatives act as chemical cross-linkers of proteins which allow them to preserve the structures of their targets [159], [160]. Fixatives are often toxic, such as osmium tetraoxide, and may destroy or damage cellular components [28]. While use of these compounds allows for high-resolution images of biological cells to be obtained, a fixed sample is

non-living and therefore not completely representative of the behaviour of the sample in question. Additionally, a primary requirement for all samples to be viewed in electron microscopy is that they cannot be exposed to the vacuum in a liquid state. As such, fixed samples are subsequently dehydrated, often with ethanol or acetone, which removes all liquid components in the tissue or cellular samples [161]. Sometimes, samples can be subsequently embedded in resin or instead may be critical point dried to complete the dehydration. Since cells are primarily composed of low atomic weight elements, the contrast obtained in the microscope will be poor when imaged without further modifications. Therefore, biological samples are often given heavy-element stains or coatings to improve contrast and allow for visualization of the immobile and non-living biological structures [161]. Other techniques that can be used to facilitate visualization of cells in the electron microscope include cryofixation and immunolabelling [162].

From a biological standpoint, fixation, staining, dehydrating and coating are undesirable as they can each create artifacts in the imaging process [46], [163]. More importantly, all of these processes can alter the morphology of cells, proteins, and other relevant molecules resulting in the imaging of a sample which has been altered from its live state [46], [163].

2.5.2 Ionic Liquids

Ionic liquids have shown promise as an alternative method of sample preparation for biological samples, such as cells [164], ticks [49], and chromosomes [51]. Ionic liquids are defined as salts that remain in the liquid state due to the ions being poorly coordinated and thus have low melting points [165]. The melting points can be sufficiently low that these salts can be in liquid phase at room temperature. Room temperature ionic liquids (RTILs) also possess low vapour pressure, are electrically conductive, and are non-volatile [166], [167]. For SEM sample preparation, these liquids can impart a sample with electrical conductivity and require significantly less preparation time compared to traditional methods. These liquids have been used in a variety of methods, from simply replacing the sputter coating step to being used in the replacement of any number of traditional methods, such as fixing or dehydrating [51], [168], [169]. Bacterial cells [170], blood cells [164], and chromosomes [51] have all been visualized using these treatments and some of these are shown in Figure 2-7. It has been said that imaging of living cells using electron microscopy is extremely difficult and has even been noted as impossible [171]. Alternative methods such low-vacuum chambers or environmental SEMs have allowed for imaging of wet cells [172], [173]. However, by combining electron microscopy with fluorescent techniques, it is possible to determine if the imaged cells are alive or dead. In Chapter 5, RTIL treatment of Saos-2 cells facilitated electron microscopy of these cells adhered to LIPSS titanium while cell viability was assessed with fluorescent assays. This technique fulfills a niche in biomaterials evaluation by enabling the simultaneous, rapid, and facile imaging of submicron biomaterial features and wet living cells.
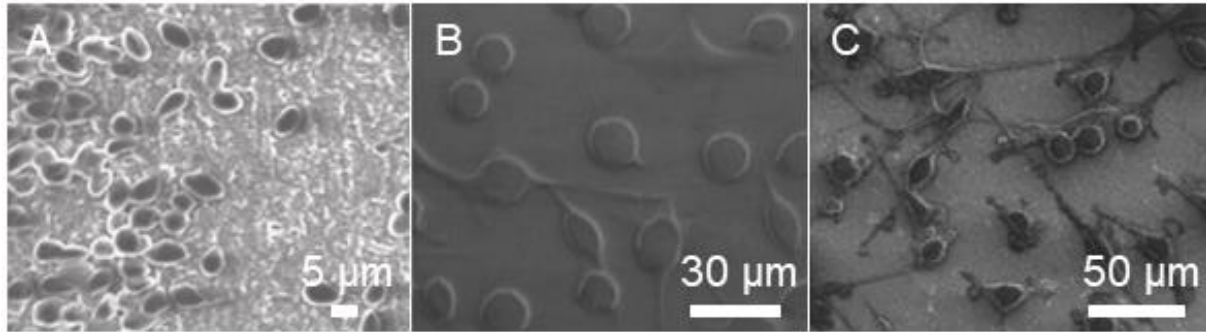
Figure 2-7. Red blood cells (A) and L929 fibroblasts cells imaged in the SEM using RTIL treatment (B/C) on flat substrates. (A) and (B/C) were reproduced from references [164] and [168] with permission.

2.6 Atom Probe Tomography (APT) as a Characterization Tool for Bone

2.6.1 Introduction to APT

Atom probe tomography (APT) uses time-controlled field evaporation of atoms from a surface to reconstruct 3D volumes with simultaneous chemical resolution [174]. As the name implies, APT theoretically facilitates atomic scale spatial resolution with chemical sensitivity for all elements down to a resolution in the parts per million [175]. The atom probe microscope provides the greatest spatial resolution for chemical analysis compared to TEM or secondary ion mass spectrometry (SIMS) [176]. APT is a destructive technique that involves the sequential evaporation of atoms from the surface of a sample [174]. To do this, a specific needle-shape sample is needed for the appropriate electrostatic field to be produced at the tip which in turn allows for field evaporation [174]. These tips ideally have a radius of 50 nm such that a high electrostatic field can be produced at the tip surface [174].
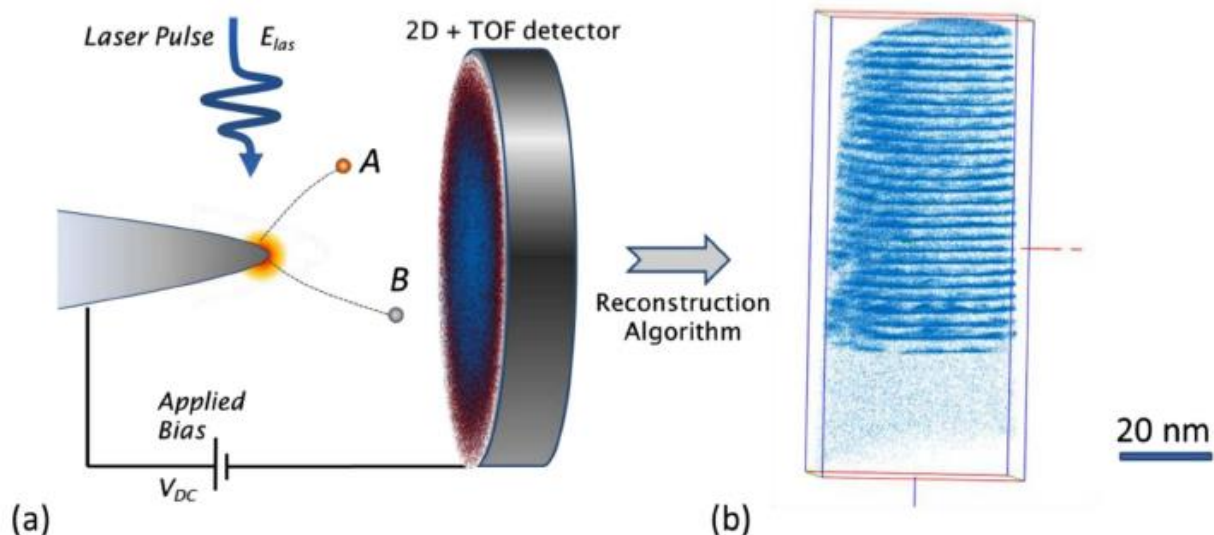
Figure 2-8. Schematic demonstrating the laser-assisted APT experimental flow from acquisition to reconstruction. Figure is reproduced from reference [177] with permission.

Once in the atom probe microscope, the tip is subjected to an electric field at an energy just below the threshold of atom evaporation. To cause field evaporation, additional energy is applied to the tip via voltage or laser pulses. The time-of-flight of the atoms from the tip to a position-sensitive detector is recorded and using this information in combination with laser tracking, atom probe allows for the specific identification of each ion that is detected and the spatial location from where it was generated. The time of flight of an individual ion is the time from the pulse to the time it contacts the detector and allows for determination of the mass to charge ratio [175]. This ratio can then be identified to a specific ion using knowledge of evaporated elements and ions [175]. The location that the ion contacts the detector provides x and y coordinates for the ion while the z coordinate is determined through reconstruction parameters [175]. The resultant data are a time-of-flight mass spectrum corresponding to a 3D point cloud which can be reconstructed into a 3D volume using an appropriate software. This 3D point cloud can be freely manipulated to perform analysis on the spatial and chemical arrangement of atoms, and therefore, This process is illustrated in Figure 2-8. APT is sometimes referred to as a four-dimensional (4D) technique, where x,y,z spatial information in 3D is combined with a fourth dimension of chemistry.

2.6.2 Sample Preparation for APT

APT sample preparation on metallic materials uses electropolishing but lacks control of the examined surface and can be time-consuming [174]. The development and proliferation of focused ion beam (FIB) microscopes worldwide have enabled use of FIB-based sample preparation for APT [178]. FIB-milling techniques allow for the fabrication of tips suitable for APT and have the advantage of being site-specific (Figure 2-9). Using lift-out techniques, it is possible to prepare

multiple APT samples from a single extracted region [178], [179]. Use of SEM within FIB microscopes enables this site-specific extraction. When considering biological samples, the lengthy sample preparation methods detailed above including fixation, dehydration and embedding are required. Additionally, there is capacity for correlative APT with TEM tomography techniques, such as STEM or EELS tomography, since the sample meets the geometrical requirements for TEM at the same time as APT [180], [181]. Tips prepared for APT can be mounted on a rotating sample holder that would allow for traditional electron tomography. These samples could subsequently be multiplexed and put in the atom probe microscope to perform correlative microscopy as demonstrated with bone-implant interfaces [16] and steels [180], [181]. The combination of these two techniques allowed for optimized APT reconstruction parameters.
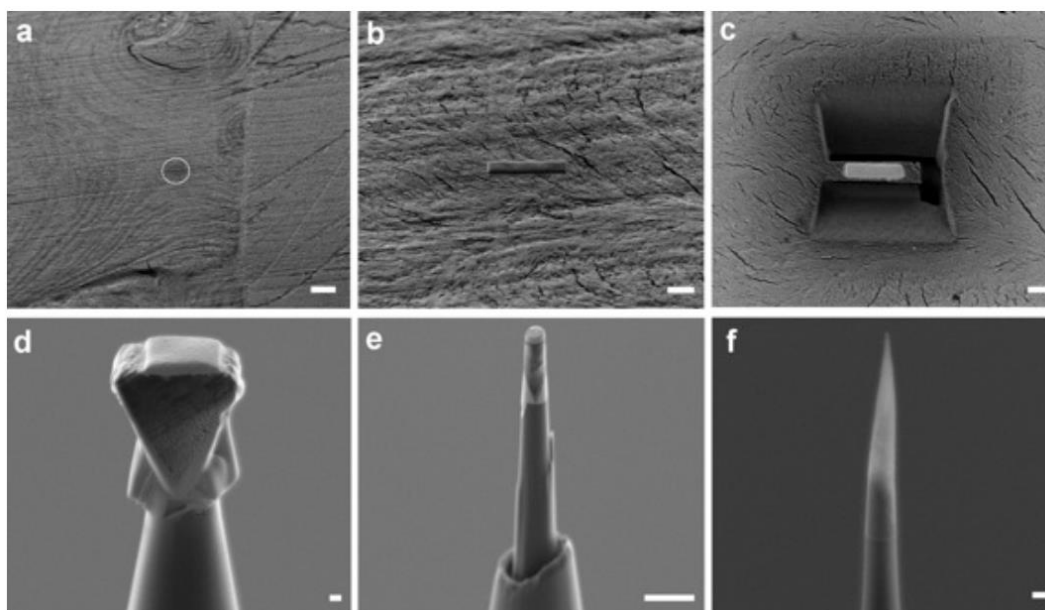
Figure 2-9. Sample preparation of human bone for APT experiments using FIB sample preparation methods. Scale bars (a) 40 µm, (b-e) 4 µm, (f) 200 nm. Figure was reproduced from reference [20] with permission.

2.6.3 APT of Biological Materials

Traditionally, APT was only possible for conductive samples as pulsed voltage was required to cause field evaporation. Biological, organic, and non-conductive materials do not typically evaporate well in the atom probe under voltage-pulsing conditions; however, laser pulsing methods have enabled the examination of insulating and organic materials [19], [176]. It has also been speculated that shortening the laser pulses could create lower local temperature spikes at the specimen surface which is ideal for all materials [179]. APT has been successfully applied to chitin [182], enamel [183], dentine [184], and human bone [20], as well as bone-implant interfaces [16], [185]. Each of these studies provided insight into the interfaces present within the materials and identified localization sites of specific elements, such as Na^+ and Mg^{2+} altering the composition of individual organic fibres in chiton [182] or Mg^{2+} and Fe^{3+} being segregated at grain boundaries in

rodent enamel [186]. Of these four biominerals, human bone has the highest percentage of organic content in the form of collagen which makes it challenging to put in the atom probe microscope. The previous APT work on human bone represents the first 4D model of bone at the atomic scale but the amount of collected ions is significantly less than many typical APT runs [20]. As the authors suggest, this may have been a consequence of the heterogeneity of bone and high organic content as well as its poor heat conduction [20]. These conditions result in increased background signal and reduced mass resolving power due to the presence of thermal tails in the mass spectra. These negative side effects have been observed in all biominerals and methods to minimize these effects have been moderately effective [20], [182]–[184]. As such, improvement on the quantity of data collected and its quality is required to further probe biomineralization of bone at the atomic scale. In Chapter 3, by altering the type of bone studied, and optimizing sample preparation to align collagen fibrils along the axis of the APT specimen, APT was used to probe biomineralization of leporine bone, resulting in much larger datasets than those previously reported as a result of condition optimization and new insights on collagen-mineral arrangement.

References

[1]   B. Clarke, "Normal Bone Anatomy and Physiology," *Clin. J. Am. Soc. Nephrol.*, pp. S131–S139, 2008.

[2]   C. I. for H. Information, "Hip and Knee Replacements in Canada , 2017 – 2018," 2018.

[3]   Albrektsson T, "Osseointegrated titanium implants," *Acta Orthop. Scand.*, vol. 52, no. 2, pp. 155–170, 1981.

[4]   K. Grandfield, "Bone, implants, and their interfaces," *Phys. Today*, vol. 68, no. 4, pp. 40–45, 2015.

[5]   V. V. D. Rani, L. Vinoth-Kumar, V. C. Anitha, K. Manzoor, M. Deepthy, and V. N. Shantikumar, "Osteointegration of titanium implant is sensitive to specific nanostructure morphology.," *Acta Biomater.*, vol. 8, no. 5, pp. 1976–89, May 2012.

[6]   T. Albrektsson, H. A. Hansson, and B. Ivarsson, "Interface analysis of titanium and zirconium bone implants.," *Biomaterials*, vol. 6, no. 2, pp. 97–101, Mar. 1985.

[7]   H. P. Schwarcz, E. A. McNally, and G. A. Botton, "Dark-field transmission electron microscopy of cortical bone reveals details of extrafibrillar crystals," *J. Struct. Biol.*, 2014.

[8]   H. P. Schwarcz, "The ultrastructure of bone as revealed in electron microscopy of ion-milled sections," *Semin. Cell Dev. Biol.*, vol. 46, 2015.

[9]   M. A. Rubin, I. Jasiuk, J. Taylor, J. Rubin, T. Ganey, and R. P. Apkarian, "TEM analysis of the nanostructure of normal and osteoporotic human trabecular bone," *Bone*, vol. 33, no. 3, pp. 270–282, 2003.

[10]   M. Bernhardsson, O. Sandberg, and P. Aspenberg, "Experimental models for cancellous bone healing in the rat Experimental models for cancellous bone healing in the rat," *Acta Orthop.*, vol. 86, no. 6, pp. 745–750, 2015.

[11]   M. A. Gallant, D. M. Brown, J. M. Organ, M. R. Allen, and D. B. Burr, "Reference-point indentation correlates with bone toughness assessed using whole-bone traditional

mechanical testing," *Bone*, vol. 53, no. 1, pp. 301–305, 2013.

[12]   N. Reznikov, R. Shahar, and S. Weiner, "Bone Hierarchical Structure in 3 Dimensions," *Acta Biomater.*, vol. 10, no. 9, pp. 3815–3826, 2014.

[13]   P. Schneider, M. Meier, R. Wepf, and R. Müller, "Serial FIB/SEM imaging for quantitative 3D assessment of the osteocyte lacuno-canalicular network," *Bone*, vol. 49, no. 2, pp. 304–311, 2011.

[14]   W. J. Landis, K. J. Hodgens, J. Arena, M. I. N. J. A. Song, and B. F. Mcewen, "Structural Relations Between Collagen and Mineral in Bone as Determined by High Voltage Electron Microscopic Tomography," *Microsc. Res. Tech.*, vol. 33, no. 2, pp. 192–202, 1996.

[15]   E. McNally, F. Nan, G. A. Botton, and H. P. Schwarcz, "Scanning transmission electron microscopic tomography of cortical bone using Z-contrast imaging," *Micron*, vol. 49, pp. 46–53, 2013.

[16]   X. Wang *et al.*, "Biomineralization at Titanium Revealed by Correlative 4D Tomographic and Spectroscopic Methods," *Adv. Mater. Interfaces*, vol. 5, no. 14, p. 1800262, 2018.

[17]   B. F. Landis, W J., Song, M.J, Leith, A.,McEwen,L.,McEwen, "Mineral and Organic Matrix Interaction in Normally Calcifying Tendon Visualized in Three Dimensions by High-Voltage Electron Microscopic Tomography and Graphic Image Reconstruction," *J. Struct. Biol.*, vol. 110, pp. 39–54, 1993.

[18]   N. Reznikov, M. Bilton, L. Lari, M. M. Stevens, and R. Kröger, "Fractal-like hierarchical organization of bone begins at the nanoscale," *Science (80-.).*, vol. 360, no. 6388, p. eaao2189, 2018.

[19]   D. Joester, A. Hillier, Y. Zhang, and T. J. Prosa, "Organic Materials And Organic / Inorganic Heterostructures In Atom Probe Tomography," *Micros. Today*, vol. 20, no. 3, pp. 11–14, 2012.

[20]   B. Langelier, X. Wang, and K. Grandfield, "Atomic scale chemical tomography of human bone," *Sci. Rep.*, vol. 7, p. 39958, 2017.

[21]   Q. Chen, C. Zhu, and G. A. Thouas, "Progress and challenges in biomaterials used for bone tissue engineering : bioactive glasses and elastomeric composites," *Prog. Biomater.*, vol. 1, no. 2, pp. 1–22, 2012.

[22]   T. A. G. Donato *et al.*, "Cytotoxicity study of some Ti alloys used as biomaterial," *Mater. Sci. Eng. C*, vol. 29, no. 4, pp. 1365–1369, 2009.

[23]   P. J. Aragon, S. F. Hulbert, and D. Interdisciplinary, "Corrosion of Ti-6A1-4V in simulated body fluids and bovine plasma.," *J. Biomed. Mater. Res.*, vol. 6, no. 3, pp. 155–164, 1972.

[24]   J. Simpson, J. Lankford, and M. E. T. Al, "Effect of titanium surface roughness on proliferation, differentiation, and protein synthesis of human osteoblast-like cells (MG63)," *J. Biomed. Mater. Res. A*, vol. 29, no. 3, pp. 389–401, 1995.

[25]   R. K. Alla, K. Ginjupalli, N. Upadhya, M. Shammas, R. K. Ravi, and R. Sekhar, "Surface Roughness of Implants: A Review," *Trends Biomater. Artif. Organs*, vol. 25, no. 3, pp. 112–118, 2011.

[26]   P. Bizi-Bandoki, S. Benayoun, S. Valette, B. Beaugiraud, and E. Audouard, "Modifications of roughness and wettability properties of metals induced by femtosecond laser treatment," *Appl. Surf. Sci.*, vol. 257, no. 12, pp. 5213–5218, 2011.

[27]   D. A. Puleo and A. Nanci, "Understanding and controlling the bone-implant interface.," *Biomaterials*, vol. 20, no. 23–24, pp. 2311–21, Dec. 1999.

[28]   C. Larsson, P. Thomsen, J. Lausmaa, M. Rodahl, B. Kasemo, and L. E. Ericson, "Bone response to surface modified titanium implants: studies on electropolished implants with different oxide thicknesses and morphology.," *Biomaterials*, vol. 15, no. 13, pp. 1062–74, Oct. 1994.

[29]   A. R. Amini, C. T. Laurencin, and S. P. Nukavarapu, "Bone tissue engineering: recent advances and challenges.," *Crit. Rev. Biomed. Eng.*, vol. 40, no. 5, pp. 363–408, 2012.

[30]   M. Baleani, M. Viceconti, and a Toni, "The effect of sandblasting treatment on endurance properties of titanium alloy hip prostheses.," *Artif. Organs*, vol. 24, no. 4, pp. 296–9, Apr. 2000.

[31]   M. Lewandowska, A. Roguska, M. Pisarek, B. Polak, M. Janik-Czachor, and K. J. Kurzydłowski, "Morphology and chemical characterization of Ti surfaces modified for biomedical applications.," *Biomol. Eng.*, vol. 24, no. 5, pp. 438–42, 2007.

[32]   T. R. Rautray, R. Narayanan, T.-Y. Kwon, and K.-H. Kim, "Surface modification of titanium and titanium alloys by ion implantation.," *J. Biomed. Mater. Res. B. Appl. Biomater.*, vol. 93, no. 2, pp. 581–91, May 2010.

[33]   F. A. Shah, M. L. Johansson, O. Omar, H. Simonsson, A. Palmquist, and P. Thomsen, "Laser-modified surface enhances osseointegration and biomechanical anchorage of commercially pure titanium implants for bone-anchored hearing systems," *PLoS One*, vol. 11, no. 6, pp. 1–24, 2016.

[34]   O. Raimbault *et al.*, "The effects of femtosecond laser-textured Ti-6Al-4V on wettability and cell response," *Mater. Sci. Eng. C*, vol. 69, pp. 311–320, 2016.

[35]   A. Y. Vorobyev and C. Guo, "Femtosecond laser structuring of titanium implants," *Appl. Surf. Sci.*, vol. 253, no. 17, pp. 7272–7280, 2007.

[36]   M. M. Stevens and J. H. George, "Exploring and engineering the cell surface interface.," *Science*, vol. 310, no. 5751, pp. 1135–1138, 2005.

[37]   G. Ciapetti, E. Cenni, L. Pratelli, and A. Pizzoferrato, "In vitro evaluation of cell/biomaterial interaction by MTT assay," *Biomaterials*, vol. 14, no. 5, pp. 359–364, 1993.

[38]   T. L. Riss *et al.*, "Cell Viability Assays," *Assay Guid. Man. [Internet]*, vol. 114, no. 8, pp. 785–796, 2013.

[39]   M. O'Donovan, "A critique of methods to measure cytotoxicity in mammalian cell genotoxicity assays," *Mutagenesis*, vol. 27, no. 6, pp. 615–621, 2012.

[40]   D. J. Stephens, "Light Microscopy Techniques for Live Cell Imaging," *Sci. (New York, NY)*, vol. 300, no. 5616, pp. 82–86, 2003.

[41]   M. a DeCoster, "The Nuclear Area Factor (NAF): a measure for cell apoptosis using microscopy and image analysis," *Mod. Res. Educ. Top. Microsc.*, pp. 378–84, 2007.

[42]   I. M. Helmy and A. M. Abdel Azim, "Efficacy of ImageJ in the assessment of apoptosis," *Diagn. Pathol.*, vol. 7, no. 1, p. 15, 2012.

[43]   S. W. Hell, "Microscopy and its focal switch," *Nat. Methods*, vol. 6, no. 1, pp. 24–32, 2009.

[44]   B. Huang, M. Bates, and X. Zhuang, "Super resolution fluorescence microscopy," *Annu. Rev. Biochem.*, vol. 78, pp. 993–1016, 2010.

[45]   G. . Danilatos, "Review and outline of environmental SEM at present," *J. Microsc.*, vol. 162, no. 3, pp. 391–402, 1991.

[46]   L. Muscariello *et al.*, "A critical overview of ESEM applications in the biological field," *J. Cell. Physiol.*, vol. 205, no. 3, pp. 328–334, 2005.

[47] R. E. Thach and S. S. Thach, "Damage to Biological Samples Caused by the Electron Beam during Electron Microscopy," *Biophys. J.*, vol. 11, no. 2, pp. 204–210, 1971.

[48] D. C. Sigee, *Environmental SEM and X-ray microanalysis of biological materials. In Modern Developments and Applications in Microbeam Analysis.* Springer Vienna, 1998.

[49] Y. Ishigaki *et al.*, "Observation of live ticks (haemaphysalis flava) by scanning electron microscopy under high vacuum pressure," *PLoS One*, vol. 7, no. 3, pp. 2–7, 2012.

[50] T. Vasantha, A. Kumar, P. Attri, P. Venkatesu, and R. S. R. Devi, "The Solubility and Stability of Amino Acids in Biocompatible Ionic Liquids," pp. 15–24, 2014.

[51] A. Dwiranti *et al.*, "Chromosome observation by scanning electron microscopy using ionic liquid," *Microsc. Res. Tech.*, vol. 75, no. 8, pp. 1113–1118, 2012.

[52] U. Kini and B. N. Nandeesh, *Physiology of Bone Formation, Remodeling, and Metabolism.* Springer Berlin Heidelberg, 2012.

[53] S. Weiner, W. Traub, and H. D. Wagner, "Lamellar Bone : Structure – Function Relations," *J. Struct. Biol.*, vol. 126, no. 3, pp. 241–255, 1999.

[54] P. Fratzl, H. S. Gupta, E. P. Paschalis, and P. Roschger, "Structure and mechanical quality of the collagen – mineral nano-composite in bone," *J. Mater. Chem.*, vol. 14, no. 14, pp. 2115–2123, 2004.

[55] Y. Pan and M. E. Fleet, "Compositions of the Apatite-Group Minerals : Substitution Mechanisms and Controlling Factors," *Rev. Mineral. Geochemistry*, vol. 48, no. 1, pp. 13–49, 2002.

[56] J. H. Shepherd, D. V Shepherd, and S. M. Best, "Substituted hydroxyapatites for bone repair," *J. Mater. Sci. Mater. Med.*, vol. 23, no. 10, pp. 2335–2347, 2012.

[57] E. Beniash, "Biominerals — hierarchical nanocomposites : the example of bone," *Wiley Interdiscip. Rev. Nanomedicine Nanobiotechnology*, vol. 3, no. 1, pp. 47–69, 2011.

[58] V. Ziv and S. Weiner, "Bone Crystal Sizes : A Comparison of Transmission Electron Microscopic and X-Ray Diffraction Line Width Broadening Techniques," *Connect. Tissue Res.*, vol. 30, pp. 165–175, 2009.

[59] A. . Hodge and J. A. Petruska, "Recent studies with the electron microscope on ordered aggregates of the tropocollagen macromolecule, in Aspects of Protein Structure," *Asp. Protein Struct.*, pp. 289–300, 1963.

[60] J. Petruska and A. Hodge, "A Subunit Model for the Tropocollagen Macromolecule," *Proc. Natl. Acad. Sci. U. S. A.*, vol. 51, no. 5, pp. 871–876, 1964.

[61] M. J. Olszta *et al.*, "Bone structure and formation : A new perspective," *Mater. Sci. Eng. R*, vol. 58, pp. 77–116, 2007.

[62] E. P. Katz and H. Li, "Structure and Function of Bone Collagen Fibrils," *J.Mol.Bio.*, vol. 80, pp. 1–15, 1973.

[63] U. G. K. Wegst, H. Bai, E. Saiz, A. P. Tomsia, and R. O. Ritchie, "Bioinspired structural materials," *Nat. Mater.*, vol. 14, no. 1, pp. 23–36, 2015.

[64] G. . Tortora and B. . Derrickson, *Principles of Anatomy and Physiology*. John Wiley & Sons, 2008.

[65] N. Reznikov, H. Chase, V. Brumfeld, R. Shahar, and S. Weiner, "The 3D structure of the collagen fi bril network in human trabecular bone : Relation to trabecular organization," *Bone*, vol. 71, pp. 189–195, 2015.

[66] W. J. Landis and M. J. Song, "Early mineral deposition in calcifying tendon characterized by high voltage electron microscopy and three-dimensional graphic imaging," *J. Struct. Biol.*, vol. 107, no. 2, pp. 116–127, 1991.

[67]   S. Weiner and W. Traub, "Bone structure: from angstroms to microns," *FASEB J.*, vol. 6, no. 3, pp. 879–885, 1992.

[68]   E. A. McNally, H. P. Schwarcz, G. A. Botton, and A. L. Arsenault, "A model for the ultrastructure of bone based on electron microscopy of ion-milled sections," *PLoS One*, vol. 7, no. 1, 2012.

[69]   K. Grandfield, V. Vuong, and H. P. Schwarcz, "Ultrastructure of Bone : Hierarchical Features from Nanometer to Micrometer Scale Revealed in Focused Ion Beam Sections in the TEM," *Calcif. Tissue Int.*, vol. 103, no. 6, pp. 606–616, 2018.

[70]   R. Florencio-silva, G. Rodrigues, E. Sasso-cerri, M. J. Simões, P. S. Cerri, and B. Cells, "Biology of Bone Tissue : Structure , Function , and Factors That Influence Bone Cells," *Biomed Res. Int.*, vol. 2015, 2015.

[71]   R. Bartl and C. Bartl, *Bone Disorders: Biology, Diagnosis, Prevention, Therapy*, Illustrate. Springer US, 2016.

[72]   A. J. Shimmin, J. Bare, and D. L. Back, "Complications associated with hip resurfacing arthroplasty," *Orthop Clin North Am*, vol. 36, no. 2, p. 187–93, ix, 2005.

[73]   A. G. Gristina, "Implant failure and the immuno-incompetent fibro-inflammatory zone.," *Clin. Orthop. Relat. Res.*, no. 298, pp. 106–118, 1994.

[74]   S. K. Mitra, D. A. Hanson, and D. D. Schlaepfer, "Focal adhesion kinase: in command and control of cell motility.," *Nat. Rev. Mol. Cell Biol.*, vol. 6, no. 1, pp. 56–68, 2005.

[75]   A. J. Ridley, "Cell Migration: Integrating Signals from Front to Back," *Science (80-.).*, vol. 302, no. 5651, pp. 1704–1709, 2003.

[76]   D. A. Lauffenburger and A. F. Horwitz, "Cell migration: A physically integrated molecular process," *Cell*, vol. 84, no. 3, pp. 359–369, 1996.

[77]   C. M. Lo, H. B. Wang, M. Dembo, and Y. L. Wang, "Cell movement is guided by the rigidity of the substrate.," *Biophys. J.*, vol. 79, no. 1, pp. 144–152, 2000.

[78]   G. Maheshwari and D. A. Lauffenburger, "Deconstructing (and reconstructing) cell migration," *Microsc. Res. Tech.*, vol. 43, no. 5, pp. 358–368, 1998.

[79]   P. E. Morton and M. Parsons, "Dissecting cell adhesion architecture using advanced imaging techniques.," *Cell Adh. Migr.*, vol. 5, no. 4, pp. 351–359, 2011.

[80]   S. van Helvert and P. Friedl, "Strain stiffening of fibrillar collagen during individual and collective cell migration identified by AFM nanoindentation," *ACS Appl Mater Interfaces*, vol. 8, no. 34, pp. 21946–21955, 2016.

[81]   S. Raghavendra *et al.*, "Early wound healing around endosseous implants: a review of the literature.," *Int. J. Oral Maxillofac. Implants*, vol. 20, no. 3, pp. 425–31, 2005.

[82]   S. Guo and L. A. Dipietro, "Factors affecting wound healing," *J Dent Res*, vol. 89, no. 3, pp. 219–229, 2010.

[83]   M. Geetha, A. K. Singh, R. Asokamani, and A. K. Gogia, "Ti based biomaterials, the ultimate choice for orthopaedic implants – A review," *Prog. Mater. Sci.*, vol. 54, no. 3, pp. 397–425, 2009.

[84]   M. Niinomi, "Recent metallic materials for biomedical applications," *Metall. Mater. Trans. A*, vol. 33, no. 3, p. 477, 2002.

[85]   J. Li and G. . Hastings, *Handbook of Biomaterial Properties*. Springer US, 1998.

[86]   J. . Katz, "Anisotropy of Young's modulus of bone.," *Nature*, pp. 106–107, 1980.

[87]   S. Nag, R. Banerjee, and H. L. Fraser, "Microstructural evolution and strengthening mechanisms in Ti–Nb–Zr–Ta, Ti–Mo–Zr–Fe and Ti–15Mo biocompatible alloys," *Mater. Sci. Eng. C*, vol. 25, no. 3, pp. 357–362, 2005.

[88]　P. Laing, "Tissue reaction in rabbit muscle exposed to metallic implants," *J. Biomed. Mater. Res.*, vol. 1, no. 1, pp. 135–149, 1967.

[89]　Y. Song, D. S. Xu, R. Yang, D. Li, W. T. Wu, and Z. X. Guo, "Theoretical study of the effects of alloying elements on the strength and modulus of i -type bio-titanium alloys," *Mater. Sci. Eng. A*, vol. 260, pp. 269–274, 1999.

[90]　E. Kobayashi, T. J. Wang, H. Doi, T. Yoneyama, and H. Hamanaka, "Mechanical properties and corrosion resistance of Ti-6Al-7Nb alloy dental castings.," *J. Mater. Sci. Mater. Med.*, vol. 9, no. 10, pp. 567–74, 1998.

[91]　X. Liu, S. Chen, J. K. H. Tsoi, and J. P. Matinlinna, "Binary titanium alloys as dental implant materials — a review," *Regen. Biomater.*, vol. 4, no. 5, pp. 315–323, 2017.

[92]　F. A. Shah, M. Trobos, P. Thomsen, and A. Palmquist, "Commercially pure titanium (cp-Ti) versus titanium alloy (Ti6Al4V) materials as bone anchored implants — Is one truly better than the other ?," *Mater. Sci. Eng. C*, vol. 62, pp. 960–966, 2016.

[93]　Y. Sul, "The significance of the surface properties of oxidized titanium to the bone response: special emphasis on potential biochemical bonding of oxidized titanium implant," *Biomaterials*, vol. 24, no. 22, pp. 3893–3907, 2003.

[94]　B. D. Boyan, T. W. Hummert, D. D. Dean, and Z. Schwartz, "Role of material surfaces in regulating bone and cartilage cell response.," *Biomaterials*, vol. 17, no. 2, pp. 137–46, 1996.

[95]　C. M. Bowers, K. T., Keller, J. C., Randolph, B. A., Wick, D. G., and Michaels, "Optimization of surface micromorphology for enhanced osteoblast responses in vitro.," *Int. J. Oral Maxillofac. Implants*, vol. 7, no. 3, pp. 302–310, 1991.

[96]　H. J. Rønold, S. P. Lyngstadaas, and J. E. Ellingsen, "Analysing the optimal value for titanium implant roughness in bone attachment using a tensile test," *Biomaterials*, vol. 24, no. 25, pp. 4559–4564, 2003.

[97]　D. Buser, R. K. Schenk, S. Steinemann, J. P. Fiorellini, C. H. Fox, and H. Stich, "Influence of surface characteristics on bone integration of titanium implants. A histomorphometric study in miniature pigs.," *J. Biomed. Mater. Res.*, vol. 25, no. 7, pp. 889–902, Jul. 1991.

[98]　L. Thair, U. Kamachi Mudali, S. Rajagopalan, R. Asokamani, and B. Raj, "Surface characterization of passive film formed on nitrogen ion implanted Ti–6Al–4V and Ti–6Al–7Nb alloys using SIMS," *Corros. Sci.*, vol. 45, no. 9, pp. 1951–1967, 2003.

[99]　Y. Yang, J. Tian, L. Deng, and J. L. Ong, "Morphological behavior of osteoblast-like cells on surface-modified titanium in vitro.," *Biomaterials*, vol. 23, no. 5, pp. 1383–9, 2002.

[100]　K. Anselme and M. Bigerelle, "Modelling approach in cell/material interactions studies," *Biomaterials*, vol. 27, no. 8, pp. 1187–1199, 2006.

[101]　Y. Sul, C. Johansson, and Y. Jeong, "Oxidized implants and their influence on the bone response," *J. Mater. Sci. Mater. Med.*, vol. 2, no. (10-12), pp. 1025–1031, 2001.

[102]　X. Zhu, J. Chen, L. Scheideler, R. Reichl, and J. Geis-Gerstorfer, "Effects of topography and composition of titanium surface oxides on osteoblast responses.," *Biomaterials*, vol. 25, no. 18, pp. 4087–103, 2004.

[103]　M. F. Baslé *et al.*, "Osteoclastic resorption of Ca-P biomaterials implanted in rabbit bone.," *Calcif. Tissue Int.*, vol. 53, no. 5, pp. 348–56, 1993.

[104]　C. Giordano, E. Sandrini, B. D. E. L. Curto, E. Signorelli, G. Rondelli, and L. D. I. Silvio, "Titanium for osteointegration: Comparison between a novel biomimetic treatment and commercially exploited surfaces," *J. Appl. Biomater. Biomech.*, vol. 2, no. 1, pp. 35–44,

2004.

[105] X. Zhu, J. L. Ong, S. Kim, and K. Kim, "Surface characteristics and structure of anodic oxide films containing Ca and P on a titanium implant material.," *J. Biomed. Mater. Res.*, vol. 60, no. 2, pp. 333–8, 2002.

[106] W. Querido, M. Farina, and K. Anselme, "Strontium ranelate improves the interaction of osteoblastic cells with titanium substrates: Increase in cell proliferation, differentiation and matrix mineralization.," *Biomatter*, vol. 5, no. 1, p. e1027847, 2015.

[107] Y. S. Tian, C. Z. Chen, S. T. Li, and Q. H. Huo, "Research progress on laser surface modification of titanium alloys," *Appl. Surf. Sci.*, vol. 242, no. 1–2, pp. 177–184, 2005.

[108] M. P. Group, C. Division, O. Ridge, and O. Ridge, "Surface modification for bioimplants: the role of laser surface engineering.," *J. Biomater. Appl.*, vol. 20, no. 1, pp. 5–50, 2005.

[109] V. Neděla, O., Slepička, P., & Švorčík, "Surface Modification of Polymer Substrates for Biomedical Applications," *Materials (Basel).*, vol. 10, no. 10, 2017.

[110] K. Washio, "Laser Devices and Optical Systems for LaserPrecision Microfabrication," in *Laser Precision Microfabrication*, Springer Berlin Heidelberg, 2010, pp. 63–89.

[111] N. B. Kurella, A., Dahotre, "Surface Modification for Bioimplants: The Role of Laser Surface Engineering," *J. Biomater. Appl.*, vol. 20, no. 1, pp. 5–50, 2005.

[112] D. Von Der Linde and J. Bialkowski, "Laser – solid interaction in the femtosecond time regime," *Appl. Surf. Sci.*, vol. 109, pp. 1–10, 1997.

[113] D. Lewis, L. J., & Perez, "Theory and simulation of laser ablation–from basic mechanisms to applications," in *Laser Precision Microfabrication*, Springer Berlin Heidelberg, 2010, pp. 35–61.

[114] D. Bauerle, *Laser processing and chemistry*, 3rd ed. Springer US, 2000.

[115] Y. Li, L. Qu, and F. Wang, "The electrochemical corrosion behavior of TiN and (Ti,Al)N coatings in acid and salt solution," *Corros. Sci.*, vol. 45, no. 7, pp. 1367–1381, 2003.

[116] S. A. Cho and S. K. Jung, "A removal torque of the laser-treated titanium implants in rabbit tibia," *Biomaterials*, vol. 24, no. 26, pp. 4859–4863, 2003.

[117] C. Hallgren, H. Reimers, D. Chakarov, J. Gold, and A. Wennerberg, "An in vivo study of bone response to implants topographically modified by laser micromachining.," *Biomaterials*, vol. 24, no. 5, pp. 701–10, 2003.

[118] M. Trtica, B. Gakovic, D. Batani, T. Desai, P. Panjan, and B. Radak, "Surface modifications of a titanium implant by a picosecond Nd:YAG laser operating at 1064 and 532nm," *Appl. Surf. Sci.*, vol. 253, no. 5, pp. 2551–2556, 2006.

[119] D. S. Milovanović, B. B. Radak, B. M. Gaković, D. Batani, M. D. Momčilović, and M. S. Trtica, "Surface morphology modifications of titanium based implant induced by 40picosecond laser pulses at 266nm," *J. Alloys Compd.*, vol. 501, no. 1, pp. 89–92, 2010.

[120] M. Bereznai, "Surface modifications induced by ns and sub-ps excimer laser pulses on titanium implant material," *Biomaterials*, vol. 24, no. 23, pp. 4197–4203, Oct. 2003.

[121] D. S. Milovanović *et al.*, "Titanium alloy surface modification by excimer laser irradiation," *Opt. Laser Technol.*, vol. 54, pp. 419–427, 2013.

[122] J. F. Van Driel, H. M., Sipe, J. E., & Young, "Laser-induced periodic surface structure on solids: a universal phenomenon," *Phys. Rev. Lett.*, vol. 49, no. 26, pp. 1955–1959, 1982.

[123] J. E. Sipe, J. F. Young, J. S. Preston, and H. M. Van Driel, "Laser-induced periodic surface structure. I. Theory," *Phys. Rev. B*, vol. 27, no. 2, pp. 1141–1154, 1983.

[124] J. F. Young, J. Preston, H. Van Driel, and J. Sipe, "Laser induced periodic surface structures II. Experiments on Ge, Si, Al and brass," *Phys. Rev. B*, vol. 27, no. 2, p. 1155,

1983.

[125] M. Huang, F. Zhao, Y. Cheng, N. Xu, and Z. Xu, "Origin of Laser-Induced Near-Subwavelength Ripples : Interference between Surface Plasmons and Incident Laser," *ACS Nano*, vol. 3, no. 12, pp. 4062–4070, 2009.

[126] C. B. Brown, M. S., & Arnold, "Fundamentals of laser-material interaction and application to multiscale surface modification," in *Laser Precision Microfabrication*, Springer Berlin Heidelberg, 2010, pp. 91–120.

[127] T. Shinonaga, M. Tsukamoto, T. Kawa, P. Chen, A. Nagai, and T. Hanawa, "Formation of periodic nanostructures using a femtosecond laser to control cell spreading on titanium," *Appl. Phys. B Lasers Opt.*, vol. 119, no. 3, pp. 493–496, 2015.

[128] N. Mirhosseini, P. L. Crouse, M. J. J. Schmidth, L. Li, and D. Garrod, "Laser surface micro-texturing of Ti – 6Al – 4V substrates for improved cell integration," *Appl. Surf. Sci.*, vol. 253, pp. 7738–7743, 2007.

[129] R. Cunha, A., Oliveira, V., Serro, A. P., Zouani, O. E. F., Almeida, A., Durrieu, M. C., & Vilar, "Ultrafast laser texturing of Ti-6Al-4V surfaces for biomedical applications," *Int. Congr. Appl. Lasers Electro-Optics.*, vol. 2013, pp. 910–918, 2013.

[130] F. A. Shah, B. Nilson, R. Brånemark, P. Thomsen, and A. Palmquist, "The bone-implant interface-nanoscale analysis of clinically retrieved dental implants.," *Nanomedicine*, vol. 10, no. 8, pp. 1729–1737, 2014.

[131] J. Yong, F. Chen, Q. Yang, U. Farooq, and X. Hou, "Photoinduced switchable underwater superoleophobicity – superoleophilicity on laser," *J. Mater. Chem. A*, vol. 3, no. 20, pp. 10703–10709, 2015.

[132] J. F. V Vincent, "Biomimetic materials," *J. Mater. Res.*, vol. 23, no. 12, pp. 3140–3147, 2008.

[133] E. Engel, A. Michiardi, M. Navarro, D. Lacroix, and J. a Planell, "Nanotechnology in regenerative medicine: the materials side.," *Trends Biotechnol.*, vol. 26, no. 1, pp. 39–47, Jan. 2008.

[134] M. Li, P, K. de Groot, and T. Kukubo, "Bonelike Hydroxyapatite Induction by sol-gel derived titania coating on a titanium substrate.," *J. Am. Ceram. Soc.*, vol. 77, no. 5, pp. 1307–1312, 1994.

[135] P. Habibovic, F. Barre, C. A. Van Blitterswijk, and K. De Groot, "Biomimetic Hydroxyapatite Coating on Metal Implants," *J. Am. Ceram. Soc.*, vol. 85, no. 3, pp. 517–522, 2002.

[136] K. E. Healy, A. Rezania, and R. A. Stile, "Designing Biomaterials to Direct Biological Responses," *Ann. N. Y. Acad. Sci.*, vol. 875, no. 1, pp. 24–35, 1999.

[137] P.-H. Chua, K.-G. Neoh, E.-T. Kang, and W. Wang, "Surface functionalization of titanium with hyaluronic acid/chitosan polyelectrolyte multilayers and RGD for promoting osteoblast functions and inhibiting bacterial adhesion.," *Biomaterials*, vol. 29, no. 10, pp. 1412–21, 2008.

[138] S.-Y. Park *et al.*, "Effects of anodized titanium implant coated with RGD peptides via chemical fixation on osseointegration and bone regeneration," *Tissue Eng. Regen. Med.*, vol. 9, no. 4, pp. 194–202, Jul. 2012.

[139] X. Liu, P. Chu, and C. Ding, "Surface modification of titanium, titanium alloys, and related materials for biomedical applications," *Mater. Sci. Eng. R Reports*, vol. 47, no. 3–4, pp. 49–121, Dec. 2004.

[140] M. Pilliar, D. A. Deporter, and P. A. Watson, "Dental implant design-Effect on bone

remodeling," *J. Biomed. Mater. Res.*, vol. 25, no. 4, pp. 467–483, 1991.

[141] R. Brånemark, L. Emanuelsson, A. Palmquist, and P. Thomsen, "Bone response to laser-induced micro- and nano-size titanium surface features," *Nanomedicine Nanotechnology, Biol. Med.*, vol. 7, no. 2, pp. 220–227, 2011.

[142] L. Salou, A. Hoornaert, G. Louarn, and P. Layrolle, "Enhanced osseointegration of titanium implants with nanostructured surfaces: An experimental study in rabbits," *Acta Biomater.*, vol. 11, no. 1, pp. 494–502, 2015.

[143] K. Anselme, "Osteoblast adhesion on biomaterials," *Biomaterials*, vol. 21, no. 7, pp. 667–681, 2000.

[144] U. Meyer, A. Büchter, H. P. Wiesmann, U. Joos, and D. B. Jones, "Basic Reactions of Osteoblasts on Structured Material Surfaces," *Eur. Cells Mater.*, vol. 9, pp. 39–49, 2005.

[145] G. Passeri, A. Cacchioli, F. Ravanetti, C. Galli, E. Elezi, and G. M. Macaluso, "Adhesion pattern and growth of primary human osteoblastic cells on five commercially available titanium surfaces.," *Clin. Oral Implants Res.*, vol. 21, no. 7, pp. 756–65, 2010.

[146] J. Rice, "Quantitative assessment of the response of primary derived human osteoblasts and macrophages to a range of nanotopography surfaces in a single culture model in vitro," *Biomaterials*, vol. 24, no. 26, pp. 4799–4818, Nov. 2003.

[147] C. Pautke *et al.*, "Characterization of Osteosarcoma Cell Lines MG-63 , Saos-2 and U-2 OS in Comparison to Human Osteoblasts," *Anticancer Res.*, vol. 24, no. 6, pp. 3743–3748, 2004.

[148] J. O'Brien, I. Wilson, T. Orton, and F. Pognan, "Investigation of the Alamar Blue (resazurin) fluorescent dye for the assessment of mammalian cell cytotoxicity," *Eur. J. Biochem.*, vol. 267, no. 17, pp. 5421–5426, 2000.

[149] I. C. Maccoubrey, P. L. Moore, and W. Roxbury, "Dual-fluorescence cell viability assay using ethidium homodimer and calcein AM," 1994.

[150] P. W. Kirk, "Neutral Red as a Lipid Fluorochrome," *Stain Technol.*, vol. 45, no. 1, 1970.

[151] J. E. Aubin, "Autofluorescence of viable cultured mammalian cells," *J. Histochem. Cyochemistry*, vol. 27, no. 1, pp. 36–43, 1979.

[152] Z. Novotna, A. Reznickova, S. Rimpelova, M. Vesely, Z. Kolska, and V. Svorcik, "Tailoring of PEEK bioactivity for improved cell interaction: plasma treatment in action," *RSC Adv.*, vol. 5, no. 52, pp. 41428–41436, 2015.

[153] K. Cai *et al.*, "Surface modification of poly (D,L-lactic acid) with chitosan and its effects on the culture of osteoblasts in vitro.," *J. Biomed. Mater. Res.*, vol. 60, no. 3, pp. 398–404, 2002.

[154] T. L. Riss and R. . Moravec, "Riss (2004) - Use of Multiple Assay Endpoints to Investigate the Effects of Incubation Time, Dose of Toxin, and Plating Density in Cell-Based Cytotoxicity Assays.pdf," *Assay Drug Dev. Technol.*, vol. 2, no. 1, 2004.

[155] H. Liu and T. J. W. Ã, "Nanomedicine for implants : A review of studies and necessary experimental tools," *Biomaterials*, vol. 28, pp. 354–369, 2007.

[156] D. C. Joy, "Control of Charging in Low-Voltage SEM," *J. Scanning Technol.*, vol. 11, pp. 1–4, 1989.

[157] U. L. F. Brunk and E. R. I. K. Arro, "The fixation , dehydration , drying and coating of cultured cells for SEM," *J. Microsc.*, vol. 123, no. August, pp. 121–131, 1981.

[158] S. Kim and C. Chu, "Synthesis and characterization of dextran – methacrylate hydrogels and structural study by SEM," *J. Biomed. Mater. Res.*, vol. 49, no. 4, 1999.

[159] M. A. Hayat, "Glutaraldehyde: Role in Electron Microscopy," *Micron Microsc. Acta*, vol.

17, no. 2, pp. 115–135, 1986.

[160] R. Bullock, "The current status of fixation for electron microscopy : a review," *J. Microsc.*, vol. 133, no. 1, pp. 1–15, 1984.

[161] J. R. Mcintosh, "Electron Microscopy of Cells : A New Beginning for a New Century," vol. 153, no. 6, pp. 25–32, 2001.

[162] A. J. Koster and J. Klumperman, "Electron microscopy in cell biology : integrating structure and function," *Nat. Rev. Mol. Cell Biol.*, vol. 4, no. 9, 2003.

[163] K. J. McKinlay *et al.*, "Comparison of environmental scanning electron microscopy with high vacuum scanning electron microscopy as applied to the assessment of cell morphology.," *J. Biomed. Mater. Res. A*, vol. 69, no. 2, pp. 359–366, 2004.

[164] A. Hyono *et al.*, "SEM observation of the live morphology of human red blood cells under high vacuum conditions using a novel RTIL," *Surf. Interface Anal.*, vol. 46, no. 6, pp. 425–428, 2014.

[165] K. E. Johnson, "What's an Ionic Liquid?," *Interface-Electrochemical Soc.*, vol. 16, no. 1, pp. 38–41, 2007.

[166] H. Tokuda, S. Tsuzuki, A. Bin, H. Susan, and K. Hayamizu, "How Ionic Are Room-Temperature Ionic Liquids ? An Indicator of the Physicochemical Properties," *J. Phys. Chem. B*, vol. 110, pp. 19593–19600, 2006.

[167] L. P. N. Rebelo, N. C. Lopes, and M. S. S. Esperanc, "On the Critical Temperature , Normal Boiling Point , and Vapor Pressure of Ionic Liquids," *J. Phys. Chem. B Lett.*, vol. 0, no. 1, pp. 6040–6043, 2005.

[168] T. Tsuda *et al.*, "SEM observation of wet biological specimens pretreated with room-temperature ionic liquid," *ChemBioChem*, vol. 12, no. 17, pp. 2547–2550, 2011.

[169] Y. Ishigaki *et al.*, "Comparative study of hydrophilic and hydrophobic ionic liquids for observing cultured human cells by scanning electron microscopy," *Microsc. Res. Tech.*, vol. 74, no. 12, pp. 1104–1108, 2011.

[170] C. Takahashi, N. Ogawa, Y. Kawashima, and H. Yamamoto, "Observation of antibacterial effect of biodegradable polymeric nanoparticles on Staphylococcus epidermidis biofilm using FE-SEM with an ionic liquid," *Microscopy*, vol. 64, no. 3, pp. 169–180, 2015.

[171] N. de Jonge and D. B. Peckys, "Live Cell Electron Microscopy Is Probably Impossible," *ACS Nano*, vol. 10, no. 10, pp. 9061–9063, 2016.

[172] N. de Jonge, D. B. Peckys, G. J. Kremers, and D. W. Piston, "Electron microscopy of whole cells in liquid with nanometer resolution," *Proc. Natl. Acad. Sci. U. S. A.*, vol. 106, no. 7, pp. 2159–2164, 2009.

[173] D. B. Peckys, G. M. Veith, D. C. Joy, and N. de Jonge, "Nanoscale imaging of whole cells using a liquid enclosure and a scanning transmission electron microscope," *PLoS One*, vol. 4, no. 12, pp. 1–7, 2009.

[174] M. K. Miller and R. G. Forbes, *Atom Probe Tomography and the Local Electrode*. Springer US, 2000.

[175] B. Gault, M. Moody, J. Cairney, and S. Ringer, *Atom Probe Microscopy*. Springer US, 2012.

[176] A. Cerezo *et al.*, "Atom probe tomography today," *Mater. Today*, vol. 10, no. 12, pp. 36–42, 2007.

[177] L. Rigutti, "Correlative Optical Spectroscopy and Atom Probe Tomography Correlative Optical Spectroscopy and Atom Probe Tomography," *Acta Phys. Pol. A*, vol. 129, 2016.

[178] M. K. Miller, K. F. Russell, K. Thompson, R. Alvis, and D. J. Larson, "Review of Atom

Probe FIB-Based Specimen Preparation Methods," *Microsc. Microanal.*, vol. 13, pp. 428–436, 2019.

[179] B. Vella, A., Vurpillot, F., Gault, B., Menand, A., Deconihout, "Evidence of field evaporation assisted by nonlinear optical rectification induced by ultrafast laser," *Phys. Rev. B*, vol. 73, no. 16, pp. 1–7, 2006.

[180] Y. Toji, H. Matsuda, M. Herbig, P. Choi, and D. Raabe, "Atomic-scale analysis of carbon partitioning between martensite and austenite by atom probe tomography and correlative transmission electron microscopy," *Acta Mater.*, vol. 65, pp. 215–228, 2014.

[181] M. Herbig, P. Choi, and D. Raabe, "Combining structural and chemical information at the nanometer scale by correlative transmission electron microscopy and atom probe tomography," *Ultramicroscopy*, vol. 153, pp. 32–39, 2015.

[182] L. M. Gordon and D. Joester, "Nanoscale chemical tomography of buried organic–inorganic interfaces in the chiton tooth," *Nature*, vol. 469, no. 7329, pp. 194–197, 2011.

[183] A. La Fontaine, A. Zavgorodniy, H. Liu, R. Zheng, M. Swain, and J. Cairney, "Atomic-scale compositional mapping reveals Mg-rich amorphous calcium phosphate in human dental enamel," no. September, 2016.

[184] L. M. Gordon, L. Tran, and D. Joester, "Atom probe tomography of apatites and bone-type mineralized tissues," *ACS Nano*, vol. 6, no. 12, pp. 10667–10675, 2012.

[185] G. Sundell, C. Dahlin, M. Andersson, and M. Thuvander, "The bone-implant interface of dental implants in humans on the atomic scale," *Acta Biomater.*, vol. 48, pp. 445–450, 2017.

[186] D. Gordon, L. M., Cohen, M. J., MacRenaris, K. W., Pasteris, J. D., Seda, T., & Joester, "Amorphous intergranular phases control the properties of rodent tooth enamel.," *Science (80-.).*, vol. 347, no. 6223, pp. 746–750, 2015.

Chapter 3: Visualization of Collagen-Mineral Arrangement as Mineralized *In vivo* using Atom Probe Tomography

Summary: The mineralized collagen fibril is an essential unit in the assembly of bone but the collagen-mineral arrangement is still subject to debate. In this chapter, leporine bone was aligned with collagen fibrils parallel to APT tip geometry and investigated to observe possible mineralization patterns of bone at the atomic scale with corresponding chemical identification. The new sample preparation approach resulted in an increased specimen yield, compared to previous studies on bone from the maxilla. The position of the mineral with respect to the collagen fibril was investigated using ionic density plots, isosurface volume rendering, and proxigram analyses, as well as quantitative statistical analyses on the point-cloud data. Within bone, the mineralized collagen fibril entity was observed with sub-nanometer accuracy and equivalent chemical composition. This work identified indicators of both intra- and extrafibrillar mineralization. Exploring the 4D point-cloud identified variations in the stochiometry of mineral (compositions consistent with hydroxyapatite or amorphous calcium phosphate) with localization based on distance to the collagen fibril. Therefore, as outlined in the objectives, this work developed the technique of APT to contribute to the understanding of bone structure and chemistry, specifically contributing to a better understanding of collagen-mineral arrangement at the atomic scale.

Visualization of Collagen–Mineral Arrangement as Mineralized *In vivo* using Atom Probe Tomography

Bryan E.J. Lee[1], Brian Langelier[2], and Kathryn Grandfield[1,3]

Corresponding Author: kgrandfield@mcmaster.ca
[1.] School of Biomedical Engineering, McMaster University, Hamilton, Canada.
[2.] Canadian Centre for Electron Microscopy, McMaster University, Hamilton, Canada.
[3.] Department of Materials Science and Engineering, McMaster University, Hamilton, Canada.

Abstract

Bone is a complex, hierarchical structure comprised of two distinct phases: the organic, collagen–rich phase and the inorganic mineral–rich phase. This collagen–mineral arrangement has implications for bone function, aging, and disease. However, strategies to extract a single mineralized collagen fibril to investigate the interplay between components with sufficient resolution have been confined to in vitro systems that only approximate the biological environment. Therefore, there is extensive debate over the location of mineral with respect to collagen in in vivo mineralized tissues as visualization and quantification of the mineral in a living system is difficult or impossible. Herein, we have developed an approach to artificially extract a single mineralized collagen fibril from bone to analyze its composition and structure atom-by-atom with 3D resolution and sub-nanometer accuracy using atom probe tomography. This enables, for the first time, a method to probe fibril-level mineralization and collagen–mineral arrangement from an in vivo system with both the spatial and chemical precision required to comment on collagen–mineral arrangement. Using atom probe tomography, 4D (spatial + chemical) reconstructed volumes of leporine bone were generated with accuracy from correlative scanning electron microscopy. Distinct, winding collagen fibrils were identified with mineralized deposits both encapsulating and incorporated into the collagenous structures. This work demonstrates a novel fibril-level detection method that can be used to probe structural and chemical changes of bone and contribute new insights to the debate on collagen–mineral arrangement in mineralized tissues such as bones, and teeth.

Introduction

Bone is an extraordinary material that provides vertebrates with skeletal support and essential metabolic functions, acting as a reservoir for ions involved in muscle activation to nerve signaling, and as a vessel for the production of blood cells [1]. By volume, bone can be divided into organic and mineral phases, 35% and 65 vol%, respectively. The majority of the organic phase is Type I collagen, while the inorganic phase is widely accepted to contain hydroxyapatite ($Ca_{10}(PO_4)_6(OH)_2$) with carbonate substitution. These two phases work in concert to create a hierarchical structure which is templated by the organic phase built from individual amino acids to collagen molecules to collagen fibrils and collagen fibres [2]–[4].

The mineralized collagen fibril is considered the building block for all higher-order structures within bone. However, identifying where the mineral is located with respect to the collagen fibril and what exactly that mineral is, are challenges that have plagued bone researchers for decades [5]. This is primarily due to the technical limitations associated with visualizing the mineralized collagen fibril with both sufficient spatial and chemical resolution in three-dimensions (3D). Previous work has employed high-resolution microscopy techniques, such as electron tomography, to facilitate visualization of collagen-mineral arrangement [5]–[9]. However, these studies have been limited by the 'missing wedge', the inability to fully rotate a sample within the TEM, leading to distortions in reconstructions [10]. Moreover, previous studies with electron tomography have visualized the 3D structure of bone mineral [4], [11]–[14] but not simultaneously probed for chemical information. This may account for the discrepancies seen in models for bone ultrastructure. Furthermore, there have been numerous attempts to mimic in vivo mineralization using in vitro [15]–[17], cryogenic [18], [19], and/or in situ approaches [20], [21], however, they are all limited by being in vitro systems and thus not truly equivalent to the biological in vivo environment.

Herein, we overcome the challenge of visualizing an individual mineralized collagen fibril from an in vivo system by utilizing atom probe tomography (APT) to extract and virtually reconstruct the exact chemistry and 3D structure of the collagen fibril. As shown in Fig. 1, this method enables us to study collagen–mineral arrangement from a precise site within the femur (Fig. 3-1A) and lamellar layers of interest (Fig. 3-1B), resulting in a 3D dataset displaying clear and winding collagen fibrils (Fig. 3-1D) that can then be explored atom-by-atom. In this paper we present the competing theories on collagen mineralization, an overview of the technical limitations associated with existing in vitro and 3D visualization approaches, and our findings that present new insights for collagen–mineral arrangement. Our work demonstrates that APT is a powerful technique for probing collagen mineralized in vivo, helping answer the questions of: (i) Where is the mineral with respect to collagen?, and (ii) What is the bone mineral composition, how does it vary spatially?
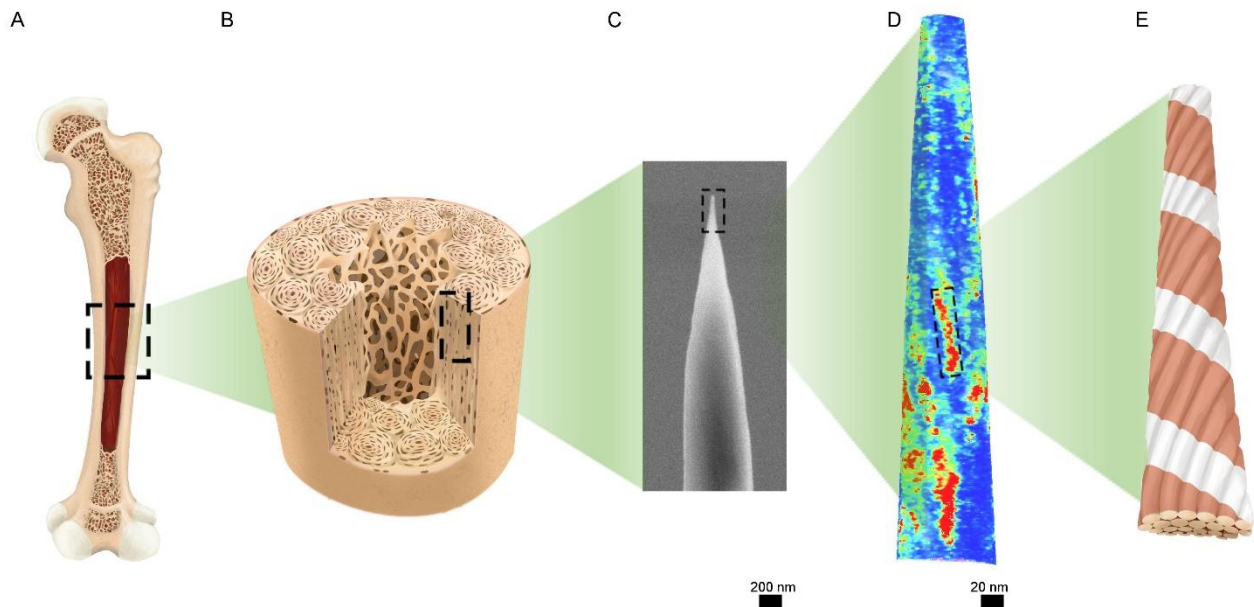
Figure 3-1. The hierarchical organization of bone as prepared for atom probe tomography. Bone is a hierarchical structure that spans the macro- to micro- to nanoscale. The femur (A) is colloquially considered to be a long bone, but upon closer inspection is comprised of complex structures, known as osteons, which act as the macroscale building blocks of bone (B). These building blocks are oriented parallel to the long axis of the femur, and within each osteon, the majority of collagen is also parallel to the femur long axis. Bone can be sectioned further using high-resolution microscopy techniques, for example by focused ion beam microscopy, a region only 50 nm in diameter with collagen oriented along its long axis is prepared (C). Using APT, collagen fibrils on the nanoscale can be visualized in bright red (D) which represent bundles of collagen molecules with their characteristic banding pattern and a right-handed helical structure (E).

Using APT to Extract Mineralized Collagen Fibrils

Atom probe tomography (APT) is a field evaporation technique that generates 4D (3D spatial + chemical) reconstructed datasets from individual atoms, as opposed to 2D projections like electron tomography [22], [23]. Using field evaporation, atoms from a specimen surface are ejected and collected by a position-sensitive detector, giving rise to *x,y* coordinates, while simultaneously identified through time-of-flight mass spectrometry, giving rise to the mass-to-charge (m/z) ratio [22]. Historically, APT was not utilized for biological materials due to the requirement for a pulsed electric field to generate field evaporation which limited analysis to conductive materials [24]. However, since the advent of laser-assisted APT the technique has gained traction for analyzing various biominerals [24], [25]. APT of enamel [26], dentin [27], [28] and human bone [29] has facilitated localization of mineralization modulating elements, such as Na^+ and Mg^{2+}, within their structures or at interfaces. Human bone examined with APT showed regions of high calcium and high carbon which may correspond to the locations of mineral and collagen respectfully, but the samples were taken from the maxilla, a more disorganized type of bone, and thus the lack of a priori information on collagen orientation prevented a thorough analysis [29].

In long bones, such as the femur, collagen fibrils are aligned parallel to the long axis of the bone providing optimal structural support [30]. In this study, leporine bone from the femur was sectioned and using a focused ion beam (FIB), was prepared such that collagen fibrils were maintained parallel to the APT tip long axis (Fig. 3-S1).
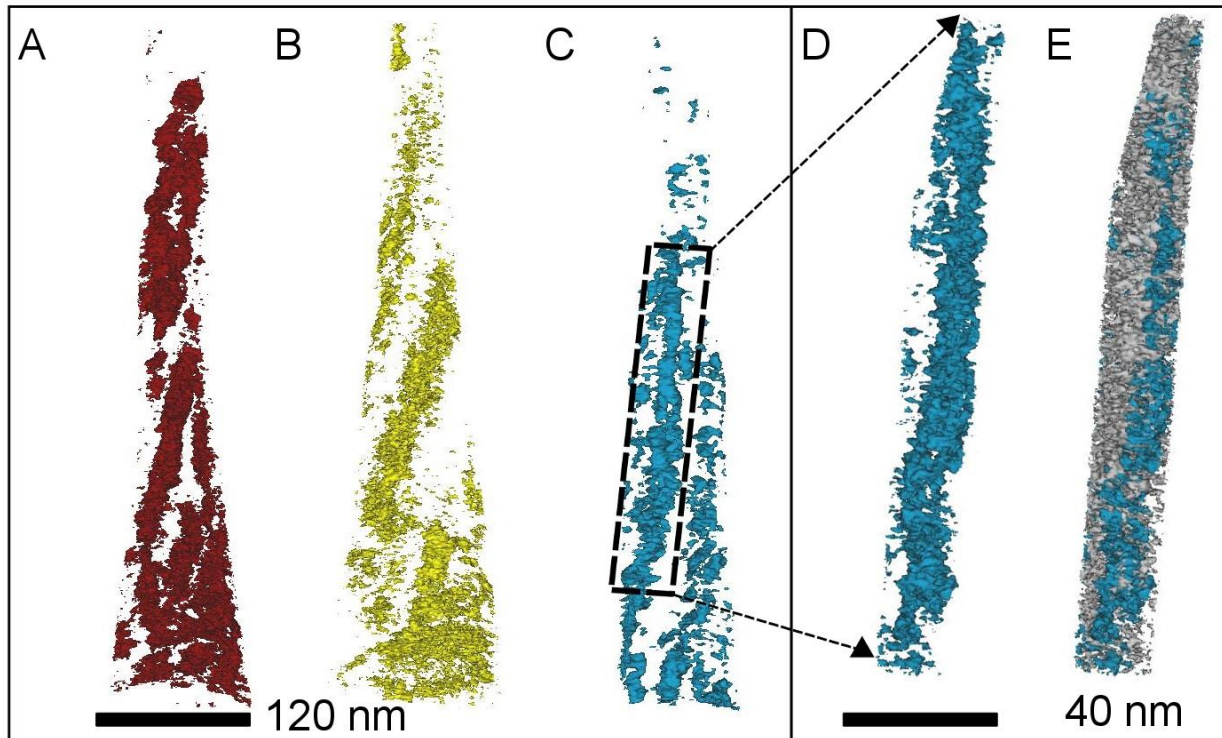
Figure 3-2. The winding collagen fibrils present with the mineralized matrix of leporine bone represented in three different reconstructed datasets. The carbon isosurfaces (A,B,C) (11 at%) show a fibril-like structure that is not directly parallel to the lift-out but instead appears to have some helical curvature. An individual fibril section from the reconstruction in C is isolated in D and shown along with calcium isosurface (29 at%) in E suggesting that the calcium envelopes the carbon fibril.

In this way, APT was performed and enabled long winding collagen fibrils mineralized in vivo to be extracted from seven APT tips, with three of the largest representing over 40 M ions each, shown here (Fig. 3-2 A,B,C). Isosurfaces of red, yellow, and blue represent three different reconstructed surfaces high in carbon concentration, representing collagen fibrils with a measured average diameter of 20 nm that is comparable to known dimensions [31]. The chemical sensitivity of APT means that a fibril can be further isolated, where a select collagen fibril is shown without (Fig. 3-2D) and with (Fig. 3-2E) corresponding calcium isosurface rendering, which represents bone mineral. Surface renderings of each of the three tips were visualized in 3D with calcium isosurfaces demonstrating the close spatial relationship throughout the entirety of the APT specimen between the collagen and mineral (Fig 3-S2,3) On the molecular level, it is known that bundles of collagen molecules formed right-handed alpha helix structures, demonstrated by Orgel

et al. that collagen molecules further formed right-handed microfibrils [32]. By using APT to extract carbon-rich collagen fibrils, our work shows that this same, right-handedness is maintained at higher ultrastructural fibril levels. Unlike previous models relying on in vitro, cryogenic, or in situ TEM, these collagen fibrils were formed and mineralized in vivo and their chemistry and spatial structure is simultaneously shown by APT.

Where is the mineral?

The extracted collagen fibril can be probed deeper to explore local changes in chemical composition to uncover the relationship between collagen and mineral. There have been numerous theories regarding the structure of bone, particularly how the collagen fibrils are mineralized. The dominant theories on collagen mineralization have been generated using electron tomography techniques [4], [11], [14], and broadly classify mineral placement as occurring inside the collagen fibril, intrafibrillar mineralization, or exterior to the fibril, extrafibrillar mineralization.

The chemical sensitivity and spatial accuracy of APT, enables us to probe the composition in both these locations in collagen. A carbon isosurface, representing the collagen fibril (Fig. 3-3B) is shown along with corresponding calcium density maps, representing the mineral (Fig. 3-3C), from each of the tips shown previously in Fig. 2. Corresponding density maps for carbon match the implied spatial coordinates from the isosurfaces (Fig. 3-S4). The collagen fibril and the mineral are predominantly present in different areas of the sample (Fig. 3-3B,C). In general, the spaces between the carbon isosurfaces (Fig. 3-3B) are filled by calcium (and phosphorous, not shown) and therefore, mineral dense regions (Fig. 3-3C). This primarily supports the argument of extrafibrillar mineralization dominating collagen mineralization. This is in agreement with the model proposed by Schwarcz et al. which proposed that the mineral surrounds the collagen in curved sheaths known as 'mineral lamallae' thus stating that crystalline mineral is completely extrafibrillar [6], [14]. However, there are regions of high calcium density, most visible in the yellow specimen in Fig. 3-3, that correspond to the same spatial coordinates as the collagen fibril, thus providing some evidence of intrafibrillar mineralization. This is supported by 3D visualization of the extended fibrils (Fig. 3-S5) which show variations in concentration of calcium and phosphorus relative to the collagen fibril and some coincidence of calcium/phosphorous with collagen and nitrogen. This spurred further investigation into the chemistry inside collagen fibrils.

Figure 3-3. Isolated collagen fibrils (B) from three different reconstructed datasets (A) with corresponding calcium atomic density maps for the same region (C). A represents the original reconstruction previously shown in Figure 2, B represents the extracted collagen fibril from indicated regions in A, and C shows calcium atomic density maps. The extracted collagen fibril isosurfaces (11 at%) from all three tips show a winding structure (B). Calcium is most dense in the regions outside of the fibril (C), and example shown by the asterisk (*) on the red/top specimen. However, calcium is also present in varying high density regions within the fibrils, most visible in the yellow/middle tip, marked by arrows (^). The dimensions for B and C are identical.

The collagenous phase of bone can be broadly described as carbon and nitrogen-based, while the mineral phase is considered calcium and phosphorus-based. Atomic density maps of a representative fibril are shown for each of these four major elements through the y and z plane of the tip (Fig. 3-4). Density maps show a projection of the atoms in the extracted fibril. The collagen fibril is characterized by a distinct periodicity of 67 nm with gap (27 nm) and overlap (40 nm) regions between the collagen molecules which was first observed in the electron microscope and proposed by Hodge and Petruska [33]. The banding associated with collagen and its helical nature is readily visible by the non-uniformity in the density map of carbon (Fig. 3-4A). Furthermore, distinct spacings between the regions of high density in the calcium (Fig. 3-4B) and phosphorus maps are approximately 30 nm apart, which could suggest that gap and overlap zones identified by Hodge and Petruska are being visualized with this imaging method. Nitrogen, a major structural element in the amino acid backbone of collagen, is directly correlated (Fig. 3-4C) to locations of dense carbon which confirms that these long winding structures are indeed collagen fibrils.

The atomic densities for both calcium and phosphorus are higher than the densities of carbon or nitrogen. This illustrates that although there are observable regions of variable density for calcium and phosphorus, the mineral is highly concentrated throughout the sample. When considering the calcium map, the majority of highest density regions appear counter to that of carbon, and along the exterior of this fibril. An example of this is shown by the asterisk marked regions in Fig 3-4. A,B which highlight that the central collagen fibril is flanked by dense regions of calcium and phosphorus. This is corroborated by the phosphorus map (Fig. 3-4D) where dense areas of

phosphorus are directly correlated to dense areas of calcium, together providing strong evidence for extrafibrillar mineralization. Visualization of the section through the *x* and *y* plane, shown on the right of Fig. 3-4, shows that most of the calcium and phosphorus is on the periphery while the carbon and nitrogen are most concentrated in the centre. This in agreement with previous work that states a majority of the mineral is external to the fibril [34].
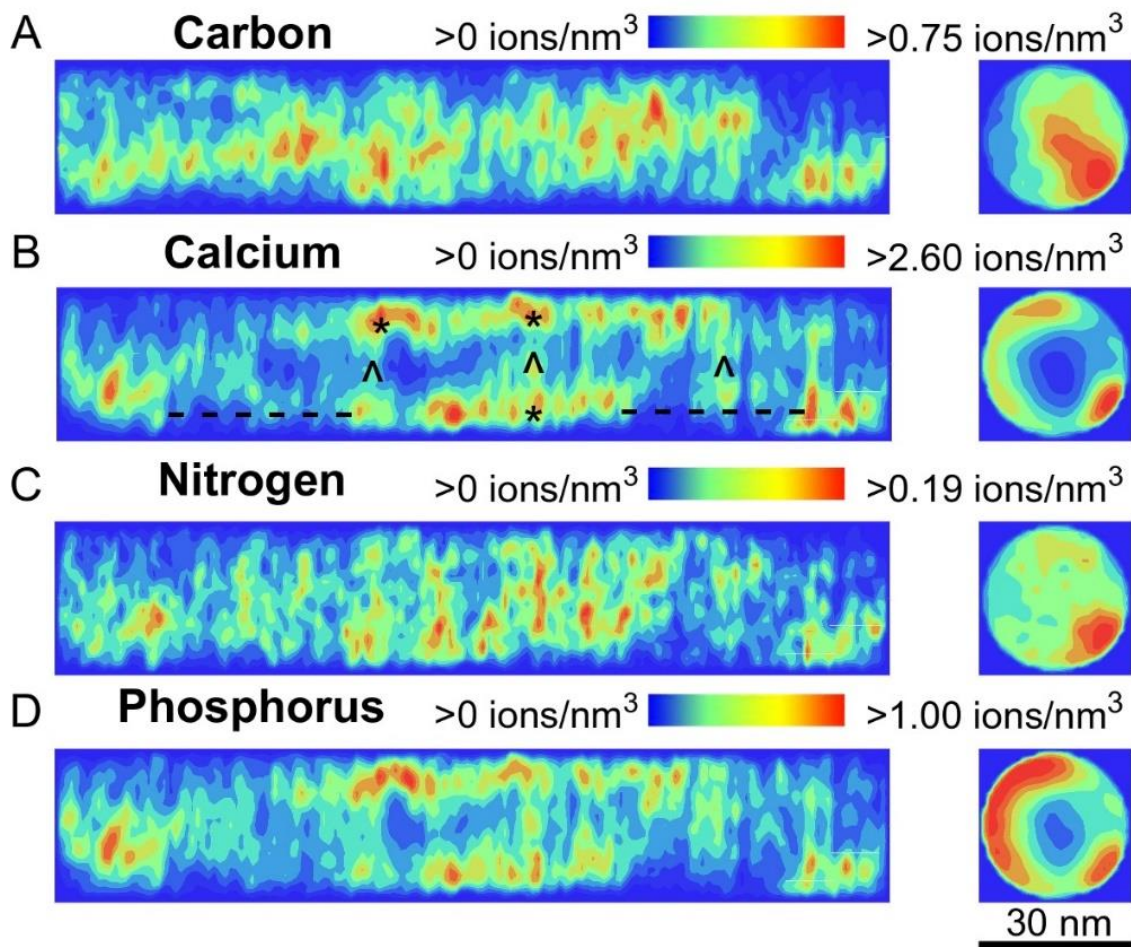
Figure 3-4. Ionic density maps visualized from the *y,z* and *x,y* planes of a collagen fibril showing distinct phases of mineral and collagen. Carbon (A) and nitrogen (C) are co-localized to form the collagen fibril while calcium (B) and phosphorus (D) are co-localized to form the mineral. The mineral is predominantly external to the collagen fibril, marked by asterisks (*) in (A) and (B). However, periodic increases in mineral density are visible within the collagen fibril, marked by arrows (^) in (A) and (B). A periodic spacing that approximates to 30 nm, indicated by dashed lines (- - -), can be observed in calcium and phosphorus maps.

However, equally important to note, is that many of the gaps observed in the carbon map appear as repeated interdigitations of calcium, marked by arrows (Fig. 3-4A), which suggests intrafibrillar mineralization. Building from the work of Hodge and Petruska, Katz and Li postulated that mineral apatite crystals were arranged within the periodic collagen gap zones [34]. The most prominent theory of intrafibrillar mineralization was proposed by Landis et al. that used mineralized turkey tendon to show that inorganic mineral formed in the gap zones and nucleated outward over time

[12]. Similar work by Weiner and Traub demonstrated that the mineral was present in the plate-like structures that were associated with the gap zone region [35]. These theories on bone mineralization have identified mineral as being present predominantly in the gap zone regions of collagen [34], [36]–[39]. While the mass resolution of our datasets was insufficient to observe distinct mineral plates, the observed chemical periodicity and interdigitation of calcium and phosphorus within the collagen fibril is strong evidence of intrafibrillar mineralization within the gap zones. However, it has been noted that the total weight of mineral in bone could not be solely present in the gap zone of collagen fibrils and that some must be present externally, via extrafibrillar mineralization [34]. Therefore, these maps suggest that a combined model occurs, with both intrafibrillar and extrafibrillar mineralization occurring simultaneously in vivo.

In order to better quantify the presence of intrafibrillar mineralization, the same sectioned fibril described above (from Fig. 3-4) is shown top-down from the *x,y* plane with both carbon and calcium isosurfaces (Fig. 3-5). A noticeable void in the calcium isosurface (grey) is visible when the carbon isosurface is not rendered (Fig. 3-5A). Whereas, rendering of the two isosurfaces (Fig. 3-5B) simultaneously gives an appearance similar to the 'lacy' mineralized crystal structure that has been frequently described [6]. The difference is that with APT, chemical sensitivity is available. Using a proxigram (Fig. 3-5C), the atomic concentration is measured moving into and away from the carbon isosurface (Fig. 3-5D; purple and red lines, respectively). The concentration of carbon greatly decreases while moving away from the collagen fibril while the calcium concentration increases, suggesting more of the calcium-rich phase is located exterior to the fibril, in extrafibrillar mineralization. In the opposite direction, moving into the collagen fibril, the concentration of carbon increases significantly while calcium drops. However, notably, the concentration of calcium and phosphorous does not completely drop off and hovers around 10 at%, indicating that there is indeed biomineral present within the collagen fibril structure, evidence of intrafibrillar mineralization. Studies by Reznikov et al. created the most recent model of mineralization which identifies mineral needles that are both in- and outside the fibril while also highlighting that differences in the ordered and disordered regions of bone can lead to alternative theories, especially when considering the small volumes that are typically analyzed in the microscope [4], [8], [37]. The results of our work show that both intrafibrillar and extrafibrillar mineralization are present in all observed APT specimens.

Figure 3-5. Demonstration of the spatial relationship between mineral and the collagen fibril. (A) Calcium isosurface (grey, 30.3 at%) alone showing a distinct gap in the centre of the sample. (B) Calcium isosurface rendered with carbon isosurface (blue, 11 at%) showing that the collagen fibril is enveloped completely by the mineral. (C) Carbon isosurface alone with red and purple arrows indicating the directions for the proxigram (D). Movement along the red arrow indicates measurements taken from the edge of the carbon isosurface towards the centre of the collagen fibril, while movement along the purple arrows indicates measurements taken from the edge of the carbon isosurface outwards into the extrafibrillar region. (D) Proxigram shows that while the collagen fibril is carbon and nitrogen dominant (under the red arrow), there are still significant amounts of calcium and phosphorus present suggesting intrafibrillar mineralization.

What is the mineral?

The specific composition of the mineral phase in bone is extensively debated as is its localization. Bone apatite can be generally considered carbonate-substituted hydroxyapatite, but it is has been proposed that other phases such as amorphous calcium phosphate and octacalcium phosphate are also present in bone structure [4], [9], [34]. Amorphous calcium phosphate, in particular, was originally proposed as a precursor to hydroxyapatite during mineralization via x-ray diffraction studies by Posner [40]. This was followed by other x-ray diffraction studies which have stated that this is not ACP and may instead be poorly crystalline hydroxyapatite [41]. More recent work by

Sommerdijk et al. has shown that ACP infiltrates collagen fibrils in vitro [18]. NMR studies have also observed ACP forming via both intra- and extrafibrillar mineralization pathways in vitro [42], [43].

The wealth of information provided by the APT mass spectra allows for quantification of elemental ratios. In theory, field evaporation results in single atoms being ejected from the APT tip at a time. The reality is that it is often ions, with varying degrees of complexity, are ejected at once. While high quantities of important, singular elements in bone structure such as C or N or Ca are present, there are also peaks in the spectra corresponding to PO, PO_2, or even more complex ions such as CaO_3 or $Ca_2P_3O_3$. By decomposing all of the peaks, the calcium to phosphorus atomic ratios (Ca/P) were calculated and compared to average values in the literature from varying techniques (Table 3-1). The average Ca/P ratio for all of the APT tips was determined to be 1.45 which is very close to the theoretical 1.5 Ca/P ratio of α & β-tricalcium phosphate or amorphous calcium phosphate (ACP). This contrasts with the established 1.67 ratio of stochiometric hydroxyapatite. However, the deviation could be explained by the substitution of carbonate groups for phosphate groups within bone, as explained elsewhere [29], [41], [44].

Table 3-1: Ca/P ratio of biominerals measured using atom probe tomography and photon absorptiometry. Ratio was determined using n=7 reconstructed datasets.

	Leporine Bone – Atom Probe Tomography	Hydroxyapatite – Atom Probe Tomography [27]	Human Calculus – Flame Photometry [45]
Ca/P Ratio	1.45	1.66	1.68

The APT dataset, consisting of an exportable 4D point cloud, could be sectioned into regions of interest inside and outside of the collagen fibril (Fig. 3-6 A,B), and the mass spectra from these regions can be extracted to probe mineral chemistry. As expected, the mass spectra show there are greater quantities of mineral associated ions, such as $Ca^{2+}/PO^+/PO_2^+$ or PO_3^+, in the mineral region located exterior to the fibril (Fig. 3-6D) as opposed to within the collagen fibril (Fig. 3-6C). However, the mineral within the collagen fibrils had Ca/P ratios comparable to the mineral that encapsulates it. There was greater variance in the measured Ca/P ratio inside the collagen fibrils but this may be due to examining a much smaller volume that is exposed to sampling issues, where in some cases only 20-30 atoms were being considered in calculations.
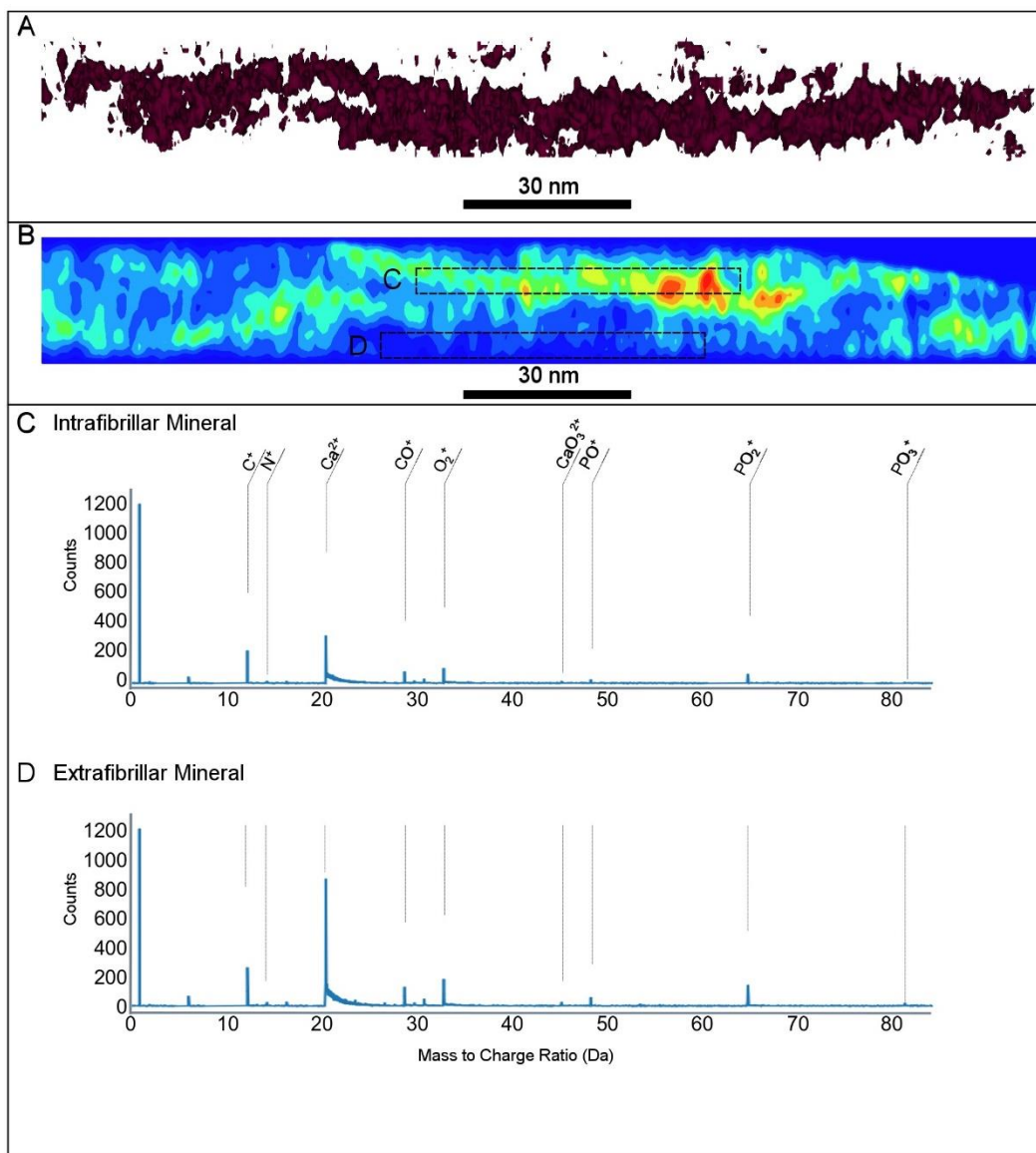
Figure 3-6. APT of a collagen fibril with representative mass spectra inside and outside of the fibril. An extracted collagen fibril (A; isosurface, 11 at%) along with carbon ionic density map (B) is shown. In the region specific mass spectra (C,D), there are greater quantities of mineral associated ions in the mineral region located exterior to the collagen fibril (D) (e.g. Ca, PO$_2$) compared to that inside the fibril (C). The select ionic species indicated on the full tip mass spectra are some of those important to bone structure.

The bulk Ca/P ratios for APT reconstructed samples averaged around 1.45. However, using radial clustering analysis, groups of Ca and P atoms were selected, such that their ratios were within the ranges of either ACP (1.4-1.6) or HA (1.6-1.8) so their spatial location could be analyzed with respect to a collagen fibril. Similar analysis of proximity histograms to investigate interfaces has been conducted by Felfer and Cairney [46]. Herein, clusters labeled as ACP or HA were evaluated based on their proximity to the collagen fibril by measuring the minimum cartesian distance between the two structures (Fig. 3-7 B,C). It was observed in all datasets but one that clusters of

ACP are present in greater quantities within 1.5 nm of the collagen fibril compared to HA clusters ($p < 0.05$). At greater distances, regardless of the Ca/P ratio of the mineral, the proximity of the mineral to the collagen fibrils was not statistically different between ACP and HA representative ratios. This finding aligns with in vitro studies that note the role of ACP as a precursor to HA and the first material to form within the gap zones of collagen. However, these results also lend themselves to a discussion on the crystallinity of the mineral phase. Previous X-ray diffraction studies show that the presence of paracrystalline or poorly crystallized HA has the same Ca/P ratio as HA [41]. Our results are predicated on the assumption that the 1.4-1.6 Ca/P ratio represents ACP, but we cannot differentiate between poorly crystalline and crystalline HA using APT leaving the possibility that mineral closest to the fibril, and therefore perhaps inside the fibril, is either ACP or poorly crystalline HA. The spatial arrangement of these mineral clusters with differing stoichiometric ratios, along with their crystallinity, requires further investigation via datasets with improved mass resolution. This necessity to improve resolution is primarily due to the presence of thermal tails in APT mass spectra which have been reported with other biominerals as well [27], [28], [47]. In addition to cluster of mineral phases, a model for the overall winding structure of the collagen fibrils was determined by fitting the extracted bundle of collagen fibrils to a helix (Fig. 3-7A). The parametric equations for the bundle determined that the radius, on average, was 29.5 nm with a pitch of 16.5 nm. The model also confirmed that the helix is right-handed which agrees with known work on collagen structure [48]. This model shows that APT can be used to extract a sub-nanometer and chemically accurate mathematical model for the helical nature of a healthy collagen fibril. Applying this approach more broadly, APT could become an essential tool in the diagnosis and investigation of bone diseases, particularly for specialized pathologies affecting the collagen organization, such as misfolding of the triple helix [49], Ehlers-Danlos syndrome [50], or osteogenesis imperfecta [51]. Combined with the chemical sensitivity demonstrated to probe compositional changes in Ca/P ratio, we have demonstrated APT has the power to probe both the mineral and organic framework of bone.
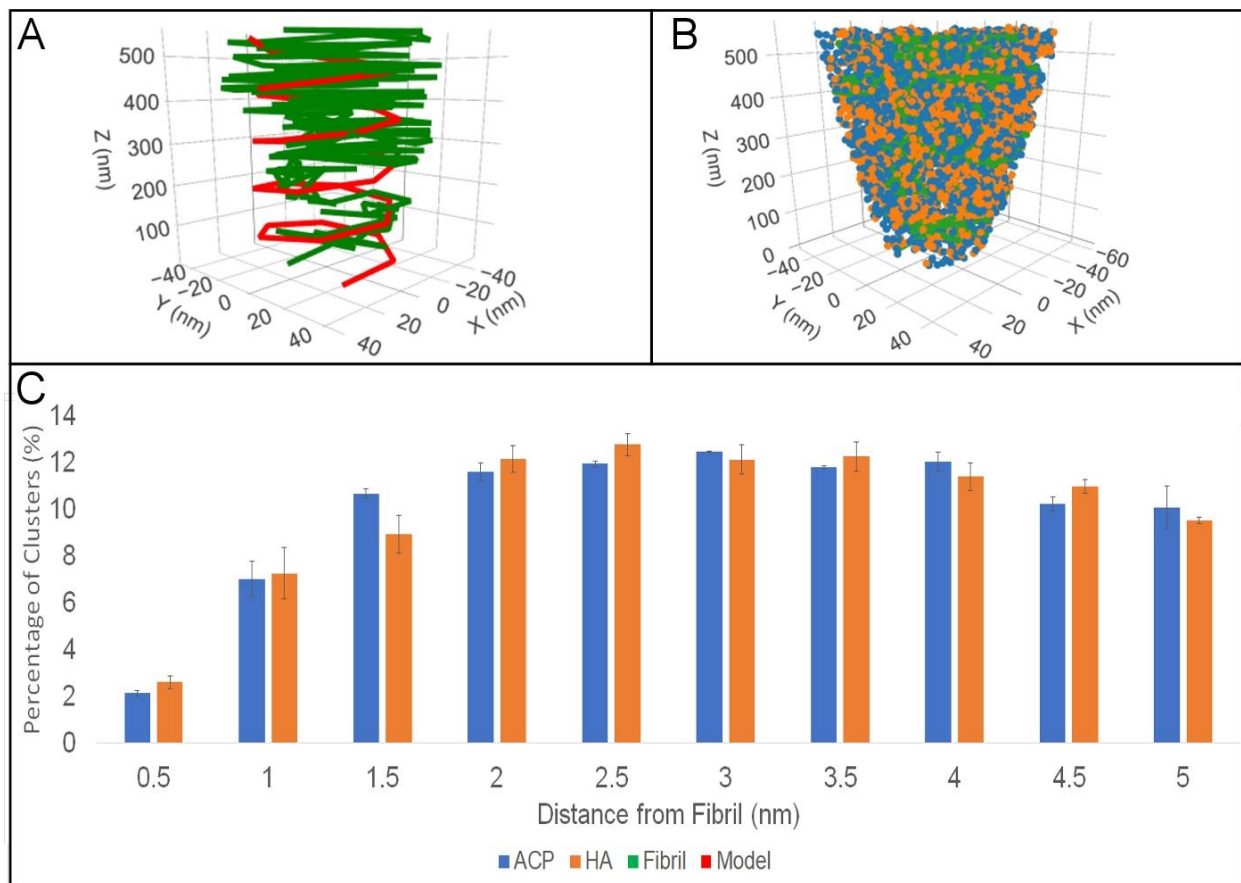
Figure 3-7. Cluster analysis of mineral proximity to collagen. Fitted helical model for a collagen fibril alongside extracted x,y,z coordinates of collagen fibril (A). Clusters of Ca/P with ratios of 1.4-1.6 (representing ACP) and 1.6-1.8 (representing HA) visualized using x,y,z coordinates (B). Histograms illustrating that up to 5 nm away from the fibril there is no difference in the amount of ACP vs. HA (C). Cluster analysis was performed using n=3 reconstructed tips.

Conclusion

The collagen-mineral arrangement in bone has been debated. Present theories are either based on in vitro systems that model but do not replicate the in vivo environment, or use analysis techniques without both spatial and chemical sensitivity. Herein, APT was used to clearly demonstrate the winding structure and localized chemistry of collagen fibrils mineralized in vivo from seven samples, each consisting of over 40 million ions. The high spatial resolution and chemical-sensitive nature of APT enabled the extraction of in vivo mineralized collagen fibrils from the femur of leporine bone. Ca/P ratios were shown to vary with respect to the collagen fibril location, suggesting possible increases in amorphous or low crystallinity apatite closer to, or perhaps within, the collagen fibril. Furthermore, this work confirms with sufficient chemical and spatial resolution that both intrafibrillar and extra-fibrillar mineralization are occurring simultaneously in naturally mineralized bone, refuting models that insist only one or the other exists. Therefore, APT has shown the capacity to tackle high spatial and chemical resolution challenges in biomineralization

to provide newfound insight to the structure and chemistry of organic and inorganic materials, such as the fundamental building block of bone shown herein, the mineralized collagen fibril.

Materials and Methods

Preparation of Bone Samples

A single femur of a fresh-frozen leporine bone, received with institutional ethical approval, was cut transversely to its long axis using a slow-speed saw (Isomet LS, Buehler Ltd.) and diamond blade to generate a cross-section from the mid-diaphysis region. Bone marrow was removed from the samples by submerging them in a 3% sodium hypochlorite solution (in Milli-Q water) for 3 hours. Samples were subsequently dehydrated in a graded series of ethanol from 25-100% (in Milli-Q water) as previously described [52]. Following dehydration, the samples were infiltrated with resin (Embed 812, Electron Microscopy Sciences) over 4 days before being placed in a 50°C oven overnight. Tissue blocks were polished manually (400, 600, 800, 1200 grit SiC paper and subsequently cloth with 0.3 µm alumina suspension (MetLab)) until embedded bone was exposed. Samples were sputter-coated with 10 nm of chromium prior to imaging. Scanning electron microscopy (SEM) in backscattered mode was performed at 10 kV (JEOL 7000F) to select regions of interest. A typical ROI is outline in Fig 3-S1.

A dual-beam focused ion beam (FIB) microscope (NVision40, Zeiss) was utilized to prepare tips for APT according to previous studies [29]. An in-situ lift-out method (Fig. S1) was used to obtain samples site-specific samples. Following lift-out, samples were mounted to pre-sharpened Si coupons or W needles, and milled to create tips with appropriate sharpness for APT (diameter approximately < 150 nm). Tips were prepared such that the collagen fibrils were aligned parallel to the long-axis of the tip.

Atom Probe Tomography

APT was performed using a LEAP 4000XHR (Cameca, WI, USA) microscope operating in laser pulsing mode (355 nm UV, 125 kHz pulse rate, 50 pJ pulse energy) at a stage temperature of 59.6 K under ultra-high vacuum (< 10-8 Pa). An evaporation rate of 0.005 ions/pulse (0.5%) was maintained by controlling the static DC potential applied to the specimen, which typically ranged from 2.0-4.3 kV. A total of seven tips were successfully run, with total evaporated ions for the runs ranging from 36-50 million ions, with three of the largest tips highlighted in this work.

Reconstructions were performed using IVAS 3.6.10a (Cameca, WI, USA). The reconstruction parameters used a field factor of k = 3.3 and an image compression factor of 1.65. There were a number of peaks that were not possible to range due to challenges associated with running a biological sample through the atom probe microscope, such as large thermal tails. As such, the average detector efficiency was adjusted based on the number of peaks that were successfully ranged, resulting in a modified detection efficiency parameter of 0.09. For analysis, all identified ions were used, a complete list is provided in Table 3-S1.

To ensure the accuracy of reconstructed datasets, correlative electron microscopy was performed. SEM images taken before and after APT runs were compared to determine the area that was evaporated. For some tips, electron tomography was attempted in a Titan 80–300 TEM operating in STEM mode (FEI Company, The Netherlands) at 300 keV at 2° tilts from -65 to 65 ° (Fig 3-S6). While the tips were suitable for runs in the APT afterwards, the electron tomography acquisition damaged the tips during its imaging making reconstruction not possible.

Statistics and Model Generation from APT Data

Helical regression and mathematical calculations of cartesian distances between clusters of various Ca and P ions, as well as Ca:P ratios and the collagen fibrils was computed using R (version x64 3.6.1). Clusters of Ca:P were extracted from IVAS using Ca, PO, PO_2, PO_3 and P clustering centres. The following packages were used in the analysis: dplyr, plot3d, plot_ly, rgeos, rgl, and sp.

References

[1]   B. Clarke, "Normal Bone Anatomy and Physiology," Clin. J. Am. Soc. Nephrol., pp. S131–S139, 2008.

[2]   U. Kini and B. N. Nandeesh, Physiology of Bone Formation, Remodeling, and Metabolism. Springer Berlin Heidelberg, 2012.

[3]   N. Reznikov, R. Shahar, S. Weiner, N. Reznikov, S. Weiner, and R. Shahar, "Bone Hierarchical Structure in Three Dimensions," no. JUNE, pp. 0–12, 2014.

[4]   N. Reznikov, M. Bilton, L. Lari, M. M. Stevens, and R. Kröger, "Fractal-like hierarchical organization of bone begins at the nanoscale," Science (80-.)., vol. 360, no. 6388, p. eaao2189, 2018.

[5]   X. Su, K. Sun, F. Z. Cui, and W. J. Landis, "Organization of apatite crystals in human woven bone," vol. 32, pp. 150–162, 2003.

[6]   E. A. McNally, H. P. Schwarcz, G. A. Botton, and A. L. Arsenault, "A model for the ultrastructure of bone based on electron microscopy of ion-milled sections," PLoS One, vol. 7, no. 1, 2012.

[7]   B. Alexander et al., "The nanometre-scale physiology of bone : steric modelling and scanning transmission electron microscopy of collagen – mineral structure," no. February, pp. 1774–1786, 2012.

[8]   N. Reznikov, R. Shahar, and S. Weiner, "Three-dimensional structure of human lamellar bone: The presence of two different materials and new insights into the hierarchical organization," Bone, vol. 59, pp. 93–104, 2014.

[9]   M. J. Olszta et al., "Bone structure and formation : A new perspective," Mater. Sci. Eng. R, vol. 58, pp. 77–116, 2007.

[10]   P. Ercius, O. Alaidi, M. J. Rames, and G. Ren, "Electron Tomography : A Three-Dimensional Analytic Tool for Hard and Soft Materials Research," Adv. Mater., vol. 27, no. 38, pp. 5638–5663, 2015.

[11]   W. J. Landis and M. J. Song, "Early mineral deposition in calcifying tendon characterized by high voltage electron microscopy and three-dimensional graphic imaging," J. Struct. Biol., vol. 107, no. 2, pp. 116–127, 1991.

[12]   B. F. Landis, W J., Song, M.J, Leith, A.,McEwen,L.,McEwen, "Mineral and Organic Matrix Interaction in Normally Calcifying Tendon Visualized in Three Dimensions by High-Voltage Electron Microscopic Tomography and Grap.pdf," J. Struct. Biol., vol. 110, pp. 39–54, 1993.

[13]   E. McNally, F. Nan, G. A. Botton, and H. P. Schwarcz, "Scanning transmission electron microscopic tomography of cortical bone using Z-contrast imaging," Micron, vol. 49, pp. 46–53, 2013.

[14]   H. P. Schwarcz, E. A. McNally, and G. A. Botton, "Dark-field transmission electron microscopy of cortical bone reveals details of extrafibrillar crystals," J. Struct. Biol., 2014.

[15]   W. Zhang, S. S. Liao, and F. Z. Cui, "Hierarchical Self-Assembly of Nano-Fibrils in Mineralized Collagen," no. 15, pp. 3221–3226, 2003.

[16]   F.-Z. Zhang, W., Huang, Z-L., Liao, S-S., Cui, "Nucleation Sites of Calcium Phosphate Crystals during Collagen Mineralization," Commun. Am. Ceram. Soc., vol. 54, no. 186871, pp. 2002–2004, 2003.

[17]   J. Tao, K. C. Battle, H. Pan, E. A. Salter, Y. Chien, and A. Wierzbicki, "Energetic basis for the molecular-scale organization of bone," vol. 112, no. 2, 2015.

[18]   F. Nudelman et al., "The role of collagen in bone apatite formation in the presence of hydroxyapatite nucleation inhibitors," Nat. Mater., vol. 9, no. December, pp. 9–14, 2010.

[19]   J. Mahamid, A. Sharir, D. Gur, E. Zelzer, L. Addadi, and S. Weiner, "Bone mineralization proceeds through intracellular calcium phosphate loaded vesicles : A cryo-electron microscopy study," J. Struct. Biol., vol. 174, no. 3, pp. 527–535, 2011.

[20]   F. Nudelman, A. J. Lausch, N. A. J. M. Sommerdijk, and E. D. Sone, "In vitro models of collagen biomineralization," J. Struct. Biol., vol. 183, no. 2, pp. 258–269, 2013.

[21]   P. J. M. Smeets, K. R. Cho, R. G. E. Kempen, N. A. J. M. Sommerdijk, and J. J. De Yoreo, "Calcium carbonate nucleation driven by ion binding in a biomimetic matrix revealed by in situ electron microscopy," vol. 14, no. January, 2015.

[22]   M. K. Miller and R. G. Forbes, Atom Probe Tomography and the Local Electrode. Springer US, 2000.

[23]   B. Gault, M. Moody, J. Cairney, and S. Ringer, Atom Probe Microscopy. Springer US, 2012.

[24]   A. Cerezo et al., "Atom probe tomography today," Mater. Today, vol. 10, no. 12, pp. 36–42, 2007.

[25]   D. Joester, A. Hillier, Y. Zhang, and T. J. Prosa, "Organic Materials And Organic / Inorganic Heterostructures In Atom Probe Tomography," Micros. Today, vol. 20, no. 3, pp. 11–14, 2012.

[26]   A. La Fontaine, A. Zavgorodniy, H. Liu, R. Zheng, M. Swain, and J. Cairney, "Atomic-scale compositional mapping reveals Mg-rich amorphous calcium phosphate in human dental enamel," no. September, 2016.

[27]   L. M. Gordon, L. Tran, and D. Joester, "Atom probe tomography of apatites and bone-type mineralized tissues," ACS Nano, vol. 6, no. 12, pp. 10667–10675, 2012.

[28]   L. M. Gordon and D. Joester, "Nanoscale chemical tomography of buried organic–inorganic interfaces in the chiton tooth," Nature, vol. 469, no. 7329, pp. 194–197, 2011.

[29]   B. Langelier, X. Wang, and K. Grandfield, "Atomic scale chemical tomography of human bone," Sci. Rep., vol. 7, p. 39958, 2017.

[30]   P. Fratzl, Collagen. Springer US, 2008.

[31]   A. S. Parry, D. A. D., Barnes, G. R. G., & Craig, "A Comparison of the Size Distribution of Collagen Fibrils in Connective Tissues as a Function of Age and a Possible Relation between Fibril Size Distribution and Mechanical Properties Author (s): D . A . D . Parry , G . R . G . Barnes and A . S . Craig," Proc. R. Soc. London. Ser. B. Biol. Sci., vol. 203, no. 1152, pp. 305–321, 1978.

[32]   J. P. R. O. Orgel, T. C. Irving, A. Miller, and T. J. Wess, "Microfibrillar structure of type I collagen in situ," Proc. Natl. Acad. Sci., vol. 103, no. 24, pp. 9001–9005, 2006.

[33]   J. Petruska and A. Hodge, "A Subunit Model for the Tropocollagen Macromolecule," Proc. Natl. Acad. Sci. U. S. A., vol. 51, no. 5, pp. 871–876, 1964.

[34]   E. P. Katz and H. Li, "Structure and Function of Bone Collagen Fibrils," J.Mol.Bio., vol. 80, pp. 1–15, 1973.

[35]   S. Weiner and W. Traub, "Bone structure: from angstroms to microns," FASEB J., vol. 6, no. 3, pp. 879–885, 1992.

[36]   W. J. Landis, K. J. Hodgens, J. Arena, M. I. N. J. A. Song, and B. F. Mcewen, "Structural Relations Between Collagen and Mineral in Bone as Determined by High Voltage Electron Microscopic Tomography," Microsc. Res. Tech., vol. 33, no. 2, pp. 192–202, 1996.

[37]   N. Reznikov, R. Shahar, and S. Weiner, "Bone hierarchical structure in three dimensions," Acta Biomater., vol. 10, pp. 3815–3826, 2014.

[38]   A. L. Arsenault, "A comparative electron microscopic study of apatite crystals in collagen fibrils of rat bone , dentin and calcified turkey leg tendons," Bone Miner., vol. 6, pp. 165–177, 1989.

[39]   W. Weiner, S., Arad, T., Traub, "Crystal organization in rat bone lamelle," Febs Lett., vol. 285, no. 1, 1991.

[40]   A. S. Posner and F. Betts, "Synthetic Amorphous Calcium Phosphate and Its Relation to Bone Mineral Structure," Acc. Chem. Res., vol. 8, no. 8, pp. 273–281, 1975.

[41]   M. J. Glimcher, L. C. Bonar, M. D. Grynpas, W. J. Landis, and A. H. Roufosse, "Recent Studies of Bone Mineral: Is the amorphous calcium phosphate theory valid?," J. Cryst. Growth, vol. 53, pp. 100–119, 1981.

[42]   Y. Kyung et al., "Mineralisation of reconstituted collagen using polyvinylphosphonic acid / polyacrylic acid templating matrix protein analogues in the presence of calcium , phosphate and hydroxyl ions," Biomaterials, vol. 31, no. 25, pp. 6618–6627, 2010.

[43]   Y. Wang et al., "The predominant role of collagen in the nucleation, growth, structure and orientation of bone apatite," Nat. Mater., vol. 11, no. 8, p. 724, 2012.

[44]   P. Fratzl, H. S. Gupta, E. P. Paschalis, and P. Roschger, "Structure and mechanical quality of the collagen – mineral nano-composite in bone," J. Mater. Chem., vol. 14, no. 14, pp. 2115–2123, 2004.

[45]   M. F. Little, C. A. Casciani, and J. Rowley, "Dental Calculus Composition . 1 . Supragingival Calculus : Ash , Calcium , Phosphorus , Sodium , and Density," J. Dent. Res., vol. 42, no. 1, pp. 78–86, 1963.

[46]   P. Felfer and J. Cairney, "Advanced concentration analysis of atom probe tomography data : Local proximity histograms and pseudo-2D concentration maps," Ultramicroscopy, vol. 189, pp. 61–64, 2018.

[47]   A. La Fontaine, A. Zavgorodniy, H. Liu, R. Zheng, M. Swain, and J. Cairney, "Atomic-scale compositional mapping reveals Mg-rich amorphous calcium phosphate in human dental enamel," Sci. Adv., vol. 2, no. 9, p. e1601145, 2016.

[48]   M. L. Huggins, "The structure of collagen," Proc. Natl. Acad. Sci. U. S. A., vol. 43, no. 2, pp. 209–213, 1957.

[49]   J. Baum and B. Brodsky, "Folding of peptide models of collagen and misfolding in disease," Curr. Opin. Struct. Biol., vol. 9, no. 1, pp. 122–128, 1999.

[50]   V. A. Cupo, L. N., Pyeritz, R. E., Olson, J. L., McPhee, S. J., Hutchins, G. M., & McKusick, "Ehlers-Danlos Syndrome with Abnormal Collagen Fibrils , Sinus of Valsalva Aneurysms , Myocardial Infarction , Panacinar Emphysema and Cerebral Heterotopias," Am. J. Med., vol. 71, no. 6, pp. 1051–1058, 1981.

[51]   S. Makareeva, E., Cabral, W. A., Marini, J. C., & Leikin, "Molecular Mechanism of α1 (I)-Osteogenesis Imperfecta/Ehlers-Danlos Syndrome Unfolding of an N-Anchor Domain at the N-terminal End of the Type I Collagen Triple Helix," J. Biol. Chem., vol. 281, no. 10, pp. 6463–6470, 2006.

[52]   F. A. Shah, B. Nilson, R. Brånemark, P. Thomsen, and A. Palmquist, "The bone-implant interface-nanoscale analysis of clinically retrieved dental implants.," Nanomedicine, vol. 10, no. 8, pp. 1729–1737, 2014.

[53]   I. Arslan, J. R. Tong, and P. A. Midgley, "Reducing the missing wedge : High-resolution dual axis tomography of inorganic materials," Ultramicroscopy, vol. 106, pp. 994–1000, 2006.

[54]   X. Wang, F. A. Shah, A. Palmquist, and K. Grandfield, "3D Characterization of Human Nano-osseointegration by On-Axis Electron Tomography without the Missing Wedge," ACS Appl. Mater. Interfaces, vol. 3, no. 1, pp. 49–55, 2017.
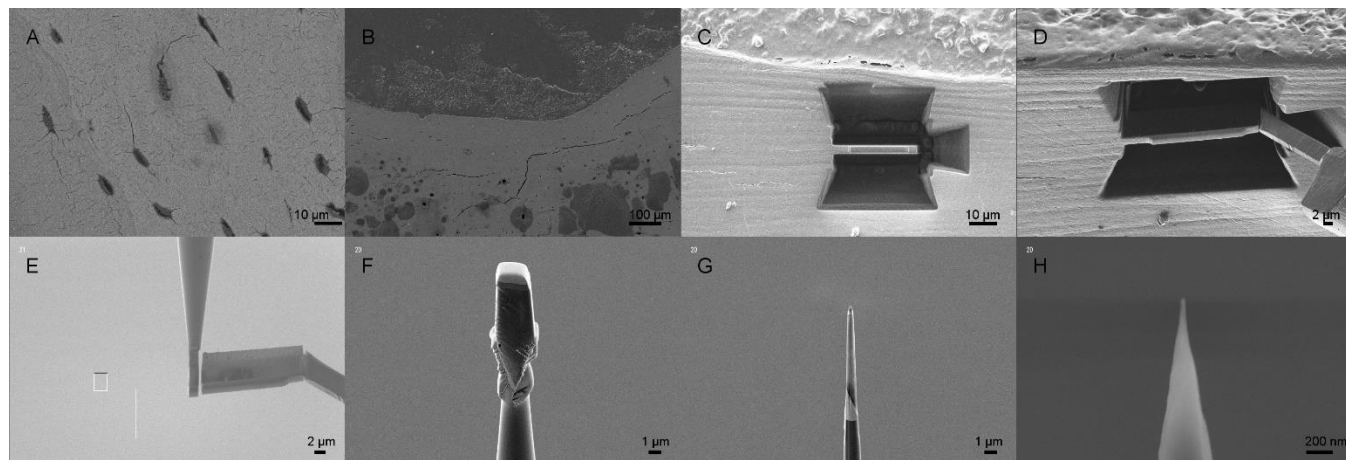
Supplementary Information

Figure 3-S1: Preparation of sectioned bone into APT tip. An appropriate region of interest was identified in SEM (A/B). The area around the ROI was milled away using Ga ions (C) before being extracted using a micromanipulator (D). The removed section was split into several pieces (E) each of which were sharpened (F/G/H) into the needle shape required to perform APT.

Table 3-S1: List of ranged ions.

Ion	Charge	Lower Range	Upper Range	Ion	Charge	Lower Range	Upper Range
C	+	5.967	6.043	As	2+	37.433	37.559
C	2+	11.949	12.08	OH	+	16.961	17.074
C	+	6.487	6.512	OH2	+	17.959	18.058
Ca	2+	19.878	20.082	Na	+	22.955	23.062
Ca	+	39.921	40.118	NH	+	14.978	15.096
N	2+	6.948	7.073	C3H	2+	18.46	18.536
N	+	13.967	14.058	C3H2	2+	18.952	19.067
O	+	15.948	16.05	C3H3	2+	19.474	19.563
Mg	2+	12.459	12.538	P2O	3+	25.96	26.051
Mg	2+	12.968	13.03	CaPO	3+	28.953	29.077
Mg	+	23.945	24.038	NaP	2+	26.963	27.076
PO	+	46.893	47.094	P2H	2+	31.442	31.534
PO2	+	62.788	63.136	CaO	+	55.899	56.088
PO3	+	78.785	79.176	CaO4	2+	51.903	52.145
O2	+	31.896	32.102	CaO3	2+	43.907	44.085
NO	+	29.939	30.073	CaP	+	70.846	71.122
CO	+	27.933	28.116	CaPO3	+	118.727	119.137
AsO	+	90.822	91.13	P2Ca2O	+	157.635	158.321
AsO2	+	106.689	107.213	P3O2Ca2	+	204.41	205.246
P	2+	15.45	15.521	Ca2P2	+	141.654	142.294
P	3+	10.278	10.373	Ca2P3O3	+	220.555	221.322
P	+	30.942	31.036	Ca2P4O5	+	283.356	284.536
As	3+	24.964	25.035	Cd	+	105.875	106.092
As	+	74.892	75.113				
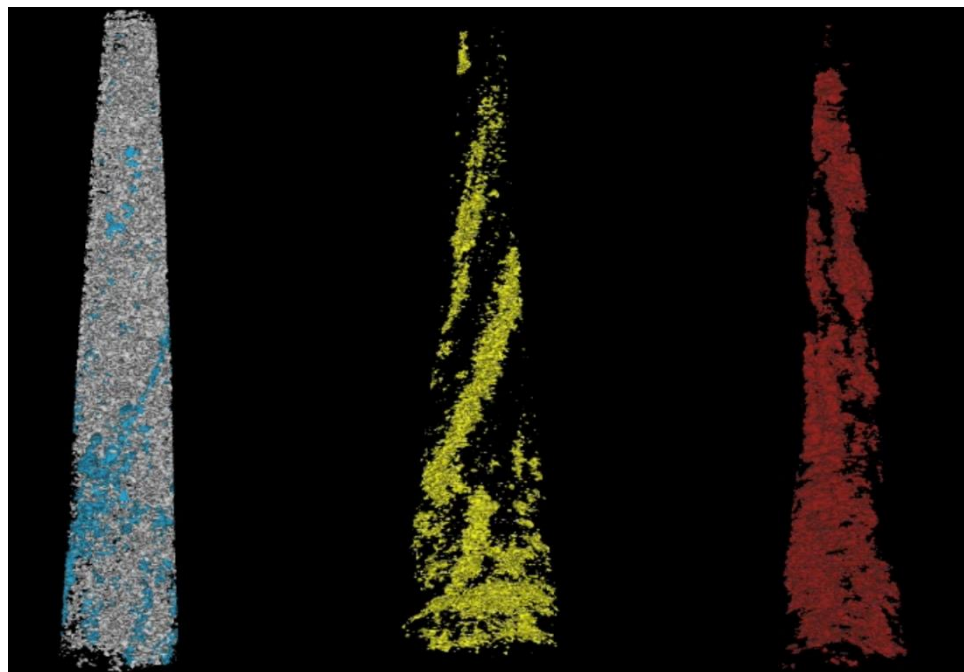
Figure 3-S2: Rotated Isosurfaces Renderings of 3 APT tips: C (11 at%, blue, yellow and red) and Ca (29 at%, grey)
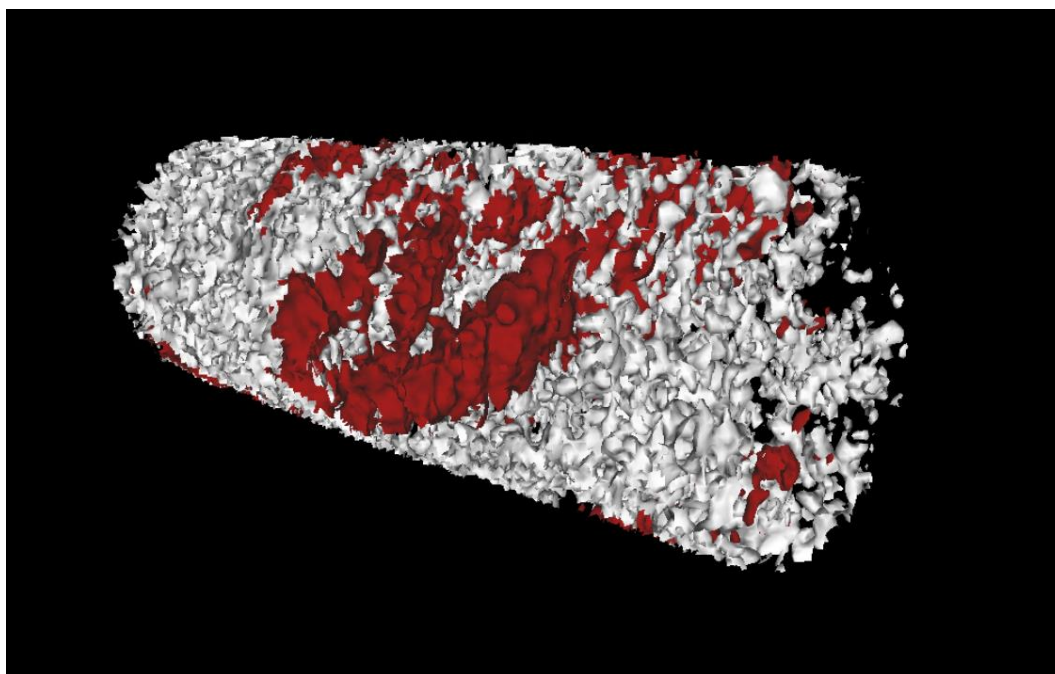
Figure 3-S3: Single isolated fibril section showing C (11 at%, red) and Ca (29 at%, grey). The encapsulation of collagen, represented by carbon, is clear.
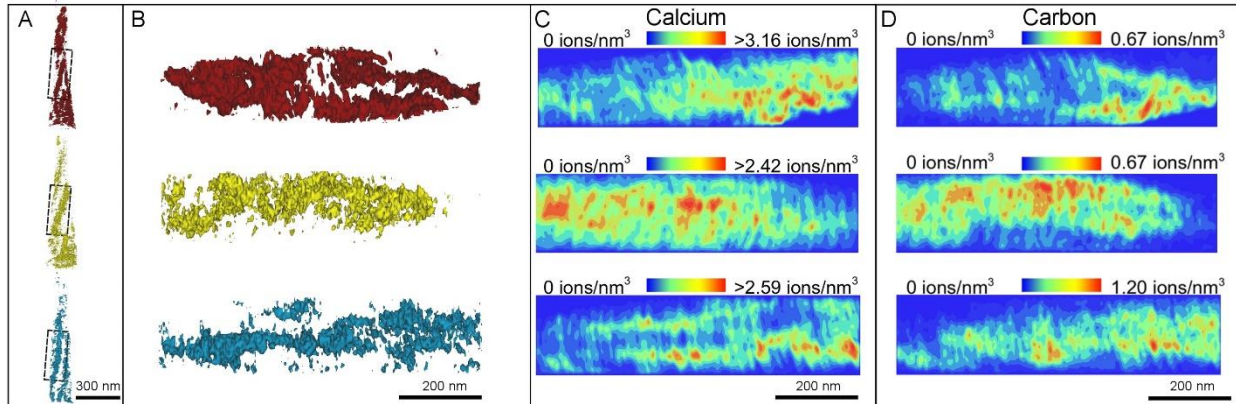
Figure S4. Isolated collagen fibrils from three different reconstructed datasets with corresponding calcium and carbon atomic density maps for the same region. Figure 3-3 with carbon ionic maps added. Dimensions for B,C, and D are the identical. D shows that the carbon density matches the spatial coordinates of the isolated collagen fibrils shown via isosurface rendering in B.

Figure 3-S5. Extracted collagen fibril superimposed on atomic density maps of calcium and phosphorous. An extracted fibril, 285 nm in length, is shown to both incorporate and be encapsulated by calcium and phosphorus demonstrating that while extrafibrillar mineralization dominates, intrafibrillar mineralization is also occurring in bone.

Figure 3-S6: Correlative electron tomography from STEM- HAADF images. APT detector and evaporation efficiency reconstruction parameters were altered using structural information from STEM imaging to improve APT reconstruction accuracy. Representative APT tip shown overlapping the STEM image in cyan.

Chapter 4: Characterization and Evaluation of Femtosecond Laser-Induced Sub-micron Periodic Structures Generated on Titanium to Improve Osseointegration of Implants.

Summary: Altering the surface topography and roughness of titanium are known to improve cellular responses and osseointegration. However, many of these modification techniques result in surfaces with random or irregular topographies. In this chapter, titanium was ablated with a pulsed femtosecond laser to generate laser-induced periodic surface structures (LIPSS) that were inspired by the natural periodicity of collagen, although patterning on a similar length scale was not feasible. These surfaces were characterized for their topography, roughness, wettability, oxide thickness, and crystallinity. The surfaces were evaluated using *in vitro* testing methods with Saos-2 cells. The LIPSS surfaces had microscale roughness and consistent topography with no negative alterations to the structure of titanium. LIPSS surfaces improved osteoblast-like cell responses *in vitro* and encouraged adhesion of the cells in preferred orientations (see Chapter 5, Fig 5-S1). As outlined in the objective, this work contributed new understanding to the response of bone-like cells to a bioinspired surface created on titanium using laser ablation techniques.

Full Length Article

Characterization and evaluation of femtosecond laser-induced sub-micron periodic structures generated on titanium to improve osseointegration of implants

Bryan E.J. Lee [a], Hourieh Exir [b,c], Arnaud Weck [b,c,d], Kathryn Grandfield [a,e,*]

[a] School of Biomedical Engineering, McMaster University, Hamilton, Canada
[b] Department of Physics, University of Ottawa, Ottawa, Canada
[c] Centre for Research in Photonics at the University of Ottawa, Ottawa, Canada
[d] Department of Mechanical Engineering, University of Ottawa, Ottawa, Canada
[e] Department of Materials Science and Engineering, McMaster University, Hamilton, Canada

ARTICLE INFO

ABSTRACT

Reproducible and controllable methods of modifying titanium surfaces for dental and orthopaedic applications are of interest to prevent poor implant outcomes by improving osseointegration. This study made use of a femtosecond laser to generate laser-induced periodic surface structures with periodicities of 300, 620 and 760 nm on titanium substrates. The reproducible rippled patterns showed consistent submicron scale roughness and relatively hydrophobic surfaces as measured by atomic force microscopy and contact angle, respectively. Transmission electron microscopy and Auger electron spectroscopy identified a thicker oxide layer on ablated surfaces compared to controls. In vitro testing was conducted using osteosarcoma Saos-2 cells. Cell metabolism on the laser-ablated surfaces was comparable to controls and alkaline phosphatase activity was notably increased at late time points for the 620 and 760 nm surfaces compared to controls. Cells showed a more elongated shape on laser-ablated surfaces compared to controls and showed perpendicular alignment to the periodic structures. This work has demonstrated the feasibility of generating submicron features on an implant material with the ability to influence cell response and improve implant outcomes.

© 2018 Elsevier B.V. All rights reserved.

1. Introduction

Various methods of modifying titanium have been examined to improve its suitability as an implant material. The goal of these modification techniques is to improve the overall osseointegration, otherwise known as a structural and functional connection, between native bone and the implant material, often achieved by modulating the surface chemistry and topography [1]. These changes often arise from the generation of roughened or porous surface features, which are known to stimulate cellular adhesion and promote bone growth by increasing the bone-implant interface surface area [2,3].

Laser machining, historically, has primarily been used in the semi-conductor industry but has gained traction in recent times as an unconventional implant modification technique [4–8]. Laser machining alters material properties by remelting, alloying or clad-

ding substrate surfaces [7]. The main benefits of using laser-based modification techniques, compared to other surface modification techniques, are that they allow for a degree of precision and control over features while being non-contact, quick, and clean [9]. This degree of precision is a limitation to many other modification techniques such as acid-etching, particle deposition, electropolishing and electric discharge machining [10–14]. Surface geometries achieved via laser modification techniques have ranged from holes, to crown-like projections, to rippled patterns [7,15,16]. Many attempts to use laser modification as a machining technique tend to also result in the formation of holes, cracks and craters, both by design and as a result of thermal damage [6,8,17]. Laser texturing has been used in the biomedical field as a method of altering surface topography to potentially improve osseointegration. Studies involving laser ablation have shown that both osteoblast differentiation and mesenchymal stem cell differentiation towards osteogenic fates can both be increased when interfacing with laser-ablated surfaces [8,15,16,18,19]. In addition, relatively random laser induced microtopographies on conventional implants have

* Corresponding author at: Department of Materials Science and Engineering & School of Biomedical Engineering, McMaster University, Hamilton, Canada.
E-mail address: kgrandfield@mcmaster.ca (K. Grandfield).

demonstrated improved osseointegration *in vivo* with these implanted materials [15,20–22].

Irradiation with linearly polarized ultrashort pulses, using a femtosecond laser, can generate laser-induced periodic surface structures (LIPSS), or ripples, on numerous types of materials, including common implant materials such as titanium [23], [24]. Recent studies have revealed the orientation of the LIPSS can be modified by varying states of laser polarization (linear, circular or elliptical). When a linearly polarized laser beam is applied, the ripples are aligned either perpendicular or parallel to the incident laser polarization [25]. Wang et al. reported that under the irradiation of left and right circularly polarized femtosecond laser pulses the ripples were angled at +45° and −45° with respect to the incident plane of the beam, respectively [25]. On the contrary, the elliptically polarized femtosecond laser pulses induced ripples that were aligned perpendicularly to the long axis, as demonstrated by Tang et al. [26] and Varlamova et al. [27]. Low-spatial frequency LIPSS (LSFL) are observed under specific conditions wherein a spatial periodicity similar to the laser irradiation wavelength is used with an alignment on metals which is perpendicular to the incident laser [23,24]. Originally, it was believed that the ripples generated as a consequence of interference between the incident laser beam and the scattered electromagnetic wave at the surface [23]. Recently, a revised scattering model was proposed by Huang et al. [28] explaining the LIPSS formation in terms of the initial direct surface plasmon (SP)-laser interference and the subsequent grating-assisted SP-laser coupling. The periodicity of these ripples can be altered and controlled by varying laser parameters. Previous studies involving LIPSS have generated ripples on the micrometer scale and have reported equivalent or better cellular responses [16,29,30]. Beyond the viability of cells, studies have reported conflicting results where sub-micron patterns were reported capable of orientating osteoblasts [31] while other studies have only observed visible cell orientation along microscale patterns [16].

In this work, LSFL were generated on the surface of titanium to create sub-micron scale surface topographies. These surfaces were subsequently characterized and evaluated as a potential biomaterial for implant purposes.

2. Methods

2.1. Disk preparation

Titanium disks were prepared by cutting Grade 2 unalloyed sheets of titanium (ASTM-B-265-13A, McMaster-Carr). The sheet was sheared into squares of approximate dimensions of 16×16 mm. These squares were subsequently cut using a lathe and blade setup to produce disks with a diameter of 15 mm and a thickness of 1.25 mm.

2.2. Laser ablation

A Yb:KGW femtosecond laser (PHAROS from Light Conversion, Inc) was used to generate linearly polarized laser pulses at a center wavelength of 1030 nm with pulse duration of 300 fs and a repetition rate of 1 kHz to generate LIPSS on the surface of the grade 2 titanium disks in ambient atmosphere. Before laser processing, the samples were ultrasonically cleaned with acetone and ethanol sequentially for 15 min each. The laser beam was perpendicular to the sample surface and focused using a $5 \times$ microscope objective lens. The combination of a Glan polarizer and a half wave plate was employed to vary the laser power. The sample was mounted on a computer-controlled xy-translation stage and illuminated from the top to enable monitoring the laser micromachining processes with a CCD camera. The laser ablation process was per-

formed by translating the sample relatively to the stationary laser beam. The focused laser beam radius ω_0 on the Ti sample surfaces (defined at e^{-2} of peak intensity of the Gaussian beam distribution) was determined using the D^2-method developed by Liu [32] to be 10.9 μm. Raster scanning method was applied to achieve complete surface coverage of an area of 10×10 mm^2 of titanium samples by scanning a line at a velocity of 1000 μm/s at the laser fluence of 0.5 J/cm^2 and then various lateral displacement of the laser beam of 3 μm, 7.5 μm and 10 μm were applied by translating the stage in a direction perpendicular to the laser beam scanning direction to partially overlap the consecutive laser induced lines to create ripples with periodicities of 300 nm, 620 nm and 760 nm, respectively.

2.3. Characterization

All machined disks were ultrasonically cleaned for 15 min intervals, first in ethanol and then in acetone. Scanning electron microscopy (SEM) images of the laser ablated surfaces were obtained on a JEOL-7000F (JEOL, Peabody, MA) at an accelerating voltage of 2.5 keV. SEM samples were sputter coated with 5 nm of platinum. Atomic force microscopy (AFM) images were acquired on a Bioscope Catalyst (Bruker, Santa Barbara, CA) using the instrument's Scanasyst tapping mode, to both observe the surface modification and to determine surface roughness for each laser-induced periodicity. Water contact angle measurements were determined for all surfaces using a high-speed contact angle measurer, OCA 35 (Future Digital Scientific, Garden City, NY), using a sessile drop method with a droplet size of 3 μL. A JAMP-9500F (JEOL, Peabody, MA) instrument was used to perform Auger electron spectroscopy (AES), at a sputtering rate of approximately 2 nm/s, which allowed for elemental depth profiling of all surfaces.

Sample preparation for transmission electron microscopy (TEM) was done using focused ion beam (FIB) microscope (NVision40, Carl Zeiss AG). An *in situ* lift-out method was used to prepare a TEM lamella less than 100 nm thick. TEM images were acquired on a JEOL 2010F microscope (JEOL, Peabody, MA) using both bright-field and high-angle annular dark-field imaging (HAADF) modes at 200 kV. The microscope is equipped with a Gatan imaging filter (Gatan Inc., Pleasanton, CA) to perform chemical analysis via electron energy loss spectroscopy (EELS). Spectra were initially processed using principal component analysis (PCA) using Digital Micrograph before relevant elemental maps and atomic concentration information were extracted. A power-law background model was used for all shown EELS data.

The periodicity of the laser-ablated disks was determined from SEM images using peak-to-peak measurements in ImageJ (National Institute of Health). Microscope associated software, Nanoscope Analysis (Bruker, Santa Barbara, CA), was used to process and analyze all AFM images. Due to the large variability in roughness of the base titanium substrate, R_{max} was used in lieu of R_a, to better characterize the amount of roughness that was added to the surface as a result of laser ablation.

2.4. Cell culture

Saos-2, osteosarcoma, cells (ATCC ®) were grown in Mccoy's modified 5A media (Life Technologies Inc.) supplemented with 15% fetal bovine serum (Life Technologies Inc.), FBS, and 1% penicillin/streptomycin (Sigma–Aldrich). Cells were kept in an incubator at 37 °C with 5% CO$_2$ and media was exchanged every 4 days. Upon reaching confluence, cells were detached with trypsin in 0.25% EDTA (Sigma–Aldrich) as per ATCC guidelines and subsequently deactivated with media after confirming detachment via light microscope. Cells were seeded on to the surface of titanium disks (15 mm diameter) placed in a 24 well plate at 10,000 cells/

cm^2. All disks were cleaned in ethanol and acetone as previously outlined before being placed into the cell culture environment. Cells were counted using Countess Automated Cell Counter (Invitrogen™). Cells were allowed to grow on the surface of the disks for up to 14 days with the media changed twice (after 5 and 10 days). 12 samples were used for each surface and time point combination.

2.5. Cell metabolism

Cell metabolism, which can be approximated to cell viability, was measured using the alamarBlue® (Life Technologies Inc.) assay. Media was removed from the wells and replaced with a 350 µL 5% alamarBlue solution (in Mccoy's 5A media) per well. The solution was left to incubate for 1 h in the dark at 37 °C with 5% CO$_2$. Fluorescence values were read using an Infinite® M1000 (Tecan, Männedorf, Switzerland) at 540–580 nm (excitation-emission). Each well was sampled at 16 points, approximating the well as a 4 × 4 square. The blank reading was subtracted from each data point to obtain the fluorescent signal corresponding to the cell number only. The alamarBlue solution was then removed and 300 µL of 0.1% triton lysis solution (in PBS) was added to each well. Well plates were frozen at −20 °C and freeze-thaw cycles were performed to conduct further assays.

2.6. Alkaline phosphatase activity

Alkaline phosphatase (ALP) activity was measured using the ALP assay (Abcam ®). 50 µL of cell lysis from each well was combined with 100 µL of p-nitrophenol phosphate in assay buffer (Prepared as per Abcam instructions) and allowed to incubate for 20 min in the dark at 37 °C with 5% CO$_2$. Absorbance was read using Infinite® M1000 (Tecan) at 405 nm. The phosphate group is cleaved by alkaline phosphatase and the resulting p-nitrophenol emits light. Each well was sampled at 16 points, approximating the well as a 4 × 4 square. A standard curve was prepared by using described concentrations of p-nitrophenol (as per Abcam instructions). The blank reading was subtracted from each data point and via the standard curve, absorbance values were converted to p-nitrophenol concentrations.

2.7. Cell orientation

Cells were seeded on the titanium surfaces for 1 day before being fixed with 0.25% glutaraldehyde in a sodium cacodylate buffer. The samples were subsequently stained with osmium tetraoxide before being dehydrated through a series of ethanol rinses starting from 25% (in Milli-Q water) to 100% ethanol. The samples were then critically point dried (Leica Microsystems, Wetzlar, Germany) before being examined under SEM. Stained cell SEM images were acquired on a TESCAN VP. SEM (Tescan, Czech Republic) at an accelerating voltage of 10 keV. Additionally, nuclear area factor and circularity measurements were obtained by relating roundness and area values determined via ImageJ [33]. Circularity and nuclear area factor are unitless measurements determined via ratios of the area and perimeter of cells. Larger values for both are generally associated with healthy cells [33]. A minimum of 3 images was used for all quantitative measurements.

2.8. Statistical analysis

Statistical analysis was performed using the programming language, R (R Core Team, New Zealand), using two-way ANOVA at a significance level of α = 0.05 and Tukey's HSD test was used to evaluate contrasts. Data for the cell metabolism and alkaline phosphatase activity was accepted to be normally distributed as per the Shapiro-Wilk test ($p > 0.05$).

3. Results

3.1. Periodicity

Use of the pulsed femtosecond laser successfully generated rippled patterns on the surface of titanium disks which are shown by SEM in Fig. 1. The mean periodicities of 340, 637 and 751 nm for the 300, 620 and 760 nm surfaces were found respectively. These values, along with 95% confidence bounds, are shown in Table 1. In addition to showing that the pattern on the surfaces is consistent, SEM imaging also revealed the presence of nodules, in particular on the 620 nm surface. Resolidified molten material can also be observed on both the 620 and 760 nm surfaces, in the valleys of the rippled pattern. There is also noticeable overlap of the peaks of the rippled pattern on the 300 nm surface.

3.2. Surface roughness

As the titanium disks have an inherent roughness prior to laser ablation, the measurement of interest when considering roughness was the maximum roughness of the rippled pattern generated by the laser. Specifically, this was considered as the difference in height between the peaks and valleys of the rippled pattern (R_{max}). Fig. 1 shows 10 × 10 µm^2 AFM scans of the 300, 620 and 760 nm surfaces. These AFM images confirm the distinct ripple pattern seen in SEM. Measured R_{max} values for each of the laser-ablated surfaces (Table 1) were all found to be in the same general range of 144–163 nm. Due to the inherent roughness of the titanium disks, these images also show variation in surface roughness on the order of approximately 0.5 µm, irrespective of the rippled pattern.

3.3. Additional characterization

Water contact angle measurements for all surfaces are shown in Table 1. These measurements show that the contact angle is larger for all the laser-ablated surfaces with mean values of 109°, 134°, and 132° for the 300, 620, 760 nm surfaces respectively compared to 84° for control surfaces (Fig. 2). AES showed that the estimated oxide thickness of 300, 620 and 760 nm surfaces were 86, 83 and 75% thicker respectively than the control surface (Fig. 3). These percentages can be approximated into relative oxide thickness values which are less than 50 nm (Table 1). The crossover time of oxygen and titanium profiles was used to approximate the thickness of the oxide layer.

3.4. Microstructure analysis

TEM images of the 620 nm surface are given in Fig. 4. Many of the dark lines observed in the images were identified as bend contours via tilting of the sample or as grain boundaries and have been indicated as such in Fig. 4. TEM imaging also revealed that the rippled pattern is not completely uniform due to the presence of partially ablated features on the surface (Fig. 4B). These images also provided a closer look at some of the resolidified molten droplets which have formed into nodules on the surface. Fig. 4C/D show an example SAED pattern taken near the surface of the 620 nm sample which shows that the material has retained a polycrystalline surface layer. Indexing of this pattern, and patterns from other regions of the sample, to determine the specific composition of the oxide was inconclusive.
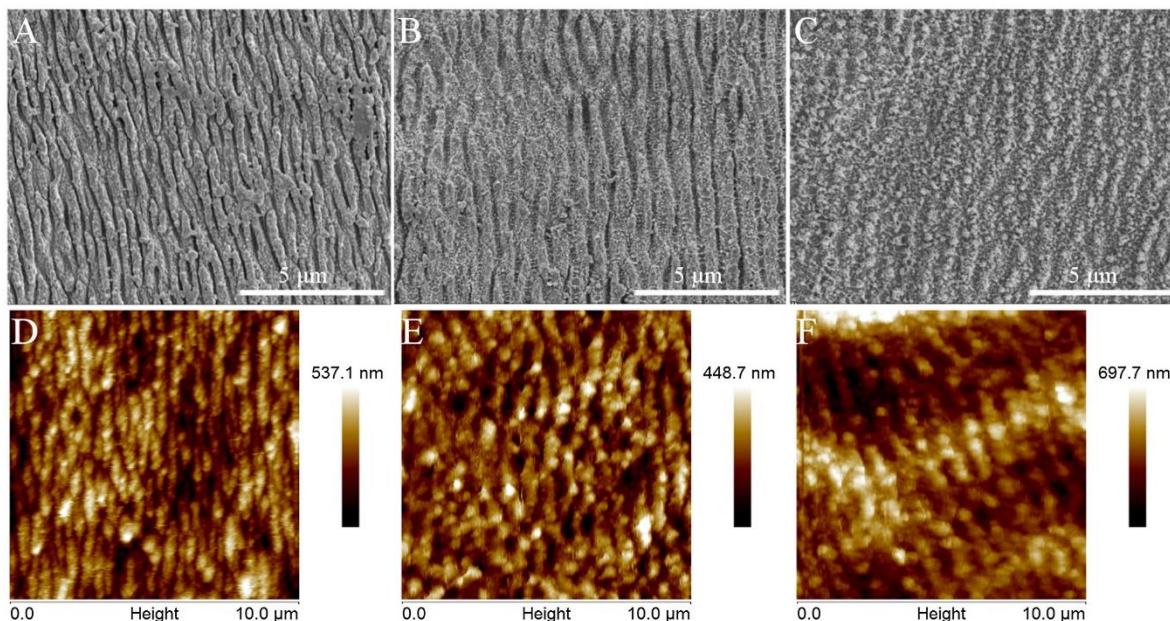
Fig. 1. Scanning electron (A, B, C) and atomic force (D, E, F) micrographs for laser ablated titanium with periodicities of 300, 620 and 760 nm. Periodic patterns have been successfully generated, with consistent laser induced roughness, at all 3 periodicities. (See Table 1 for measured values).

Table 1
Measured periodicity of the ripples, difference in height between the peaks and valleys of the rippled pattern (roughness, R_{max}), water contact angle and relative oxide thickness estimates from AES for all surfaces (300 nm, 620 nm, 760 nm and control) with 95% confidence intervals. The measured periodicities of the surfaces are shown to be very consistent and the laser generated roughness is similar, regardless of the chosen periodicity. The surfaces with larger periodicities demonstrate distinctly hydrophobic behaviour while the control surface is hydrophilic. The oxide thickness estimations show that the laser modified surfaces have a thicker oxide layer compared to the control surface.

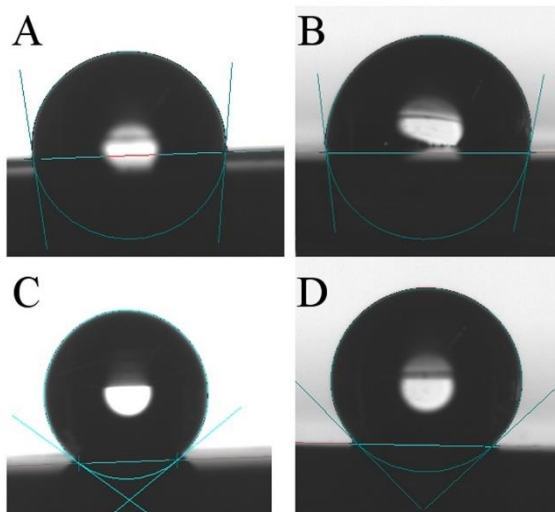| Surface	Periodicity (nm)	Roughness (nm)	Contact angle (°)	Oxide thickness (nm)
Control	N/A	N/A	84 ± 3	5
300 nm	340 ± 21	163 ± 4	109 ± 6	37
620 nm	637 ± 8	144 ± 8	134 ± 14	20
760 nm	751 ± 25	155 ± 15	132 ± 5	29

Fig. 2. Demonstration of the different behaviour of milli-q water droplets on the control, 300, 620 and 760 nm (A, B, C & D respectively) substrates. Measured water contact angles were 84, 109, 134 and 132° for the control, 300, 620 and 760 nm substrates respectively. The 620 and 760 nm surfaces demonstrate noticeably more hydrophobic behaviour compared to the control and 300 nm surfaces.

EELS data was able to show the presence of a thin (~35 nm) surface oxide layer. Fig. 5 shows a HAADF image with a corresponding EELS line scan. The line scan shows that the oxygen signal, while present, is extremely minimal in comparison to the titanium signal and the estimated oxide thickness is comparable to what was observed in AES. The EELS spectrum map shown in Fig. 5 provides additional support to the thin oxide layer as the concentrated or bright green regions of oxygen are only present along the surface of the sample.

3.5. Cell metabolism

The cell metabolism results in Fig. 6A directly correlate fluorescence to cell metabolism. For each surface, from 3 to 7 days, the magnitude of cell metabolism increased for each surface but was only statistically significant for the 760 nm surface ($p < 0.05$). There were no statistically significant differences noted between 7 and 14 days for any of the individual surfaces. At the 3 day time point, both the 620 nm and control surfaces show statistically significant increases in metabolism compared to the 300 nm surface. This effect extends to the 7 day time point for the control surface. The control surface also showed statistically significant increases in metabolism compared to the 760 nm surface after 3 days. However, all of these effects disappear after 14 days.
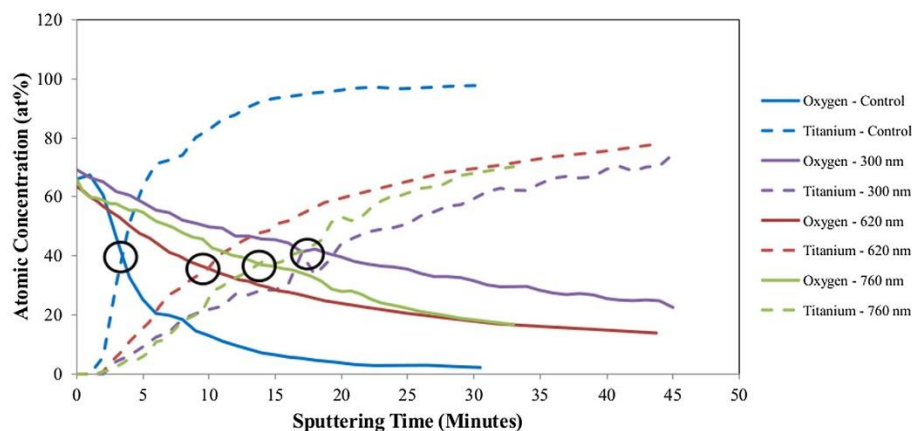
Fig. 3. Auger electron spectroscopy (AES) depth profiles for control and laser ablated (300 nm, 620 nm and 760 nm) surfaces. Profiles reveal that the oxide layer for all laser ablated surfaces are thicker than the unmodified titanium. Relative oxide layer thickness estimates were obtained by comparing the crossover times (circled intersections of Ti and O profiles) between the laser ablated surfaces and controls (See Table 1 for values), where a crossover at longer sputtering times represents a larger oxide thickness.
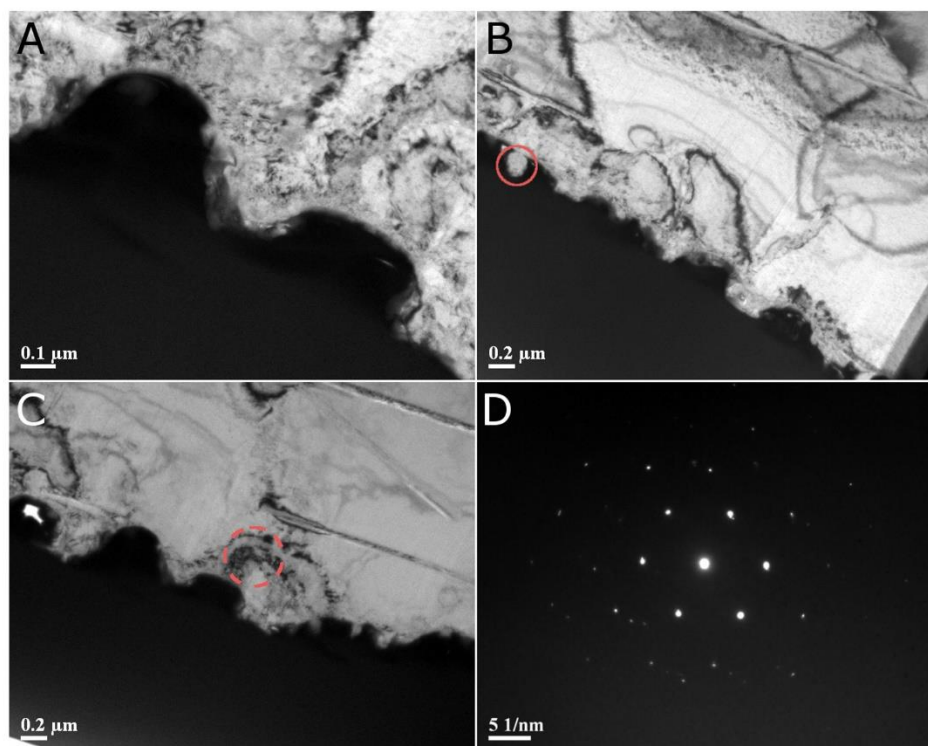

Fig. 4. Cross-sectional TEM micrographs of the 620 nm surface (A, B) showing the generated rippled pattern while revealing the presence of additional surface features (circle – resolidified molten droplet, arrowhead – contour line, solid arrow – grain boundary). Diffraction pattern (D) taken from the surface of the substrate (C) reveals a polycrystalline surface layer.

3.6. Alkaline phosphatase activity

Alkaline phosphatase activity for each surface after 3, 7 and 14 days of cell seeding time is shown in Fig. 6B. Similar to cell metabolism, the magnitude of alkaline phosphatase activity increased from 3 to 7 days but was only statistically significant for the 620 nm and control surfaces ($p < 0.05$). Notably, the alkaline phosphatase activity on the control surface showed a statistically significant decrease from 7 to 14 days. However, no corresponding decrease in cell metabolism was observed. Similarly, a statistically

significant difference between both the 620 and 760 nm surfaces and the control surface after 14 days of cell seeding was noted. Additionally, the 620 nm surface showed statistically significant increases at the 3 day time point compared to the 760 nm surface.

3.7. Cell orientation

SEM images of Saos-2 cells on laser-ablated and control surfaces can be observed in Fig. 7. This shows that the cells on the laser ablated surface have an elongated phenotype compared to the cells
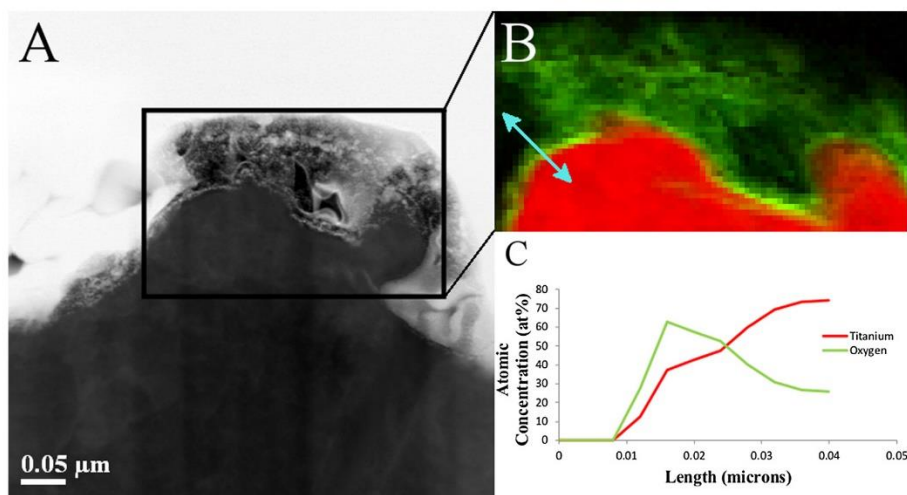
Fig. 5. EELS line scan (C) with accompanying HAADF image (A) of the 620 nm surface. EELS spectrum colour map (B) for a nodule on the 620 nm surface. The red indicates the titanium while the green indicates the oxygen. The presence of high concentrations of oxygen can only be seen at the surface of the substrate. The line scan (C; double-sided blue arrow) reveals a higher concentration of oxygen over a small length and supports AES estimates that the oxide layer is 20–30 nm in thickness.
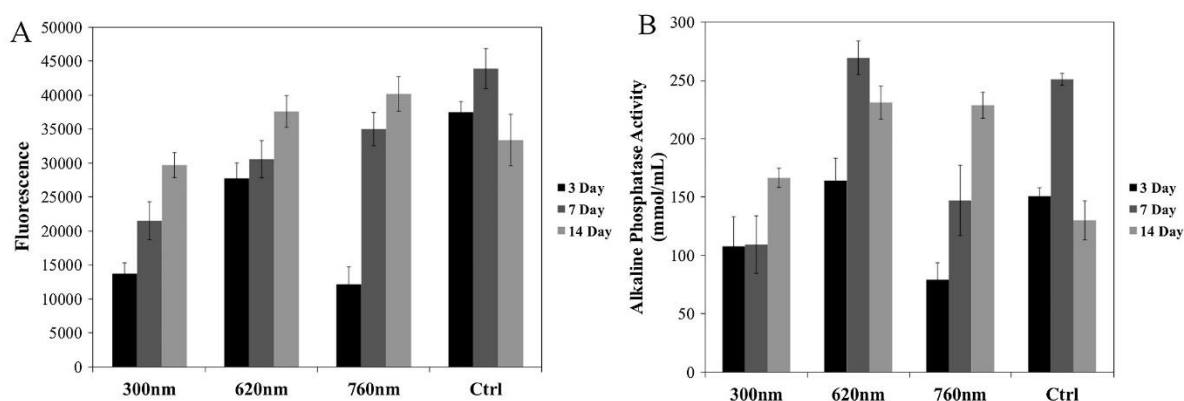

Fig. 6. (A) Cell metabolism at early time points was significantly greater on the control surface than the 300 and 760 nm surfaces but this effect disappeared at later time points. The 620 nm surface had statistically significant increased metabolism after 3 days compared to 300 and 760 nm surfaces and after 7 days compared to the 300 nm surface. At late time points there was no difference between the laser modified surfaces and controls. Error bars represent standard error. (B) ALP activity [mmol/mL] for control and laser modified surfaces. The 620 nm surface had statistically significant ($p < 0.05$) improvements in ALP activity at 3 and 7 days compared to the 760 nm surface. The 620 and 760 nm surfaces had statistically significant ($p < 0.05$) improvements in ALP activity after 14 days compared to the control surface. Error bars represent standard error.

on the unmodified titanium surface. The cells on the laser ablated surfaces appear to be oriented perpendicular to the periodic structures which can be observed in Fig. 7C/D. Fig. 7D shows that many of the filopodia have attached directly to the peaks of the rippled pattern. The circularity and nuclear area factor, a common indicator of cell health, are listed in Table 2. The circularity of the cells is higher on the control surface compared to the laser-ablated surfaces while the average nuclear area factor is larger for cells on the laser-ablated surfaces. These effects were only noticeable at lower seeding densities, confluent layers displayed no detectable differences in orientation or circularity (results not shown).

4. Discussion

The generation of ripples using a femtosecond laser allowed for a specific and ordered surface modification of titanium for implant purposes. These patterns are consistent and significantly differen-

tiate themselves from more random or disorganized modification techniques. This is potentially advantageous in industrial or clinical settings as the consistency observed in the periodicity measurements is promising from a quality-control standpoint. The ripples generated visibly distinguish themselves from unmodified titanium and, with regards to periodicity, are similar in appearance to that of collagen fibrils. TEM imaging revealed the presence of grain boundaries and bend contours, the grains were noted to be smaller towards the surfaces compared to the bulk material. This effect has been noted previously where grain size distributions were observed at the surface of femtosecond treated materials [34]. In addition, this refined grain structure may contribute to a tougher surface coating [35]. The observed nodules are likely resolidified molten droplets from the laser ablation process which may benefit biological adhesion by increasing surface contact area.

Results showed that the laser ablation had effects on both the surface chemistry and topography that warrant discussion. Firstly,
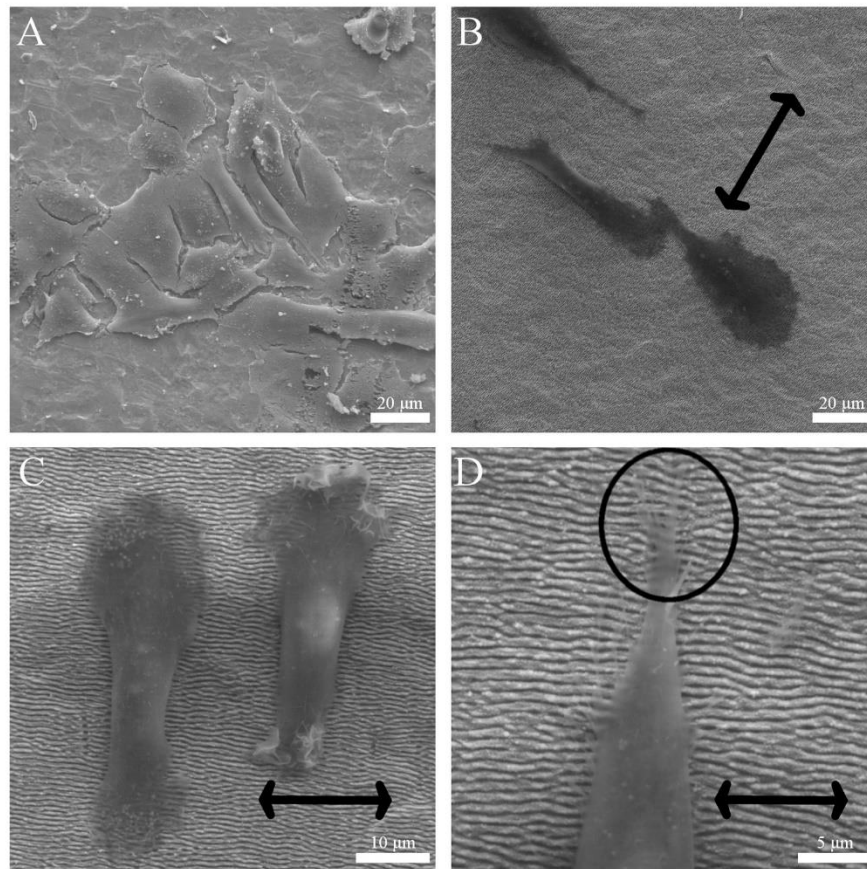
Fig. 7. SEM images of fixed and stained Saos-2 cells on control (A) and laser modified surfaces (B; 300 nm ripples, C and D; 620 nm ripples) after 1 day of seeding. The cells on the laser ablated surfaces appear to be perpendicularly aligned with the periodic structures (B, C, D). (D) shows interactions with the filopodia of the cells with the peaks of the rippled pattern. Double-sided arrows indicate the direction of the periodic patterns while the circle in (D) indicates filopodia attachments.

Table 2
Average circularity and nuclear area factor of cells fixed on to 300, 620, 760 nm and control surfaces. Measurements were obtained from SEM images via ImageJ, a minimum of 3 images was used for each parameter. Circularity was lower for the laser-ablated surfaces compared to the control while the nuclear area factor was higher for the laser-ablated surfaces compared to the control.

Surface	Circularity	Nuclear Area Factor
Control	0.45	152
300 nm	0.33	432
620 nm	0.32	302
760 nm	0.11	239

all modified surfaces showed a very consistent roughness resulting from the laser modification. These roughness values, like with the periodicity measurements, were very consistent regardless of chosen periodicity and this shows that the modification technique is easily reproduced. This is a positive result as one of the main limitations to understanding sub-micron topographies is the lack of consistency in the preparation of the surfaces [36,37]. In terms of magnitude, the roughness values for the laser modified surfaces and the base titanium substrate were on the submicron and micron scale respectively. This resulting dual-stage roughness ultimately increases the surface area which is good from an osseointegration standpoint [21,37]. Additionally, the laser-ablated surface

was found to be significantly more hydrophobic than unmodified controls. It should be noted that the 300 nm surface was less hydrophobic compared to the 620 and 760 nm surfaces. Preference, when considering biomaterials, is given to hydrophilic surfaces to allow for greater interaction between material and the *in vivo* environment as a hydrophobic surface has the potential of leading to isolation of the material via thrombosis or similar pathways [38,39]. Chemical analysis revealed that the naturally occurring oxide layer of titanium on modified surfaces was still present and noticeably thicker in magnitude compared to the control surface. This was confirmed via results from AES and EELS. It was expected that the laser ablation would increase the overall thickness of the oxide layer due to the laser ablation occurring in air. This is beneficial because this naturally occurring oxide layer is known to be a major contributing factor to titanium's position as a favourable biomaterial for osseointegration. It has been previously reported that thicker, more uniform oxide layers are more stable compared to natural titanium which has a relatively thin, defect-heavy oxide layer [40,41].

Evaluation of the surface from *in vitro* testing showed that the laser modified surface allowed for cell metabolism and subsequently alkaline phosphatase activity. As expected, both of the measured parameters showed an increase in magnitude with increasing cell-seeding time. When considering seeding time, only

the 760 nm surface showed statistically significant increases in cell metabolism from 3 to 7 days. However, by 14 days all statistically significant effects disappear and there is no difference between the four surfaces. From an osseointegration standpoint this is positive as it demonstrates that all the modified surfaces are not cytotoxic and do not down-regulate cell growth or proliferation. These results have shown that the cells are capable of exhibiting typical cell growth behaviour from log to stationary phases. It was previously observed by Raimbault et al. that micron-sized ripples showed no difference compared to control surfaces with regard to cell growth [16]. This work used sub-micron ripples and a similar outcome has been observed. Statistically significant increases in alkaline phosphatase activity were observed for each surface except for the 300 nm from 3 to 7 days which corresponded to the increased metabolism observed over time. Interestingly, there was a statistically significant decrease in alkaline phosphatase activity in the control group from 7 to 14 days and there was no corresponding decrease in metabolism. This was not an effect that was observed for the laser-ablated surfaces. In fact, the 620 and 760 nm surfaces showed improved alkaline phosphatase activity compared to the control group at 14 days. This decrease in ALP activity may have resulted from cells on the control surface at 14 days entering the death phase of cell growth which may have reduced the overall ALP activity measurement. The decreased circularity of cells observed on the laser ablated surface compared to the control surface show that the cells have a greater spread, which has been associated with improved cell health [42–44]. Lower nuclear area factor has been shown to be a strong indicator of cell apoptosis [33], [45]. While the in vitro assays show that cell apoptosis is not prevalent during the examined timeframe, the increased nuclear area factor of cells observed on the laser-ablated surfaces suggests that these cells may be relatively healthier. SEM images of fixed cells on the laser ablated surfaces show that the filopodia of the cells appear to be attaching to the peaks of the laser ablated pattern. It has been shown by Dalby et al. that there is a response between filopodia and features as small as 10 nm [42,46,47]. This suggests that the laser ablated features may experience nanocontact guidance which is why the cells on the laser-ablated surfaces showed reduced circularity compared to the control surface.

Overall, the 620 nm surface performed better than the other laser-ablated surfaces in terms of cell metabolism and alkaline phosphatase at all time points. The 620 nm surface also showed statistically significant increased alkaline phosphatase activity compared to the control surface. This suggests that the surface modification may have an effect on adherent Saos-2 cells. Studies have shown that different cells tend to prefer different sized features when considering their growth and proliferation on biomaterials [16,48,49]. Saos-2 cells are of similar length scale to osteoblasts, so their behaviour on the laser-ablated surfaces can be considered an appropriate model of osteoblast adhesion [50]. It is noteworthy that the 300 nm surface, the laser-ablated surfaces with the thickest estimated oxide layer and the least hydrophobic, performed the worst when considering the in vitro studies. This leads to suspicion from the authors that the difference in wettability between the laser-ablated surfaces is not significant or that the generated rippled pattern, and its corresponding change to the surface roughness, is counterbalancing these alterations. It should also be noted that this study primarily focused on early osseointegration. From that perspective, the 620 nm and control surfaces performed the best. Thus, when evaluating the 300 and 760 nm surfaces, it should be noted that tests associated with long-term osseointegration or in vivo studies have shown that nanoscale roughness is beneficial [51–53].

Additional studies on these laser-modified surfaces are needed to completely understand how the contrasting effects of surface topography and chemistry are affecting cell adhesion, metabolism and proliferation. Additional in vitro studies with different cell lines, perhaps non-osteoblast-like, may be necessary to understand the specific adhesion and proliferation mechanics in place. Finally, in vivo studies are a logical next step to further investigate the osseointegration ability of the laser modified surfaces over longer times in a more clinically relevant scenario.

5. Conclusions

The use of a pulsed femtosecond laser to generate reproducible and sub-micron patterns using laser-ablation methods on titanium substrates was successfully demonstrated. The surfaces were consistent with regards to periodicity, laser-induced roughness and oxide thickness. Of the three designed periodicities, the 620 nm surface showed improved capacity as an implant surface from a biocompatibility standpoint. This study has demonstrated the potential of using LIPSS to generate potentially biologically relevant patterns that may have potential for titanium modification in orthopaedic or dental implant applications.

Acknowledgements

Conflict of interest

The authors declare no conflict of interest.

References

[1] T. Albrektsson, Osseointegrated Titanium Implants, 1981, pp. 155–170.
[2] B.D. Boyan, T.W. Hummert, D.D. Dean, Z. Schwartz, Role of material surfaces in regulating bone and cartilage cell response, Biomaterials 17 (2) (1996) 137–146.
[3] S.F. Hulbert, F.W. Cooke, J.J. Klawitter, R.B. Leonard, B.W. Sauer, D.D. Moyle, Attachment of prostheses to the musculo-skeletal system by tissue ingrowth and mechanical interlocking, J. Biomed. Mater. Res. 23 (4) (1973) 1–23.
[4] F. Guillemot, F. Prima, V.N. Tokarev, C. Belin, M.C. Port-Durrieu, T. Gloriant, C. Baquey, S. Lazare, Single-pulse KrF laser ablation and nanopatterning in vacuum of beta-titanium alloys used in biomedical applications, Appl. Phys. A 79 (4–6) (2004) 811–813.
[5] D.S. Milovanović, S.M. Petrović, M.a. Shulepov, V.F. Tarasenko, B.B. Radak, Š.S. Miljanic, M.S. Trtica, Titanium alloy surface modification by excimer laser irradiation, Opt. Laser Technol. 54 (2013) 419–427.
[6] D.S. Milovanović, B.B. Radak, B.M. Gaković, D. Batani, M.D. Momčilović, M.S. Trtica, Surface morphology modifications of titanium based implant induced by 40picosecond laser pulses at 266nm, J. Alloys Compd. 501 (1) (2010) 89–92.
[7] Y.S. Tian, C.Z. Chen, S.T. Li, Q.H. Huo, Research progress on laser surface modification of titanium alloys, Appl. Surf. Sci. 242 (1–2) (2005) 177–184.
[8] M. Trtica, B. Gakovic, D. Batani, T. Desai, P. Panjan, B. Radak, Surface modifications of a titanium implant by a picosecond Nd:YAG laser operating at 1064 and 532nm, Appl. Surf. Sci. 253 (5) (2006) 2551–2556.
[9] N.B. Kurella, A. Dahotre, Review paper: surface modification for bioimplants: the role of laser surface engineering, J. Biomater. Appl. 20 (1) (2005) 5–50.
[10] G. Passeri, A. Cacchioli, F. Ravanetti, G. Galli, E. Elezi, G.M. Macaluso, Adhesion pattern and growth of primary human osteoblastic cells on five commercially available titanium surfaces, Clin. Oral Implants Res. 21 (7) (2010) 756–765.
[11] H. Solař, P. Kylián, O. Marek, A. Vandrovcová, M. Bacáková, L. Hanuš, J. Biederman, Particles induced surface nanoroughness of titanium surface and its influence on adhesion of osteoblast-like MG-63 cells, Appl. Surf. Sci. 324 (2015) 99–105.
[12] E.M. Lotz, R. Olivares-Navarrete, S. Berner, B.D. Boyan, Z. Schwartz, Osteogenic response of human MSCs and osteoblasts to hydrophilic and hydrophobic nanostructured titanium implant surfaces, J. Biomed. Mater. Res. Part A (2016) 1–12.
[13] C. Larsson, P. Thomsen, B.O. Aronsson, M. Rodahl, J. Lausmaa, B. Kasemo, L.E. Ericson, Bone response to surface-modified titanium implants: studies on the

early tissue response to machined and electropolished implants with different oxide thicknesses, Biomaterials 17 (6) (Mar. 1996) 605–616.

[14] B.E.J. Lee, S. Ho, G. Mestres, M. Karlsson Ott, P. Koshy, K. Grandfield, Dual-topography electrical discharge machining of titanium to improve biocompatibility, Surf. Coatings Technol. 296 (2016) 149–156.

[15] A.Y. Vorobyev, C. Guo, Femtosecond laser structuring of titanium implants, Appl. Surf. Sci. 253 (17) (2007) 7272–7280.

[16] O. Raimbault, S. Benayoun, K. Anselme, C. Mauclair, T. Bourgade, A.-M. Kietzig, P.-L. Girard-Lauriault, S. Valette, C. Donnet, The effects of femtosecond laser-textured Ti-6Al-4V on wettability and cell response, Mater. Sci. Eng. C 69 (2016) 311–320.

[17] M. Kreisler, H. Al Haj, H. Götz, H. Duschner, B. D'Hoedt, Effect of simulated CO_2 and GaAlAs laser surface decontamination on temperature changes in Ti-plasma sprayed dental implants, Lasers Surg. Med. 30 (3) (2002) 233–239.

[18] E. Mariscal-Muñoz, C.A.S. Costa, H.S. Tavares, J. Bianchi, J. Hebling, J.P.B. Machado, U.H. Lerner, P.P.C. Souza, Osteoblast differentiation is enhanced by a nano-to-micro hybrid titanium surface created by Yb:YAG laser irradiation, Clin. Oral Investig. 20 (3) (2016) 503–511.

[19] M. Radmanesh, A.M. Ektesabi, R.A. Wyatt, B.D. Crawford, A. Kiani, Mouse embryonic fibroblasts accumulate differentially on titanium surfaces treated with nanosecond laser pulses, Biointerphases 11 (3) (2016) 31009.

[20] R. Bránemark, L. Emanuelsson, A. Palmquist, P. Thomsen, Bone response to laser-induced micro- and nano-size titanium surface features, Nanomed. Nanotechnol., Biol. Med. 7 (2) (2011) 220–227.

[21] F.A. Shah, M.L. Johansson, O. Omar, H. Simonsson, A. Palmquist, P. Thomsen, Laser-modified surface enhances osseointegration and biomechanical anchorage of commercially pure titanium implants for bone-anchored hearing systems, PLoS One 11 (6) (2016) 1–24.

[22] C. Hallgren, H. Reimers, D. Chakarov, J. Gold, A. Wennerberg, An in vivo study of bone response to implants topographically modified by laser micromachining, Biomaterials 24 (5) (2003) 701–710.

[23] J.E. Sipe, J.F. Young, J.S. Preston, H.M. Van Driel, Laser-induced periodic surface structure. I. Theory, Phys. Rev. B 27 (2) (1983) 1141–1154.

[24] J.F. Young, J. Preston, H. Van Driel, J. Sipe, Laser induced periodic surface structures II. Experiments on Ge, Si, Al and brass, Phys. Rev. B 27 (2) (1983) 1155.

[25] J. Wang, C. Guo, Permanent recording of light helicity on optically inactive metal surfaces, Opt. Lett. 24 (2006) 3641–3643.

[26] Y. Tang, J. Yang, B. Zhao, M. Wang, X. Zhu, Control of periodic ripples on metals by femtosecond laser ellipticity, Opt. Express 23 (2012) 25826–25833.

[27] O. Varlamova, F. Costache, M. Ratzke, J. Reif, Control parameters in pattern formation upon femtosecond laser ablation, Appl. Surf. Sci. 253 (2007) 7932–7936.

[28] M. Huang, F. Zhao, Y. Cheng, N. Xu, Z. Xu, Origin of laser-induced near-subwavelength ripples: interference between surface plasmons and incident laser, ACS Nano 3 (2009) 4062–4070.

[29] M.C. Cunha, A. Zouani, O.F. Plawinski, L. Do Rego, A.M.B. Almeida, A. Vilar, R. Durrieu, Human mesenchymal stem cell behavior on femtosecond laser-textured Ti-6Al-4V surfaces, Nanomedicine 10 (5) (2015) 725–739.

[30] P. Bizi-Bandoki, S. Benayoun, S. Valette, B. Beaugiraud, E. Audouard, Modifications of roughness and wettability properties of metals induced by femtosecond laser treatment, Appl. Surf. Sci. 257 (12) (2011) 5213–5218.

[31] T. Shinonaga, M. Tsukamoto, T. Kawa, P. Chen, A. Nagai, T. Hanawa, Formation of periodic nanostructures using a femtosecond laser to control cell spreading on titanium, Appl. Phys. B Lasers Opt. 119 (3) (2015) 493–496.

[32] J.M. Liu, Simple technique for measurements of pulsed Gaussian-beam spot sizes, Opt. Lett. 7 (1982) 196–198.

[33] M.a. DeCoster, The Nuclear Area Factor (NAF): a measure for cell apoptosis using microscopy and image analysis, Mod. Res. Educ. Top. Microsc. (2007) 378–384.

[34] M.V. Shugaev, C. Wu, O. Armbruster, A. Naghilou, N. Brouwer, D.S. Ivanov, T.J.-Y. Derrien, N.M. Bulgakova, W. Kautek, B. Rethfeld, L.V. Zhigilei, Fundamentals of ultrafast laser–material interaction, MRS Bull. 41 (12) (2016) 960–968.

[35] S. Zhang, D. Sun, Y. Fu, H. Du, Recent advances of superhard nanocomposite coatings: a review, Surf. Coatings Technol. 167 (2–3) (2003) 113–119.

[36] L. Le Guéhennec, A. Soueidan, P. Layrolle, Y. Amouriq, Surface treatments of titanium dental implants for rapid osseointegration, Dent. Mater. 23 (7) (2007) 844–854.

[37] M.M. Shalabi, A. Gortemaker, M.A. Van't Hof, J.A. Jansen, N.H.J. Creugers, Implant surface roughness and bone healing: a systematic review, J. Dent. Res. 85 (6) (2006) 496–500.

[38] M. Chiapasco, F. Biglioli, L. Autelitano, E. Romeo, R. Brusati, Clinical outcome of dental implants placed in fibula-free flaps used for the reconstruction of maxillo-mandibular defects following ablation for tumors or osteoradionecrosis, Clin. Oral Implants Res. 17 (2) (2006) 220–228.

[39] P. Thevenot, W. Hu, L. Tang, Surface chemistry influences implant biocompatibility, Curr. Top. Med. Chem. 8 (4) (2008) 270–280.

[40] N. Huang, P. Yang, Y.X. Leng, J.Y. Chen, H. Sun, J. Wang, G.J. Wang, P.D. Ding, T.F. Xi, Y. Leng, Hemocompatibility of titanium oxide films, Biomaterials 24 (13) (2003) 2177–2187.

[41] J. Pouilleau, D. Devilliers, F. Garrido, S. Durand-Vidal, E. Mahé, Structure and composition of passive titanium oxide films, Mater. Sci. Eng. B 47 (3) (1997) 235–243.

[42] M.J. Dalby, M.O. Riehle, H.J.H. Johnstone, S. Affrossman, A.S.G. Curtis, Polymer-demixed nanotopography: control of fibroblast spreading and proliferation, Tissue Eng. 8 (6) (2002) 1099–1108.

[43] P. Brun, M. Scorzeto, S. Vassanelli, I. Castagliuolo, G. Palù, F. Ghezzo, G.M.L. Messina, G. Iucci, V. Battaglia, S. Sivolella, A. Bagno, G. Polzonetti, G. Marletta, M. Dettin, Mechanisms underlying the attachment and spreading of human osteoblasts: from transient interactions to focal adhesions on vitronectin-grafted bioactive surfaces, Acta Biomater. 9 (4) (2013) 6105–6115.

[44] J. Schwartz, M.J. Avaltroni, M.P. Danahy, B.M. Silverman, E.L. Hanson, J.E. Schwarzbauer, K.S. Midwood, E.S. Gawalt, Cell attachment and spreading on metal implant materials, Mater. Sci. Eng. C 23 (3) (2003) 395–400.

[45] I.M. Helmy, A.M. Abdel Azim, Efficacy of ImageJ in the assessment of apoptosis, Diagn. Pathol. 7 (1) (2012) 15.

[46] M.J. Dalby, M.O. Riehle, H. Johnstone, S. Affrossman, A.S.G. Curtis, Investigating the limits of filopodial sensing: A brief report using SEM to image the interaction between 10 nm high nano-topography and fibroblast filopodia, Cell Biol. Int. 28 (3) (2004) 229–236.

[47] M.J. Dalby, N. Gadegaard, M.O. Riehle, C.D.W. Wilkinson, A.S.G. Curtis, Investigating filopodia sensing using arrays of defined nano-pits down to 35 nm diameter in size, Int. J. Biochem. Cell Biol. 36 (10) (2004) 2015–2025.

[48] P.M. Davidson, M. Bigerelle, G. Reiter, K. Anselme, Different surface sensing of the cell body and nucleus in healthy primary cells and in a cancerous cell line on nanogrooves, Biointerphases 10 (3) (2015) 31004.

[49] M. Eichhorn, C. Stannard, K. Anselme, J. Rühe, Nucleus deformation of SaOs-2 cells on rhombic μ-pillars, J. Mater. Sci. Mater. Med. 26 (2) (2015) 1–6.

[50] C. Pautke, M. Schieker, T. Tischer, A. Kolk, P. Neth, W. Mutschler, S. Milz, Characterization of osteosarcoma cell lines MG-63, Saos-2 and U-2 OS in comparison to human osteoblasts, Anticancer Res. 24 (6) (2004) 3743–3748.

[51] L. Salou, A. Hoornaert, G. Louarn, P. Layrolle, Enhanced osseointegration of titanium implants with nanostructured surfaces: an experimental study in rabbits, Acta Biomater. 11 (1) (2015) 494–502.

[52] S.L. Hyzy, A. Cheng, D.J. Cohen, G. Yatzkaier, A.J. Whitehead, R.M. Clohessy, R.A. Gittens, B.D. Boyan, Z. Schwartz, Novel hydrophilic nanostructured microtexture on direct metal laser sintered Ti-6Al-4V surfaces enhances osteoblast response in vitro and osseointegration in a rabbit model, J. Biomed. Mater. Res. – Part A 104 (8) (2016) 2086–2098.

[53] D. Karazisis, A.M. Ballo, S. Petronis, H. Agheli, L. Emanuelsson, P. Thomsen, O. Omar, The role of well-defined nanotopography of titanium implants on osseointegration: cellular and molecular events in vivo, Int. J. Nanomedicine 11 (2016) 1367–1382.

Chapter 5: Capturing Mammalian Cell Adhesion to Sub-Micron Surface Features with Ionic Liquids in Low-Vacuum SEM.

Summary: Observing wet biological samples, such as mammalian cells, in the scanning electron microscope (SEM) is challenging due to the high-vacuum and electron beam radiation. Visualizing cellular responses to biomaterials with micro or nanoscale topographies can improve our understanding of cellular adhesion and biomaterials design. However, is not possible with conventional optical microscopy techniques which lack resolution to image surface features on this length scale. Room temperature ionic liquids (RTIL) have low vapour pressure and high electrical conductivity which gives them stability in the SEM. In this chapter, osteoblast-like cells adhered to the LIPSS titanium generated in Chapter 4 were observed in the SEM by developing a RTIL treatment. Osteoblast-like cells were imaged in low-vacuum mode SEM while immersed in a solution of their natural media and RTIL. Following exposure under the SEM, cells were evaluated using fluorescent imaging and assays to assess viability. These cells were visualized with respect to the submicron features of the LIPSS titanium under wet conditions. Cells not directly exposed to the electron beam remained viable for repeated measures. In line with the objectives of this thesis, this work developed a new method of evaluating biomaterials with RTIL and SEM that enables simultaneous visualization of cells and surface features.

Capturing Mammalian Cell Adhesion to Sub-Micron Surface Features with Ionic Liquids in Low-Vacuum SEM

Bryan E.J. Lee[1], Hourieh Exir[2,3], Arnaud Weck[2,3,4], Kathryn Grandfield[1,5]

[1] School of Biomedical Engineering, McMaster University, Hamilton, Canada.
[2] Department of Physics, University of Ottawa, Ottawa, Canada.
[3] Centre for Research in Photonics at the University of Ottawa, Ottawa, Canada.
[4] Department of Mechanical Engineering, University of Ottawa, Ottawa, Canada.
[5] Department of Materials Science and Engineering, McMaster University, Hamilton, Canada.

Abstract

This work presents a successful method to image mammalian cells under the scanning electron microscope operating in low-vacuum mode following ionic liquid treatment. Human osteoblast-like Saos-2 cells were treated with a room temperature ionic liquid, 1-Ethyl-3-methylimidazolium tetrafluoroborate, and subsequently imaged under the SEM. Using a combination of fluorescence-based cell metabolism along with light microscopy and SEM image analysis, the shape and location of irradiated cells was confirmed to be unchanged after multiple irradiation sessions while the viability of minimally irradiated cells was unaltered. The wet imaging conditions combined with a rapid protocol allows this technique to fulfill a niche in examining cellular behavior on biomaterials with sub-micron surface features. The demonstrated method to track observed cell adhesion to sub-micron surface features with the SEM has great implications for the understanding of cell migration on nanostructured surfaces.

Introduction

Imaging of biological samples using electron microscopy is a great challenge that has yet to be overcome. The mechanism by which the electron microscope works is, in of itself, incredibly detrimental to the viability of biological specimens. In the case of transmission or scanning transmission electron microscope (TEM/STEM), it has been considered almost impossible to image living biological cells although attempts have been made by encapsulating fixed cells in between silicon nitride windows [1], [2].There have been attempts to reduce the most harmful effects of the scanning electron microscope (SEM) by reducing the accelerating voltage, operating under low-vacuum or utilizing environmental microscopes (ESEM) [3], [4]. However, these techniques still struggle to image cells without causing irreversible damage. Chemical fixation, dehydrating and staining are other commonly employed methods to image cells but these techniques come with the drawback of altering the morphology of cells, proteins and other relevant molecules resulting in the imaging of a sample which has been altered from its living state [5]. These dried samples lack the fluidity of cells in their native environment and thus are not completely representative of the system.

The advent of super-resolution techniques has enabled optical techniques to achieve nanoscale resolution via creative use of fluorescent tools which has encroached upon the territory once owned by electron microscopy [6]. Unfortunately, these techniques only apply for components that can be fluorescently tagged. This means that the visualization of all other objects is limited to the diffraction of light or the micron-scale. As such, to allow for simultaneous imaging of the interface between cells and sub-micron substrates, electron microscopy remains the best choice. This is particularly important for the biomedical device industry which frequently uses sub-micron or nanoscale features to improve outcomes using bioactive coatings, laser modification and anodization [7]–[10]. Nanostructures are used in dynamic biomedical applications ranging from implant materials, biosensors,and tissue engineering to drug delivery [11]–[14]. The proliferation and adhesion of cells in each of these applications and how they change over time is often tied to the overall success of the biomaterial [15].Therefore, a method to image cells on these surfaces would facilitate better biomaterial design through the visualization of the direct cell to micro/nano-scale feature interaction.

Recently, attempts have been made to use ionic liquid (IL) treatments to image biological cells in the SEM. Specifically, room temperature ionic liquids (RTIL) have the unique properties of high conductivity along with minimal vapour pressure [16]. This combination of properties allows RTIL to be used in lieu of conventional metal coatings for non-conductive samples. Of particular interest is their usage for providing a conductive layer for biological samples while in liquid form. On a macro scale, imaging of living ticks was made possible using RTIL treatment as the process was aided by wild ticks being resistant to vacuum pressure [17]. Other researchers have utilized RTIL purely as an alternative to metal sputter coating [18], [19] while others have used RTIL to image living bacterial cells and red blood cells with SEM[20], [21]. While these studies have shown the capacity to image cells they have often been limited to single endpoint studies on non-complex substrates with simple organisms such as bacteria. Additionally, some of these studies have examined cells that were already fixed or dehydrated. Of importance for biological cells and medical devices are the interactions that occur at the cell-substrate interface.

This work utilized RTIL treatment to image mammalian cells with respect to sub-micron surface features using SEM. The cells were imaged under SEM and subsequently evaluated using biochemical assays and light microscopy to confirm cellular viability following both RTIL treatment and SEM imaging. The minimal vapour pressure of the IL combined with low-vacuum imaging facilitates imaging of cells under liquid conditions which are more representative of the native cellular environment. This paper demonstrates RTIL treatment can facilitate imaging of cells in liquid conditions in the SEM.

Materials and Methods

Titanium Sample Preparation

Grade 2, commercially pure, titanium was cut using a lathe and blade setup to produce disks with a diameter of 15 mm and a thickness of 1.25 mm. Titanium disks were polished using a 4 step procedure in which the titanium was exposed, in order, to silicon carbon sandpaper, 9 μm and 3 μm diamond polishing suspensions, and for final polishing a colloidal silica suspension (OPS) mixed with 10% H_2O_2. Laser modified disks were prepared using a Yb:KGW femtosecond laser as outlined in previous work [22]. All disks were ultrasonically cleaned for 15 minutes in both ethanol and acetone. Titanium disks were scratched using a dremel tool to create distinct features to allow for tracking of cell migration.

Cell Culturing and Metabolism

Saos-2, osteosarcoma, cells (ATCC ®) were grown in McCoy's 5A modified media (Life Technologies Inc.) with 15% fetal bovine serum (Life Technologies Inc.) and 1% penicillin/streptomycin (Sigma-Aldrich). Cells were incubated at 37oC with 5% CO2. Cells were seeded on the titanium samples while placed in 12-well plates and allowed to adhere for 1 day before imaging. For longer term viability experiments, the media was exchanged every day following cell metabolism experiments.

Scanning Electron Microscope Imaging using RTIL

The RTIL process is highlighted schematically in Figure 5-1A. Media was removed from wells containing samples and was replaced with a 5% ionic liquid solution (in Mccoy's 5A modified media). The ionic liquid used was 1-Ethyl-3-methylimidazolium tetrafluoroborate (Sigma-Aldrich). The ionic liquid solution was left in the well for 5 minutes before being aspirated after which samples were removed from the well plate and dried gently on both sides. Samples were then mounted on to 6 inches in diameter SEM stubs using carbon tapes and then placed in the SEM.
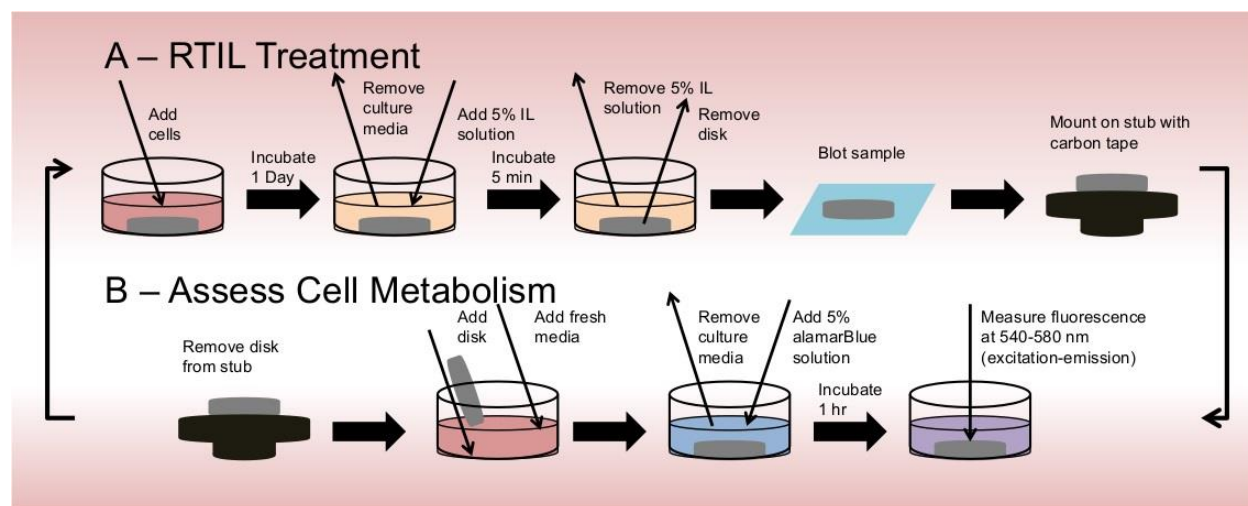

Figure 5-1. Schematic demonstrating the method used in this paper. A) Preparation of samples for imaging. B) Evaluation of cell metabolism following imaging in SEM.

A TESCAN VPSEM (Tescan, Czech Republic) was operated under two different conditions. Primarily, the SEM was operated in low-vacuum mode using a backscattered electron detector using an accelerating voltage of 10kV. For specific experiments the SEM was also operated under traditional vacuum and utilized secondary electron acquisition. Samples were imaged for no longer than 30 minutes at a time, no more than three times a day. In between experiments samples were kept in an incubator at 37oC and 5% CO2. All measurements from SEM images were obtained using ImageJ (National Institute of Health).

Cell Metabolism after RTIL and SEM

Cell metabolism was measured using an alamarBlue® (Life Technologies Inc.) assay. According to Figure 5-1B, following imaging under the SEM, cells were rinsed with PBS before a 5% alamarBlue solution (in Mccoy's 5A media) was added to each well. The samples were incubated in the dark for 1 hour at 37°C(37oC) before obtaining fluorescent readings using an Infinite ® M1000 (Tecan, Männedorf, Switzerland) at 540-580 nm (excitation-emission). Blank readings were subtracted from each data point and data was normalized by cells grown in untreated wells. In non-endpoint studies, following fluorescent reading, the alamarBlue solution was removed and replaced with media and samples were placed back in the incubator at 37oC with 5% CO2. These samples would subsequently be treated with RTIL and imaged using SEM at a later date.

Cell Viability after RTIL, SEM and cell metabolism

To determine long-term viability of the cells following both ionic liquid treatment and SEM imaging, cells were detached from titanium samples using trypsin in 0.25% EDTA (Sigma–Aldrich) as per ATCC guidelines and deactivated with media after detachment was observed. Cells were then re-plated on to tissue culture 12-well plates and allowed to grow on the plates. Some samples, prior to imaging, were stained with a Nile Red stain (ThermoFisher Scientific). A solution of 10 mL PBS and 10 µL (µL) Nile Red was added to the replated cells and left to incubate for 10 minutes before being removed. Images of the cells were taken using an Olympus IX51 Inverted microscope (Olympus, United States of America).

Results and Discussion

Initial treatments of the cells with the RTIL, growing in tissue culture plates, was determined to be overall non-toxic to cells as cells were able to grow and proliferate following IL treatment (Figure 5-2). There were no statistically significant differences ($p < 0.05$) in cell metabolism (Fig 5-2 A) between cells that were RTIL treated and this is qualitatively visible in the stained cells that were incubated following initial RTIL treatment (Fig 5-2 B/C). While some RTIL have shown various degrees of toxicity towards cells, these results demonstrate that 1-Ethyl-3-methylimidazolium tetrafluoroborate in the quantities and approach used in this work is non-toxic to Saos-2 cells.
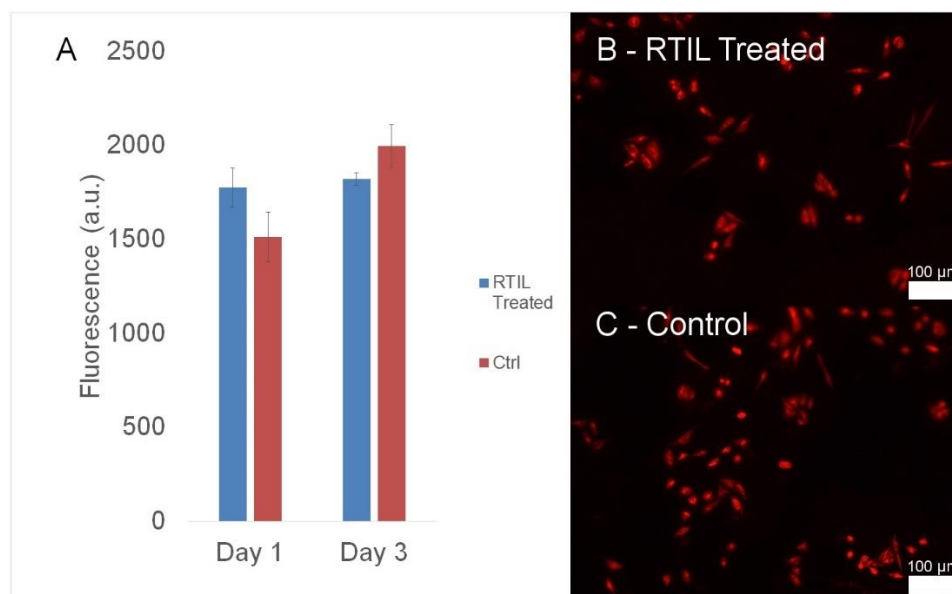
Figure 5-2. Cell metabolism data for cells, plated on 12 well plates that were either exposed to RTIL for 5 minutes or unaltered. There was no statistically significant ($p < 0.05$) difference in cell metabolism of treated and non-treated cells (A). Cells were stained with Nile Red after 3 days and show comparable morphology in RTIL compared to control treatments.

The ability to visualize cells adhered to opaque materials with sub-micron features is a specific niche that can only be solved with electron microscopy. Cells adhered to titanium substrates with and without sub-micron features are observed with SEM in Figure 5-3. Numerous cells can be seen with an elongated morphology which is indicative of their viability when placed in the microscope. Additionally, the RTIL treatment also provides some contrast, even in backscattered mode, as the RTIL becomes trapped in the sub-micron features which allows for the generation of some topographical contrast. This pooling of has been noted in other work with RTIL and has been speculated to be a result of variations in viscosity of the solution [19]. Fixation or dehydration protocols could also be used in a manner but would result in the imaging of dry samples and timeline for those techniques is in the hours to days range compared to RTIL treatment which takes minutes. While low magnification images reveal confluent or highly concentrated areas (Fig 5-3A/B), the higher magnification images (Fig 5-3C/D) show that cells may be interacting with the sub-micron features. While low-vacuum backscattered imaging was utilized for all imaging in this work, there are pros and cons to utilizing other imaging modes such as secondary electron imaging or high-vacuum ESEM. Studies have shown that radiation damage was greater in the low-vacuum mode, but general cell viability was noted worse in high-vacuum methods [23]. The difference in vapour pressures in the high-vacuum ESEM were believed to contribute to a large driving force for mass transfer of water out of cells [24], [25]. Conversely, low-vacuum has an increased concentration of water molecules which have been shown to increase the rate of specimen degradation [24], [25]. Therefore, in this study we have used a combination of low-vacuum along with RTIL treatment to enable cell imaging with minimal damage to the cells.
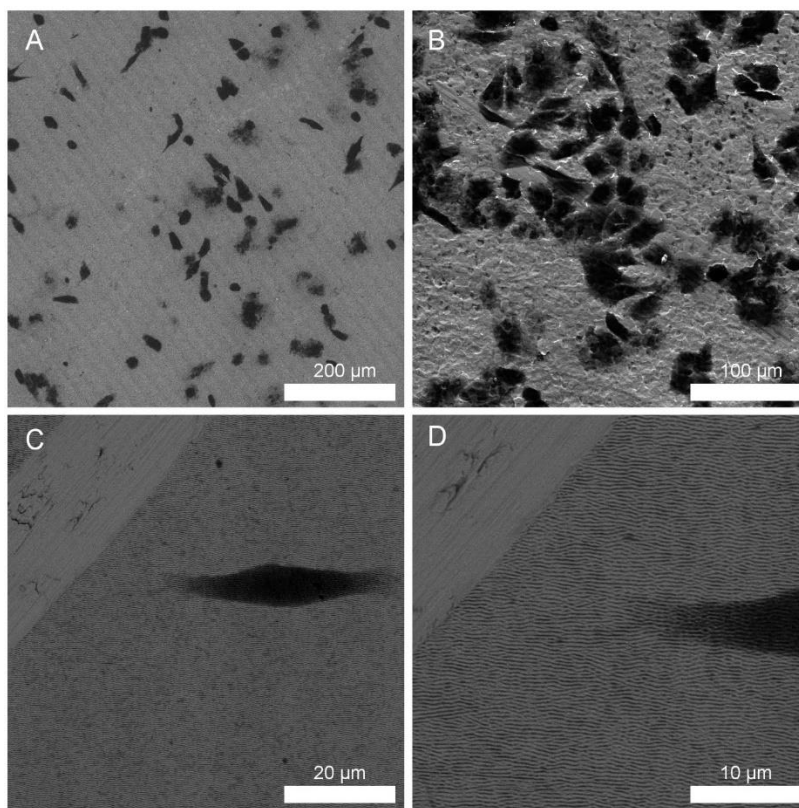
Figure 5-3. Cells adhered to titanium substrates after 5 minutes of ionic liquid treatment. Cells can be observed across the entire substrate (A/B) and in detail with respect to sub-micron features (C/D).

Table 5-1. Cell to cell and scratch to cell measurements taken in ImageJ demonstrating how the cells have migrated across the laser modified surface over time. Cell metabolism readings indicate that cells are healthy after multiple IL treatments and multiple SEM sessions. (1) – scratch to close cell, (2) – scratch to far cell, (3) – cell to cell correspond to measurements indicated in Figure 4.

Substrate	Time Point	(1) - Scratch to Close Cell (µm)	(2) - Scratch to Far Cell (µm)	(3) - Cell to Cell (µm)	Cell Metabolism (a.u.)
LIPSS Titanium	Day 1	3.6	42.3	22.9	736
	Day 3	4.8	43.4	26.1	742
	Change	1.2	1.1	3.2	N/A
Unmodified Titanium	Day 1	98.5	177.1	33.9	740
	Day 3	98.5	177.1	34.1	686
	Change	0	0	0.2	N/A

The adhesion of cells along the surfaces of biomaterials is essential to understand cell-material interactions. Here, cells were seeded on titanium substrates with laser induced periodic surface structures (LIPSS) [22] and visualized after 1 (Figure 5-4A) and 3 (Figure 5-4B) days. From previous work, it was determined that these laser modified surfaces have periodicities between 300

and 620 nm with an average roughness of 145 nm [22]. Tracking the position of the same cells over multiple days was possible because of the large, macroscale scratches that were applied with a dremel tool. However, in theory, any consistent macroscale feature could be utilized to aide in the tracking of cells, be it naturally occurring in the material or artificially added. The cells remained intact and viable from 1 to 3 days as per corresponding cell metabolism readings (Table 5-1). The differences in cell position may be too small to be considered meaningful and are likely imaging artifacts. Subsequent viability experiments indicate that cell death occurred for the cells exposed directly to the electron beam following RTIL treatment and being placed in the SEM. It is notable that the cells appear identical in shape and location in micrographs up to 3 days following initial RTIL treatment and SEM irradiation at 1 day and then a subsequent repeat at 3 days. This demonstrates that while the cells may no longer be viable, their location and shape remain intact and thus this quick treatment can be used multiple times on the same sample. A major concern of utilizing electron microscopy to image biological materials is the risk of irreversible damage to the cells. As such, following RTIL treatment and SEM imaging, cells were detached from their titanium substrates and re-plated on to tissue-culture plates to confirm that the cells maintained their phenotype. Figure 5 shows cells imaged with an inverted light microscope 1 (Figure 5-5 A) and 3 (Figure 5-5 B/C) days following re-plating. These images show adhered cells with an elongated morphology which demonstrates that the cells grow and proliferate under typical cell culture conditions following repeated RTIL treatment and SEM imaging. Figure 5-5C shows cells that were stained by Nile Red, a dye that stains lipids [26], [27]. The cell membrane and numerous organelles have lipid bilayers which would have been ruptured if damage from the electron beam or the vacuum was fatal [1]. The cells are well stained with the membranes visibly intact suggesting that damage from this procedure was minimal or negligible. This confirms that while directly irradiated cells were rendered unviable, cells in the periphery or those that were only briefly irradiated were not altered by RTIL treatment or by SEM imaging. This is confirmed by the cell metabolism readings (Table 5-1) observed after 1 and 3 days which show that the overall viability of the surrounding cells is unaltered. Previous work on cells adhered to LIPSS titanium identified that cells tended to be adhered perpendicular to the alignment of the LIPSS [22] but this study using RTIL treatment did not observe the same mechanisms (Fig 5-S1). This questions the validity of cell orientation findings after being subjected to rigorous sample preparation protocols and required further investigation of which processing method provides the best representation of cell alignment. The cells observed in previous work [22], and shown in chapter 4, were prepared using a lengthy sample preparation process involving fixation, dehydration, staining and coating and thus it is possible that only certain cells remained properly attached to the LIPSS following the sample preparation steps. The simpler process of RTIL treatment, however, presents an advantage over more traditional biological SEM sample preparation as cells are still in liquid conditions and are not fixed or dehydrated. Further improvements to biological imaging in the SEM could achieved via software implemented rastering protocols, as shown in beam irradiation studies of epoxy resin [28].
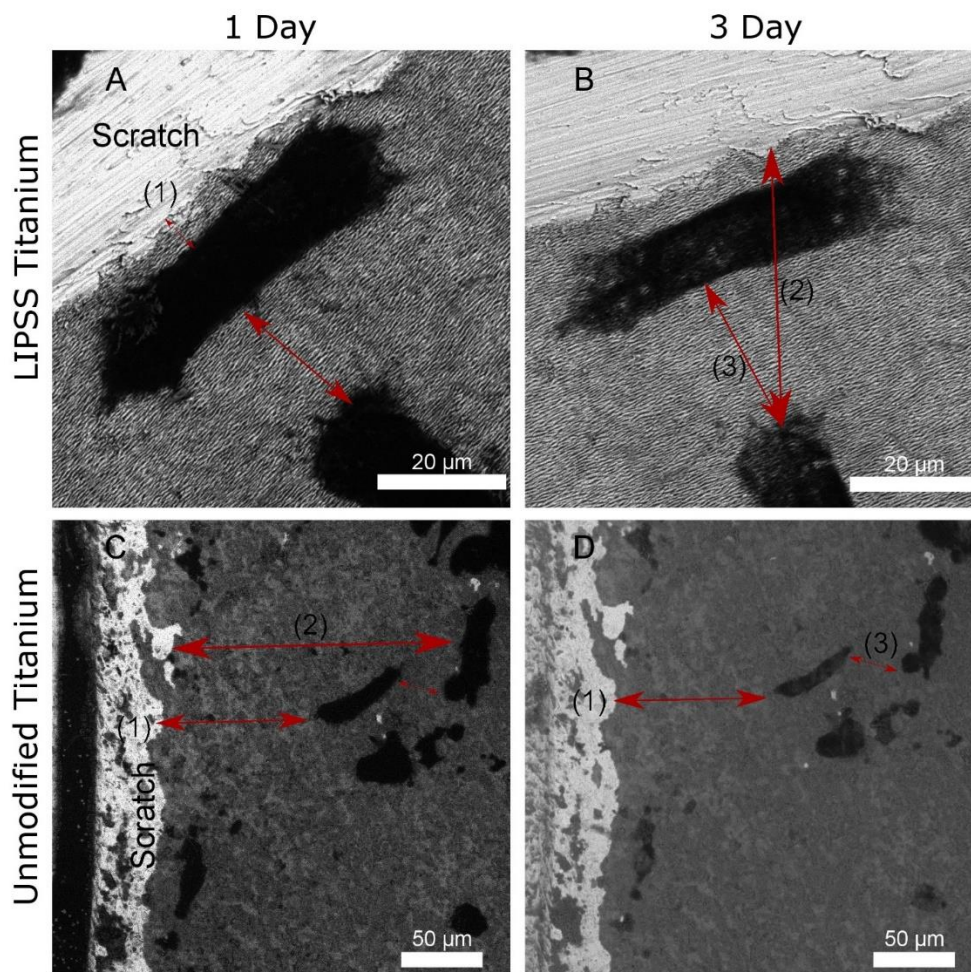
Figure 5-4. Demonstration of cells visualized on laser ablated (A/B) and unmodified (C/D) titanium observed using SEM with ionic liquid treatment alongside correlated fluorescent cell metabolism readings. The difference in position of the cells in (A/C) compared to (B/D) show how the cells are unchanged in shape or location following multiple SEM irradiations sessions and RTIL treatments. (1) – scratch to close cell, (2) – scratch to far cell, (3) – cell to cell.

The compatibility of biomaterials is highly associated with cellular adhesion and migration along their surfaces. While this work has demonstrated the capacity for imaging of wet cells on a metallic substrates, the RTIL treatment developed for mammalian cells can be expanded more broadly to other cell-surface applications that require wet conditions, such as to understand cell interactions with three-dimensional scaffolds, or to monitor the effect of pharmaceuticals on cells, for example. Examination of the specific interactions of cells with micro to nanostructured surfaces will contribute to information essential to the design of future biomaterials, drug-delivery platforms, and tissue engineered scaffolds.
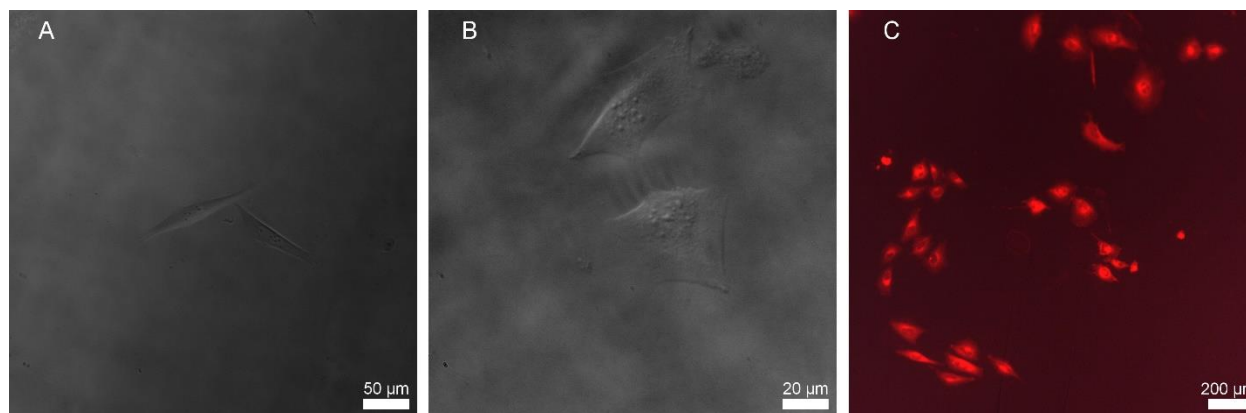
Figure 5-5. Demonstration of the viability of cells following RTIL treatment and imaging, in low-vacuum mode, in the SEM. Cells appear elongated which is indicative of cellular viability following treatments. Cells were detached from titanium substrates with trypsin and re-plated into empty 12 well plates. Cells were imaged 1 (A) and 3 (B/C) days after replating. (C) shows cells that were stained by Nile Red, a lipid stain.

This work presents a new RTIL treatment to facilitate imaging of wet mammalian cells in the SEM. More importantly, this work demonstrates the power of using these treatments to evaluate cell adhesion to sub-micron features. Cell migration along surfaces is an example of a phenomenon that requires equal attention to both the cells and the surface itself, and, herein, we have demonstrated a method to image both with the nanometer resolution afforded by SEM. This technique can fill an important niche providing sub-diffraction limit resolution for both cells and their interfacing surfaces.

Acknowledgements

Conflicts of Interest

The authors declare no conflict of interest.

References

[1]   N. de Jonge and D. B. Peckys, "Live Cell Electron Microscopy Is Probably Impossible," ACS Nano, vol. 10, no. 10, pp. 9061–9063, 2016.
[2]   N. de Jonge and F. M. Ross, "Electron microscopy of specimens in liquid," Nat. Nanotechnol., vol. 6, no. 11, pp. 695–704, 2011.
[3]   L. Muscariello et al., "A critical overview of ESEM applications in the biological field," J. Cell. Physiol., vol. 205, no. 3, pp. 328–334, 2005.

[4]   K. J. McKinlay et al., "Comparison of environmental scanning electron microscopy with high vacuum scanning electron microscopy as applied to the assessment of cell morphology.," J. Biomed. Mater. Res. A, vol. 69, no. 2, pp. 359–366, 2004.

[5]   R. E. Thach and S. S. Thach, "Damage to Biological Samples Caused by the Electron Beam during Electron Microscopy," Biophys. J., vol. 11, no. 2, pp. 204–210, 1971.

[6]   B. Huang, M. Bates, and X. Zhuang, "Super resolution fluorescence microscopy," Annu. Rev. Biochem., vol. 78, pp. 993–1016, 2010.

[7]   C. Morrison, R. Macnair, C. Macdonald, A. Wykman, I. Goldie, and M. H. Grant, "in-Vitro Biocompatibility Testing of Polymers for Orthopedic Implants Using Cultured Fibroblasts and Osteoblasts," Biomaterials, vol. 16, no. 13, pp. 987–992, 1995.

[8]   U. Reich et al., "Differential fine-tuning of cochlear implant material-cell interactions by femtosecond laser microstructuring," J. Biomed. Mater. Res. - Part B Appl. Biomater., vol. 87, no. 1, pp. 146–153, 2008.

[9]   R. Solmi et al., "Interactions of fibroblasts with soldered and laser-welded joints," Biomaterials, vol. 25, no. 4, pp. 735–740, 2004.

[10]   K. Gulati et al., "Anodized 3D – printed titanium implants with dual micro- and nano-scale topography promote interaction with human osteoblasts and osteocyte-like cells," no. December 2016, pp. 3313–3325, 2017.

[11]   D. Uppalapati, B. J. Boyd, S. Garg, J. Travas-sejdic, and D. Svirskis, "Biomaterials Conducting polymers with de fi ned micro- or nanostructures for drug delivery," Biomaterials, vol. 111, pp. 149–162, 2016.

[12]   R. M. Streicher, M. Schmidt, and S. Fiorito, "Nanosurfaces and nanostructures for artificial orthopedic implants," no. July, 2014.

[13]   Z. Ma, D. Ph, M. Kotaki, D. Ph, and R. Inai, "Potential of Nanofiber Matrix as Tissue-Engineering Scaffolds," vol. 11, no. 1, 2005.

[14]   M. Goldberg, R. Langer, and X. Jia, "Nanostructured materials for applications in drug delivery and tissue engineering," vol. 5063, 2012.

[15]   A. Hunter, C. W. Archer, P. S. Walker, and G. W. Blunn, "Attachment and proliferation of osteoblasts and fibroblasts on biomaterials for orthopaedic use," Biomaterials, vol. 16, no. 4, pp. 287–295, 1995.

[16]   T. Tsuda et al., "SEM observation of wet biological specimens pretreated with room-temperature ionic liquid," ChemBioChem, vol. 12, no. 17, pp. 2547–2550, 2011.

[17]   Y. Ishigaki et al., "Observation of live ticks (haemaphysalis flava) by scanning electron microscopy under high vacuum pressure," PLoS One, vol. 7, no. 3, pp. 2–7, 2012.

[18]   A. Dwiranti et al., "Chromosome observation by scanning electron microscopy using ionic liquid," Microsc. Res. Tech., vol. 75, no. 8, pp. 1113–1118, 2012.

[19]   Y. Ishigaki et al., "Comparative study of hydrophilic and hydrophobic ionic liquids for observing cultured human cells by scanning electron microscopy," Microsc. Res. Tech., vol. 74, no. 12, pp. 1104–1108, 2011.

[20]   C. Takahashi, N. Ogawa, Y. Kawashima, and H. Yamamoto, "Observation of antibacterial effect of biodegradable polymeric nanoparticles on Staphylococcus epidermidis biofilm using FE-SEM with an ionic liquid," Microscopy, vol. 64, no. 3, pp. 169–180, 2015.

[21]   A. Hyono et al., "SEM observation of the live morphology of human red blood cells under high vacuum conditions using a novel RTIL," Surf. Interface Anal., vol. 46, no. 6, pp. 425–428, 2014.

[22]   B. E. J. Lee, H. Exir, A. Weck, and K. Grandfield, "Characterization and evaluation of femtosecond laser-induced sub-micron periodic structures generated on titanium to improve osseointegration of implants," Appl. Surf. Sci., vol. 441, pp. 1034–1042, 2018.

[23]   Y. Ren, A. M. Donald, and Z. Zhang, "Investigation of the morphology, viability and mechanical properties of yeast cells in environmental SEM," Scanning, vol. 30, no. 6, pp. 435–442, 2008.

[24]   S. Kitching and A. M. Donald, "Beam damage of polypropylene in the environmental scanning electron microscope: An FTIR study," J. Microsc., vol. 190, no. 3, pp. 357–365, 1998.

[25]   C. P. Royall, B. L. Thiel, and A. M. Donald, "Radiation damage of water in environmental scanning electron microscopy," J. Microsc., vol. 204, no. January, pp. 185–195, 2001.

[26]   P. Greenspan, E. P. Mayer, S. D. Fowler, P. Greenspan, E. P. Mayer, and S. D. Fowler, "Nile Red A Selective Fluorescent Stain for Intracellular Lipid Droplets_Greenspan_1985.pdf," vol. 100, no. 3, pp. 965–973, 1985.

[27]   A. R. Jones et al., "Type 1 diabetes alters lipid handling and metabolism in human fibroblasts and peripheral blood mononuclear cells," PLoS One, vol. 12, no. 12, pp. 1–16, 2017.

[28]   W. Zhang, L. G. D. A. Melo, A. P. Hitchcock, and N. Bassim, "Electron beam damage of epoxy resin fi lms studied by scanning transmission," Micron, vol. 120, no. February, pp. 74–79, 2019.
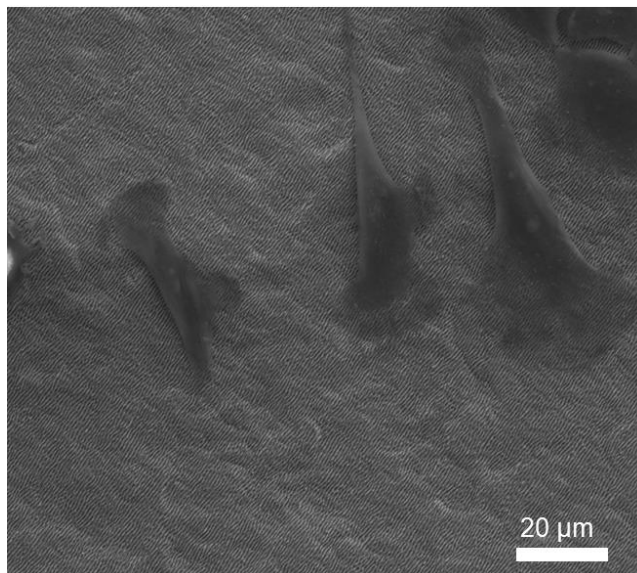
Supplementary Information

Figure 5-S1: Example of cells adhered perpendicular to the LIPSS pattern. Cells adhered to LIPSS titanium, and visualized via traditional SEM sample preparation, tended to be adhered perpendicular to the LIPSS pattern.

Chapter 6: Conclusion

Knowledge of the mechanisms occurring at both sides of the bone-biomaterial interface is essential to improve the understanding of osseointegration. This thesis reveals how identifying the structure of bone can be used as inspiration to design biomaterials and leads to new methods of characterizing said designs. This work demonstrated how the mineralized collagen fibril, the bone building block, contains both intra- and extrafibrillar mineralization. Next, using this knowledge a biomaterial with a periodicity inspired from the natural periodicity of collagen was designed and evaluated for its ability to influence cell adhesion. This design involved submicron scale structures and a room temperature ionic liquid treatment was developed to allow for visualization of these structures and biological cells under the scanning electron microscope (SEM) simultaneously. Therefore, this thesis utilized advanced microscopy techniques alongside biomaterials synthesis and development of new characterization methods to provide a framework for improved biomaterials design.

Key Findings and Contributions

(i) Evidence of Intra- and Extrafibrillar Mineralization in In Vivo Mineralized Collagen Fibrils
In Chapter 3, visualization of mineralized collagen fibrils confirmed existing theories of collagen mineralization by demonstrating both intra- and extrafibrillar mineralization. Collagen fibrils were identified to have a right-handed helical motif while mineral was identified, elementally, to be present both inside and outside the collagen fibril. This helps corroborate the conflicting existing theories of intra- and extrafibrillar mineralization. Localization of clusters of Ca/P with differing ratios indicates that the mineral within bone varies with proximity to the collagen fibril. This work is also the first time leporine bone was visualized using the atom probe microscope along with the largest reported datasets for any type of bone using atom probe tomography. This demonstrates that APT is a powerful tool for facilitating analysis of bone ultrastructure and mineral chemistry.

While this investigation may seem disconnected from the following two investigations on the modification and evaluation of biomaterials, this work is critical to optimize design of bioinspired biomaterials. For example, this study by APT emphasized the organization of collagen fibrils with 3D winding structures and developed an approach to model their pitch. While biomaterials investigated later in the thesis in Chapter 4 and 5 focused on 2.5D structures mimicking the organization of collagen on larger length scales, which is not representative of the true structure of collagen now unveiled in this work. The process of analyzing bone and then using that analysis to inform biomaterials design should be extended with these new findings, for example by using the new information provided by APT to design biomaterials inspired by the 3D winding collagen fibrils. For example, biomaterials could be designed to accommodate this geometry by utilizing laser modification methods in combination with additive manufactured materials to create helical structures more similar to collagen. In addition, chemical modifications to mimic the segregation of inorganic components of bone, as found in this work by APT, could be incorporated as well.

Using these further novel methods of designing bone-interfacing biomaterials like this would subsequently require advanced methods of evaluating biomaterials, as presented in Chapter 5, and the cycle of using characterization to inform design continues.

(ii) Submicron Laser Patterning on Titanium Inspired by the Natural Periodicity of Collagen
In Chapter 4, a femtosecond laser was used to generate reproducible and consistent submicron surface features on titanium. Three different submicron scale LIPSS periodicities were generated on titanium, bioinspired by the banding pattern of collagen. The laser ablation was observed to increase roughness and oxide layer thickness without damage to the native titanium crystal structure. These features are among the smallest generated via laser ablation to date and showed improved cellular responses compared to control surfaces. The improved response of the 620 nm periodicity compared to other surfaces indicates that there is an optimal size for LIPSS features on titanium. Additionally, cells were observed to be oriented perpendicular to these LIPSS features which has implications for guiding cell migration and adhesion. The generation and effectiveness of submicron features described here demonstrate how innovation in biomaterial topography can be achieved with bioinspiration.

(iii) Simultaneous Visualization of Wet Cells and Submicron Substrate Features
In Chapter 5, a room temperature ionic liquid treatment was developed for visualizing wet cells and biomaterials with submicron surface structures simultaneously. This RTIL treatment was determined to be non-cytotoxic to cells. The combination of using this treatment for cells on micro- or nanopatterned substrates allows for rapid identification of the specific location where cells adhere to and where their processes attach to. Evaluation of these cells using cell metabolism and cell stains show that while there is some damage to cells by the electron beam or vacuum, the majority of cells are still viable following treatment. This facile technique does not compromise cells unlike typical fixation or dehydration routines and thus the visualized cells are more representative of their native structure. The development of this technique allows for the bridging of biomaterials with cell microscopy at the smallest length scales. This may have great use in the evaluation of biomaterials with respect to nanoscale cell-biomaterial interactions.

Future Work
(i) Intra- and Extrafibrillar Mineralization
Chapter 3 provided strong evidence for intra- and extrafibrillar mineralization, however, individual mineral platelets were not observed. These nanoscale platelets of hydroxyapatite are known to be within the collagen-mineral composite [1]. The solution to this problem is to improve APT reconstructions. The first method is to improve correlative methods between APT and STEM tomography. Correlation between the two has been attempted but primarily with conductive materials such as steels [2], [3]. STEM tomography could be used to match features such that they are reconstructed faithfully in APT. Another improvement to be made is with the acquired APT dataset. For heterogenous materials such as bone, the resolution of the mass spectra is not ideal which leads to reduced detector efficiency and difficulty in identifying all evaporated species [4].

Variations in sample preparation, such as coatings, need to be considered to attempt to improve the conductivity of the samples and thus the overall data quality. Diseased and compromised bone could also be evaluated using atom probe tomography which could lead to novel methods of designing bone-interfacing biomaterials.

(ii) Replication of Collagen Banding with Laser Ablation
In Chapter 4, it was possible to mimic the banding of collagen with LIPSS, but the features were not small enough to fully replicate the structure of collagen. However, the generated structures had a 300 nm periodicity at smallest compared to the 67 nm periodicity in collagen. This will require technical innovation with laser design to achieve periodicities much smaller than the wavelength of the laser used. It is possible that use of periodicities closer to or matching that of native collagen could lead to improved cellular response and potentially better *in vivo* responses.

(iii) Visualize Cell Motion with Electron Microscopy
In Chapter 5, the goal of the work was to use RTIL treatments to visualize cell motion and migration on substrates with submicron surface features. This was not possible as it was determined in cell viability experiments that the cells directly irradiated by the electron beam were not viable, despite the cells on the periphery being alive. This indicated that operating in low-vacuum with the current RTIL treatment was acceptable for the cells, but the irradiation from the electron beam was too significant. Future work should look at further optimization of the RTIL treatment in concert with reduced accelerating voltages. Beam rastering algorithms also have potential for reducing overall beam damage [5]. Additionally, use of the RTIL in concert with *in situ* liquid enclosures in the SEM might improve image quality as live cells have been maintained in the TEM but the image quality has not been ideal [6].

References

[1]   P. Fratzl, H. S. Gupta, E. P. Paschalis, and P. Roschger, "Structure and mechanical quality of the collagen – mineral nano-composite in bone," J. Mater. Chem., vol. 14, no. 14, pp. 2115–2123, 2004.

[2]   Y. Toji, H. Matsuda, M. Herbig, P. Choi, and D. Raabe, "Atomic-scale analysis of carbon partitioning between martensite and austenite by atom probe tomography and correlative transmission electron microscopy," Acta Mater., vol. 65, pp. 215–228, 2014.

[3]   M. Herbig, P. Choi, and D. Raabe, "Combining structural and chemical information at the nanometer scale by correlative transmission electron microscopy and atom probe tomography," Ultramicroscopy, vol. 153, pp. 32–39, 2015.

[4]   M. K. Kelly, T. F., & Miller, "Atom probe tomography," Rev. Sci. Instrum., vol. 78, no. 3, p. 31101, 2009.

[5]   W. Zhang, L. G. D. A. Melo, A. P. Hitchcock, and N. Bassim, "Electron beam damage of epoxy resin fi lms studied by scanning transmission," Micron, vol. 120, no. February, pp. 74–79, 2019.

[6]   D. B. Peckys and N. de Jonge, "Visualizing Gold Nanoparticle Uptake in Live Cells with Liquid," Nano Lett., vol. 11, pp. 1733–1738, 2011.

Appendix 1: Identification of Collagen Fibrils in Cross Sections of Bone by Electron Energy Loss Spectroscopy (EELS).

Lee, B. E.J., Luo, L., Grandfield, K., Andrei, C. M., & Schwarcz, H. P. (2019). Identification of collagen fibrils in cross sections of bone by electron energy loss spectroscopy (EELS). *Micron*, 102706.

This paper provides insight into the ongoing debate regarding the visualization of mineralized collagen fibrils. Bovine bone was visualized in cross-section by sectioning normal to the long axis using two different methods: ion-milling and ultramicrotome. Samples were placed in the TEM and electron energy loss spectroscopy (EELS) was used to provide chemical compositional maps. Carbon and nitrogen were found in bonding states similar to those observed in collagen in ultramicrotomed but not ion-milled samples. This work showed that ion-milling techniques are damaging to bone samples and may have contributed to some misinterpretation of cross-sectionally viewed features in bone. This work is a complementary to my study of bone structure in this thesis. I conducted all the EELS data analysis and because of my findings wrote the second draft of the manuscript. Lucy Luo prepared samples and conducted experiments with Carmen Andrei. The manuscript was edited by Henry Schwarcz and Kathryn Grandfield. This paper has been published in Micron.

Contents lists available at ScienceDirect

Micron

journal homepage: www.elsevier.com/locate/micron
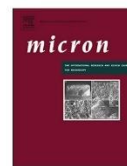
Tutorial

Identification of collagen fibrils in cross sections of bone by electron energy loss spectroscopy (EELS)

Bryan E.J. Lee[a], Lucy Luo[b], Kathryn Grandfield[a,c], Carmen M. Andrei[d], Henry P. Schwarcz[a,e,*]

[a] School of Biomedical Engineering, McMaster University, Hamilton, ON, L8S 4L7, Canada
[b] Bachelor of Health Sciences (BHSc) Program, McMaster University, Hamilton, ON, L8S4L8, Canada
[c] Dept. of Materials Science and Engineering, McMaster University, Hamilton, ON L8S 4L7, Canada
[d] Canadian Centre for Electron Microscopy, Hamilton, ON, L8S 4M1, Canada
[e] School of Geography and Earth Sciences, McMaster University, Hamilton, ON, L8S 4K1, Canada

A B S T R A C T

Transmission electron microscopic (TEM) images of ion-milled bovid cortical bone cut approximately normal to the axes of fibrils show that mineral occurs in the form of plates surrounding and laying between circular or elliptical features about 50 nm in diameter. The classification of these features as either pores or collagen fibrils is highly debated. Electron energy loss spectroscopy (EELS) mapping of these features in ion milled sections shows that they are lacking significant amounts of mineral or collagen, although their appearance suggests that they are cross sections of collagen fibrils. However, analogous sections prepared using an ultramicrotome show that, while these circular features show reduced concentrations of calcium and phosphorus, some of them contain quantities of carbon and nitrogen in bonding states comparable to the composition of collagen. This work demonstrates that the observed circular features are sections of collagen fibrils, but that bombardment by argon ions during broad beam ion milling destroys the collagen and associated gap-zone mineral.

1. Introduction

Bone is a composite material in which fibrils about 50 nm in diameter, bundles of triple helices of collagen, are spatially associated with an approximately equal volume of apatite mineral. The crystals of mineral are widely believed to occur inside gaps between the C and N termini of collinear collagen molecules inside the fibrils (Alexander et al., 2012; Landis and Song, 1991; McEwen et al., 1991; Weiner et al., 1991). In transmission electron microscopic (TEM) studies of ion-milled sections of bone we have shown, however, that most of the mineral in bone occurs in the form of discrete, elongated, and plate-like mosaics of apatite crystals which surround and lie between the fibrils. We have previously described these plates as "mineral lamellae" (Grandfield et al., 2018; Schwarcz, 2015a). In bone sections cut parallel to the long axis of long bones, the fibrils are recognizable by the presence of gap and overlap zones spaced every 67 nm along the fibril (Fig. 1). Mineral lamellae and fibrils can be seen in ion-milled and focused ion beam (FIB) sections of bone and dentine (Cressey and Cressey, 2003; Jantou-Morris et al., 2010; Jantou et al., 2009; McNally et al., 2012; Nalla et al., 2005; Srot et al., 2012; Tertuliano and Greer, 2016), but are not readily observable in ultramicrotome prepared sections of bone. This is

believed to be a consequence of the diamond knife fracturing the brittle mineral lamellae (Jantou et al., 2009; McNally et al., 2012; Schwarcz, 2015b; Srot et al., 2012).

When viewed in cross section, it is more difficult to identify the presence of collagen fibrils since the sections are cut normal to the distinctive gap/overlap zones and collagen itself has a low average atomic number leading to very low contrast in TEM images. However, all cross sections of cortical bone display a characteristic "lacy" appearance (Grandfield et al., 2018; McNally et al., 2012; Reznikov et al., 2014a) (Fig. 2). Mineral plates surround what appear to be holes which can appear circular, elliptical or irregular in shape. Some of the "holes" appear to be partially or completely filled with material which exhibits even lower electron contrast than the lowest-contrast areas of longitudinal sections. The "holes" are typically between 50 and 70 nm across, which is in agreement with known dimensions of collagen fibrils in bone (Katz and Li, 1973). Note that sections of the same bone sample, when viewed on a plane oriented at 90^0 to these sections, clearly display the presence of collagen fibrils (McNally et al., 2012). Therefore, fibrils must be present somewhere in these cross sectional images and it seems possible that they were present in these circular features. McNally et al., (2012) suggest that the absence of material in many of
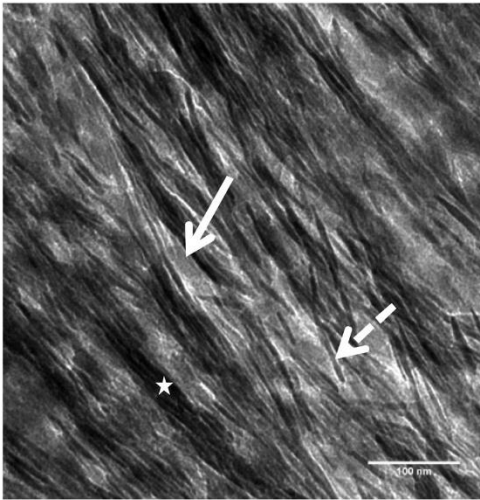

Fig. 1. Bright field transmission electron microscopy (BF-TEM) image of an ion milled section of bone cut parallel to the long axis of the femur of a mature cow. The characteristic gap-zone of collagen is readily observable along with what the authors define as a mineral lamellae. Solid arrow: gap-zone marked by higher electron density (darker); Dashed arrow: single mineral lamella; Star: stack of mineral lamellae, viewed edge-wise. Scale = 100 nm.

Fig. 2. BF-TEM image of an ion milled transverse section of a cow femur. Solid arrow: hole representing a possible site of collagen fibril; Dashed arrow: stack of multiple (~6) mineral lamellae, viewed edgewise; Star: lower electron density material, partially filling a hole. Scale = 100 nm.

these features is due to erosion of the softer collagen by the beam of Ar^+ ions used to thin the section during broad beam ion milling. A similar proposal was made by Jantou et al. (2009) to account for the absence of material in holes observed in FIB sections of dentine and proposed that these features were sections of collagen fibrils. They noted that weakly electron-dense material was present in similar shaped features seen in ultramicrotome-cut sections of the same material. Conversely, Reznikov et al. (2014a, 2014b) have described the holes or circular features as devoid of material and are a consequence of viewing collagen from an oblique angle.

Here we attempt to demonstrate that these hole-like features are in fact cross-sections of collagen fibrils by analyzing the material in these features using electron energy loss spectroscopy (EELS). By evaluating the presence and bonding states of carbon and nitrogen in these features, we can determine whether collagen is present or not. EELS analyses have been carried out previously on bone sections cut parallel to the long axis and mineralized turkey tendon by Kłosowski et al. (2015, 2017, 2018). They show spectra for C and N K-edges in bone and note the presence of discrete peaks which represent the bonding states characteristic of collagen. Wang et al. (2018) also studied the C and N signals of bone with EELS in a correlative study of biomineralization.

2. Methods

2.1. Sample Preparation by Ion Milling

A section of the cortex of the femoral diaphysis of a mature cow (*Bos taurus*) was obtained from a frozen specimen. The sample was defatted in a 3:1 mixture of chloroform/methanol overnight and subsequently dehydrated in a graded series of ethanol. Sections were cut from this block perpendicular to the long axis of the femur so that the collagen fibrils would tend to be oriented normal to the plane of the section. Sections 1 mm in thickness were cut using a water-cooled diamond wafering blade mounted in an IsoMet Low Speed Saw (Buehler). The sections were polished on both sides with 600 grit SiC papers to a final thickness of 100 μm. Discs (3 mm diameter) were cut from the 100 μm sections using a Gatan Model 601 ultrasonic disc cutter, and their centers were thinned to < 50 μm with a Gatan Model 656 dimple grinder with 3 μm diamond paste. The discs were further dimpled to < 30 μm with 1 μm diamond paste. Dimpled discs were then ion milled in a liquid nitrogen cooled Fischione 1010 ion mill until a hole was eroded in the sample. The ion mill stage was cooled to −75 °C and rotated back and forth between -90° and +90°, with a 4 mA, 4 keV Ar^+ ion beam angled 4 to 6 degrees. A 5 nm coating of amorphous carbon was applied to the ion milled sections to reduce sample charging and heating in the electron microscope.

2.2. Sample preparation by ultramicrotomy

An identical section of cow bone was embedded in Spurr's epoxy resin under vacuum for several hours and then embedded in fresh resin and polymerized in a 60° C oven overnight. Thin sections (100 – 150 nm) were cut with a diamond knife on a Leica UCT ultramicrotome and picked up onto formvar-coated Cu grids. Some of the sections were post-stained with uranyl acetate.

The presence of a thin (~10 nm) carbon coating on the ion-milled sections would contribute some uniform signal intensity to measurements of the carbon K-edge signal even in areas where no carbon was present in the sample. Additionally, the microtome-cut sections were mounted on a formvar-coated copper grid and this sample was embedded in Spurr's resin, both of which could contribute to the C K-edge signal uniformly across the entire sample. Therefore, significant point-to-point differences in the EELS C K-edge intensity and spectrum are due to the sample itself and not the grid or coating. EELS analysis of the resin showed that it did not contain detectable quantities of nitrogen, so even if present in the holes, it would not contribute a spurious N K-edge signal.

2.3. Transmission electron microscopy and EELS

BF-TEM images of all the sections were obtained on a Phillips CM12 electron microscope operated at 120 kV. Electron energy loss spectroscopy (EELS) and high-angle annular dark-field (HAADF) images were obtained using a JEOL 2010 F electron microscope equipped with a Gatan Imaging Filtering (GIF) system (Gatan Inc., Pleasanton, CA, USA) operated at 200 kV.

2

EELS spectrum images were collected in STEM mode at 200 kV with 1 nm electron probe size with a convergence semi-angle of 10 mrad and collection semi-angle was 30 mrad. Energy resolution defined by full width at half maximum (FWHM) was 1-1.2 eV using an energy dispersion of 0.3 eV/channel. The acquisition time for spectra was 0.1 s. In order to keep the acquisition short, pixel size varied from 2 to 4 nm.

Digital Micrograph (Gatan Inc., Pleasanton, CA, USA) was used for EELS analysis. Spectra were background subtracted and processed using principal component analysis (PCA). The bonding of specific elements was determined using energy-loss near-edge structure (ELNES). Colour maps were generated from elemental composition and excluded ELNES from the quantification.

3. Results

3.1. EELS spectra of ion-milled sections

HAADF images of a section cut using the ion mill resembled that shown in Fig. 2. Individual mineral lamellae surround the circular or elliptical regions ("holes") in which only patches of weakly electron-scattering material can be seen. The remainder of these hole-like features appears to be empty. One such hole is shown in a map of Ca abundance for one of these holes (Fig. 3), from which we have obtained representative EELS spectra for the C, N, Ca, and P edges.

The Ca and P signals are present in both areas, but are relatively stronger in the mineral compared to the edge of the hole. It was not possible to obtain signal for any element within the hole as it was devoid of any signal. The observed spectra for Ca and P resemble the Ca L_{2-3} and P L_{2-3} edges shown in Kłosowski et al. (2017, Supplemental

material). The carbon signal is effectively identical both in terms of bonding and intensity within the mineral and at the edge. This C edge resembles the energy-loss near-edge structure (ELNES) shown by Kłosowski et al. (2017, Supplemental material) but is much less well resolved. There is minimal to no detection of nitrogen in the sample both at the mineral and edge sampling regions. When examined extremely precisely, a singular peak of nitrogen can be observed in the mineral region only. This peak shape appears to be similar to that of elemental nitrogen but the energy resolution of this data limits the capacity of the authors to properly characterize it.

The result that no signal is detected within the hole agrees with previous observations that cross sections of fibrils in ion milled sections are too severely eroded by the ion beam to permit conclusive testing. Therefore, despite the risk of damage to the mineral lamellae, ultra-microtome-cut sections were prepared in an attempt to avoid ion-beam erosion of the collagen fibrils.

3.2. EELS spectra of microtome-cut sections

While collagen should be still present in microtome-cut sections, TEM images of such sections show (Jantou et al., 2009; McNally et al., 2012; Schwarcz, 2015b; Srot et al., 2012) that many structural features of the bone are seriously damaged by the action of the diamond blade. As a result, HAADF images of microtomed sections often lack well-defined mineral lamellae. Nevertheless, it is still possible to identify in this section cut normal to the long axis of the femur, the presence of hole-like features. Many of the holes in the microtome-cut section were empty or contained only residual patches of weakly electron-dense material. However, a few holes were largely or completely filled with
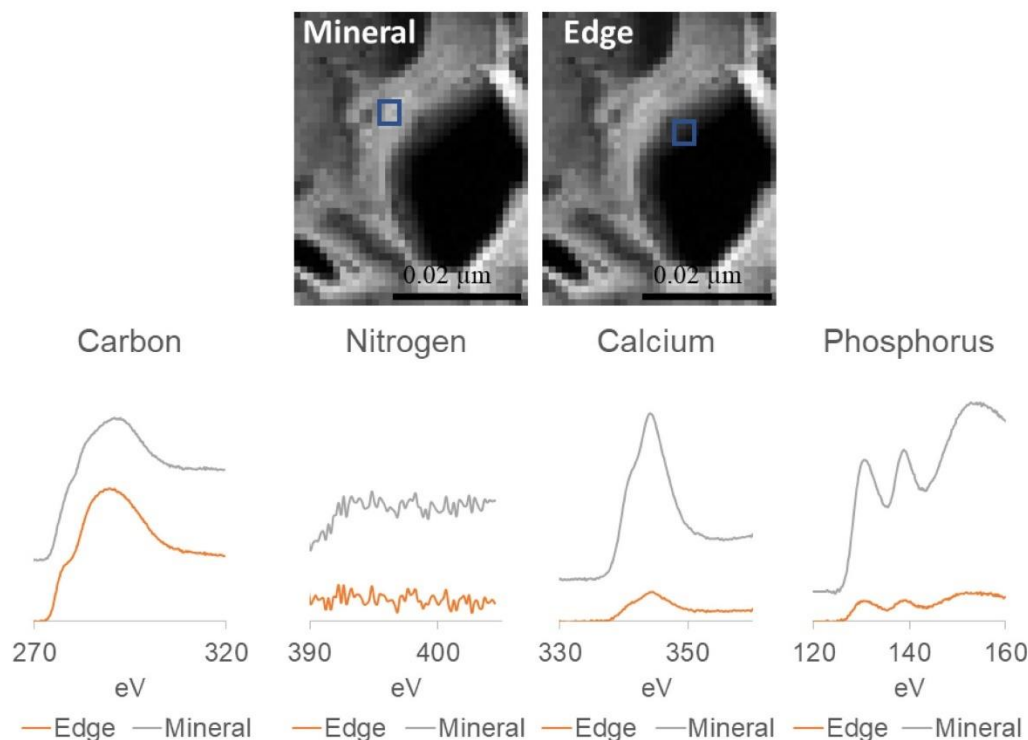

Fig. 3. EELS spectrum images of a single hole-like feature in a cross section of cow bone prepared by ion milling, showing the EELS edge spectra for C, N, Ca and P, as recorded at two positions on the image: at the edge of the hole ("Edge"), and in the mineral matrix surrounding the hole ("Mineral"). The y-axis is arbitrary units and represents only relative intensities of signals.
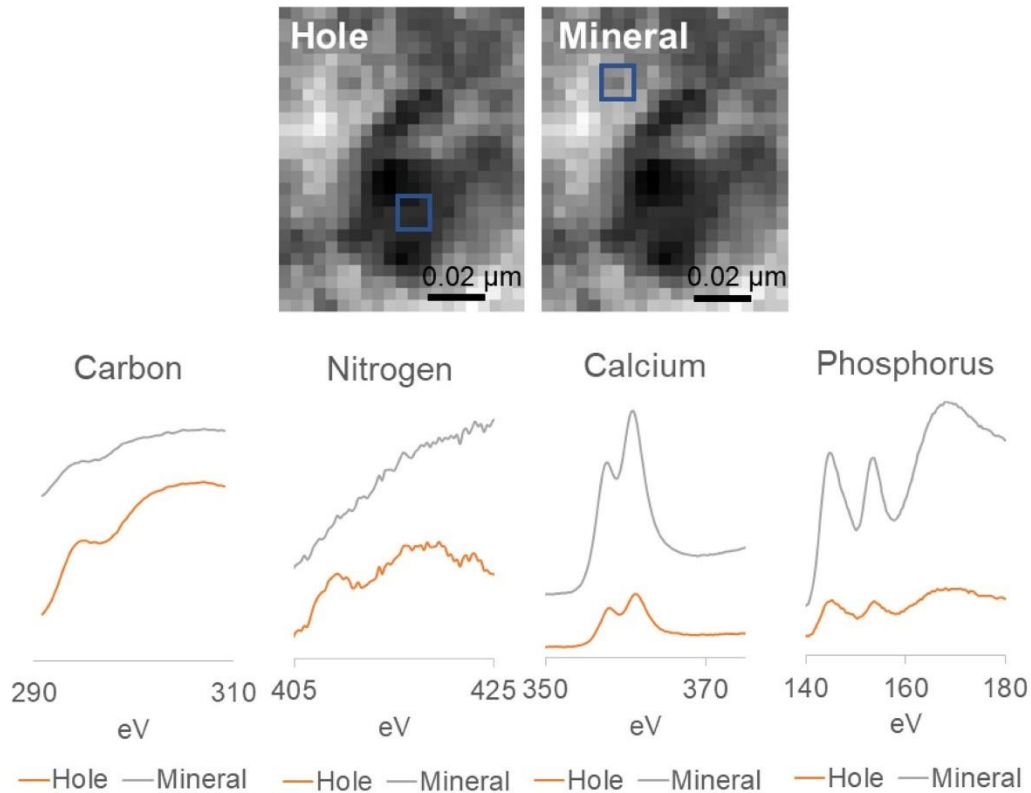
Fig. 4. EELS spectrum images of microtome-cut section of cow bone and EELS spectra for C, N, Ca and P from selected locations: outside hole ("Mineral") and inside hole ("Hole"). The y-axis is arbitrary units and represents only relative intensities of signals.
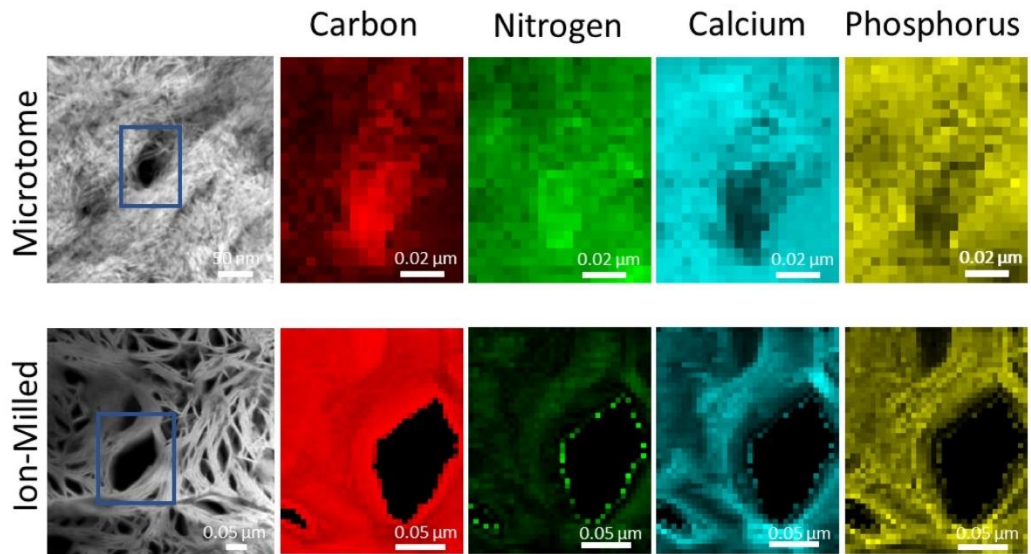

Fig. 5. HAADF images of ion milled and microtome cut sections of cow bone, together with EELS maps of relative intensities of for C, N, Ca and P. It is clear that stronger C and N signals are present in the hole of the microtomed section, likely representing collagen.

4

this material, and the EELS spectrum for one of them is shown in Fig. 4.

The EELS spectra for Ca and P and for C in the mineral outside the hole are similar to those for the ion milled section. The relative intensities of Ca and P are again greater in the mineralized region compared to in the hole, but are nevertheless still present in the same bonding states in both locations. For carbon, there is a relative increase in signal intensity in the hole region compared to the mineral region, suggesting an additional contribution to the signal above the background formvar grid. There is a very minor peak in the shoulder following the initial primary peak which has been attributed to aromatic groups or from collagen crosslinking (Bhattacharyya et al., 2002; Leinweber et al., 2007). The broad peak following the initial peak and shoulder is attributed to carbonate bonding. Similar carbon structures were also shown by Kłosowski et al.(2017, Supporting information). Unlike with the ion-milled sample, there are well-defined nitrogen peaks in the microtomed section. The bonding structure appears different in the mineral region compared to the hole region. The presence of two distinct nitrogen peaks, similar to the observations in the carbon edge, can be considered contribution from aromatic rings or collagen (Bhattacharyya et al., 2002; Leinweber et al., 2007). Additionally, other authors have shown that specific amino acids such as glycine and proline, both involved in collagen structure, have dual broad peaks (Plekan et al. (2007)) and these peaks could potentially be attributed to these amino acids as well.

3.3. Comparative maps of element abundance

To provide additional evidence on whether or not collagen was present in the holes of the sectioned bone, EELS maps showing the relative abundance of the four elements for which we had collected spectral data were collected. These are shown in Fig. 5, which also shows corresponding HAADF images. As was mentioned previously, there is a lack of recognizable mineral lamellae in the HAADF image of the microtome-cut sample.

The figure shows that significantly higher concentrations of both carbon and nitrogen are present in the hole of the microtome-cut section, compared with the levels outside the hole. This is consistent with spectral analysis. The relative intensity of the Ca and P EELS signals in the holes is less than the surrounding region but both Ca and P are still very evident in the hole.

In contrast, the hole shown in the ion milled section is devoid of any of the elements for which we measured EELS intensity. The surrounding area shows a high carbon content which can be partly attributed to the carbon coating as well as other sample preparation methods. This is consistent with previous observations that the ion beam milling process selectively removes collagen from these holes.

4. Discussion

TEM images of ion-milled sections of cortical bone cut normal to the axes of collagen fibrils typically display open regions which appear to be holes in the section. The content of these holes is debated within the bone structure community. This work shows, via EELS spectra in microtome-cut sections, that the contents of the holes appear to have carbon and nitrogen constituents consistent with characteristic EELS peaks for collagen, which suggests that there is indeed collagen present in these holes. It follows that this material could be assumed to be collagen as this is the most abundant organic material in bone. The disadvantage of using such sections is that the diamond knife used to cut them causes significant damage to the structure of bone (McNally et al., 2012; Schwarcz, 2015a), leading to breakage of the relatively brittle mineral lamellae into small fragments. However, in sections cut normal to the axes of collagen fibrils, the circular form of these fibrils can still be detected (McNally et al., 2012; Rubin et al., 2003). Nevertheless, we noted that many of the holes in the microtome-cut sections were also either empty or only partially filled with organic material.

These data show that the holes identified in cross sections of bone may not be as empty as has been claimed by some authors (Reznikov et al., 2014a)). The findings of our work are more in line with what was first suggested by Jantou et al.,(2009) who state that these circular or elliptical features appear to be cross sections of collagen fibrils. Subsequent work has suggested that the collagen fibrils tend to be eroded away by the ion beam in both ion and focused ion beam milling sample preparation (McNally et al., 2012; Grandfield et al., 2018). A complicating and unavoidable factor is of course bone sample preparation, which often involves fixation, staining, dehydration, and embedding. In this work we attempted to limit sample processing to dehydration, embedding and post-staining, the effects of which we can safely identify via elemental analysis.

The hypothesis that these circular structures represent collagen fibrils is not particularly outlandish when one considers other independent evidence. First, it is well known that collagen constitutes about 25 wt% of bone (Arnold et al. 2001) which, due to the lower density of collagen compared to mineral, corresponds to about 50 volume percent. This logic suggests that in any section of bone a substantial area should be occupied by collagen fibrils; in the cross sectional views shown here it is apparent that the only place where these could be located would be in the hole-like structures. Reznikov et al. (2014b) argue that the holes seen in the images shown by Cressey and Cressey (2003) and McNally et al. (2012) would only be found in what they refer to as disordered material, rather than ordered, normal bone. However, in every section which we have made, where the plane of the section is normal to the fibril axes, we have seen holes like those discussed in this paper (e.g., Grandfield et al., 2018)). While it is possible that every section of bone the authors have prepared was fortuitously of disordered material, it is unlikely that all these randomly positioned sections were of disordered bone, which makes up only a few percent of bone (Reznikov et al., 2014a, 2014b).

5. Conclusions

Elemental analysis is a key component to understanding the ultrastructural organization of bone. By sectioning bovine bone normal to its long axis we were able to observe hole-like features that EELS analysis suggests are indeed collagen fibrils. Specifically, the presence and chemical bonding of nitrogen in these regions is consistent with collagen. This work has also identified that the method of preparing bone sections has a drastic influence on the interpretation of bone ultrastructure, where ion milled sections are completely devoid of material in these holes while ultramicrotomy disrupts mineral. A careful optimization of bone sample preparation for TEM that maintains collagen and mineral may be possible by focused ion beam methods.

Acknowledgements

References

Alexander, B., Daulton, T.L., Genin, G.M., Lipner, J., Pasteris, J.D., Wopenka, B., Thomopoulos, S., 2012. The nanometre-scale physiology of bone: steric modelling and scanning transmission electron microscopy of collagen-mineral structure. J. R. Soc. Interface 9, 1774–1786. https://doi.org/10.1098/rsif.2011.0880.

Arnold, S., Plate, U., Wiesmann, H.P., Stratmann, U., Kohl, H., Höhling, H.J., 2001. Quantitative analyses of the biomineralization of different hard tissues. J. Microsc. 202, 488–494. https://doi.org/10.1046/j.1365-2818.2001.00831.x.

Bhattacharyya, S., Lubbe, M., Bressler, P.R., Zahn, D.R.T., Richter, F., 2002. Structure of nitrogenated amorphous carbon films from NEXAFS. Diam. Relat. Mater. 11, 8–15. https://doi.org/10.1016/S0925-9635(01)00525-8.

Cressey, B.A., Cressey, G., 2003. A model for the composite nanostructure of bone

suggested by high-resolution transmission electron microscopy. Mineral. Mag. 67, 1171–1182. https://doi.org/10.1180/0026461036760156.

Grandfield, K., Vuong, V., Schwarcz, H.P., 2018. Ultrastructure of bone: hierarchical features from nanometer to micrometer scale revealed in focused ion beam sections in the TEM. Calcif. Tissue Int. 103, 606–616. https://doi.org/10.1007/s00223-018-0454-9.

Jantou-Morris, V., Horton, M.A., McComb, D.W., 2010. The nano-morphological relationships between apatite crystals and collagen fibrils in ivory dentine. Biomaterials 31, 5275–5286. https://doi.org/10.1016/j.biomaterials.2010.03.025.

Jantou, V., Turmaine, M., West, G.D., Horton, M.A., McComb, D.W., 2009. Focused ion beam milling and ultramicrotomy of mineralised ivory dentine for analytical transmission electron microscopy. Micron 40, 495–501. https://doi.org/10.1016/j.micron.2008.12.002.

Katz, E.P., Li, H., 1973. Structure and function of bone Collagen Fibrils. J. Mol. Bio. 80, 1–15 https://doi.org/https://doi-org.libaccess.lib.mcmaster.ca/10.1016/0022-2836(73)90230-1.

Kłosowski, M.M., Abellan, P., Ramasse, Q., Mccomb, D.W., Porter, A.E., Shefelbine, S.J., 2017. Electron Microscopy Reveals Structural and Chemical Changes at the Nanometer Scale in the Osteogenesis Imperfecta Murine Pathology. pp. 2788–2797. https://doi.org/10.1021/acsbiomaterials.6b00300.

Kłosowski, M.M., Carzaniga, R., Shefelbine, S.J., Porter, A.E., Mccomb, D.W., 2018. Nanoanalytical electron microscopy of events predisposing to mineralisation of turkey tendon. pp. 1–11. https://doi.org/10.1038/s41598-018-20072-2.

Kłosowski, M.M., Friederichs, R.J., Nichol, R., Antolin, N., Carzaniga, R., Windl, W., Best, S.M., Shefelbine, S.J., Mccomb, D.W., Porter, A.E., 2015. Acta Biomaterialia Probing carbonate in bone forming minerals on the nanometre scale 20, 129–139. https://doi.org/10.1016/j.actbio.2015.03.039.

Landis, W.J., Song, M.J., 1991. Early mineral deposition in calcifying tendon characterized by high voltage electron microscopy and three-dimensional graphic imaging. J. Struct. Biol. 107, 116–127. https://doi.org/10.1016/1047-8477(91)90015-O.

Leinweber, P., Kruse, J., Walley, F.L., Gillespie, A., Eckhardt, K., Blyth, I.R., Regier, T., 2007. Nitrogen K -edge XANES – an overview of reference compounds used to identify "unknown" organic nitrogen in environmental samples. J. Synchrot. Radiat. 500–511. https://doi.org/10.1107/S0909049507042513.

McEwen, B.F., Song, M.J., Landis, W.J., 1991. Quantitative determination of the mineral distribution in different collagen zones of calcifying tendon using high voltage electron microscopic tomography. J. Comput. Assist. Microsc. 3, 201–210.

McNally, E.A., Schwarcz, H.P., Botton, G.A., Arsenault, A.L., 2012. A model for the ultrastructure of bone based on electron microscopy of ion-milled sections. PLoS One. https://doi.org/10.1371/journal.pone.0029258.

Nalla, R.K., Porter, A.E., Daraio, C., Minor, A., Radmilovic, V., Stach, E., Tomsia, A., Ritchie, R., 2005. Ultrastructural examination of dentin using focused ion-beam cross-sectioning and transmission electron microscopy. Micron 36, 672–680. https://doi.org/10.1016/j.micron.2005.05.011.

Plekan, O., Feyer, V., Richter, R., Coreno, M., de Simone, M., Prince, K.C., Carravetta, V., 2007. An X-ray absorption study of glycine, methionine and proline. J. Electron Spectros. Relat. Phenomena. https://doi.org/10.1016/j.elspec.2006.11.004.

Reznikov, N., Shahar, R., Weiner, S., 2014a. Three-dimensional structure of human lamellar bone: The presence of two different materials and new insights into the hierarchical organization. Bone 59, 93–104. https://doi.org/10.1016/j.bone.2013.10.023.

Reznikov, N., Shahar, R., Weiner, S., 2014b. Bone hierarchical structure in 3 dimensions. Acta Biomater. 10, 3815–3826. https://doi.org/10.1016/j.actbio.2014.05.024.

Rubin, M.A., Jasiuk, I., Taylor, J., Rubin, J., Ganey, T., Apkarian, R.P., 2003. TEM analysis of the nanostructure of normal and osteoporotic human trabecular bone. Bone 33, 270–282. https://doi.org/10.1016/S8756-3282(03)00194-7.

Schwarcz, H.P., 2015a. The ultrastructure of bone as revealed in electron microscopy of ion-milled sections. Semin. Cell Dev. Biol. 46. https://doi.org/10.1016/j.semcdb.2015.06.008.

Schwarcz, H.P., 2015b. The ultrastructure of bone as revealed in electron microscopy of ion-milled sections. Semin. Cell Dev. Biol. 46, 44–50. https://doi.org/10.1016/j.semcdb.2015.06.008.

Srot, V., Bussmann, B., Salzberger, U., Koch, C.T., van Aken, P.A., 2012. Linking microstructure and nanochemistry in human dental tissues. Microsc. Microanal. 18, 509–523. https://doi.org/10.1017/S1431927612000116.

Tertuliano, O.A., Greer, J.R., 2016. The nanocomposite nature of bone drives its strength and damage resistance. Nat. Mater. 15, 1195–1202. https://doi.org/10.1038/nmat4719.

Wang, X., Langelier, B., Shah, F.A., Korinek, A., Bugnet, M., Hitchcock, A.P., Palmquist, A., Grandfield, K., 2018. Biomineralization at titanium revealed by correlative 4d tomographic and spectroscopic methods. Adv. Mater. Interfaces. https://doi.org/10.1002/admi.201800262.

Weiner, S., Arad, T., Traub, W., 1991. Crystal organization in rat bone lamellae. FEBS Lett. 285, 49–54. https://doi.org/10.1016/0014-5793(91)80722-F.

Appendix 2: Dual-topography Electrical Discharge Machining of Titanium to Improve Biocompatibility.

Lee, B. E. J., Ho, S., Mestres, G., Karlsson Ott, M., Koshy, P., & Grandfield, K. (2016). Dual-topography electrical discharge machining of titanium to improve biocompatibility. *Surface and Coatings Technology*, *296*, 149–156.

This paper provides an example of a surface modification technique capable of creating a random dual-topography on the surface of titanium using electrical discharge machining. Using two different currents and a hierarchical multi-current, three different surfaces were generated. The use of a multi-current approach resulted in a unique dual-topography surface. This dual-topography surface showed improved cell differentiation at 7 days compared to other surfaces. This work is a complementary to my study of titanium surface modification in this thesis. I wrote the initial manuscript draft, conducted x-ray diffraction experiments, and performed x-ray diffraction and auger electron spectroscopy analysis. *In vitro* tests were performed by Gemma Mestres under the supervision of Marjam Karlsson Ott. Surface modification was performed by Samantha Ho under the supervision of Phil Koshy, and materials characterization by Samantha Ho. This paper has been published in Surface & Coatings Technology.

Contents lists available at ScienceDirect

Surface & Coatings Technology

journal homepage: www.elsevier.com/locate/surfcoat

ELSEVIER

Dual-topography electrical discharge machining of titanium to improve biocompatibility

CrossMark

Bryan E.J. Lee [a], Samantha Ho [b], Gemma Mestres [c], Marjam Karlsson Ott [c], Philip Koshy [d], Kathryn Grandfield [a,b,*]

[a] School of Biomedical Engineering, McMaster University, Hamilton, Canada
[b] Department of Materials Science and Engineering, McMaster University, Hamilton, Canada
[c] Department of Engineering Sciences, Uppsala University, Uppsala, Sweden
[d] Department of Mechanical Engineering, McMaster University, Hamilton, Canada

ARTICLE INFO

ABSTRACT

Surface modifications of titanium are widespread in an effort to improve the osseointegration capabilities of the metal for orthopaedic and dental applications. Here, electrical discharge machining (EDM) was used to create modified, notably, dual-topography surfaces on titanium. By swapping conventional copper electrodes for a titanium electrode and water dielectric, modified surfaces free of trace element contaminants were produced. Three surfaces were produced by varying the peak currents at 10 A, 29 A and a uniquely hierarchical multi-current combination of 29 A followed by 2.4 A. The physicochemical properties of these surfaces were analyzed by scanning electron microscopy (SEM), Energy Dispersive X-Ray Spectroscopy (EDX), and Auger Spectroscopy. These revealed the topography of the modified surfaces and a titanium oxide layer that was markedly thicker on the EDM samples compared to controls. *In vitro* cell testing was carried out with osteoblast-like MC3T3-E1 cells. Cell differentiation was increased in all EDM modified surfaces compared to controls and early differentiation was promoted on the dual-topography surface. The present study suggests the promise of dual-topography surfaces created using EDM for implant applications.

© 2016 Elsevier B.V. All rights reserved.

1. Introduction

Due to its widespread use in the medical industry as an implant material, titanium has been modified extensively with the goal of improving osseointegration, where both the surface chemistry and topography are known to contribute to the attachment of bone tissue to implanted devices [1]. In particular, roughened or porous surfaces are known to stimulate cellular attachment, differentiation and bone growth [2–4], while the naturally occurring titanium oxide surface layer provides biocompatibility. Numerous techniques have been examined for these purposes, such as sandblasting, acid-etching treatments, ion coating, laser-modification and plasma spraying for applications in dentistry and orthopaedics [4–11].

Electrical discharge machining (EDM), a non-conventional machining technique, is one such method that has previously been applied to titanium with the goal of improving its osseointegration capabilities [12–15]. EDM is a precision material removal process that utilizes the heat generated from controlled, rapid and repetitive spark discharges to remove small volumes of material by melting and vaporization, altering the surface topography and roughness in

the process. The tool and workpiece electrodes are separated by a small gap of several micrometers filled with a dielectric fluid, across which a high-frequency pulsed voltage is applied to strike the discharges. While metallic materials, such as titanium, can be difficult to cut due to their hardness and strength, the lack of direct contact between the electrode and workpiece allows for effective machining by EDM [16–20].

Die sink EDM has been previously used to change the surface composition and roughness of titanium-based implants for bone applications [12,17,21,22]. However, previous studies utilized copper or graphite electrodes with hydrocarbon oil or deionized water dielectrics for EDM surface modification for bone applications [19,20]. These studies found that significant quantities of copper and/or carbon compounds were incorporated into the titanium surfaces [19,20,23]. In addition to being undesirable from a biological standpoint, these carbon deposits can form a mechanically detrimental hard layer of TiC on the EDM modified surfaces [13,23–25]. In addition to a biocompatible surface oxide, the length scale of surface topographies is crucial for bone integration. Multi-length scale surfaces with features ranging from micron, to submicron, and to the nano-scale have been shown to enhance implant-bone biomechanical stability and integration [26–28]. Until presently, hierarchical EDM surfaces for bio-applications were yet to be explored.

In this study, EDM modification of Grade II commercially pure titanium was employed with a titanium electrode and distilled

* Corresponding author at: School of Biomedical Engineering, McMaster University, Hamilton, Canada.
E-mail address: kgrandfield@mcmaster.ca (K. Grandfield).

water dielectric fluid to create a micro-roughened surface with a contaminant-free titanium oxide surface chemistry, ideal for bone interfacing implant applications. Notably, a dual-topography surface was explored, where sub-micron features were imposed on micron features by using a sequential multi-current discharge machining protocol. Surface characterization and the effect of EDM modification on the biocompatibility and cellular response were evaluated.

2. Materials and methods

2.1. Electric discharge machining

Grade II commercially pure titanium (ASTM B265) was used as the workpiece (the surface to be modified). Specimens were cut to 25 mm × 25 mm × 4.76 mm for surface characterization, while15 mm diameter discs, 0.889 mm thick, were cut for cell testing and Auger Spectroscopy. The samples were machined using die sinking EDM (AgieTron Impact 2 Ram-type EDM System, Agie Ltd, Illinois, USA). The electrode (positive polarity) material was a cylindrical rod (200 mm × Ø 9.53 mm) of Grade II titanium (ASTM B348). While keeping pulse on-time constant at 21 μs at a duty factor of 0.33 and a working voltage of 40 V, two different single peak currents (10 A and 29 A) and a multi-current (29 A followed by 2.4 A) were used in a water dielectric. Within the parameters of the equipment, these were the minimum and maximum currents that could be produced, and thus selected as a starting point for dual-topography machining.

2.2. Surface characterization

Following machining, samples were ultrasonically cleaned in acetone, then ethanol for 15 min respectively and air-dried before any characterization. Sample surfaces were observed using scanning electron microscopy (SEM; JSM-6610LV, JEOL) at an accelerating voltage of 10 kV. In addition, cross sections of each EDM modified surface were prepared by cold mounting, cutting with a precision cutter, grinding with 500, 800, 1200 and 2400 grit SiC paper and polishing with 9 μm diamond suspension and, lastly, colloidal silica with 10 vol% of hydrogen peroxide before viewing in the SEM. A chemical analysis of the surface and cross section was conducted using energy dispersive X-ray spectroscopy (EDS). Auger electron spectroscopy (AES; JAMP-9500F, JEOL) was used for elemental depth profiling of the untreated sample and a representative modified surface, the 10 A EDM surface, performed at a sputtering rate between 0.33 nm/s up to 240 nm/s. X-ray diffraction (XRD) measurements were obtained using a CuKα| rotating anode X-ray generator with parallel-focusing monochromatic optics (Rigaku RU 200) with a CCD area detector (Bruker SMART 6000). The detector distance was 16.74 cm with an exposure time of 1200 s per frame. Microhardness measurements were performed on cross sections by a Vickers hardness tester (MMT-X7, Matsuzawa, Japan) under 50 g load and 15 s dwell time.

2.2.1. Cell culture

The growth and differentiation of osteoblast-like cells on the titanium samples was thoroughly evaluated by seeding the cells on the surface of the material (direct contact assay). Mouse pre-osteoblast-like MC3T3-E1 cells (Subclone 14, ATCC) were used as the cell model. The cells were maintained in cell culture flasks in an incubator with a humidified atmosphere of 5% CO_2 in air at 37 °C. AlphaMEM medium free of ascorbic acid (Life Technologies, Gibco, ref. n. A10490-01, Carlsbad, CA, USA) supplemented with 1% penicillin/streptomycin (Sigma Aldrich, ref. n. P4333, St. Louis, Mo, USA) and 10% fetal bovine serum (Thermo Scientific, HyClone, ref. n. SV30160.03, Logan, UT, USA) was used as culture medium. The medium was renewed every second day. Upon confluence, cells were detached with a minimum amount of trypsin 0.25% in EDTA (Thermo Scientific, HyClone, ref. n. SH30042.02) and it was inactivated with supplemented medium after 10 min.

Ti samples were sterilized with isopropanol 70% for 2 h with gentle shaking after which the samples were washed 5 times with autoclaved distilled water (5 × 10 min agitation). The samples were placed in 24 well plates and 19 100 cells were seeded on each disk (10 000 cells/cm^2). Wells without cells were used as blank readings. The media employed for the experiment was Alpha MEM Modification (Thermo Scientific, Hyclone, ref. n. SH30265.01) and it was replaced (500 μl) every two days. From day 3 onwards an osteogenic media was prepared by supplementing the MEM Alpha Modification with 1% of 2.5 mg/ml L-sodium ascorbate (Sigma, ref. n. A-7631) and 1 M glycerophosphate (Sigma, ref. n. G-9422) just before adding the media to the cells. After 3, 7 and 14 days, the cell growth and cell differentiation was quantified. Triplicates were used and the experiment was performed twice.

2.2.2. Cell viability

Cell viability was evaluated using an AlamarBlue® assay (Invitrogen, ref. n. DAL1100, Carlsbad, CA, USA). AlamarBlue® or resazurin, is a known indicator of cell viability which is irreversibly reduced by metabolically active cells to its oxidized form resorufin which fluoresces. In each 24 well plate, the old media was replaced by 350 μl of 5% Alamar Blue/MEM (Life Technologies, Gibco, ref. n. 51200). After incubation in the dark for 1 h at 37 °C, fluorescence was measured on a microplate reader (Infinite M200, Tecan, Männedorf, Switzerland) at 560 nm excitation and 590 nm emission. The blank fluorescent value was subtracted from each data point which allowed the fluorescent signal to directly correspond to cell number. Afterwards, wells were washed with a phosphate buffered saline solution (PBS) and 300 μl of a lysis solution (0.1% triton in PBS) was added. The well plate was frozen at −20 °C and three freeze-thawing cycles were performed to further quantify total amount of proteins and alkaline phosphatase.

2.2.3. Protein quantification

The total amount of proteins was quantified by a microBCA® assay (Thermo Scientific, ref. n. 23235). 25 μl of cell lysis and 25 μl microBCA reagents (prepared as indicated by the manufacturer) were incubated in dark at 37 °C for 2h. Finally, 50 μl of distilled water was added in every well and absorbance was measured at 562 nm in the microplate reader. A standard curve was prepared with different concentrations of bovine serum albumin (BSA, provided in the microBCA® kit). The blank reading was subtracted from every data point and absorbance was transformed to concentration of BSA.

2.2.4. Cell differentiation — alkaline phosphatase activity assay

The cell differentiation was quantified by measuring the alkaline phosphatase (ALP, Sigma Aldrich, ref. n. P7998) activity, an early marker of osteoblast differentiation that is expressed just before matrix mineralization begins [29]. Cell lysis (50 μl) and ALP reagent (100 μl) were incubated together in dark at room temperature. The reaction was stopped after 20 min with 3M NaOH and absorbance was measured at 405 nm. A standard curve was prepared with different concentrations of p-nitrophenol (Sigma, ref. n. N7660). Blank was subtracted from every data, absorbance was transformed to concentration of p-nitrophenol and data were normalized by the total number of proteins and the reaction time.

2.3. Statistical analysis

Statistical analysis was done using IBM SPSS Statistics 19 software (IBM, Chicago, IL, USA) using one-way ANOVA at a significance level of α = 0.05. Scheffe's post-hoc test was used in the case of homogeneity of variances (Levene's test); otherwise, Tamhane's post-hoc test was chosen.

3. Results

3.1. Surface topography

The surface topography of the EDM modified surfaces can be seen in Fig. 1. All peak currents created surfaces with a random distribution of porous features not observed on unmodified substrates. Larger pores and greater amounts of resolidified molten material were observed at higher peak current, 29 A, EDM (Fig. 1B). On the multi-current (Fig. 1C) surface, a dual topography can be observed where the smaller features from the 2.4 A current appear to be superimposed upon the larger ablations from the 29 A current. Microcracks are present on all EDM modified surfaces, which were likely formed due to thermal stresses. Cross-sections of all EDM samples in SEM, as shown in Fig. 2, reveal that cracks of thicknesses between 2 and 10 μm penetrated the surface layers of all EDM modified samples. Adjustment of the EDM parameters and post-EDM heat treatments could potentially reduce the significance of these cracks. Microhardness values, shown in Fig. 3, from Vickers hardness testing showed that there were statistically significant differences (Two-way ANOVA, $p < 0.05$) in the hardness between all surfaces. The microhardness decreased with increasing penetration depth (up to 150 μm) for all surfaces and the range of microhardness values (HV) across all surfaces was between 190 to 230 HV. All EDM modified surfaces had statistically significant lower average microhardness values compared to the control surface (Untreated > 10 A > 29 A > 29 A + 2.4 A). There was notable variation in the microhardness for all surfaces, which may be a result of the varied topography observed under SEM.

3.2. Surface chemistry

Chemical analysis of the surface layer was performed using both EDS and AES. EDS mapping of the multi-current surface in Fig. 4 confirmed that the surface layer contains titanium oxide, which is expected due to the presence of H_2O during machining. A corresponding elemental

spectrum for the area shown in Fig. 4 can be seen in Fig. 5. AES depth profiling in Fig. 6 highlights the main elements detected. Besides a few nm of surface carbon (~35 wt.%), which is representative of naturally occurring adsorbed carbon-contamination, appreciable amounts of carbon or other contaminants were not present in the surface. This indicates a more contaminant-free surface chemistry was achieved by using water during EDM, as opposed to hydrocarbon (petroleum) based dielectrics. An enrichment of oxygen and titanium oxide, which can be detected separately with AES, were present within the first minute of sputtering time in both untreated and 10 A EDM surfaces. After this enrichment, which can be attributed to the naturally occurring oxide formation on titanium, the untreated surface showed a rapid decrease in oxygen content towards pure Ti after just 2 min sputtering time, at an estimated depth of 25 nm. The EDM surface however, plateaued at a significantly higher oxygen and oxide atomic percentage, indicating a continued oxide layer past the initial surface. This composition remained constant and the sputtering speed was slowly ramped up from 0.33 nm/s up to 240 nm/s to analyse deeper into the specimen. No further compositional changes were seen in the EDM surface after up to 36 min of sputtering and analysis. This result is expected and corroborated by the cross-sectional SEM images of approximately 5–10 μm thick oxide layers on all of the EDM surfaces, including on the 29 A and 29 A + 2.4 A surfaces not investigated by AES. X-ray diffraction measurements for the 29 A, 29 A + 2.4 A and untreated titanium surfaces can be seen in Fig. 7. The measurements showed the presence of TiO with two different crystal structures, one of which was only found in the EDM modified surfaces. TiO — Hongquiite was found on all three surfaces with the peak being extremely miniscule for the untreated surface and relatively strong peaks at approximately 37° and 43° for the EDM modified surfaces. Titanium oxide with a hexagonal crystal structure ($TiO_{0.325}$) was found on all surfaces with its peaks roughly corresponding to the placement of the base titanium peaks (35°, 37°, 40°, 52° and 63°). However, the magnitude of the $TiO_{0.325}$ peaks was noted to be much larger compared to the base titanium at all 2θ values. There were no notable differences between the EDM modified surfaces with regards to crystal structure.
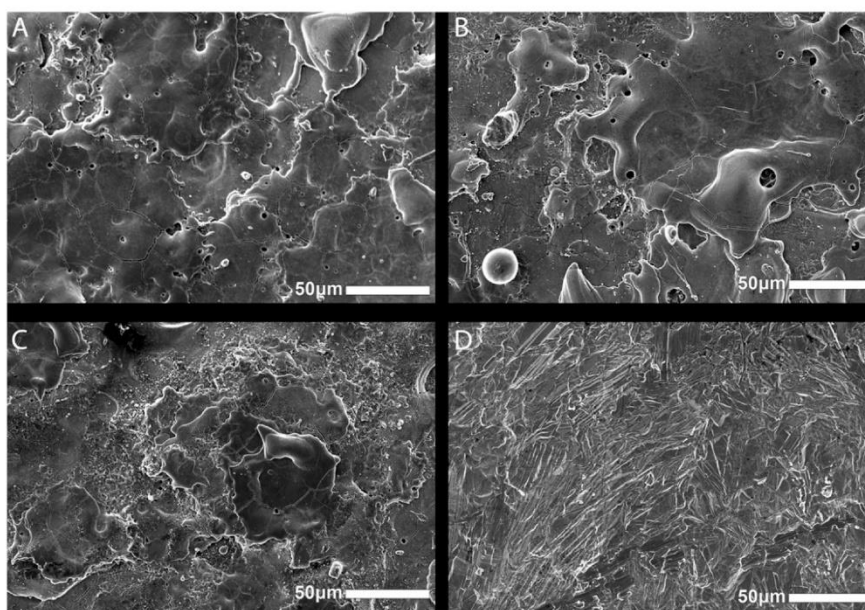

Fig. 1. SEM images of EDM modified titanium surfaces with different peak currents: A) 10 A, B) 29 A, C) multi-current 29 A + 2.4 A, D) untreated. The multi-current surface of C) shows both micron large craters, created by the 29 A current, and smaller sub-micron features superimposed from the 2.4 A current.
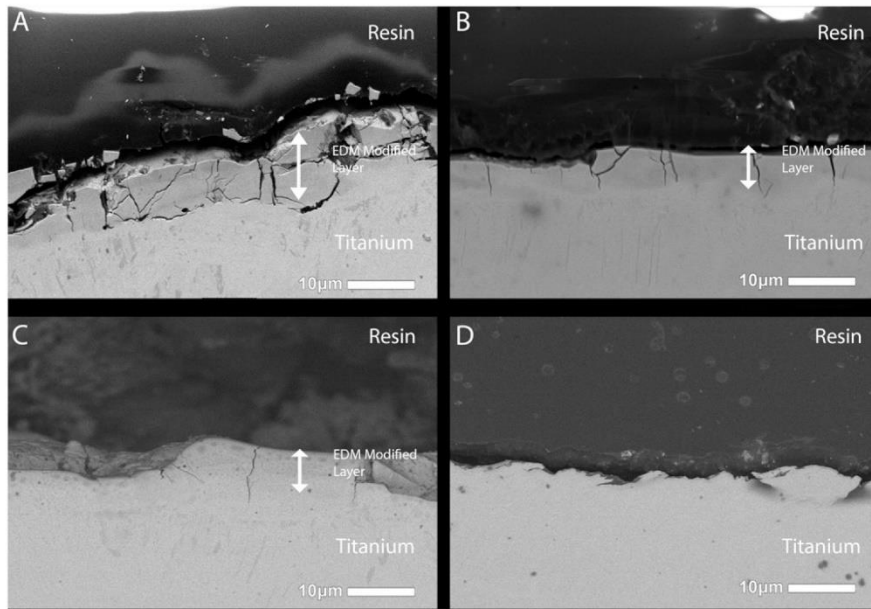
Fig. 2. Back-scattered electron images of cross sections of EDM modified titanium surfaces with different current: A) 10 A, B) 29 A, C) 29 A + 2.4 A, D) untreated. The lighter contrast of the EDM surface oxide layer enables its quick and easy identification with a thickness ranging from 5 to 10 μm (marked by arrows), compared to the complete lack of this layer on the native untreated titanium.

3.3. Cell viability

The number of viable cells on each surface was directly correlated with the fluorescent signal of AlamarBlue® (Fig. 8). Whereas the cell number decreased slightly between 3 and 7 days ($p > 0.05$ for all samples except for 10 A and 29 A), the number of cells significantly increased between 7 and 14 days ($p < 0.05$). No statistical differences ($p > 0.05$) were detected within the EDM modified titanium samples at any time point.
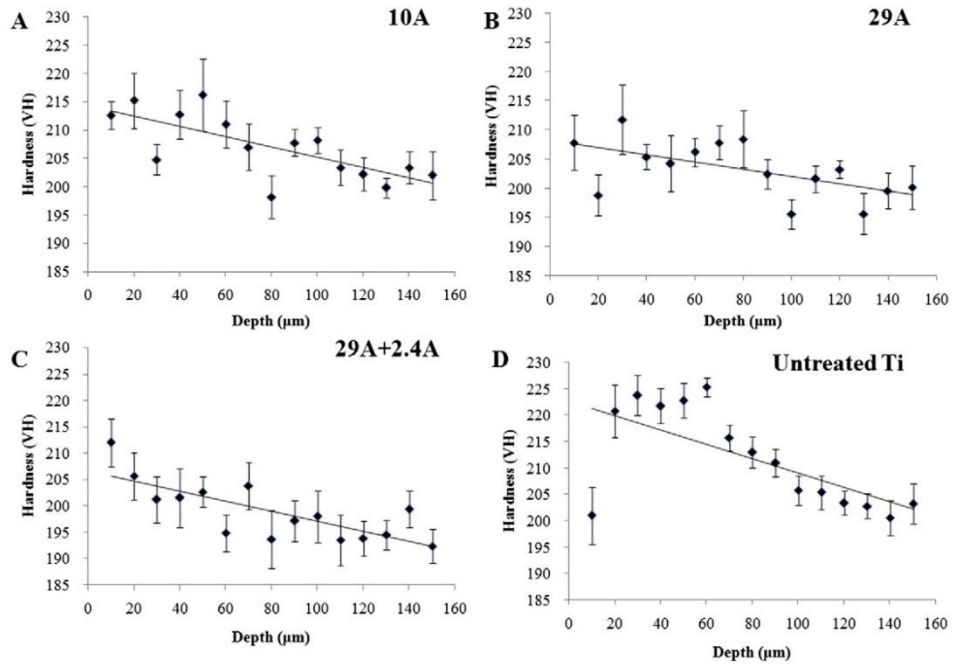

Fig. 3. Average Vickers microhardness values from the surface to a depth of 150 μm for A) 10 A, B) 29 A, C) 29 A + 2.4 A and D) untreated titanium. Average microhardness decreased with increased penetration depth with the overall hardness not compromised by the EDM treatment.
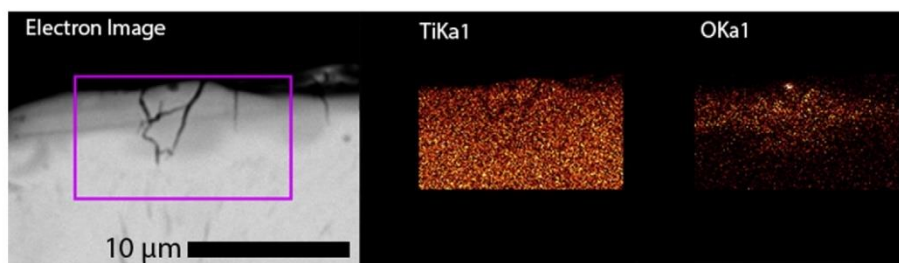
Fig. 4. EDS elemental mapping representing the distribution of Ti and O throughout the multi-current EDM surface. EDS confirms the formation of titanium oxide layer several microns thick. Some cracks may be present as a result of EDM machining, while others may be due to the rigorous cross-sectioning method employed.

3.4. Cell differentiation

The cell differentiation (ALP activity was normalized using quantity of proteins, from BSA assay, and the reaction time) showed a steady increase ($p < 0.05$) with time for the majority of samples (Fig. 9). Only the untreated and 10 A EDM surface did not show a statistical increase between 3 and 7 days ($p > 0.05$). No statistical differences between samples were detected at day 3 ($p > 0.05$). After 7 days, the subsequent trend was observed ($p < 0.05$): 29 A + 2.4 A > 29 A > 10 A ~ Ti. However, following 14 days of cell growth, all EDM Ti surfaces (10 A, 29 A, 29 A + 2.4 A) showed a significantly higher ALP activity than the untreated Ti surface ($p < 0.05$) but negligible statistic difference between them.

4. Discussion

EDM represents a novel method to modify titanium for implant-based purposes. The combination of the ease and rapidness at which this technique can be performed are advantageous for industrial implant production. The topography of titanium was successfully altered to create roughened surfaces that visibly distinguish themselves from untreated titanium surfaces. In particular, a dual-topography was generated with the use of multi-current EDM that consisted of micron and sub-micron features. Use of a titanium electrode along with a distilled water dielectric helped avoid the common pitfall where the substrate is contaminated by deposition of elements from the electrode material on to the workpiece.

A major concern with surface modification of titanium is the potential to alter inherent physicochemical properties that make it suitable as an implant material. Studies have shown that the surface integrity of the workpiece is highly dependent on machining parameters such as the peak current and pulse duration [17,30]. Use of higher pulse current and longer pulse duration result in the production of larger and deeper pores in commercially pure titanium, and thus a higher surface roughness [25,31]. In this study, results from EDS and AES showed that the naturally forming oxide layer was substantially enhanced in thickness and that no additional compounds formed on the surface or within the bulk. The increased oxide thickness is due to the resolidification of the melt in the presence of water during the EDM process, favoring formation of titanium oxide. Results from XRD support this by showing that the amount of TiO – Hongquiite and $TiO_{0.325}$ present on the native surface was notably increased following EDM modification. Yet, the presence of microcracks, which we observed in the EDM samples, otherwise absent in untreated titanium, represents an area of potential concern [32]. While some of the cracks viewed in the cross-sectional images may be a result of the embedding, cutting and grinding procedure, some smaller cracks were visible in plane-view images. The presence of these microcracks is likely a contributing factor to the lower average microhardness observed in the EDM modified surfaces compared to the untreated surface. Due to the high thermal stresses induced in the EDM process, surface cracks are typical which can lead to lower fatigue endurance of the workpiece [15,18]. However, it has been found that higher pulse current and shorter pulse durations can reduce surface crack density in Ti–6Al–4V alloys [17], while subsequent heat treatments can improve fatigue endurance and reduce flaw size [33,34]. Another suitable alternative to circumvent the formation of microcracks, while maintaining the surface topography of interest, could be utilizing the EDM surface to create a mold for surface replication or altering machining parameters. As micro-cracking and recast material on EDM surfaces can be detrimental to the performance of an implant, it is essential to control these by limiting the pulse energy in the finishing passes of
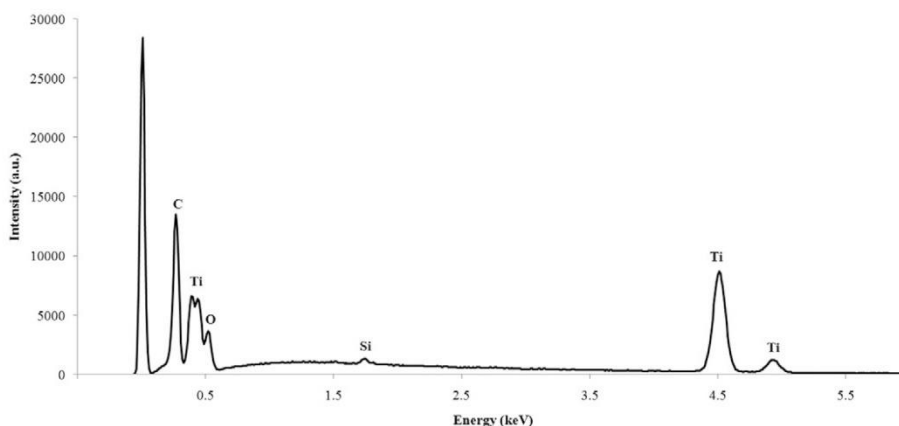

Fig. 5. EDS elemental spectrum corresponding to Fig. 4. The spectrum shows the presence of carbon, titanium, vanadium, oxygen, and silicon.
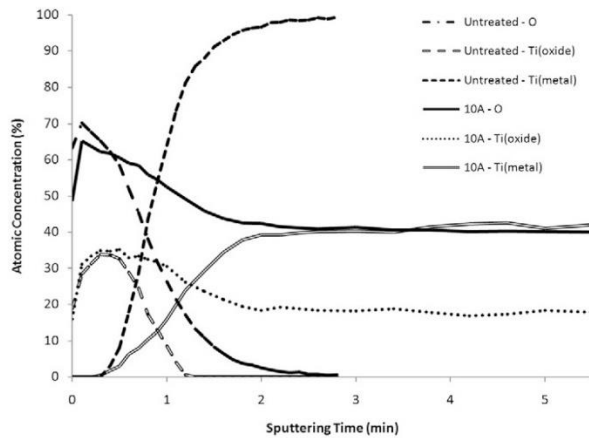
Fig. 6. AES depth profile of EDM modified 10 A and untreated surfaces. Profiles show an immediate drop in oxygen/oxide layer after penetrating the naturally occurring surface oxide layer on untreated samples after just 1–2 min sputtering time corresponding to several nm. Conversely, the 10 A-machined surface shows a sustained oxygen/oxide content well into the depth of the surface, indicating a much thicker surface oxide formed during the EDM process in water.

Fig. 8. Cell proliferation measured by AlamarBlue® assay at 3, 7 and 14 days. EDM surface modification did not adversely affect cell viability.

material removal. By using such a strategy, punches manufactured by EDM have been found to be as reliable as those manufactured by fine grinding [35], and indeed EDM is being used to manufacture safety-critical, highly-stressed rotating jet engine components [36]. In the context of implant manufacture, the challenge is to adapt such a strategy to promote biocompatibility. Additionally, the geometric shape of the titanium used in these experiments is not representative of the shape of a titanium implant that would be used *in vivo*. As such, analysis of microcracks on larger and more clinically relevant substrates would be necessary to determine if the reduced microhardness and microcracks are sufficient to induce failure.
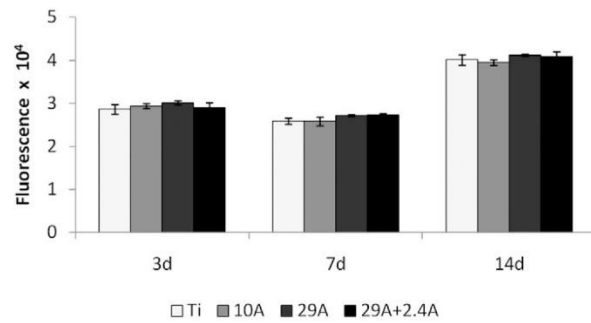
From the biocompatibility standpoint, both cell viability and differentiation were noted to be elevated in the EDM surfaces. While there was no significant difference in cell viability between untreated and EDM modified surfaces, this result confirms that the modification is not cytotoxic. However, there was a significant increase in cell differentiation in the modified surfaces suggesting that cells plated on different surfaces are expressing different phenotypes. This increased cell differentiation is likely related to both the increased surface area and the subsequently increased quantity of titanium oxide resulting from EDM. This is consistent with findings which have shown that increasingly roughened surfaces encourage differentiation of osteoblast-like cells [37–39]. It was also reported by Otsuka et al. that seeding MC3T3-E1 cells on wire EDM modified surfaces showed increased cell proliferation compared to controls [14,15].

While the ablations created with single current EDM themselves showed a degree of improvement, the multi-current EDM surface appears the most promising. The ALP activity (p<0.05) was elevated in the dual-topography surface relative to the 10 A, 29 A and untreated after 7 days. While a significance difference was not noted at 14 days,
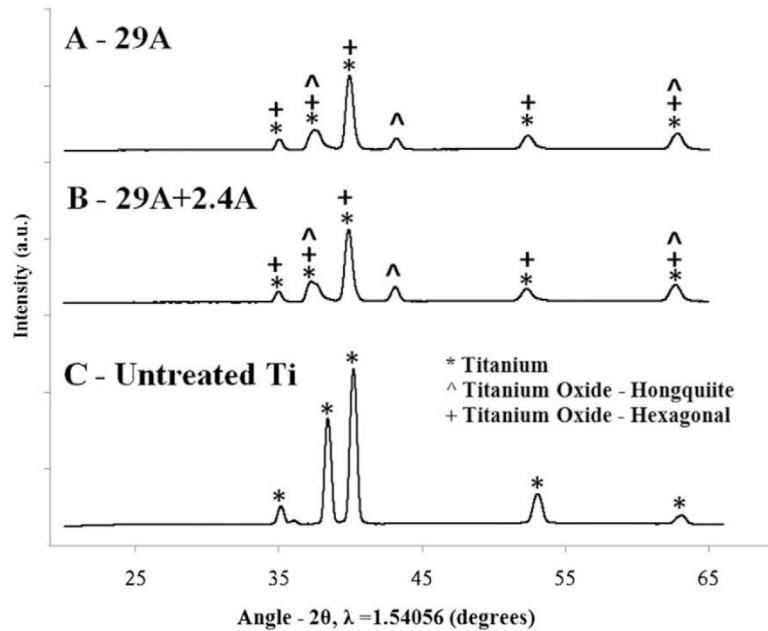

Fig. 7. XRD patterns for A) 29 A, B) 29 A + 2.4 A and C) untreated titanium surfaces. Titanium oxide was the dominate phase created by EDM on both single and multi-current EDM surfaces.
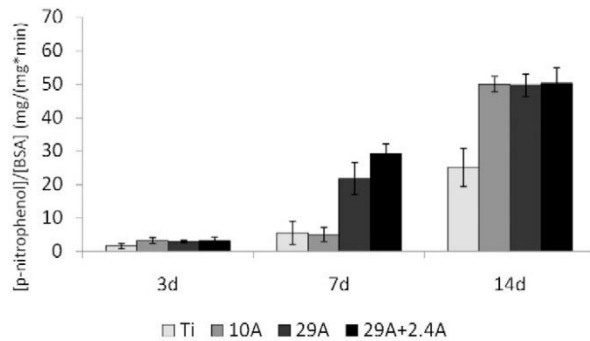
Fig. 9. Cell differentiation measured as [p-nitrophenol]/(cell number * reaction time). The dual-topography 29 A + 2.4 A surface showed statistically significant improvement over untreated and other EDM surfaces at early (7 days) time points.

this could be related to confluence of cells from a high seeding density. Early osseointegration is a key factor in the success of an implant and thus this improvement at 7 days represents a significant advantage for the dual-topography surface in clinical scenarios, perhaps even enabling earlier implant loading. The dual topography with micron and sub-micron features is particularly interesting since microroughened surfaces have previously been found to encourage the differentiation of osteoblasts, while nanoporous structures are known to promote bone in-growth [40–42].

Additional studies on multi-current EDM to elucidate how the surface features facilitate an improved cell differentiation are needed. In addition, other osteoblast-like cells, such as MG-63 cells, have been reported to adhere and proliferate in greater quantities on EDM modified surfaces [10,13]. Therefore, *in vivo* studies are the logical next step to further investigating the osseointegration capabilities of the EDM modified surface. In particular, *in vivo* studies would be necessary to more clearly understand the reasons for improved cell differentiation at early time points on the multi-current dual-topography surface.

5. Conclusions

The feasibility of using electrical discharge machining as a surface modification technique for titanium implant surfaces was demonstrated. In particular, this study highlighted the use of a novel multi-current machining approach to create dual-topography surfaces with both micron and enhanced sub-micron topographies. Cell differentiation with pre-osteoblast-like MC3T3-E1 cells showed that the EDM modified surfaces increased ALP activity compared to untreated titanium, in particular when examining the dual-topography surface. Furthermore, by using a titanium electrode and water as a dielectric versus oil- or petroleum-based baths, the EDM surfaces consisted of a contaminant-free titanium oxide layer. This study demonstrates the potential of using dual-topography EDM on titanium as a surface modification technique for dental and orthopaedic implant applications.

Conflict of interest

The authors declare no conflict of interest.

Acknowledgements

References

[1] Y. Sul, The significance of the surface properties of oxidized titanium to the bone response: special emphasis on potential biochemical bonding of oxidized titanium implant, Biomaterials 24 (22) (Oct. 2003) 3893–3907.
[2] B.D. Boyan, T.W. Hummert, D.D. Dean, Z. Schwartz, Role of material surfaces in regulating bone and cartilage cell response, Biomaterials 17 (2) (Jan. 1996) 137–146.
[3] S.F. Hulbert, F.W. Cooke, J.J. Klawitter, R.B. Leonard, B.W. Sauer, D.D. Moyle, Attachment of prostheses to the musculo–skeletal system by tissue ingrowth and mechanical interlocking, J. Biomed. Mater. Res. 23 (4) (1973) 1–23.
[4] C.M. Bowers, K. T., J.C. Keller, B.A. Randolph, D.G. Wick, Michaels, Optimization of surface micromorphology for enhanced osteoblast responses in vitro, Int. J. Oral Maxillofac. Implants 7 (3) (1991) 302–310.
[5] H.J. Rønold, S.P. Lyngstadaas, J.E. Ellingsen, Analysing the optimal value for titanium implant roughness in bone attachment using a tensile test, Biomaterials 24 (25) (Nov. 2003) 4559–4564.
[6] D. Buser, R.K. Schenk, S. Steinemann, J.P. Fiorellini, C.H. Fox, H. Stich, Influence of surface characteristics on bone integration of titanium implants. A histomorphometric study in miniature pigs, J. Biomed. Mater. Res. 25 (7) (Jul. 1991) 889–902.
[7] L. Thair, U. Kamachi Mudali, S. Rajagopalan, R. Asokamani, B. Raj, Surface characterization of passive film formed on nitrogen ion implanted Ti–6Al–4V and Ti–6Al–7Nb alloys using SIMS, Corros. Sci. 45 (9) (Sep. 2003) 1951–1967.
[8] Y. Yang, J. Tian, L. Deng, J.L. Ong, Morphological behavior of osteoblast-like cells on surface-modified titanium in vitro, Biomaterials 23 (5) (Mar. 2002) 1383–1389.
[9] A. Palmquist, L. Emanuellson, R. Brånemark, Thomsen, Biomechanical, histological and ultrastructural analyses of laser micro- and nano-structured titanium implant after 6 months in rabbit, J. Biomed. Mater. Res. A 97B (2) (2011) 289–298.
[10] Y. Zhao, S.M. Wong, H.M. Wong, H. Pan, K.W.K. Yeung, P.K. Chu, Improved in vitro and in vivo biocompatibility of dual plasma modified titanium alloy, Surf. Coat. Technol. 229 (2013) 130–134.
[11] W. Ma, S.-H. Wang, G.-F. Wu, B.-L. Liu, J.-H. Wei, C. Xie, D.-H. Li, Preparation and in vitro biocompatibility of hybrid oxide layer on titanium surface, Surf. Coat. Technol. 205 (6) (2010) 1736–1742.
[12] P. Harcuba, L. Bačáková, J. Stráský, M. Bačáková, K. Novotná, M. Janeček, Surface treatment by electric discharge machining of Ti–6Al–4V alloy for potential application in orthopaedics, J. Mech. Behav. Biomed. Mater. 7 (Mar. 2012) 96–105.
[13] A. Ntasi, W.D. Mueller, G. Eliades, S. Zinelis, The effect of electro discharge machining (EDM) on the corrosion resistance of dental alloys, Dent. Mater. 26 (12) (Dec. 2010) e237–e245.
[14] F. Otsuka, Y. Kataoka, T. Miyazaki, Enhanced osteoblast response to electrical discharge machining surface, Dent. Mater. J. 31 (2) (2012) 309–315.
[15] C. Prakash, H.K. Kansal, B. Pabla, S. Puri, A. Aggarwal, Electric discharge machining — a potential choice for surface modification of metallic implants for orthopedic applications: a review, Proc. Inst. Mech. Eng. B J. Eng. Manuf. (2015).
[16] B.H. Yan, H.C. Tsai, F.Y. Huang, The effect in EDM of a dielectric of a urea solution in water on modifying the surface of titanium, Int. J. Mach. Tools Manuf. 45 (2) (Feb. 2005) 194–200.
[17] A. Hasçalık, U. Çaydaş, Electrical discharge machining of titanium alloy (Ti–6Al–4V), Appl. Surf. Sci. 253 (22) (Sep. 2007) 9007–9016.
[18] H.-T. Lee, F.-C. Hsu, T.-Y. Tai, Study of surface integrity using the small area EDM process with a copper–tungsten electrode, Mater. Sci. Eng. A 364 (1–2) (Jan. 2004) 346–356.
[19] M. Kunieda, B. Lauwers, K.P. Rajurkar, B.M. Schumacher, Advancing EDM through fundamental insight into the process, CIRP Ann. Manuf. Technol. 54 (2) (Jan. 2005) 64–87.
[20] M. Janeček, F. Nový, J. Stráský, P. Harcuba, L. Wagner, Fatigue endurance of Ti–6Al–4V alloy with electro-eroded surface for improved bone in-growth, J. Mech. Behav. Biomed. Mater. 4 (3) (Apr. 2011) 417–422.
[21] X. Liu, P. Chu, C. Ding, Surface modification of titanium, titanium alloys, and related materials for biomedical applications, Mater. Sci. Eng. R. Rep. 47 (3–4) (Dec. 2004) 49–121.
[22] L. Le Guéhennec, A. Soueidan, P. Layrolle, Y. Amouriq, Surface treatments of titanium dental implants for rapid osseointegration, Dent. Mater. 23 (7) (Jul. 2007) 844–854.
[23] A. Wennerberg, C. Hallgren, C. Johansson, T. Sawase, J. Lausmaa, Surface characterization and biological evaluation of spark-eroded surfaces, J. Mater. Sci. Mater. Med. 8 (12) (1997) 757–763.
[24] S. Zinelis, Surface and elemental alterations of dental alloys induced by electro discharge machining (EDM), Dent. Mater. 23 (5) (May 2007) 601–607.
[25] S. Zinelis, Y.S. Al Jabbari, A. Thomas, N. Silikas, G. Eliades, Multitechnique characterization of CPTi surfaces after electro discharge machining (EDM), Clin. Oral Investig. 18 (1) (Jan. 2014) 67–75.
[26] R. Brånemark, L. Emanuelsson, A. Palmquist, P. Thomsen, Bone response to laser-induced micro- and nano-size titanium surface features, Nanomed. Nanotechnol. Biol. Med. 7 (2) (2011) 220–227.
[27] J.E. Davies, E. Ajami, R. Moineddin, V.C. Mendes, The roles of different scale ranges of surface implant topography on the stability of the bone/implant interface, Biomaterials 34 (14) (2013) 3535–3546.
[28] F.A. Shah, B. Nilson, R. Brånemark, P. Thomsen, A. Palmquist, The bone-implant interface-nanoscale analysis of clinically retrieved dental implants, Nanomedicine 10 (8) (2014) 1729–1737.
[29] J.E. Liu, The osteoblast lineage, in: F. Aubin, J.P. Bilezikian, L.G. Raisz, G.A., Rodan (Eds.), Principles of Bone Biology, Academic Press, San Diego 1996, pp. 51–67.

[30] H.T. Lee, J.P. Yur, Characteristic analysis of EDMed surfaces using the Taguchi approach, Mater. Manuf. Process. 15 (6) (Nov. 2000) 781–806.

[31] W.-F. Lee, T.-S. Yang, Y.-C. Wu, P.-W. Peng, Nanoporous biocompatible layer on Ti–6Al–4V alloys enhanced osteoblast-like cell response, J. Exp. Clin. Med. 5 (3) (Jun. 2013) 92–96.

[32] K. Yokoyama, T. Ichikawa, H. Murakami, Y. Miyamoto, K. Asaoka, Fracture mechanisms of retrieved titanium screw thread in dental implant, Biomaterials 23 (12) (2002) 2459–2465.

[33] J. Stráský, M. Janeček, P. Harcuba, M. Bukovina, L. Wagner, The effect of microstructure on fatigue performance of Ti-6Al–4V alloy after EDM surface treatment for application in orthopaedics, J. Mech. Behav. Biomed. Mater. 4 (8) (Nov. 2011) 1955–1962.

[34] B. Casas, Y. Torres, L. Llanes, Fracture and fatigue behavior of electrical-discharge machined cemented carbides, Int. J. Refract. Met. Hard Mater. 24 (1–2) (2006) 162–167.

[35] B. Lauwers, J.-P. Kruth, W. Eeraerts, Wear behaviour and tool life of wire-EDM-ed and ground carbide punches, CIRP Ann. Manuf. Technol. 54 (2) (2005) 163–166.

[36] F. Klocke, A. Klink, D. Veselovac, D.K. Aspinwall, S.L. Soo, M. Schmidt, J. Schilp, G. Levy, J.P. Kruth, Turbomachinery component manufacture by application of electrochemical, electro-physical and photonic processes, CIRP Ann. Manuf. Technol. 63 (2) (2014) 703–726.

[37] P. Linez-Bataillon, F. Monchau, M. Bigerelle, H.F. Hildebrand, In vitro MC3T3 osteoblast adhesion with respect to surface roughness of Ti6Al4V substrates, Biomol. Eng. 19 (2–6) (2002) 133–141.

[38] S.F. Lamolle, M. Monjo, M. Rubert, H.J. Haugen, S.P. Lyngstadaas, J.E. Ellingsen, The effect of hydrofluoric acid treatment of titanium surface on nanostructural and chemical changes and the growth of MC3T3-E1 cells, Biomaterials 30 (5) (2009) 736–742.

[39] K. Anselme, P. Linez, M. Bigerelle, D. Le Maguer, A. Le Maguer, P. Hardouin, H.F. Hildebrand, A. Iost, J.M. Leroy, The relative influence of the topography and chemistry of TiAl6V4 surfaces on osteoblastic cell behaviour, Biomaterials 21 (15) (2000) 1567–1577.

[40] P.W. Peng, K.L. Ou, H.C. Lin, Y.N. Pan, C.H. Wang, Effect of electrical-discharging on formation of nanoporous biocompatible layer on titanium, J. Alloys Compd. 492 (1–2) (Mar. 2010) 625–630.

[41] N. Tsukimura, N. Kojima, K. Kubo, W. Att, K. Takeuchi, Y. Kameyama, H. Maeda, T. Ogawa, The effect of superficial chemistry of titanium on osteoblastic function, J. Biomed. Mater. Res. A 84 (1) (Jan. 2008) 108–116.

[42] Y. Sugita, K. Ishizaki, F. Iwasa, T. Ueno, H. Minamikawa, M. Yamada, T. Suzuki, T. Ogawa, Effects of pico-to-nanometer-thin TiO$_2$ coating on the biological properties of microroughened titanium, Biomaterials 32 (33) (Nov. 2011) 8374–8384.

Appendix 3: A Bioprinted *in vitro* Model for Osteoblast to Osteocyte Transformation by Changing Mechanical Properties of the ECM.

Lee, B. E.J.*, Shahin-Shamsabadi, A.*, Wong, M, K., Raha, S., Selvaganapathy, R., Grandfield, K. (2019) A Bioprinted *in vitro* Model for Osteoblast to Osteocyte Transformation by Changing Mechanical Properties of the ECM. *Advanced Biosystems.* 1900126. **These authors contributed equally to this work.*

This paper demonstrates how a model of osteocyte-like activity can be generated using bioprinting. Osteoblast-like cells were encapsulated in an alginate hydrogel while being printed on a paper surface. The hydrogels were crosslinked to create gels with two different stiffnesses. This mimics how osteocytes arise from entrapped osteoblasts during the bone remodelling process. Protein production and gene expression of osteocyte-like genes were greater in the stiffer gel with no effect on the viability of the cells. This work is a complementary to my study of improving *in vitro* testing methods in this thesis. A bioprinted model of bone, such as that created herein capable of differentiating osteoblasts to osteocytes, has the potential to be used as an *in vitro* testing platform for other questions in mineralization. This study was conceptualized, designed, and all experiments and data analysis were conducted jointly by Alireza Shahin-Shamsabadi and myself. The manuscript was initially drafted jointly by Alireza Shahin-Shamsabadi and myself. Michael Wong performed polymerase chain reaction (PCR) experiments under the supervision of Sandy Raha. The manuscript was subsequently edited by Ravi Selvaganapathy and Kathryn Grandfield. This paper has been published in Advanced Biosystems and is featured as the back cover.

A Bioprinted In Vitro Model for Osteoblast to Osteocyte Transformation by Changing Mechanical Properties of the ECM

Bryan E. J. Lee, Alireza Shahin-Shamsabadi, Michael K. Wong, Sandeep Raha, Ponnambalam Ravi Selvaganapathy,* and Kathryn Grandfield*

Osteocytes are key contributors to bone remodeling. During the remodeling process, trapped osteoblasts undergo a phenotypic change to become osteocytes. The specific mechanisms by which osteocytes work are still debatable and models that exist to study them are sparse. This work presents an in vitro, bioprinted model based on the previously developed technique, ExCeL, in which a cell-embedded hydrogel is printed and immediately crosslinked using paper as a crosslinker-storing substrate. This process mimics the phenotypical change of osteoblast to osteocyte by altering the mechanical properties of the hydrogel. By printing Saos-2, osteosarcoma cells, embedded in the alginate hydrogel with differing mechanical properties, their morphology, protein, and gene expression can be changed from osteoblast-like to osteocyte-like. The stiffer gel is 30 times stiffer and results in significantly smaller cells with reduced alkaline phosphatase activity and expression of osteoblast-marker genes such as MMP9 and TIMP2. There is no change in viability between cells despite encapsulation in gels with different mechanical properties. The results show that the phenomenon of osteoblasts becoming encapsulated during the bone remodeling process can be replicated using the ExCeL bioprinting technique. This model has potential for studying how osteocytes can interact with external mechanical stimuli or drugs.

1. Introduction

Bone is a dynamic, hierarchical material that actively remodels itself in response to mechanical signals. One of the major con-

stituents of the bone remodeling process is osteocytes, which comes from osteoblasts that were entrapped during the bone remodeling.[1,2] During the remodeling process, osteoblasts are slowly buried by bone matrix which is a combination of collagenous fibers and mineral deposits, otherwise known as osteoid. Over time this osteoid becomes mineralized leading to the formation of new bone tissue with embedded osteoblasts which have now been differentiated into osteocytes. The expression of many proteins differs greatly between osteoblasts and osteocytes despite their shared lineage.[3,4] One of the primary characteristics of osteocytes is that they translate external mechanical cues into biochemical actions which fuels the bone remodeling process, a process termed mechanotransduction.[5] Despite this important role in bone biology, there is a lack of available models or cell lines for in vitro studies of osteocytes role in bone remodeling or their response to stimuli. This is compounded by the fact that most in vitro systems are two dimensional (2D) in nature and incapable of entrapping osteocytes. 2D culture systems are dominant and have been used extensively but often do not accurately represent the in vivo response.[6] This is predominantly due to their dimensional limitations and lack of

B. E. J. Lee, A. Shahin-Shamsabadi, P. R. Selvaganapathy, K. Grandfield
School of Biomedical Engineering
McMaster University
1280 Main Street West, L8S 4L7, Hamilton, Ontario, Canada
E-mail: selvaga@mcmaster.ca; kgrandfield@mcmaster.ca
M. K. Wong, S. Raha
Graduate Program of Medical Science
McMaster University
1280 Main Street West, L8S 4K1, Hamilton, Ontario, Canada
Prof. S. Raha
Department of Pediatrics
McMaster University
1280 Main Street West, L8S 4K1, Hamilton, Ontario, Canada

Prof. P. R. Selvaganapathy
Department of Mechanical Engineering
McMaster University
1280 Main Street West, L8S 4L7, Hamilton, Ontario, Canada
Prof. K. Grandfield
Department of Material Science and Engineering
McMaster University
1280 Main Street West, L8S 4L7, Hamilton, Ontario, Canada

environmental cues that cells would otherwise receive in the physiological environment such as mechanical properties of the extracellular matrix (ECM), nutrient and oxygen gradients, and inter-cellular and cell–matrix interactions.[7,8] Different three dimensional (3D) systems have been developed that yield more accurate responses similar to natural tissues by recapitulating some of these features.[9] Compared to 2D cell culture systems, these 3D models can maintain the phenotype of cells[10] by controlling the polarity of cell–cell and cell–matrix contacts,[11,12] as well as mechanical properties of their environment[11,12] and transport characteristics of important soluble growth factors.[13]

The MLO-Y4 mouse cell line has been most commonly used to study osteocyte behavior with success but they are primarily utilized in 2D in vitro culture methods.[14,15] Other researchers have created a 3D model of osteocytes by embedding human osteoblasts in a mineral matrix comprised of biphasic calcium phosphate similar in composition to that of natural bone but this work has not considered the organic phase.[16] However, the specific mechanical entrapment required to initiate phenotypical changes of osteoblasts to osteocytes has yet to be determined. Many studies involving 3D models for bone or osteocyte-behavior do not consider the specific mechanical properties required to entrap and influence differentiation from osteoblast to osteocyte.[16,17] For a 3D model to be accurate it should exhibit the architectural complexities of native tissue and bioprinting has emerged as a promising technique[18,19] for this purpose. Bioprinting evolved from additive manufacturing methods to use soft materials like gels and extracellular matrices which could support growth of cells and formation of tissue-like constructs.[20,21] Bioprinting has enabled researchers to manufacture complex structures and constructs with biomaterials containing extracellular matrices and cells[21,22] and to reproduce biophysical and biochemical microenvironment in physiological or pathological conditions in a well-defined manner with high accuracy.[18,23,24]

This work investigates how changes in mechanical properties of non-mineralized bone matrix can influence the osteoblast to osteocyte phenotype transformation in a 3D environment using a bioprinting based technique named Combing Extrusion printing on Cellulose scaffolds with Lamination (ExCeL).

2. Methods Summary

A 3D in vitro model was developed using the ExCeL bioprinting technique[25] to study effect of mechanical properties of ECM on osteoblast to osteocyte phenotype transformation. **Figure 1** summarizes this process. First, two different calcium chloride solutions (0.1 and 1 M) were printed, with printing speeds of 1000 and 2000 mm sec^{-1}, respectively, on chromatography paper. The first condition is referred to further as the low calcium (Low-Ca) content paper, and the second high calcium (High-Ca) content paper. The papers were allowed to dry overnight. Subsequently, two different concentrations of alginate (2 and 3 wt% in McCoy's culture medium) embedded with bone cells from the Saos-2 cell line were printed on each of them (2 wt% on Low-Ca (2L) and 3 wt% on High-Ca papers (3H)). Alginate as a material lends itself well to the ExCeL process, which allows for tuning of the gel stiffness, compared to collagen or gelatin.[25] Additionally, it is also the most commonly used hydrogel in bioprinting processes and has seen success printing with Saos-2 cells.[26,27] These hydrogels crosslink immediately upon contact with the paper and reside on top of it thus giving it mechanical properties independent of the paper. The 300 µm tall cylinder shape, calculated from volume of printed hydrogel and covered area, was chosen such that the scaffold would be a homogeneous shape and thus prevent mass transfer induced gas or nutrient gradients which could alter the morphology or phenotype of the cells. It was assumed that 2L condition would yield lower stiffness compared to the 3H condition and hence cells would change to more osteocyte-like phenotype in the 3H samples with higher stiffness. Other conditions were experimented with but did not generate sufficient differences in preliminary protein expression experiment to warrant further investigation (Figure S1, Supporting Information).

Mechanical properties of the two conditions were evaluated and compared using a Microsquisher mechanical tester. Viability of the cells in these conditions was compared using Alamar blue assay (ABA) and live/dead staining kit. Total protein synthesized by cells in each condition, as well as amount of alkaline phosphatase activity, a biomarker of osteoblast cells, was studied using pierce BCA protein and alkaline
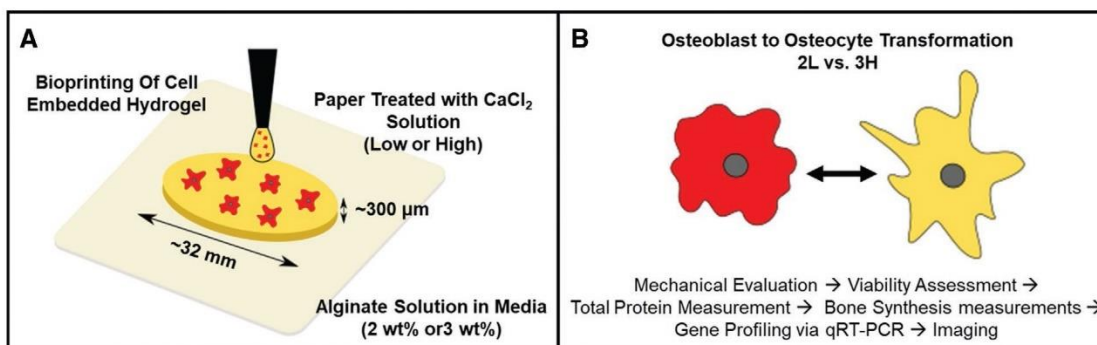

Figure 1. Design of experiment: A) Bioprinting procedure, B) phenotype change confirmation through a series of experiments. Using the ExCeL process, Saos-2 cells are encapsulated in an alginate hydrogel using different amounts of crosslinker and weight percentage to create scaffolds with differing stiffnesses. The encapsulated cells in these scaffolds are subsequently evaluated based on their phenotype.

phosphatase kits. Using Quantitative Reverse Transcription Polymerase Chain Reaction (qRT-PCR) several genes that are highly expressed in either osteoblasts or osteocytes were investigated to further study the phenotype change. SEM of these 3D printed samples was performed to compare morphology of cells in each of these conditions. Fluorescent microscopy of samples stained with DAPI and Nile Red was performed, and cell sizes were compared in different conditions.

3. Experimental Section

3.1. Bioprinting Setup

Development of the 3D in vitro model was performed using the ExCeL process.[28] It started by pretreating the paper (Whatman cellulose chromatography papers, Grade 3 MMCHR) with the alginate crosslinker (calcium chloride solution, Sigma-Aldrich). In order to create the required 3D structures, alginic acid sodium salt (Sigma-Aldrich) solutions were printed in concentric circles that are 1.5 mm apart with the printing speed of 500 mm min^{-1} and hydrogel flow rate of 0.5 mL min^{-1} to form a circle with diameter of 26 mm. Because of the presence of calcium (Ca) on paper, the hydrogel crosslinked rapidly upon touching the paper and maintained the desired pattern. After printing was complete, samples were kept on the printing stage for 10 more min to allow complete crosslinking of the hydrogel and then they were transferred to a 6-well plate, where they were washed with PBS to remove excess amounts of Ca. Eventually samples were soaked in 2 mL culture medium that was changed every 2 days.

3.2. Mechanical Testing

Mechanical properties of the printed structures were evaluated using a MicroSquisher machine (Cell Scale Biomaterials Testing, model). A 2×2 mm stainless steel platen connected to a 0.5 mm diameter cantilever was pressed toward the center part of the hydrogel at a defined rate (10% of the total thickness of the hydrogel per minute) in a displacement-controlled setup. Displacement of the platen was tracked by analyzing images taken by a camera while a load cell connected to the other end of cantilever measured the amount of force exerted by the hydrogel. The force-displacement data were then translated to stress–strain curves and the Young's modulus was defined as the slope of the initial linear range of the diagram. The ratio of Young's modulus of 3H to 2L was reported to compare difference between mechanical properties of the chosen conditions. Five samples were tested for each condition.

3.3. Viability

Saos-2 (ATCC), osteosarcoma, cells were cultured in McCoy's 5A modified medium (Life Technologies Inc) with 15% fetal bovine serum (FBS) (Life Technologies Inc) and 1% penicillin/streptomycin (Life Technologies Inc). Cells were detached

when confluent and mixed with alginate (2 or 3 wt% in McCoy's medium) before printing at a concentration of 2×10^6 cells mL^{-1} alginate solution.

Viability of the cells was assessed using a live/dead assay kit (Molecular Probes, Oregon, USA) where the concentration was 2 μM Calcein AM and 4 μM ethidium homodimer-1 for live and dead, respectively. Media were removed from wells following 1 day of the cells being embedded in the hydrogel matrix and the stain was added for 1 h. Following incubation at 37 °C, the samples were observed using an Olympus BX53F upright light microscope (Olympus, USA) using 475–485/485-536 nm (FITC) and 542–582/582-644 nm (TXRED) filters for the live and dead stains, respectively. Samples were also examined for cell metabolism using an Alamar blue (Life Technologies Inc.) assay following 1 day of incubation. Media were removed from the samples and replaced with a 5% Alamar blue solution (in McCoy's 5A medium). Samples were incubated for 1 h in the dark at 37 °C before measuring fluorescence using an Infinite M200 (Tecan, Männedorf, Switzerland) at 540–580 nm (excitation-emission).

In order to measure the effect of chosen conditions on cell morphology, 7-day old samples were fixed and stained using Nile Red and DAPI. First 10 μL of Nile Red stock solution (10 mg mL^{-1} in acetone) was diluted in 10 mL PBS and 3 mL of this solution was added to each sample followed by 10 min incubation. Then samples were counterstained with 3 mL of working solution of DAPI that was prepared by dissolving 2.9 μL of its stock solution (5 mg mL^{-1} in PBS) in 10 mL PBS. Incubation time for this step was also 10 min. Finally, samples were washed with PBS and imaged using an upright microscope and 10× magnification.

3.4. Protein Assays

Following 4, 7, and 14 days of incubation, hydrogel samples were rinsed with PBS before being dissolved using 3 mL of sodium citrate (0.1 M) on a shaker. 2 mL of the suspended cell solution was aliquoted for PCR while the remaining 1 mL was used for protein assays.

For the protein assays, 1 mL of a 0.1% triton lysis solution (in PBS) was added to each well to lyze the cells. 25 μL from each well was taken (in triplicate) and placed in two different 96-well plates to determine total protein content and alkaline phosphatase activity. A Pierce BCA Protein assay was performed using provided protocol (Thermo Scientific) to determine total protein content. Samples in the BCA 96-well plate were incubated for 30 min with 200 μL of BCA solution. Absorbance readings were taken on an Infinite M200 (Tecan, Männedorf, Switzerland) at 562 nm. The alkaline phosphatase assay was performed using the ALP assay (Abcam). Samples in the ALP 96-well plate were incubated for 20 min with 100 μL of p-nitrophenol phosphate in assay buffer. Absorbance readings were taken on an Infinite M200 (Tecan, Männedorf, Switzerland) at 405 nm. Blank readings were subtracted from each data point of each assay and via the standard curve absorbance values were converted to total protein content and ALP activity for the BCA and ALP assays, respectively.

Table 1. Forward and reverse sequences for the primers used for qPCR.

Gene	Forward	Reverse	GenBank
18S (RNA18S5)	CACGCCAGTACAAGATCCCA	AAGTGACGCAGCCCTCTATG	NR_003286.2
ACTB	TTACAGGAAGTCCCTTGCCATC	GCAATGCTATCACCTCCCCTG	NM_001101.5
GAPDH	TCACCATCTTCCAGGAGCGA	ATGACGAACATGGGGGCATC	NM_001357943.1
ALPL	AGGACGCTGGGAAATCTGTG	CATGAGCTGGTAGGCGATGT	AH005272.2
MMP9	CCGGCATTCAGGGAGACGCC	TGGAACCACGACGCCCTTGC	NM_004994.2
TIMP1	GGGCTTCACCAAGACCTACA	TGCAGGGGATGGATAAACAG	NM_003254.3
TIMP2	GAAGAGCCTGAACCACAGGT	GGGGGAGGAGATGTAGCAC	NM_003255.4

3.5. qRT-PCR

2 mL aliquots were centrifuged at 200 g for 6 min. Supernatant was removed and aliquots were flash-frozen in liquid nitrogen. Total RNA (250 ng) was isolated and reserve-transcribed to cDNA as previously described.[29] Primer sets directed against gene targets of interest were designed through National Center for Biotechnology Information's Primer-BLAST primer designing tool and synthesized at McMaster's Mobix Labs (**Table 1**). Quantitative analysis of mRNA expression was performed via qPCR using SsoAdvanced Universal SYBR Green Supermix (BioRad) and CFX384 Touch Real-Time PCR Detection System (BioRad). The cycling conditions were 95 °C for 10 min, followed by 40 cycles of 95 °C for 10 s and 60 °C for 10 s and 72 °C for 15 s. Relative fold changes were calculated using the comparative cycle times (Ct) method, normalizing all values to the geometric mean of three endogenous control genes (18S, ACTB, GAPDH). The endogenous control gene was selected based on experimentally determined Ct stability across all treatment groups. Given that all primer sets had equal priming efficiency, the ΔCt values for each primer set were calibrated to the average of all control Ct values, and the relative abundance of each primer set compared with calibrator was determined by the formula 2$\Delta\Delta$Ct, in which $\Delta\Delta$Ct was the normalized value.

3.6. Scanning Electron Microscopy

Bioprinted samples were prepared and allowed to incubate for 1 day. Samples were then fixed with 0.25% glutaraldehyde in a sodium cacodylate buffer. Following this, the samples were stained with osmium tetraoxide before being sequentially dehydrated with ethanol starting at 25% (in Milli-Q water) to 100%. Samples were critically point-dried (Leica Microsystems, Wetzlar, Germany) and coated with 5 nm of platinum before being examined under SEM (TESCAN VP. SEM at 10kV). Samples were cut in half using a scalpel blade and imaged in cross section.

3.7. Statistics

Statistical analysis for cell viability, protein assays, PCR, and SEM image analysis was performed using the programing language, R (R Core Team, New Zealand). Protein assays used two-way ANOVA at a significance of $\alpha = 0.05$ and Tukey's HSD

test was used to evaluate contrasts. All other methods were evaluated using the Student's t-test with an accepted statistical significance of $p < 0.05$.

4. Results

4.1. Mechanical Testing

The mechanical properties of the samples were evaluated to determine the difference in Young's modulus between the 2L and 3H conditions using the initial linear region (**Figure 2**). Using Microsquisher testing machine, a platen was pressed against surface of the hydrogel and force applied to the platen and its displacement was measured. Figure 2 shows the stress versus strain diagram for each of the samples. As expected, 3H samples had greater Young's modulus compared to 2L samples (35.8 ± 1.98 MPa vs 1.08 ± 0.56 MPa for 3H and 2L, respectively).
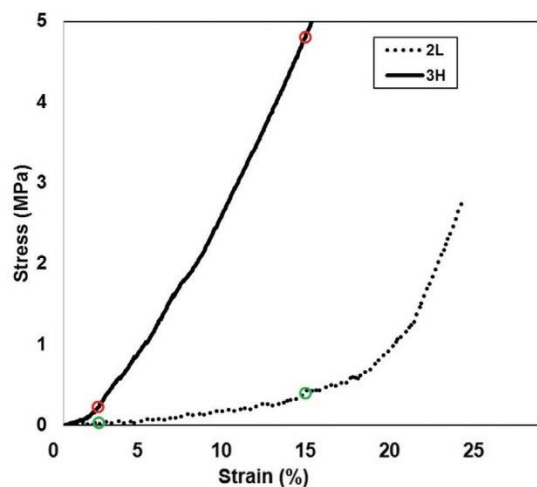

Figure 2. Stress versus strain diagram of 2L and 3H bioprinted samples demonstrating the improved mechanical properties of the 3H compared to 2L samples. The 2L and 3H samples both deform elastically with the 3H (35.8 MPa) being considerably stiffer ($p < 0.05$) than 2L (1.08) for four samples. The red circles indicate the start and end points for determining the modulus of the 3H samples while the green circles do the same for the 2L samples.
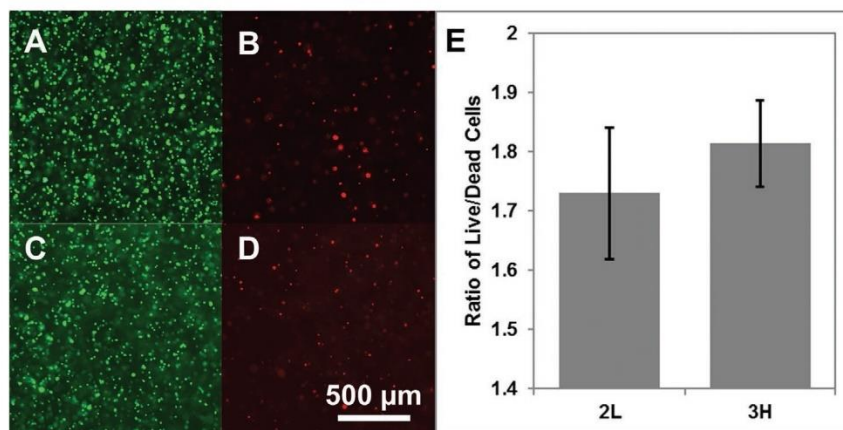
Figure 3. Live/dead stain fluorescent images taken for 2L A,B) and 3H C,D) after 1 day of incubation following bioprinting ($n = 3$). Qualitatively, there are numerous live cells in both 2L and 3H samples and relatively few dead cells. The ratio of live to dead cells through fluorescent readings E) was determined to be statistically the same for 2L and 3H samples.

4.2. Viability

The viability of cells bioprinted within 2L and 3H hydrogels was evaluated using a live/dead stain kit after 1 day of incubation following printing (**Figure 3**). There were numerous live cells in both 2L and 3H samples, indicating that the printing process has a minimal effect on the cell viability. This is confirmed by Figure 3E which shows that there is no difference in the ratio of live to dead cells ($p < 0.05$) between 2L and 3H samples. There is noticeable autofluorescence in the images which is a consequence of the printing process as the cellulose-based paper fluoresces significantly. As a control, cells were cultured on paper alone and evaluated in terms of cell metabolism after one day of incubation. The results indicate that there is no statistically significant change in metabolism between cells cultured on paper or traditional cell culture polystyrene ($p < 0.05$) (Figure S2, Supporting Information). Cells embedded in the 2L and 3H samples were stained with Nile Red and DAPI and imaged under an upright microscope (**Figure 4**). The cells in the 3H samples were found to be statistically significantly smaller than the cells in the 2L samples ($p < 0.05$ over three
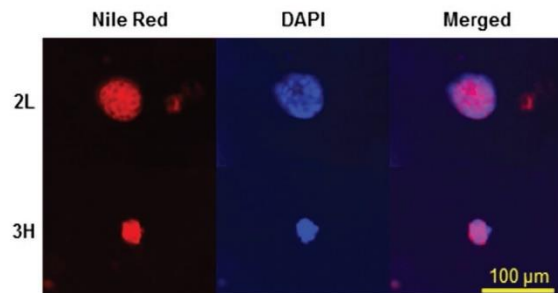
samples). The average diameter, with the cells being modeled as circles, for the 2L and 3H samples were 40.1 and 21.3 µm, respectively. With ten different focal planes being considered in the analysis for each sample, the cells in the 3H samples were found to be 70–80% smaller by area compared to the cells in the 2L samples.

4.3. Protein Assays

2L and 3H samples with cells were evaluated in vitro for alkaline phosphatase (ALP) activity and total protein content (**Figure 5**). Over time, ALP activity showed statistically significant increases from 1 to 4 to 7 to 14 days for 2L ($p < 0.05$). This effect was not observed for the 3H surface where ALP activity was statistically the same across all time points. When comparing between the groups, at the 4, 7, and 14 time points, the 3H samples showed statistically significantly less ALP activity compared to 2L samples ($p < 0.05$). For total protein content, there were no significant differences between 2L and 3H sample groups. When normalizing ALP activity with respect to total protein content, the same statistical effects were observed as were seen in ALP activity alone. This provides additional evidence that comparable amounts of cells were successfully embedded, and viability was the same within the different printed hydrogel samples.

Confirmation that the embedding effect is influencing the change in ALP activity was achieved by comparing ALP activity and total protein content between cells embedded and cells simply cultured on paper for 4 days (Figure S3, Supporting Information). There was no statistically significant difference in ALP activity or total protein content between cells cultured only on the two different calcium treated papers ($p < 0.05$).

Figure 4. Nile Red and DAPI stained A) 2L and B) 3H samples. Saos-2 cells are multinucleated resulting in significant staining of membranes from both Nile Red and DAPI. Cells are visibly and quantifiably smaller in size (20.3 vs 40.1 mm by diameter) in the 3H hydrogel compared to 2L hydrogel.

4.4. PCR

qRT-PCR was performed on 2L and 3H samples after 4 days of incubation. mRNA levels of ALPL, MMP9, and TIMP2 were
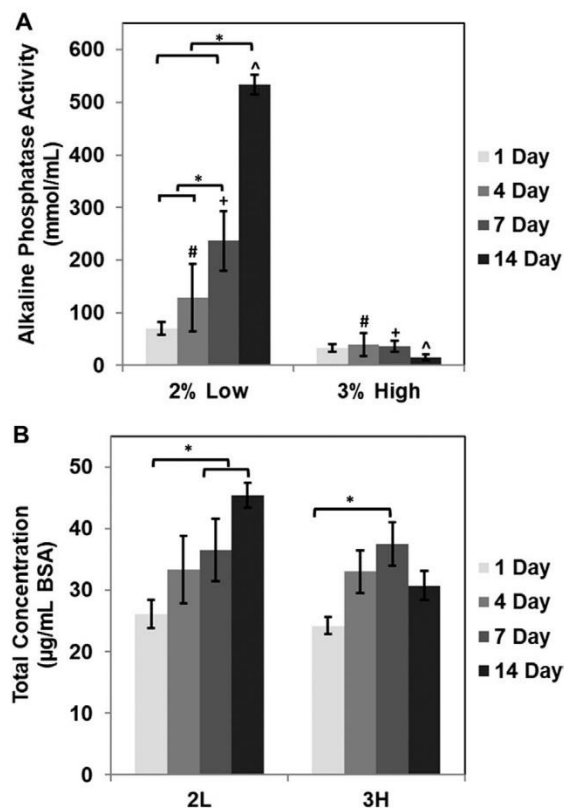
Figure 5. Alkaline phosphatase (ALP) activity, normalized by A) volume and B) total protein content for 2L and 3H samples after 1, 4, 7, and 14 days of incubation ($n = 5$). ALP activity increases over time with 2L samples but remains statistically constant in 3H samples. ALP activity was significantly less in 3H samples at 4, 7, and 14 time points ($p < 0.05$). There are no statistically significant differences in total protein content between samples at each time point.

significantly decreased in 3H samples compared to 2L samples ($p < 0.05$; **Figure 6**A,B,D). mRNA levels of TIMP1 remained unchanged (Figure 6C).

4.5. SEM

2L and 3H bioprinted samples were examined under SEM to observe how cells were embedded within the hydrogel matrix (**Figure 7**). Numerous cells can be identified in cross section and top-down SEM images (**Figure 7**A,B). The cells appear as nodules on the surface and pores are not visible due to the hydrogel thickness being reduced during the dehydration steps required to image in SEM. The cells appear well distributed throughout the matrix and there are cellular processes that appear to extend within the hydrogel matrix (Figure 7C).

5. Discussion

Osteoblast-like cells were successfully encapsulated in hydrogel using an ExCeL bioprinting setup to alter their phenotype to that similar to osteocytes. This change in phenotype was induced by differing hydrogel stiffness as a result of altering the amount of crosslinking agent and hydrogel solution. Two distinct hydrogels, 2L and 3H, were printed with notable differences in Young's modulus under compression. By increasing the stiffness of the matrix, it was hypothesized that osteoblasts would be entrapped and less capable of migration and that this system would encourage a change in phenotype from osteoblast to osteocyte.

The different printing conditions were determined to have no statistically significant effect on the viability of the cells. Other work has identified that materials with differing stiffness can effect cell function, viability and in some cases induce apoptosis,[30,31] however, this was not the case for the 2L and 3H hydrogels used in this work. It was further confirmed by SEM images which demonstrate that cells were distributed across the entirety of the hydrogel matrix with cellular processes extended within the matrix. In natural bone, these extended cellular processes enable osteocytes to communicate with other cells through the lacunar–canalicular network. As such, it is promising that these cellular processes have been preserved and that the osteogenic cells embedded in hydrogel are expressing an osteocyte-like phenotype.

The change in phenotype of osteoblast-like, Saos-2, cells toward that of osteocytes was confirmed via Nile red/DAPI staining, protein assays, and qRT-PCR. Fluorescent staining showed the cells were 70–80% smaller in 3H samples compared to 2L samples. This provides evidence that an osteocyte-like phenotype was induced as other work has shown that mature osteocytes are ≈70% smaller than osteoblasts.[32,33] Alkaline phosphatase (ALP) is an enzyme primarily produced at sites of bone growth and is considered a marker for osteoblastic activity.[34] ALP is also typically not expressed, or weakly expressed, in osteocytes.[16] Protein assays demonstrated that ALP activity was significantly decreased for cells printed in the 3H hydrogels without any change in total protein content. This effect, both for ALP activity and total protein content, was observed over time up to 14 days suggesting that the cells maintain their altered phenotype in the designed system. qRT-PCR confirmed this change in expression as the ALPL gene was significantly down-regulated at the mRNA level for cells encapsulated in the 3H hydrogel. mRNA levels of MMP9 and TIMP2 were also significantly down-regulated in 3H samples, which suggests a reduction in cell migration[30,31] and further supports that the Saos-2 cells are encapsulated by the hydrogel matrix. MMP9 and TIMP2 are known to be markers of bone remodeling,[35,36,28] as increased expression of both genes have been observed at sites of bone remodeling or high osteoblastic activity.[35,36] Mouse in vivo studies conducted by others indicate that TIMP2 may inhibit osteoblastic differentiation into osteocytes,[37] while emphasizing the importance of the MMP family for proper transformation of osteoblasts
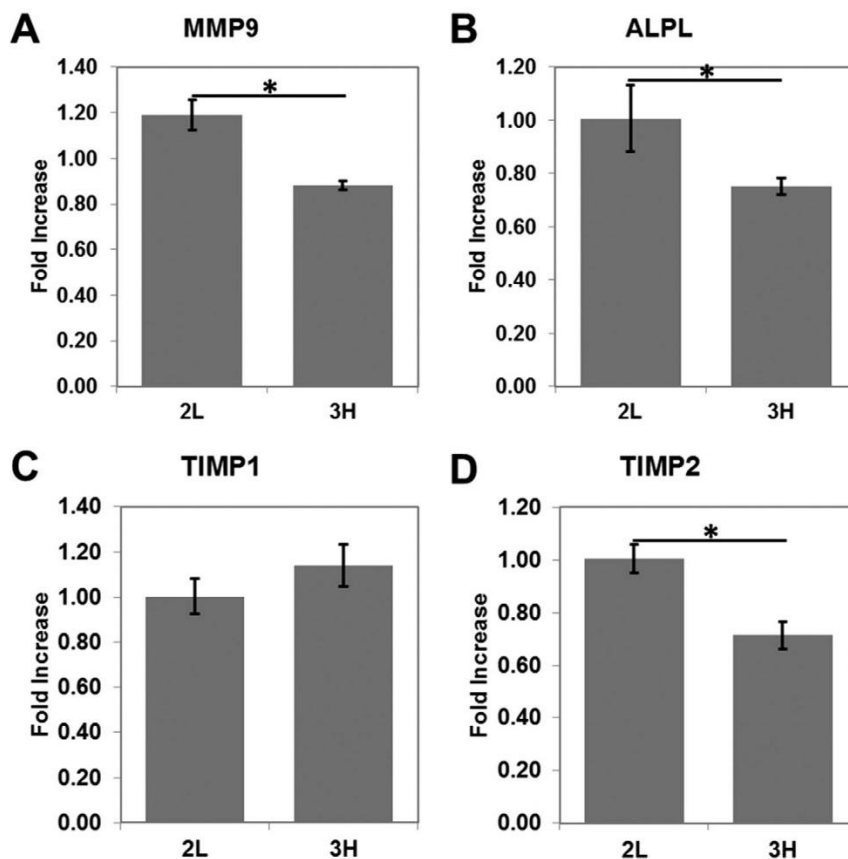
Figure 6. Normalized fold increases of A) ALPL, B) MMP9, C) TIMP1, and D) TIMP2 genes from qRT-PCR of 2L and 3H samples. There were statistically significant decreases ($p < 0.05$, *) in expression of ALPL, MMP9, and TIMP2 genes in the 3H samples compared to 2L samples.

into osteocytes.[38] These studies are in agreement with the decreased TIMP2 expression observed in 3H samples compared to 2L samples. Similarly, the balance of expression between the two is important as an imbalance of MMP to TIMP genes has been suggested to lead to bone loss.[36] These changes in expression, at the protein and gene level, indicate that the different mechanical properties between the 2L and

3H hydrogel are capable of inducing osteoblast-like to osteocyte-like differentiation.

This work used Saos-2 cells, an immortalized cell line considered a good model for osteoblast activity.[34] These cells are generally considered incapable of differentiating into other types of cells, osteocytes included,[34] and as such, this work represents the first step toward the development of a model for
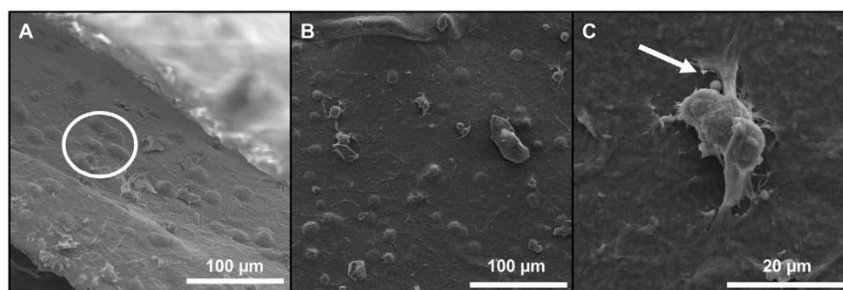

Figure 7. SEM images demonstrating how embedded cells are organized within the hydrogel matrix. Cells embedded (white circle) in 2L samples can be viewed in A) cross section and B) top-down and are well-distributed. Cellular processes (white arrow) from the cells that extend into and within the matrix can also be observed in C).

osteocyte differentiation. Future iterations would require either bone mesenchymal stem cells or primary human osteoblasts to identify how the phenotype of these cells could be adjusted by modulating the mechanical properties of the printed hydrogels. Mesenchymal stem cells could be differentiated into osteoblasts using known methods, such as dexamethasone treatment, and subsequently encapsulated in the process described in this work.[39] The modulus of the scaffolds, while noticeable different from each other, does not approach the known modulus of bone which is typically estimated to be between 7–30 GPa.[40] The current scaffolds do not have any mineral present beyond what is produced by the cells, so future work could see the addition of hydroxyapatite to simulate the mineral presence in bone and subsequently stiffen the material.[16] Additionally, a more physiologically relevant model could be constructed using a co-culture system to characterize the interactions between the various cell types present during bone remodeling.

6. Conclusion

An in vitro model to study osteoblast entrapment was created using a paper-based bioprinting technique. By altering the amount of crosslinking in an alginate hydrogel, two gels with drastically different Young's moduli were generated. When osteoblast-like cells were bioprinted, the stiffer gels resulted in smaller cells without any decrease in overall cell viability. The alkaline phosphatase activity was greatly reduced in the stiffer hydrogel while the total protein content remained the same. Similarly, expression levels of osteoblast relevant genes were all reduced in the stiffer hydrogel, which along with the reduced size and protein expression demonstrates that an osteocyte-like behavior has been induced. This in vitro model is a stepping stone toward larger studies of osteocyte-osteoblast behavior that could be explored by interfacing this in vitro model with mechanical stimuli, or by using it as a platform for drug discovery, or biomaterials testing to observe complex bone cell behavior.

Supporting Information

Supporting Information is available from the Wiley Online Library or from the author.

Acknowledgements

Conflict of Interest

The authors declare no conflict of interest.

Keywords

[1] T. A. Franz-Odendaal, B. K. Hall, P. E. Witten, *Dev. Dyn.* **2006**, *235*, 176.
[2] S. L. Dallas, L. F. Bonewald, *Ann. N. Y. Acad. Sci.* **2010**, *1192*, 437.
[3] F. Paic, JC. Igwe, R. Nori, MS. Kronenberg, T. Franceschetti, P. Harrington, L. Kuo, DG. Shin, DW. Rowe, SE. Harris, I. Kalajzic, *Bone* **2009**, *45*, 682.
[4] M. Capulli, R. Paone, N. Rucci, *Arch. Biochem. Biophys.* **2014**, *561*, 3.
[5] R. Civitelli, *Arch. Biochem. Biophys.* **2008**, *473*, 188.
[6] K. Duval, H. Grover, LH. Han, Y. Mou, AF. Pegoraro, J. Fredberg, Z. Chen, *Physiology* **2017**, *32*, 266.
[7] B. M. Baker, C. S. Chen, *J. Cell Sci.* **2012**, *125*, 3015.
[8] D. Anton, H. Burckel, E. Josset, G. Noel, *Int. J. Mol. Sci.* **2015**, *16*, 5517.
[9] C. M. Nelson, J. L. Inman, M. J. Bissell, *Nat. Protoc.* **2008**, *3*, 674.
[10] A. Abbott, *Nature* **2003**, *424*, 870.
[11] A. Wodarz, I. Näthke, *Nat. Cell Biol.* **2007**, *9*, 1016.
[12] S. J. Morrison, J. Kimble, *Nature* **2006**, *441*, 1068.
[13] F. Coşkun, C. R. Parks, *Pakistan J. Bot.* **2009**, *41*, 1587.
[14] Y. Kato, J. J. Windle, B. A. Koop, G. R. Mundy, L. F. Bonewald, *J. Bone Miner. Res.* **2010**, *12*, 2014.
[15] D. Nicolella, V. Dusevich, M. R. Dallas, J. D. Eick, L. F. Bonewald, *Calcif. Tissue Int.* **2006**, *79*, 340.
[16] F. Boukhechba, T. Balaguer, J. F. Michiels, K. Ackermann, D. Quincey, J. M. Bouler, W. Pyerin, G. F. Carle, N. Rochet, *J. Bone Miner. Res.* **2009**, *24*, 1927.
[17] K. Uchihashi, S. Aoki, A. Matsunobu, S. Toda, *Bone* **2013**, *52*, 102.
[18] I. T. Ozbolat, W. Peng, V. Ozbolat, *Drug Discov. Today* **2016**, *21*, 1257.
[19] W. Peng, D. Unutmaz, I. T. Ozbolat, *Trends Biotechnol.* **2016**, *34*, 722.
[20] G. Gao, Y. Huang, A. F. Schilling, K. Hubbell, X. Cui, *Adv. Healthcare Mater.* **2018**, *7*, 1.
[21] Y. S. Zhang, O. Rahmi, M. R. Dokmeci, A. Khademhosseini, *Cold Spring Harbor Perspect.* **2017**, *8*, a025718.
[22] S. Noh, *3D Bioprinting for Tissue Engineering*, Springer, Singapore **2018**.
[23] H. W. Kang, S. J. Lee, I. K. Ko, C. Kengla, J. J. Yoo, A. Atala, *Nat. Biotechnol.* **2016**, *34*, 312.
[24] J. Jang, H. G. Yi, D. W. Cho, *ACS Biomater. Sci. Eng.* **2016**, *2*, 1722.
[25] A. Shahin-Shamsabadi, P. R. Selvaganapathy, *Biofabrication* **2019**, *11*, 035002.
[26] E. Axpe, M. L. Oyen, *Int. J. Mol. Sci.* **2016**, *17*, 1976.
[27] Q. Feng, X. Wang, HC. Schröder, Q. Feng, B. Diehl-Seifert, T. Ziebart, R. Steffen, S. Wang, WEG. Müller, *Biomaterials* **2014**, *35*, 8810.
[28] E. Kostovski, N. Hjeltnes, E. F. Eriksen, S. O. Kolset, P. O. Iversen, *Calcif. Tissue Int.* **2015**, *96*, 145.
[29] M. K. Wong, S. A. Shawky, A. Aryasomayajula, M. A. Green, T. Ewart, P. R. Selvaganapathy, S. Raha, *PLoS One* **2018**, *13*, e0199632.
[30] J. D. Hood, D. A. Cheresh, *Nat. Rev. Cancer* **2002**, *2*, 91.
[31] G. Murphy, J. Gavrilovic, *Curr. Opin. Cell Biol.* **1999**, *11*, 614.

[32] C. Palumbo, *Cell Tissue Res.* **1986**, *246*, 125.

[33] Y. Sugawara, H. Kamioka, T. Honjo, K. I. Tezuka, T. Takano-Yamamoto, *Bone* **2005**, *36*, 877.

[34] C. Pautke, M. Schieker, T. Tischer, A. Kolk, P. Neth, W. Mutschler, S. Milz, *Anticancer Res.* **2004**, *24*, 3743.

[35] G. Dew, G. Murphy, H. Stanton, R. Vallon, P. Angel, JJ. Reynolds, RM. Hembry, *Cell Tissue Res.* **2000**, *299*, 385.

[36] P. A. Hill, J. J. Reynolds, *Biochim. Biophys. Acta—Mol. Cell Res.* **1993**, *1177*, 71.

[37] M. A. Karsdal, T. A. Andersen, L. Bonewald, C. Christiansen, *DNA Cell Biol.* **2004**, *23*, 155.

[38] K. Holmbeck, P. Bianco, J. Caterina, S. Yamada, M. Kromer, SA. Kuznetsov, M. Mankani, PG. Robey, AR. Poole, I. Pidoux, JM. Ward, H. Birkedal-Hansen*Cell* **1999**, *99*, 81.

[39] A. Khojasteh, MH. Ghahremani, SN. Ostad, M. Eslami, P. Motahhary, G. Morad, S. Shidfar, *Iran. Endod. J.* **2013**, *8*, 118.

[40] Q. Chen, C. Zhu, G. A. Thouas, *Prog. Biomater.* **2012**, *1*, 1.